

2010

## High Strain Rate Response Of Eco-Core And Its Modification.

Raghu Panduranga

*North Carolina Agricultural and Technical State University*

Follow this and additional works at: <https://digital.library.ncat.edu/dissertations>

---

### Recommended Citation

Panduranga, Raghu, "High Strain Rate Response Of Eco-Core And Its Modification." (2010). *Dissertations*.  
7.  
<https://digital.library.ncat.edu/dissertations/7>

This Dissertation is brought to you for free and open access by the Electronic Theses and Dissertations at Aggie Digital Collections and Scholarship. It has been accepted for inclusion in Dissertations by an authorized administrator of Aggie Digital Collections and Scholarship. For more information, please contact [iyanna@ncat.edu](mailto:iyanna@ncat.edu).

# HIGH STRAIN RATE RESPONSE OF ECO-CORE AND ITS MODIFICATION

by

Raghu Panduranga

A dissertation submitted to the graduate faculty  
in partial fulfillment of the requirements for the degree of  
DOCTOR OF PHILOSOPHY

Department: Mechanical and Chemical Engineering  
Major: Mechanical Engineering  
Major Professor: Dr. Kunigal N. Shivakumar

North Carolina Agricultural and Technical State University  
Greensboro, North Carolina  
2010

## ABSTRACT

**Panduranga, Raghu** HIGH STRAIN RATE RESPONSE OF ECO-CORE AND ITS MODIFICATION. (Major Advisor: **Dr. Kunigal N. Shivakumar**), North Carolina Agricultural and Technical State University.

Eco-Core was previously developed as a fire resistant core material for composite sandwich structures. It was made using a large volume of fly ash (Cenosphere) and a small volume of high char yield binder by a syntactic process. The cellular structure of the material offers a potential for shock and blast mitigation applications. Based on the present study, it was concluded that the processing of Eco-Core is repeatable and the static properties are reproducible. Eco-Core was subsequently modified by a surface coating method and an Impregnation method to enhance its energy absorption capability. The modified Eco-Core was characterized by static confined compression tests. Surface coating with polyurea resulted in an improvement in compression strength by 12%; compression modulus by 64%; and energy absorption density by 14%. The impregnation of Eco-Core with polyurethane enhanced the compression strength by 138% with a penalty of increased density and decreased modulus.

The Split Hopkinson Pressure Bar was not available at NC A & T State University for characterizing materials at high strain rates. A compression SHPB test apparatus with 7075 T6 aluminum pressure bars was successfully designed, fabricated, and developed. The SHPB apparatus was verified for 6061-T651 aluminum and polycarbonate specimens and the results were in good agreement with research literature.

The dynamic compressive stress-strain response of Eco-Core was measured over strain rates ranging from 1,000/s to 3,100/s with a split Hopkinson pressure bar apparatus. The SHPB test results showed that Eco-Core is not strain rate sensitive over the range of strain rates studied. Microbubble bond failure followed by crushing are the failure modes of Eco-Core under a dynamic loading. The SEM studies clearly showed that the amount of crushed microbubbles increases with an increasing strain rate and proved that Eco-

Core undergoes a crushing mode of failure at high strain rates. A phenomenological constitutive model was developed for Eco-Core.

The dynamic compressive stress-strain responses of Eco-Core coated with polyurea in different configurations was measured at two strain rates near 3,000/s and 3,900/s. All the PU coated Eco-Core samples showed stress-strain responses similar to that of Eco-Core but with a prolonged densification region. The energy absorption capacity of the Eco-Core and its modification were analyzed and compared with each other. Among all the coating arrangements and thickness, 10-PU front-back Eco-Core samples showed about 51% increase of energy absorption density at a strain rate of 2,500/s. Even a very thin coating (0-thickness) of polyurea on the front side of Eco-Core improved the energy absorption by 33%.

The high strain rate compressive behavior of the polyurethane impregnated Eco-Core was measured over strain rates 1,000/s - 3,200/s. The dynamic plateau stress of impregnated Eco-Core is 2.5 times higher than that of Eco-Core. The impregnated Eco-Core is not sensitive to strain rates below 1,700/s but at strain rates beyond 1,700/s, the impregnated Eco-Core is mildly strain rate sensitive. At strain rates near 3,100/s, polyurethane impregnated Eco-Core samples showed a very significant improvement of approximately 125% increase of energy absorption density in comparison with Eco-Core with a penalty of increased density.

School of Graduate Studies  
North Carolina Agricultural and Technical State University

This is to certify that the Doctoral Dissertation of

Raghu Panduranga

has met the dissertation requirements of  
North Carolina Agricultural and Technical State University

Greensboro, North Carolina  
2010

Approved by:

---

Dr. Kunigal N. Shivakumar  
Major Professor

---

Dr. Vinayak N. Kabadi  
Committee Member

---

Dr. Leonard Uitenham  
Committee Member

---

Dr. Mannur J. Sundaresan  
Committee Member

---

Dr. Dhananjay Kumar  
Committee Member

---

Dr. Samuel Owusu-Ofori  
Department Chairperson

---

Dr. Wanda F. Lester  
Interim Associate Vice Chancellor for Academic Affairs

## **DEDICATION**

After giving praise to God, this dissertation is dedicated to my loving parents, Panduranga Gupta and Vasavambal, without whose love, passion, wisdom, and guidance, I would not be standing where I am today; my wife, Saritha, for her endless love and care and for continuously motivating me to achieve my goals and for abundantly helping me while typing, generating excel tables, and formatting the dissertation.

## **BIOGRAPHICAL SKETCH**

Raghu Panduranga was born on July 22, 1976, in Mysore, India. He received his bachelor's degree in Polymer Science and Technology from Sri Jayachamarajendra College of Engineering affiliated to University of Mysore, India in 1998. He was ranked fourth among 45 graduates. He was offered a prestigious Junior Research Fellowship by University Grants Commission to continue his graduate studies in Plastics Processing at Mumbai University Institute of Chemical Technology (formerly U.D.C.T). He worked in the area of processing of blends, alloys and polymer matrix composites and graduated in 2001 with a M.S (Tech) degree with a GPA of 4.0. In the same year, he joined India's most respected and elite engineering company Larsen & Toubro Limited. He worked more than four years in the area of advanced composite materials with Technology Development arm of the company. He developed several state-of-the-art advanced composite processing technologies which saved more than 3 million USD for the company. He got a patent on A PLANT AND PROCESS TO MANUFACTURE UD PRE-PREG TAPES. He then came to the United States of America for pursuing doctoral studies. In 2005, he joined the Ph.D. program at NCA&TSU and worked at the Center for Composite Materials Research (CCMR).

During his five years at CCMR, he worked in the area of High Strain Rate Characterization of Eco-Core and other composite materials, Shock mitigation response of polyurea coated Eco-Core and other composite materials on a project funded by the Office of Naval Research (ONR) and U. S. Army Research Office (ARO). While pursuing Ph. D, he also worked as Graduate Teaching Assistant and was mentoring undergrad and graduate students in stress and structural analysis using finite element modeling software ANSYS. During his Ph.D. studies, he was awarded five certificates of achievement for his academic excellence in maintaining a 4.0 GPA. He also took a lead role and successfully established state-of-the-art Split Hopkinson Pressure Bar test facility right from scratch at CCMR (first of its kind in the university) for testing high strain rate properties of composite materials, core materials and polymeric materials.

## ACKNOWLEDGMENTS

I would like to express my thanks and deep appreciation to Dr. Kunigal N. Shivakumar, my major advisor, for his constructive guidance, great effort, and valuable advice throughout the entire time it took me to complete this research and write the dissertation. The research program he conducted while I was pursuing my degree was one of the most important and formative experiences of my life. I am profoundly grateful to him for his effective guidance that made it possible for me to complete my degree.

The members of my dissertation committee: Dr. Vinayak N. Kabadi, Dr. Leonard Uitenham, Dr. Mannur J. Sundaresan, Dr. Dhananjay Kumar and Dr. Larry Russell Jr, have generously given their time and expertise to better my work. I thank them for their contribution and their good-natured support.

I would like to acknowledge the financial support of the Office of Naval Research (grant N00014-01-1-1033 and Dr. Yapa Rajapakse) and the U.S. Army Research Office (grant W911NF-04-D-0002 and Dr. Bruce LaMattina).

I thank the Center for Composite Materials Research (CCMR) and the Department of Mechanical Engineering for providing me the opportunity to pursue my Ph.D. degree in Mechanical Engineering in a creative environment.

I am very grateful to Matthew Sharpe, John Skujins, and Robert Sadler for sharing with me their valuable time, effort and expertise, and for providing, whenever needed, technical support and advice. Without their help, the lab work would not have been possible.

I must also acknowledge former and current students of CCMR: Anil Bhargava, Feras Hilmi Darwish, Gowthaman Swaminathan, Paul Akangah, and Jogi Gowda, and CCMR researchers: Dr. Huanchun Chen, and Dr. Shivalingappa Lingaiah, who advised and provided assistance over the years.

Finally, I would like to acknowledge Dr. N. S. Brar at the University of Dayton Research Institute for guiding me in setting up the Split Hopkinson Pressure Bar facility at CCMR, NCAT & SU.

# TABLE OF CONTENTS

LIST OF FIGURES .....	x
LIST OF TABLES.....	xvii
NOMENCLATURE.....	xix
CHAPTER 1. INTRODUCTION .....	1
1.1 Background.....	1
1.2 High Strain Rate Testing of Materials.....	4
1.2.1 Cam Plastometer .....	5
1.2.2 Drop Tower Compression Test.....	6
1.2.3 Split Hopkinson Pressure Bar.....	7
1.2.4 Rod Impact (Taylor) Testing .....	8
1.2.5 Expanding Ring Test .....	9
1.2.6 Flyer Plate Impact.....	10
1.3 History and Development of Split Hopkinson Pressure Bar .....	11
1.4 SHPB Testing of Materials.....	14
1.4.1 Soft Materials.....	14
1.4.2 Brittle Materials.....	15
1.4.3 Syntactic Foam Materials.....	17
1.5 Challenges.....	20
1.6 Objectives of the Research .....	20
1.7 Scope of the Dissertation.....	21
CHAPTER 2. PROCESSING AND CHARACTERIZATION OF ECO-CORE .....	22
2.1 Introduction.....	22
2.2 Materials .....	22
2.3 Processing .....	24
2.4 Mechanical Characterization .....	30
2.4.1 Compression Test.....	32

2.4.1.1	Unconfined .....	32
2.4.1.2	Confined .....	34
2.4.2	Tensile Test.....	35
2.4.3	Flexural Test .....	37
2.4.4	Shear Test .....	38
2.4.5	Fracture Test .....	39
2.5	Results and Discussions .....	41
2.5.1	Unconfined Compression.....	41
2.5.2	Confined Compression .....	42
2.5.3	Tension .....	43
2.5.4	Flexure.....	44
2.5.5	Shear.....	45
2.5.6	Fracture.....	46
2.6	Development of Constitutive Material Model .....	48
2.7	Summary .....	50
<b>CHAPTER 3. PROCESSING AND CHARACTERIZATION OF MODIFIED ECO-CORE.....</b>		<b>51</b>
3.1	Introduction.....	51
3.1.1	Rationale for Modification.....	51
3.2	Materials and Processing .....	52
3.2.1	Coated Eco-Core .....	54
3.2.2	Impregnated Eco-Core.....	55
3.3	Testing .....	57
3.4	Discussion of Results .....	57
3.4.1	Unconfined Compression.....	57
3.4.1.1	Failure Modes .....	60
3.4.2	Confined Compression .....	63
3.4.2.1	Comparison of Energy Absorption Density with Conventional Materials.....	66
3.5	Summary .....	67

CHAPTER 4 DEVELOPMENT OF SPLIT HOPKINSON PRESSURE BAR TEST FACILITY .....	69
4.1 Introduction .....	69
4.2 Operating Principle of a Split Hopkinson Pressure Bar Test .....	69
4.3 Theory of SHPB Test.....	71
4.4 Development of SHPB Test Facility .....	76
4.4.1 SHPB Hardware.....	78
4.4.1.1 Components and Assemblies.....	78
4.5 Calibration of the SHPB System.....	86
4.6 Specimen Configuration and Requirements .....	90
4.7 SHPB Test .....	91
4.7.1 Test Procedure .....	91
4.7.2 Data Recording and Analysis .....	96
4.8 Validation of SHPB Testing.....	98
4.9 Summary .....	105
CHAPTER 5. DYANMIC CHARACTERIZATION OF ECO-CORE AND ITS MODIFICATION .....	106
5.1 Introduction .....	106
5.2 Dynamic Characterization of Baseline Eco-Core.....	106
5.2.1 Sample Preparation.....	106
5.2.2 SHPB Test .....	109
5.2.2.1 Test Procedure .....	109
5.2.2.2 Test Matrix .....	110
5.2.3 Results and Discussions – Baseline Eco-Core.....	111
5.2.3.1 Effect of Specimen Geometry (L/D ratio).....	115
5.2.3.1.1 Dynamic Test for Different L/D Specimens .....	117
5.2.3.1.2 Selection of Specimen L/D based on the Dynamic Force Equilibrium .....	122
5.2.3.2 Effect of Strain Rate .....	126
5.2.3.3 Development of phenomenological constitutive material model .....	132

5.2.3.4 Energy Absorption .....	138
5.3 Dynamic Characterization of Modified Eco-Core.....	141
5.3.1 Polyurea Coated Eco-Core.....	141
5.3.1.1 Sample Preparation .....	141
5.3.1.2 Test Matrix .....	144
5.3.1.3 Results and Discussions – Polyurea Coated Eco-Core .....	145
5.3.1.3.1 Front Face Coated Eco-Core .....	145
5.3.1.3.2 Back Face Coated Eco-Core.....	151
5.3.1.3.3 Front-Back Face (Two-Side) Coated Eco-Core.....	156
5.3.1.3.4 Effect of Coating Thickness on Polyurea Coated Eco-Core .....	162
5.3.1.3.5 Effect of Strain Rate on Polyurea Coated Eco-Core.	164
5.3.1.3.6 Energy Absorption .....	166
5.3.2 Polyurethane Impregnated Eco-Core.....	171
5.3.2.1 Sample Preparation .....	171
5.3.2.2 Test Matrix .....	173
5.3.2.3 Results and Discussions – Impregnated Eco-Core .....	173
5.3.2.3.1 Energy Absorption .....	181
5.4 Comparison of Energy Absorption of Eco-Core and Modified Eco-Core .....	183
5.5 Summary.....	185
<b>CHAPTER 6. CONCLUDING REMARKS AND FUTURE WORK.....</b>	<b>187</b>
6.1 Concluding Remarks.....	187
6.2 Future Work.....	190
<b>BIBLIOGRAPHY.....</b>	<b>191</b>

## LIST OF FIGURES

FIGURES	PAGE
1.1. Strain Rate Regimes and Corresponding Instruments and Experimental Conditions.....	5
1.2. Schematic of Cam Plastometer .....	6
1.3. Schematic of Drop Tower Compression Test System .....	7
1.4. Schematic of Split Hopkinson Bar Apparatus .....	8
1.5. Schematic of Sequence of Events of Classic Taylor Impact Test .....	9
1.6. Schematic of Gas-Gun-Launched Flyer Plate Impact Test Setup .....	11
1.7. Peak Stress Values for Various Syntactic Foam Densities at Different Strain Rates .....	19
2.1. Microscopic Structure of Cenosphere (a) As received (b) Surface washed .....	23
2.2. Process Flow Diagram for Producing Eco-Core from Fly Ash.....	24
2.3. Photograph of Pre-Compacted Cenosphere Mix.....	25
2.4. Photograph of Pre-Heated Cenosphere Mix .....	26
2.5. Laboratory Hot Press and Control Panel .....	26
2.6. Press Curing Cycle .....	27
2.7. Post-Curing Cycle .....	27
2.8. Photograph of the Molded Panel .....	28
2.9. SEM Micrograph of the base Eco-Core (a) 250x (b) 1000x.....	28
2.10. Locations of Dimensional Measurement in a Panel .....	29
2.11. Specimen Configurations .....	31
2.12. Specimen Layout.....	32
2.13. Tensile Specimen Layout.....	33
2.14. Confined Compression Test Set-up .....	36
2.15. Typical Compression Stress-Strain Response of Foam Material .....	36
2.16. Determination of $P_Q$ as per Standard.....	40
2.17. Compression Stress vs. Strain Curve for Eco-Core.....	42

2.18.	Confined Compression Stress vs. Strain Curve for Eco-Core.....	43
2.19.	Tensile Stress vs. Strain Curve for Eco-Core .....	44
2.20.	Flexural Load vs. Displacement Curve for Eco-Core .....	45
2.21.	Shear Load vs. Displacement Curve for Eco-Core .....	46
2.22.	Fracture Load vs. Displacement Curve for Eco-Core .....	47
2.23.	Comparison of Compressive Stress-Strain Curves of Eco-Core from Experiments and from Model Description .....	49
3.1.	Typical Stress-Strain Graph of Polyurea .....	53
3.2.	Typical Stress-Strain Graph of Polyurethane .....	53
3.3.	Photograph of Polyurea Coated Eco-Core Panels .....	54
3.4.	Optical Micrographs of PUR Impregnated Eco-Core (a) Vacuum method (40x) (b) Pressure Method (20x) and (c) Vacuum-Pressure Method (20x).....	56
3.5.	Typical Compression Stress-Strain Plot for Modified Eco-Core .....	59
3.6.	Variation of Compression Strength of Modified Eco-Core with Thickness of PU Coating.....	62
3.7.	Compression Modulus of Modified Eco-Core vs. Thickness of PU Coating.....	62
3.8.	Images of the damage/failure modes for (a) Base Eco-Core; (b) 0-PU; (c) 10-PU; (d) 20-PU; (e) 40-PU; and (f) PUR Impregnated Eco-Core.....	63
3.9.	Typical Confined Compression Stress-Strain Plot for Modified Eco-Core .....	64
3.10.	Variation of Energy Absorption Density of Modified Eco-Core with Thickness of PU Coating .....	65
3.11.	Comparison of Energy Absorption Density vs. Density for Various Foams.....	67
4.1.	Schematic of SHPB Test Apparatus .....	70
4.2.	Typical Strain Signal for Aluminum Specimen (Al 6061-T651-1) in a Split Hopkinson Pressure Bar Test .....	71
4.3.	One-Dimensional Wave Propagation Analysis in SHPB .....	72
4.4.	Photograph of SHPB Test Apparatus.....	78
4.5.	Incident and Transmission Bars Supported on Pillow Blocks .....	79
4.6.	Pillow Block (a) Front View (b) Opened .....	80
4.7.	Simple Free Body Diagram of the Striker Bar.....	80
4.8.	Gas Gun Assembly .....	82

4.9.	Top View of Breech Assembly.....	83
4.10.	Pneumatic Control Panel.....	83
4.11.	Gas Gun Remote Control.....	83
4.12.	Laser Velocity Detection System (a) Photograph (b) Schematic .....	84
4.13.	Half-Bridge Circuit along with Shunt Calibration Resistor ( $R_c$ ) for SHPB Apparatus .....	85
4.14.	Strain Gage Signal Conditioner .....	86
4.15.	Digital Storage Oscilloscope .....	86
4.16.	Strain Data Acquisition System.....	86
4.17.	Velocity-Pressure Calibration Curve for the SHPB Apparatus .....	88
4.18.	Calculation of Wave Speed in a SHPB Experiment.....	90
4.19.	SHPB Test Apparatus .....	91
4.20.	Station A and Schematic of Assembly of Striker Bar into the Gun Barrel .....	92
4.21.	Schematic of Aligning Incident Bar and Transmission Bar Prior to Testing .....	93
4.22.	Station D and Schematic of Placing the Specimen Between the Bars .....	93
4.23.	Station B and Schematic of Placing the Copper Pulse Shaper at the Incident Bar Face.....	94
4.24.	Station C and Schematic of Placing the Striker Bar into the Firing Position using Flexible Plastic Rod.....	94
4.25.	Block Diagram of Typical Data Processing Procedure .....	96
4.26.	Strain Rate vs. Time Plot for 6061-T651 Aluminum .....	99
4.27.	Strain vs. Time Plot for 6061-T651 Aluminum .....	100
4.28.	Stress vs. Time Plot for 6061-T651 Aluminum .....	100
4.29.	Stress vs. Time Plot for 6061-T651 Aluminum based on 1-wave, 2-wave and 3-wave Analysis.....	101
4.30.	Comparison of Dynamic Stress-Strain Plot for 6061-T651 Aluminum.....	101
4.31.	Strain Rate vs. Time Plot for Polycarbonate.....	103
4.32.	Strain vs. Time Plot for Polycarbonate .....	103
4.33.	Stress vs. Time Plot for Polycarbonate .....	104
4.34.	Stress vs. Time Plot for Polycarbonate based on 1-wave, 2-wave and 3-wave Analysis.....	104

4.35.	Comparison of Dynamic Stress-Strain Plot for Polycarbonate at 1,310/s.....	105
5.1.	Eco-Core Specimens of Various L/D Ratio's .....	108
5.2.	Eco-Core Specimens for Dynamic Failure Model Development .....	109
5.3.	Typical Dynamic Responses from the Strain Gages Mounted on the Incident and Transmission Bars for Eco-Core Specimen ECB-12.....	110
5.4.	Typical Dynamic Compressive Stress-Strain Curve of Eco-Core Specimen ECB-12 at the Strain Rate of 3,150/s .....	112
5.5.	Images of the Eco-Core Specimen (L/D = 0.25) Deformation in a Dynamic Test (time interval: 9.8 $\mu$ s) .....	114
5.6.	Eco-Core Specimen after Dynamic Testing .....	114
5.7.	SEM Micrograph of Eco-Core Specimens after Testing at a Strain Rate of (a) 989/s (b) 1,600/s (c) 2,574/s and (d) 3,139/s .....	115
5.8.	Typical Compressive Stress-Strain Response of Core Material.....	117
5.9.	High Strain Rate Compressive Stress-Strain Response of Eco-Core Specimen with L/D = 0.17 .....	119
5.10.	High Strain Rate Compressive Stress-Strain Response of Eco-Core Specimen with L/D = 0.25 .....	119
5.11.	High Strain Rate Compressive Stress-Strain Response of Eco-Core Specimen with L/D = 0.3 .....	120
5.12.	High Strain Rate Compressive Stress-Strain Response of Eco-Core Specimen with L/D = 0.5 .....	120
5.13.	High Strain Rate Compressive Stress-Strain Response of Eco-Core Specimen with L/D = 1 .....	121
5.14.	Dynamic Compressive Stress-Strain Curves of Eco-Core Specimens with Aspect Ratio from 0.17 to 1 .....	122
5.15.	Time History of the Force on the Incident and Transmitted Ends of Eco-Core Specimen Having L/D = 0.17.....	124
5.16.	Time History of the Force on the Incident and Transmitted Ends of Eco-Core Specimen Having L/D = 0.25.....	124
5.17.	Time History of the Force on the Incident and Transmitted Ends of Eco-Core Specimen Having L/D = 0.3 .....	125
5.18.	Time History of the Force on the Incident and Transmitted Ends of Eco-Core Specimen Having L/D = 0.5 .....	125
5.19.	Time History of the Force on the Incident and Transmitted Ends of	

Eco-Core Specimen Having L/D = 1 .....	126
5.20. Dynamic Compressive Stress-Strain Curves for Eco-Core at a Strain Rate ~1,000/s .....	129
5.21. Dynamic Compressive Stress-Strain Curves for Eco-Core at a Strain Rate ~1,700/s .....	129
5.22. Dynamic Compressive Stress-Strain Curves for Eco-Core at a Strain Rate ~2,500/s .....	130
5.23. Dynamic Compressive Stress-Strain Curves for Eco-Core at a Strain Rate ~3,100/s .....	130
5.24. Dynamic Compressive Stress-Strain Curves for Eco-Core at Strain Rates from 1,000/s to 3,100/s .....	131
5.25. Illustration of the Influence of Model Parameter $k$ .....	136
5.26. Illustration of the Influence of Model Parameter $n$ .....	136
5.27. Comparison of Dynamic Stress-Strain Curves of Eco-Core from Experiments and from Model Description over the Strain Rate 1,000/s - 3,100/s.....	137
5.28. Energy Absorption Density of Eco-Core as a Function of Strain Rate.....	141
5.29. 0-PU Coated Eco-Core Specimens .....	143
5.30. 10-PU Coated Eco-Core Specimens .....	144
5.31. Dynamic Compressive Stress-Strain Curves for 0-PU Front Coated Eco-Core at Breech Pressure of 22 Psi .....	146
5.32. Dynamic Compressive Stress-Strain Curves for 0-PU Front Coated Eco-Core at Breech Pressure of 26.5 psi .....	147
5.33. Dynamic Compressive Stress-Strain Curves for 0-PU Front Coated Eco-Core at Breech Pressure of 22 and 26.5 psi.....	147
5.34. Dynamic Compressive Stress-Strain Curves for 10-PU Front Coated Eco-Core at Breech Pressure of 22 psi.....	148
5.35. Dynamic Compressive Stress-Strain Curves for 10-PU Front Coated Eco-Core at Breech Pressure of 26.5 psi .....	148
5.36. Dynamic Compressive Stress-Strain Curves for 10-PU Front Coated Eco-Core at Breech Pressure of 22 and 26.5 psi.....	149
5.37. Photographs Recorded During a High Strain Rate Compression Test on 0-PU Front Coated Eco-Core Specimen at a Strain Rate ~ 2,900/s (Time Interval: 30.8 $\mu$ s) .....	150
5.38. Photographs Recorded During a High Strain Rate Compression Test on	

10-PU Front Coated Eco-Core specimen at a Strain Rate ~ 3,000/s (Time Interval: 30.8 $\mu$ s) .....	151
5.39. Dynamic Compressive Stress-Strain Curves for 0-PU Back Coated Eco-Core at Breech Pressure of 22 psi .....	153
5.40. Dynamic Compressive Stress-Strain Curves for 0-PU Back Coated Eco-Core at Breech Pressure of 26.5 psi .....	153
5.41. Dynamic Compressive Stress-Strain Curves for 0-PU Back Coated Eco-Core at Breech Pressures of 22 and 26.5 psi.....	154
5.42. Dynamic Compressive Stress-Strain Curves for 10-PU Back Coated Eco-Core at Breech Pressure of 22 psi.....	154
5.43. Dynamic Compressive Stress-Strain Curves for 10-PU Back Coated Eco-Core at Breech Pressure of 26.5 psi .....	155
5.44. Dynamic Compressive Stress-Strain Curves for 10-PU Back Coated Eco-Core at Breech Pressures of 22 and 26.5 psi.....	155
5.45. Dynamic Compressive Stress-Strain Curves for 0-PU Front-Back Coated Eco-Core at Breech Pressure of 22 Psi .....	157
5.46. Dynamic Compressive Stress-Strain Curves for 0-PU Front-Back Coated Eco-Core at Breech Pressure of 26.5 Psi .....	158
5.47. Dynamic Compressive Stress-Strain Curves for 0-PU Front-Back Coated Eco-Core at Breech Pressures of 22 and 26.5 psi.....	158
5.48. Dynamic Compressive Stress-Strain Curves for 10-PU Front-Back Coated Eco-Core at Breech Pressure of 22 psi.....	159
5.49. Dynamic Compressive Stress-Strain Curves for 10-PU Front-Back Coated Eco-Core at Breech Pressure of 26.5 psi .....	159
5.50. Dynamic Compressive Stress-Strain Curves for 10-PU Front-Back Coated Eco-Core at Breech Pressures of 22 and 26.5 psi.....	160
5.51. Photographs Recorded During a High Strain Rate Compression Test on 0-PU Front-Back Coated Eco-Core Specimen at a Strain Rate ~ 3,000/s (Time Interval: 30.8 $\mu$ s).....	161
5.52. Photographs Recorded During a High Strain Rate Compression Test on 10-PU Front-Back Coated Eco-Core Specimen at a Strain Rate ~ 3,000/s (Time Interval: 30.8 $\mu$ s).....	162
5.53. Dynamic Compressive Stress-Strain Curves for 0-PU Coated Eco-Core .....	163
5.54. Dynamic Compressive Stress-Strain Curves for 10-PU Coated Eco-Core .....	164
5.55. Dynamic Compressive Stress-Strain Curves for PU Coated Eco-Core at a	

Strain Rate ~2,900/s.....	165
5.56. Dynamic Compressive Stress-Strain Curves for PU Coated Eco-Core at a Strain Rate ~3,600/s.....	166
5.57. Energy Absorption Density vs. Strain Rate for 0-PU Coated Eco-Core.....	170
5.58. Normalized Energy Absorption Density vs. Strain Rate for 0-PU Coated Eco-Core.....	170
5.59. Energy Absorption Density vs. Strain Rate for 10-PU Coated Eco-Core.....	172
5.60. Normalized Energy Absorption Density vs. Strain Rate for 10-PU Coated Eco-Core .....	172
5.61. Polyurethane Impregnated Eco-Core Specimens .....	173
5.62. Dynamic Compressive Stress-Strain Curves for Polyurethane Impregnated Eco-Core at a Strain Rate ~1,000/s .....	176
5.63. Dynamic Compressive Stress-Strain Curves for Polyurethane Impregnated Eco-Core at a Strain Rate ~1,700/s .....	177
5.64. Dynamic Compressive Stress-Strain Curves for Polyurethane Impregnated Eco-Core at a Strain Rate ~2,300/s .....	177
5.65. Dynamic Compressive Stress-Strain Curves for Polyurethane Impregnated Eco-Core at a Strain Rate ~2,800/s .....	178
5.66. Dynamic Compressive Stress-Strain Curves for Polyurethane Impregnated Eco-Core at a Strain Rate ~3,200/s .....	178
5.67. Average Stress-Strain Curves for Polyurethane Impregnated Eco-Core at Strain Rates from 1,000/s to 3,200/s .....	179
5.68. Photographs Recorded During a High Strain Rate Compression Test on PUR Impregnated Eco-Core at a Strain Rate ~ 3,000/s (Time Interval: 30.8 $\mu$ s).....	180
5.69. Impregnated Eco-Core Specimen after Dynamic Testing .....	180
5.70. Energy Absorption Density vs. Strain Rate for PUR Impregnated Eco-Core ....	182
5.71. Normalized Energy Absorption Density vs. Strain Rate for PUR Impregnated Eco-Core .....	183
5.72. Comparison of Energy Absorption Density vs. Strain Rate for Eco-Core and Modified Eco-Core .....	184
5.73. Comparison of Normalized Energy Absorption Density vs. Strain Rate for Eco-Core and Modified Eco-Core .....	185

## LIST OF TABLES

<b>TABLES</b>	<b>PAGE</b>
1.1. Experimental Methods for High Strain Rate Testing .....	4
1.2. Change in Modulus of Syntactic Foams with Strain Rate .....	19
2.1. Physical Properties of Cenosphere.....	22
2.2. Chemical Properties of Cenosphere .....	23
2.3. Physical and Chemical Properties of Phenolic (Durite SC1008) Resin .....	23
2.4. Density and Dimensions of Eco-Core Panels .....	29
2.5. Density of Eco-Core Specimens .....	30
2.6. Unconfined Compression Properties of Eco-Core .....	34
2.7. Confined Compression Properties of Eco-Core .....	37
2.8. Tensile Properties of Eco-Core.....	37
2.9. Flexural Properties of Eco-Core .....	38
2.10. Shear Properties of Eco-Core .....	39
2.11. Fracture Properties of Eco-Core .....	41
2.12. Comparison of Mechanical Properties of Eco-Core with Other Commercially Available Core Materials .....	48
3.1. Typical Physical and Mechanical Properties of Polyurea Elastomers .....	52
3.2. Typical Physical and Mechanical Properties of Polyurethane Elastomers.....	52
3.3. Density and Dimensions of Modified Eco-Core Panels .....	57
3.4. Density and Dimensions of Modified Eco-Core Compression Specimens .....	58
3.5. Unconfined Compression Test Results .....	61
3.6. Confined Compression Test Results .....	66
4.1. Properties of 7075 Aluminum Pressure Bars.....	77
4.2. Velocity-Pressure Calibration Test Data .....	87
5.1. Density and Dimensions of Eco-Core Specimens of Various L/D Ratio.....	107
5.2. Density and Dimensions of Eco-Core Specimens for Dynamic Failure Model Development.....	108
5.3. Test Plan for Investigating the Effect of Specimen Aspect Ratio .....	116

5.4.	Strain Rate and Strain Limit Data from Eco-Core SHPB Tests .....	132
5.5.	Energy Absorption Density of Eco-Core at Various Strain Rates.....	140
5.6.	Density and Dimensions of 0-PU Coated Eco-Core Specimens .....	142
5.7.	Density and Dimensions of 10-PU Coated Eco-Core Specimens .....	143
5.8.	Dynamic Test Matrix for Polyurea Coated Eco-Core .....	144
5.9.	Energy Absorption Density of 0-PU Coated Eco-Core at Various Strain Rates .....	167
5.10.	Energy Absorption Density of 10-PU Coated Eco-Core at Various Strain Rates .....	168
5.11.	Density and Dimensions of Polyurethane Impregnated Eco-Core Specimens...	174
5.12.	Energy Absorption Density of Polyurethane Impregnated Eco-Core at Various Strain Rates .....	181

## NOMENCLATURE

A	cross-sectional area
$A_b$	cross-sectional area of the pressure bar
$A_s$	cross-sectional area of the specimen
amp.	ampere
ASCII	The American Standard Code for Information Interchange
ASM	American Society of Materials
ASTM	American Society of Testing and Materials
Avg.	average
C	model constant
$c_b$	wave speed in the bar
CC	confined compression
CCW	counter clock wise
cps	cycles per second
CV	co-efficient of variation
CW	clock-wise
DC	direct current
$D_s$	specimen diameter
DSO	Digital Storage Oscilloscope
$E$	elastic modulus
$E_b$	elastic modulus of the bar
$\epsilon_c$	failure strain
ECB	Eco-Core Baseline
$\epsilon_{\text{crush}}$	crushing strain
$E_{\text{EA}}$	energy absorption density
$E_{\text{foam}}$	elastic modulus of foam
$\epsilon_l(t)$	incident strain signal

$\varepsilon_l$	strain limit
$\varepsilon_p$	plateau strain
EPU	Polyurea coated Eco-Core
EPUR	Polyurethane Impregnated Eco-Core
$\varepsilon_R(t)$	reflected strain signal
$E_s$	elastic modulus of the specimen
$E_{solid}$	elastic modulus of solid
$\varepsilon_T(t)$	transmitted strain signal
$F_1$	axial force at the incident bar end of the specimen
$F_2$	axial force at the transmitted bar end of the specimen
$F_{av}$	average force
ft	feet
g	gram
g/cc	gram per cubic centimeter
GPa	giga pascal
mm of Hg	millimeter of mercury
$H_s$	specimen height
$I_{bar}$	incident bar
$I_{bar-S}$	incident bar-specimen interface
in	inch
JC	Johnson-Cook
JM3	Johns Manville
$k$	model parameter
$K_{Ic}$	mode-I fracture toughness
kJ	kilo joules
kN	kilo Newton
kPa	Kilo Pascal
L/D	Length-Diameter Ratio
m	model parameter

m/s	meter per sec
mg	miligram
MHz	mega hertz
min	minute
mm	millimeter
MPa	mega Pascal
$\mu$ s	microsecond
ms	millisecond
$n$	model parameter
N	Newton
OFHC	Oxygen Free High Thermal Conductivity
PC	polycarbonate
$P_{\max}$	maximum pressure
PMMA	polymethyl methacrylate
psi	pounds per square inch
psig	pounds per square inch (guage)
PU	polyurea
PUR	polyurethane
PUR-Imp	polyurethane impregnated Eco-Core
PVC	polyvinyl chloride
$\rho$	mass density
$R_c$	calibration resistance
RTV	room temperature vulcanizate
$\sigma(\epsilon)$	stress function
$\sigma_c$	static compression strength of the material
$S_{\text{bar}}$	striker bar
$\sigma_c$	compression strength
SEM	Scanning Electron Microscope
SHPB	Split Hopkinson Pressure Bar

$\sigma_{pl}$	plateau stress
$\sigma_s(t)$	specimen stress
$\varepsilon_s(t)$	specimen strain
$\dot{\varepsilon}_s(t)$	specimen strain rate
t	time
$T^*$	homologous temperature
$T_{bar}$	transmitted bar
$T_m$	melting temperature
$T_r$	reference temperature
$U_0$	strain energy
UC	unconfined compression
USB	Universal Serial Bus
vol	volume
vol%	volume fraction
$v_{sb}$	velocity of the striker bar
$\Omega$	Ohm
wt%	weight Percent
$\dot{\varepsilon}$	plastic strain rate
$\dot{\varepsilon}_0$	reference strain rate
$\dot{\varepsilon}^*$	dimensionless strain rate
$\alpha$	model parameter
$\beta$	model parameter
$\gamma$	model parameter
$\theta$	model parameter
0-PU	0- thickness polyurea coating
10-PU	ten mil thickness polyurea coating
20-PU	twenty mil thickness polyurea coating
40-PU	forty mil thickness polyurea coating

# CHAPTER 1

## INTRODUCTION

A background of core materials used in sandwich structures applications, including syntactic foam and Eco-Core is presented. A review of high-strain rate test methods, the history and development of the Split Hopkinson Pressure Bar (SHPB) test (including high strain rate testing of soft polymeric materials, brittle materials, and syntactic foams) is described. Finally, challenges in the current research, objectives of the research, and the scope of the dissertation are presented.

### 1.1 Background

Core materials are used extensively throughout the composites industry to fabricate lightweight and stiff sandwich structures. The sandwich structure offers an order of magnitude increased flexural stiffness compared to solid laminates. The typical use of core materials is in sandwich structures, which consist of top and bottom face-sheets and a middle core material. The face-sheets are comparatively thin ( $\sim 1/20$  core thickness) and are made of a material with high strength and stiffness. The core is relatively thick ( $\sim 20$  face sheet thickness) and provides stiffness and strength through-the-thickness direction. In sandwich construction, the face-sheets carry the bending and core carries the compression and shear loading [1-3].

A variety of core materials are used in the composites industry. In aerospace applications honeycomb cores made from aluminum, phenolic-resin impregnated fiberglass, paper, polypropylene, and Aramid fiber are extensively utilized. Face-sheets may be sheets of aluminum alloys or polymeric composite materials. Fabrication of extremely lightweight honeycomb is possible; however, costs and moisture problems negate its superior stiffness advantage [3-5].

In structures that are less weight critical and where cost is an important factor, core materials of the following types are used: end-grain balsa; closed-cell foams made thermoplastics such as PVC or polyimide; thermoset foams, carbon foams and syntactic foams [4]. End-grain balsa wood and many foamed plastics are not suitable for complex shape constructions because of problems with shaping. Furthermore, balsa wood is subjected to rotting and degradation of property due to moisture ingression and thermal cycles. Plastic foams could emit noxious gases when exposed to fire [6].

Syntactic foams are light weight composite materials (density about 0.5 g/cc) and are made by embedding pre-formed hollow microbubbles in a resin matrix for buoyancy applications. Generally, syntactic foams are made by mixing microbubbles and resin into a thick mixture that can be casted or sprayed. The design advantages of syntactic foams have been recognized for a long time and are the choice of material in off-shore, marine, petroleum, and mass transport applications. Experimental and analytical studies of syntactic foams have been reported in the literature [7-12]. Some of the limitations of the syntactic foams are;

- High density (0.5 - 0.8 g/cc)
- Resin content is high (around 30 - 40 wt %)
- High volatiles content (75 to 80 wt%) that fuel the fire
- Expensive
- Shrinkage during cure

Fire has been a major problem for both mobile (mass transit and marine) and immobile (buildings and civil infrastructure) structures. With the wide use of polymer composites in structural applications, potential for fire hazards has increased. Norwegian composite minesweeper fire [13] demonstrated the vulnerability of composite ships against fire. September 11, 2001 twin tower fire and collapse have demonstrated the vulnerability of our unprotected steel skyscrapers. Although fire cannot be completely eliminated, it can be mitigated to reduce the loss of life and property. Extensive research is being conducted to improve fire safety of composite materials for various applications. Some of these results are summarized by Sorathia and Perez [6] for naval applications.

Recently, Shivakumar and his co-researchers [14-17] have developed an extreme version, low resin content syntactic foam called “Eco-Core” for fire mitigation applications. Differences between the conventional syntactic foam and Eco-Core are: the resin content is less than 18% by weight or 5% by volume, the microbubbles coating is thin enough to make sphere to sphere contact; and the resin which is a high char yield binder. The microbubbles used in Eco-Core were Cenospheres, which are a waste product from coal-fired electric power plants, hence the name Eco-Core (meaning the recycling of waste product). Because this foam (Eco-Core) has very low resin content and Cenosphere, which is a ceramic oxide, the resulting material has excellent fire resistant properties. The base Eco-Core has been evaluated for superior mechanical, fire resistance, toxicity, and sea and tap water resistant properties [14-20]. The base Eco-Core is brittle and has been modified for improved toughness [16,21]. Some of the advantages of Eco-Core are;

- Inexpensive and Manufactured from a Waste Product
- Excellent Fire Resistance
- Nontoxic in Fire
- Superior Mechanical Properties
- Potentially Good Thermal and Sound Insulator
- Moldable and Shapeable
- Adaptable to Existing Manufacturing Facility
- Potential for Blast Mitigation

Potential application for Eco-Core are in sandwich core material for Ships, Mass Transportation (Subway train, Busses) structures, Fire walls in Buildings, Automobiles, and anywhere fire is an issue.

Dynamic characterization of Eco-Core or similar low binder content syntactic foam has not been studied in the literature. Furthermore, the energy absorption property of the material needs to be understood if Eco-Core is considered for blast mitigation applications.

## 1.2 High Strain Rate Testing of Materials

High strain rate characterization of materials is important and essential where material is exposed to impacts and blasts. In structural applications, various components must be designed to operate over a broad range of strain rates and temperatures. The constituent materials must, therefore, be characterized at the strain rates and temperatures of the intended application. For example, strain rates ranging from  $100 \text{ s}^{-1}$  to  $10,000 \text{ s}^{-1}$  occur in many processes or events of practical importance, such as foreign object damage, explosive forming, earthquakes, blast/shock loading, structural impacts, terminal ballistics, and metal working.

This section briefly reviews the experimental methods available for high strain rate characterization. Conventional servo hydraulic machines are generally used for testing at quasi-static strain rates of  $1 \text{ s}^{-1}$  or less. In conventional load frames with a special design it is possible to achieve strain rates up to  $100 \text{ s}^{-1}$ . For attaining higher strain rates other test methods are required. Table 1.1 summarizes various methods in terms of the ranges of strain rates they can achieve [22]. The dynamic aspects, strain rate regime and corresponding instruments and experimental conditions of material testing are depicted in Figure 1.1 [22].

**Table 1.1. Experimental Methods for High Strain Rate Testing**

<b>Applicable strain rate, <math>\text{s}^{-1}</math></b>	<b>Testing technique</b>
<b>Compression tests</b>	
< 0.1	Conventional load frames
0.1 - 100	Special servohydraulic frames
0.1 - 500	Cam plastometer and drop test
200 - $10^4$	Hopkinson (Kolsky) bar in compression
$10^3$ - $10^5$	Taylor impact test
<b>Tension tests</b>	
< 0.1	Conventional load frames
0.1 - 100	Special servohydraulic frames
100 - $10^3$	Hopkinson (Kolsky) bar in compression
$10^4$	Expanding ring

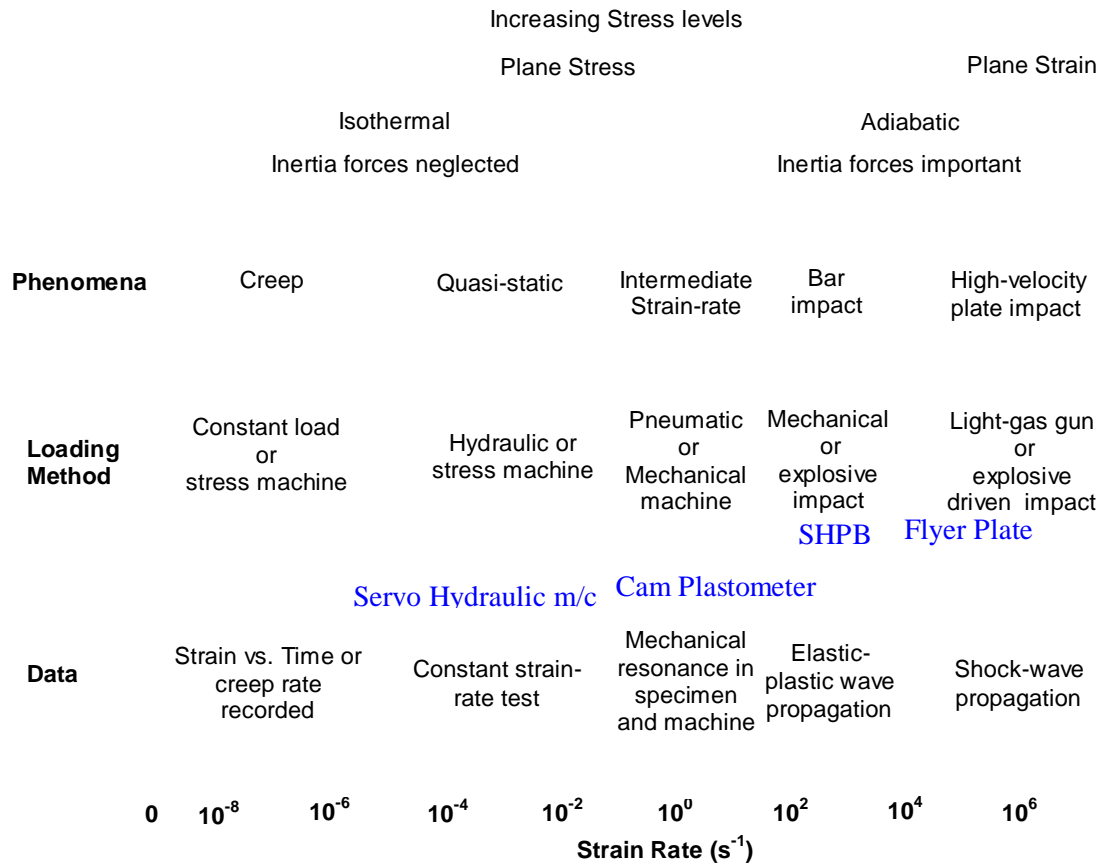


**Figure 1.1. Strain Rate Regimes and Corresponding Instruments and Experimental Conditions**

For testing mechanical properties of materials at high strain rates up to and over  $10,000 \text{ s}^{-1}$ , the commonly used test methods are briefly described in the following sections.

### 1.2.1 Cam Plastometer

The cam plastometer is designed specifically for compression testing at strain rates from  $0.5$  to  $200 \text{ s}^{-1}$ . Figure 1.2 shows a diagram of a Cam plastometer testing machine. The axial load to compress the specimen is transferred from massive rotating flywheels through a cam; this process provides the distinct advantage of maintaining a constant strain rate experiment. The cam-plastometer is used to obtain the resistance to

compressive deformation of materials, principally metals, at constant strain rates over a useful and significant range of strain rates and a practical range of testing temperatures. Most plastometers have the capacity to compress cylindrical specimens homogeneously to a 50% reduction in height, assuming the material is tested at temperatures ductile enough to permit this reduction.

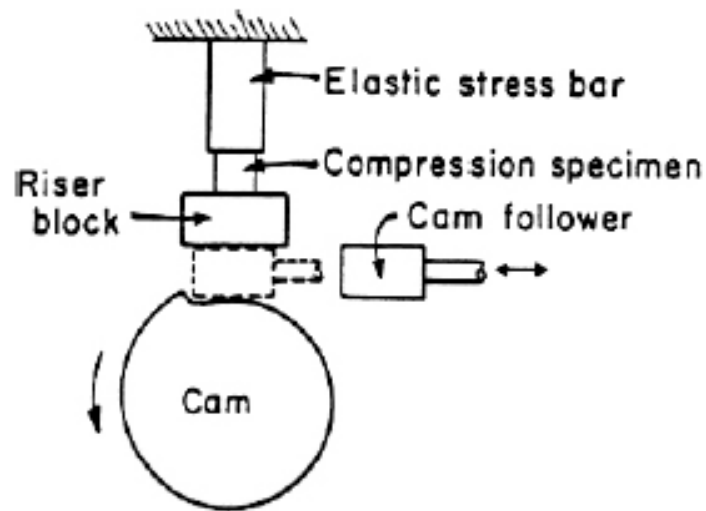


**Figure 1.2. Schematic of Cam Plastometer**

### ***1.2.2 Drop Tower Compression Test***

A drop weight tower is used for compression testing at strain rates from 10 to 300/s. The drop tower compression test uses a falling weight to provide a compressive load to the specimen. The test technique has the capability to generate high loads at medium strain rates, which cannot be readily obtained by servohydraulic load frames or cam plastometers. The drop tower compression test has been used to measure compressive fracture strengths, to determine the compressive stress-strain behavior of material at medium strain rates, and to evaluate the dimensional stability of components subjected to impact compressive loads. A typical drop tower compression system is shown in Figure 1.3.

Drop crosshead

Striking head

Specimen

Rigid base

**Figure 1.3. Schematic of Drop Tower Compression Test System**

### ***1.2.3 Split Hopkinson Pressure Bar***

The most widely used method for testing material between strain rates of 100 and 10,000 s<sup>-1</sup> is the split Hopkinson pressure bar. The Compressive Split Hopkinson Pressure Bar (CSHPB) consists of two elastic pressure bars that sandwich the specimen between them. Figure 1.4 shows a schematic of this apparatus. Upon impact of a striker bar on an incident bar, an elastic compressive wave is generated within the incident bar, and the time-dependent strain in the pressure bar is measured at strain gage A at the midpoint of the incident bar (Figure 1.4). The velocity of the striker controls the strain rate achieved, while the length of the striker determines the duration of the test. Depending on the striker bar velocity, low or high strain rate testing can be conducted. At the incident bar/specimen interface, the wave is partially reflected and partially transmitted into the specimen. A portion of the incident wave is reflected back along the incident bar as a tensile wave. This reflected strain is measured by strain gage A. Strain measurements are also taken on the transmitter bar with strain gage B. These strain measurements on the pressure bars are used to determine the stress-strain



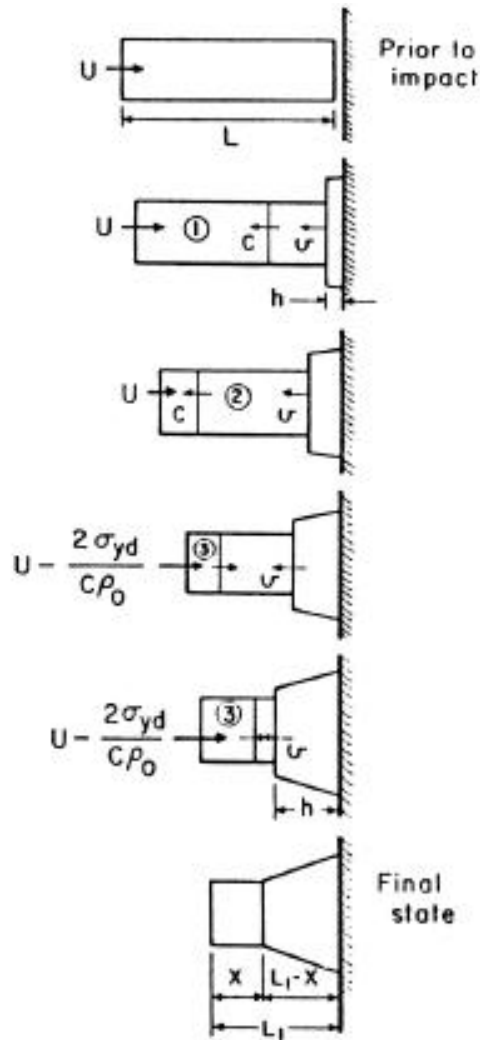


**Figure 1.5. Schematic of Sequence of Events of Classic Taylor Impact Test**

### ***1.2.5 Expanding Ring Test***

The expanding ring test is a highly sophisticated technique for subjecting metals to tensile strain rates over  $10,000 \text{ s}^{-1}$  [24]. The ring test can determine the high-rate stress-strain relationships but a simplified, more widely used version can be employed to determine ultimate strain only [24]. This test involves the sudden radial acceleration of a ring due to detonation of an explosive charge or electromagnetic loading. The ring rapidly becomes a free-flying body, expanding radially and decelerating due to its own

internal circumferential stresses. A thin ring must be used for the analysis to be valid; the wall thickness should be less than one-tenth the ring diameter, which is typically 25 mm (1 in.). In order to determine the stress strain curve for the material, the velocity history of the ring is recorded. The velocity history can be related to stress and strain through a set of simple equations. This technique uses varying amounts of explosives to select the strain rate desired.

### ***1.2.6 Flyer Plate Impact***

Flat plate impact tests have been used to obtain high strain rate yield data, shock wave response data, and an equation of state data for materials undergoing uniaxial strain [24]. The flyer plate impact technique was developed to study the behavior of materials that undergo homogeneous deformations at extremely high strain rates of  $10^4$ - $10^6$ /s. Uniaxial strain refers to a three-dimensional state of stress in which deformation or strain occurs in only one direction - the direction of loading. The uniaxial strain condition persists for only a short period of time until stress waves originating at lateral boundaries reach the specimen interior. In a typical experiment, this time period is of the order of several to tens of microseconds. The flat plate impact test is performed by launching a flat flyer plate against a second stationary target plate. Compressed gas guns, propellant guns, magnetic accelerators, and explosives have all been used to launch the flyer plate. Extreme precision must be achieved to eliminate relative tilt at the instant of impact. A typical experimental setup using a gas gun is shown in Figure 1.6. The flyer plate is carried in the gas gun in a plastic sabot. The flyer plate is accelerated towards a target plate secured in a target holder. At the instant of impact as measured by the trigger pins, two shock waves are generated at the impact plane. One shock wave propagates into the target, and the other propagates into the impactor. The velocity of the flyer is determined from the transit time between the shorting pin in the gun barrel and the time-of-arrival pins in the target. The target is supported by a spall ring that suppresses late-time radial tensile waves. For diagnostic purposes, a transparent polymethyl methacrylate (PMMA) window is attached to the backside of the target. The shock wave traveling through the target eventually enters this transparent window. As it does, it causes the interface



end (reflected wave). It has been shown “that half the velocity of impact needed to break the wire near the mass is sufficient to break it at the fixed point.”

In 1914, B Hopkinson [27] developed an experimental procedure to measure the pressure produced by the impact of a bullet or by the detonation of gun cotton. This particular technique, which became well known as the *Hopkinson Pressure Bar* technique, is famous as a method for the dynamic characterization of materials. Hopkinson observed that “if a rifle bullet be fired against the end of a cylindrical steel rod there is a definite pressure applied on the end of the rod at each instant of time during the period of impact,” essentially forming a pressure pulse. By measuring the maximum displacement and period, and knowing the mass of the ballistic pendulum, the momentum of the flying *piece* can easily be determined. Hopkinson showed that by varying the length of the momentum of the *piece*, the maximum amplitude of the pressure and the total duration could be measured; however, a perfect pressure pulse shape could not be obtained. With this data, Hopkinson was able to identify peak pressures and estimate the longitudinal wave speeds in a variety of test specimens. However, since he lacked reliable methods of data storage and reduction, he was unsuccessful in generating reliable pressure versus time relationships for the impact experiments. He had, however, unknowingly laid out a method of material testing that would be revisited by future researchers and scientists investigating the dynamic response of material subjected to high strain rates.

In 1944, Davies [28] presented the first dynamic axial and radial strain measurements in Hopkinson Pressure Bar experiments using parallel plate and cylindrical condensers in conjunction with a double beam cathode ray oscillograph. Davies’s idea was that the displacement (strain) in the pressure bar was proportional to the stress developed in the bar, provided the pressure in the bar was well under the elastic limit of the pressure bar material. With this assumption in mind, Davies designed a condenser mechanism to generate an electrical output that was proportional to the displacement of the pressure bar in Hopkinson’s original apparatus. Thus, Davies improved the data acquisition process of Hopkinson’s experiment by replacing the ballistic pendulum with

his condenser strain measurement system, which reduced error and eliminated uncertainty.

Other work related to the Hopkinson bar was completed by physicists and material scientists interested in the wave propagation phenomena in solids. Researchers such as Love [29] derived equations describing the wave dispersion in rods. Pochhammer [30] and Chree [31] developed equations for 3D longitudinal stress wave propagation in an infinite cylindrical rod. Scientists knew that short duration impact events yielded stress waves with large amounts of spectral content. Thus, acoustic waves of many different frequencies resulted from a single impact event. A great amount of research was completed in an attempt to characterize this spectral content in terms of frequency, wave speed and impact pulse shape. Dennison Bancroft [32] published a series of solved equations for the longitudinal wave velocities in cylindrical bars. His equations were reduced to forms including Poisson's Ratio, infinite wavelength, pressure bar density and pressure bar diameter – wavelength ratio. Although Bancroft did little research directly with Hopkinson's original experiment, his work provided future researchers a method for determining wave velocities in the pressure bars used in Hopkinson bar testing.

The most profound addition to Hopkinson's research came in 1949 when Kolsky [33] published his famous paper on the measurement of the mechanical properties of several different materials (polythene, rubber, PMMA, copper, and lead) at high rates of loading using a modified Hopkinson Pressure Bar, later known as the "Kolsky Bar" or "Split-Hopkinson Pressure Bar." Kolsky used a silver steel pressure bar and increased the length of the time *piece* of the Hopkinson Pressure Bar, terming it an *extension bar*. He used a thin specimen sandwiched between the pressure bar and the extension bar and similar parallel plates and cylindrical condenser units as Davies [28] to measure the axial and radial displacements under dynamic loading. Kolsky described the modified Hopkinson Bar technique and experimental procedure, derived equations for converting experimental data into the stress and strain of the materials tested, briefly discussed the inertia effect of specimens, and modeled the relaxation behavior of materials tested using a modified Boltzmann [34] model described by Taylor [35]. Due to its improved

robustness, versatility and accuracy, the Kolsky bar or the split Hopkinson pressure bar (SHPB) quickly became one of the preferred methods for testing materials at strain rates from  $100 \text{ s}^{-1}$  to  $10,000 \text{ s}^{-1}$ .

Scientists and engineers have widely used Kolsky's original compression *pressure bar* technique in characterizing the high-strain rate behavior of engineering materials. In the 20th century, the use of the Hopkinson Bar technique has been extended to accommodate tension, shear, torsion, bending, indentation, and combined load cases. Specimen design with materials other than elastic-plastic metals such as polymers, rubbers, foamed materials, composites, and ceramics requires additional consideration and diagnostics.

## **1.4 SHPB Testing of Materials**

This review covers SHPB testing of soft materials, brittle materials, and syntactic foam materials.

### ***1.4.1 Soft Materials***

It is well accepted in the Hopkinson Bar research community [24] that SHPB experimental methods and 1D data analysis is generally valid for elastic-plastic metals. However, additional difficulties arise in the case of soft and hard materials, which include all kinds of engineering materials other than elastic-plastic metals. The ASM Handbook [24] devotes two separate sections on the SHPB testing of soft materials [36] and ceramics [37]. Soft materials include a wide variety of polymeric materials, foams of metals and polymers, and granular materials. This class of materials is characterized by their very low acoustic impedances, and under SHPB testing conditions, they generate very weak/poor transmitted pulses if the traditional steel bar with high gain is used. Researchers have used low impedance bars such as titanium, aluminum, and magnesium bars [38,39] where good transmission signals can be obtained. Others have used polymeric bars [40-42] such as polycarbonate and polymethyl methacrylate (PMMA) to test soft materials.

The use of a polymeric bar requires additional analyses of the visco-elastic bar behavior, adding more complexity than that associated with low impedance metallic bars. In addition to the low impedance solid metallic and polymeric bars, Chen et al [43] used a hollow aluminum transmission bar to obtain better signal to noise ratio over solid bars. The main issue in testing soft materials is to obtain a good transmitted pulse, which can be achieved by the use of low impedance bars. However, all the assumptions of stress equilibrium, uniform and uniaxial stress, inertia and friction effects, and dispersion conditions need to be satisfied for a valid SHPB experiment.

The low wave speed in soft materials makes the transit time in the specimen much longer than that of metallic materials. Thus, a thin specimen is necessary to satisfy the stress equilibrium condition. In fact, a strong dependence of the  $H_s/D_s$  ratio on the stress-strain behavior of soft materials has been found [36]. Chen et al [43] observed substantial wave attenuation in thick (0.25 inch) RTV630 rubber samples as compared with thin (0.06 inch) samples, suggesting that, depending on test temperature and specimen material, a  $H_s/D_s$  ratio of 0.25 - 0.50 can be used to minimize attenuation.

#### ***1.4.2 Brittle Materials***

Most of the material behavior of interest for relatively brittle materials such as ceramics [44,45] and rocks [46] occurs at strains less than approximately 1%. It has been determined that the loading of brittle specimens with a rectangular pulse fractures the specimen, even before the specimen reaches stress equilibrium. A way of shaping the incident pulse for split Hopkinson pressure bar experiments was discussed in 1981. Franz et al [47] and Follansbee [48] wrote review papers that discussed pulse shaping for SHPB experiments with metal samples. In these review papers, the authors emphasized that a slowly rising incident pulse is preferred to a pulse that rises steeply in order to minimize the effects of dispersion and to allow the samples to achieve dynamic stress equilibrium. Franz et al [47] and Follansbee [48] discussed experimental techniques for pulse shaping and a numerical procedure [49] for correcting raw data for wave dispersion in the bars. To shape the incident pulse these authors [47,48] machined a large radius on the impact face of the striker bar or placed a tip material between the striker and incident bars. The

tip material or pulse shaper was a disk slightly larger than the bars (0.1 - 2.0 mm thick). The pulse shaper materials used were paper, aluminum, brass or stainless steel. Franz et al [47] presented experimental results that showed the advantages of pulse shaping for a 3041 stainless steel sample at an approximate strain rate of  $4,500 \text{ s}^{-1}$ . In addition, these authors and Ellwood et al [50] showed that a properly chosen tip material or pulse shaper could also be used to generate a nearly constant strain rate in a sample. Gray [24] and Gray and Blumenthal [36] have presented additional information in recent survey papers that include these subjects. However, Duffy et al [51] were probably the first authors to use pulse shapers to smooth pulses generated by explosive loading for the torsional Hopkinson pressure bar.

While pulse shaping techniques have been successfully used to achieve the goals of many different experiments, pulse shapers are usually designed in experimental trials that exclude a model to guide the design parameters. For other examples, Wu and Gorham [52] used paper on the impact surface of the incident bar to eliminate high frequency oscillations in the incident pulse for Kolsky compression bar experiments. Togami et al [53] used a thin, Plexiglas disk to produce nondispersive compression pulses in an incident bar, and Chen et al [43] used a polymer disk to spread the incident compressive pulses for experiments with elastomers. Christensen et al [54] used striker bars with a truncated-cone on the impact end in an attempt to produce ramp pulses. In contrast to other pulse shaping studies, Nemat-Nasser et al [55] modeled the plastic deformation of an OFHC copper pulse shaper, predicted the incident strain pulse, and showed good agreement with some measured incident strain pulses.

For the stress-strain response of relatively brittle materials that have a nearly linear response to failure and failure strains less than 1%, Nemat-Nasser et al [55] recommended pulse shaping with an OFHC copper disk to achieve a ramp pulse in the incident bar. Again, these authors [55] also had an experimentally verified model for pulse shaping with an OFHC copper disk to predict incident pulses. In addition, Ravichandran and Subhash [56] presented a method of characteristics analysis for wave motions in a ceramic sample and provided a criterion for dynamic sample equilibrium.

Frew et al [46] extended this work [55,56] to obtain high-rate, stress-strain data for limestone samples. Data from experiments with limestone samples and analytical models showed that the samples were in dynamic stress equilibrium and had nearly constant strain rates over most the test durations for a ramp pulse in the incident bar.

#### ***1.4.3 Syntactic Foam Materials***

Large number of studies can be found on high strain rate properties of many materials. Recently, the SHPB was modified to obtain more accurate dynamic properties of materials, including metals [57], shape-memory alloys [58], ceramics [59], composites [60], rubbers [61], and even polymeric foams [62]. It is much more challenging to determine the dynamic properties of polymeric foams than metals because of the low mechanical impedance, wave speeds, and the strength of the foams.

Syntactic foam such as epoxy/microsphere behaves in a brittle manner and has a maximum failure strain of 2 - 4% under quasi-static compressive loadings [63-65]. It is difficult for the conventional SHPB technique to obtain valid stress-strain curves for any material at small strains at high strain rates [24]. The SHPB was modified with accurate pulse-shaping to obtain accurate small-strain behaviors of metals, composites and polymeric foams under dynamic loading conditions [57,60,66]. A pulse-shaping technique [67] ensured nearly constant strain rates and dynamically equilibrated stresses at small strains during dynamic loadings allowing examination of the strain rate effects on these engineering materials.

In 2004, B. Song et al. [68] studied the high strain rate compressive behavior of epoxy syntactic foam made from epoxy resin as binder and hollow glass microballoons as fillers. The density of syntactic foam was 0.77 g/cc. The researchers used a pulse-shaped split Hopkinson pressure bar (SHPB), modified for low impedance material testing, to ensure that the sample deformed under dynamic equilibrium and at a nearly constant strain-rate. They demonstrated that the compressive strength of the foam increased with strain rates up to a transition rate between 550 and 1,030 s<sup>-1</sup>. They also discovered that at strain rates above the transition range (1,900 s<sup>-1</sup>), the strain rate induced damage caused the compression strength of the foam to decrease. They attributed the reduction of

compression strength to adiabatic temperature rising in the specimen during dynamic tests, which causes softening phenomenon. The constitutive equation for the epoxy syntactic foam proposed by the authors was

$$\sigma = A \left[ 1 + B e^{-C(\ln \dot{\epsilon} - \alpha)^2} \right] \left[ 1 - (\beta + \gamma \dot{\epsilon}^\theta) \epsilon^2 \right] \epsilon \quad (1.1)$$

Where  $A$ ,  $B$ ,  $C$ ,  $\alpha$ ,  $\beta$ ,  $\gamma$ , and  $\theta$  are constitutive constants.

In 2005, Woldesenbet et al. [69] studied the strain rate sensitivity of the epoxy syntactic foams containing microballoons of densities varying from 0.20 to 0.46 g/cc. The volume fraction of microballoons was maintained at 0.65 for all syntactic foams. The density of the syntactic foams studied was varied from 0.49 to 0.65 g/cc. They concluded that syntactic foams were highly strain rate sensitive; almost twofold increase in the maximum stress was observed for the samples tested at a strain rate of approximately  $1,700 \text{ s}^{-1}$  as compared to the quasi-static value (Figure 1.7). The researchers observed that the maximum stress was found to vary with the density of the foam and the strain rate. One more observation was that strain at maximum stress was found to be almost constant for foams containing all types of microballoon internal radius. The strain rate sensitivity of failure strain for syntactic foam depended on the density of the foam and the applied strain rate. The authors also found that the modulus of all kinds of syntactic foams studied continuously increased with the strain rate due to the viscoelastic nature of the polymeric matrix (Table 1.2).

In 2008, Wehmer et al. [70] studied the effect of strain rate on epoxy syntactic foams of various densities containing rubber particles in the size range of 40 to 75  $\mu\text{m}$ . They discovered that rubber modified epoxy syntactic foam containing 63 vol % glass microspheres and 2 % volume fractions of ground rubber fragments showed increased peak stress values with an increasing strain rate. They reported that the performance of the hybrid syntactic foams of densities 0.22 g/cc and 0.32 g/cc containing 40 micron rubber particles was basically the same at strain rates ranging from 450 to 900/s. For syntactic foam of density 0.38 g/cc, they discovered that peak stress increased as the strain rate increased.

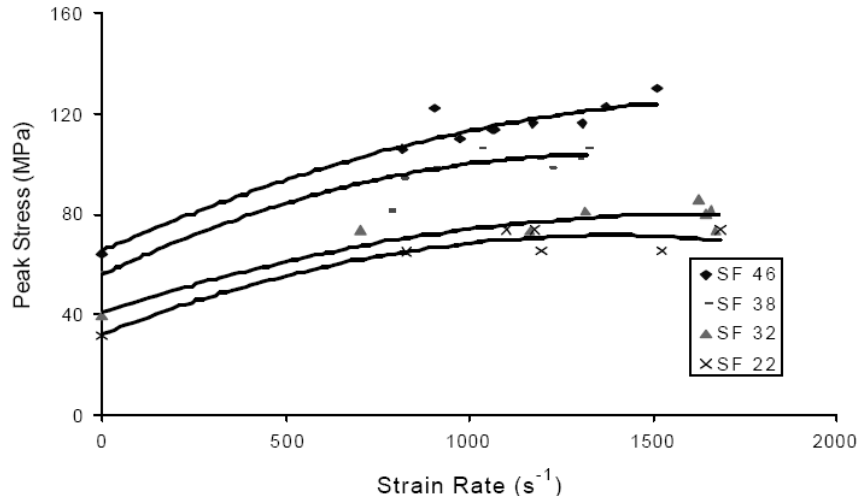


**Figure 1.7. Peak Stress Values for Various Syntactic Foam Densities at Different Strain Rates [69]**

**Table 1.2. Change in Modulus of Syntactic Foams with Strain Rate [69]**

Syntactic Foam Type	Strain Rate, s <sup>-1</sup>	Elastic Modulus, Mpa	Percentage Change
SF 22	Static	1,547	----
	830	1,777	14.9
	1,200	1,969	27.8
	1,688	2,503	37.3
SF 32	Static	2,025	----
	703	2,191	8.2
	1,164	2,372	17.1
	1,636	2,601	28.4
SF 38	Static	2,394	----
	830	2,796	16.8
	1,030	2,888	20.6
	1,324	2,864	19.7
SF 46	Static	2,639	----
	979	3,132	18.7
	1,015	3,161	19.8
	1,460	3,564	35.2

In 2008, Woldeesenbet et al. [71] also studied the effect of strain rates on nanoclay reinforced syntactic foam composites fabricated with 10, 30 and 60% microballoon volume fractions, each having 0, 1, 2 and 5% volume fraction of nanoclay. They found that the peak stress and modulus of all types of syntactic foam composites were directly affected by the strain rate. At lower strain rates, cracks traveled preferentially through the matrix avoiding most of the microballoons and nanoclay platelets. The volume fraction of the nanoclay was also found to affect the composite strength when tested at the same strain rate.

## **1.5 Challenges**

Dynamic characterization of Eco-Core or similar low binder content syntactic foam has not been studied in the literature. Furthermore, the energy absorption property of the material needs to be understood if Eco-Core is considered for blast mitigation applications. A split Hopkinson Pressure Bar test facility was not available at NC A&T State University. The SHPB test facility was designed, fabricated, and validated for this study.

## **1.6 Objectives of the Research**

The overall objective of this research is to develop the dynamic properties of Eco-Core at various strain rates and then quantify its energy absorption capability.

The specific objectives of the research are

- Processing and modification of Eco-Core
- Static characterization of Eco-Core
- Design, fabrication and validation of SHPB test apparatus
- Dynamic characterization and development of the failure constitutive equation of Eco-Core

## **1.7 Scope of the Dissertation**

The dissertation consists of six chapters. In Chapter 1, an overview of syntactic foams, Eco-Core, and dynamic characterization of materials is presented. This includes literature review on syntactic foams and high strain rate characterization of different materials. Subsequently, the technical gaps are identified, the problem is defined and the objectives of the present research are listed. Chapter 2 presents Eco-Core processing and static properties characterization. Chapter 3 presents modification methods for Eco-Core, testing after modification and discussion of the results of tests with modified Eco-Core. Chapter 4 presents the development of the Split Hopkinson Bar test facility and its validation for known materials. Chapter 5 presents dynamic characterization of the base and modified Eco-Core materials at different strain rates. This chapter includes the development of a constitutive model, identification of failure process and modes, and computation of energy absorption density. Finally, the concluding remarks and recommendations for future work are presented in Chapter 6.

## CHAPTER 2

# PROCESSING AND CHARACTERIZATION OF ECO-CORE

### 2.1 Introduction

This chapter describes the processing of baseline Eco-Core panels and its quasi-static mechanical characterization. Eco-Core panels are compression molded and characterized for compression, tensile, flexural, shear and fracture properties.

### 2.2 Materials

A class of fly ash known as Cenosphere (BIONIC BUBBLE™-XL-150 was obtained from Sphere Services Inc. The binder resin was a phenol-formaldehyde resole resin, Durite SC 1008 supplied by Borden Chemical Company. The physical and chemical properties of the Cenosphere and phenolic resin, as provided by the material supplier, are shown in Tables 2.1, 2.2 and 2.3, respectively. The microscopic structure of the Cenosphere as received (untreated) and surface washed with water and saline treated are shown in Figure 2.1.

**Table 2.1. Physical Properties of Cenosphere**

Size	10 - 350 $\mu\text{m}$ (63 $\mu\text{m}$ at 50% passing)
Wall Thickness	10 - 30 $\mu\text{m}$
pH in Water	6.0 - 8.0
Bulk Density	0.29 - 0.32 g/cc
Specific Gravity	0.5 - 0.6
Compressive Strength	12 MPa (average)
Softening Point	above > 1000 °C
Shape	Spherical
Color	Off White to Light Grey

**Table 2.2. Chemical Properties of Cenosphere**

Composition	Wt. %
Silica	15% - 50%
Alumina	30% - 35%
Iron Oxide	1 % - 5%
Titania	0.5% - 1.5%

**Table 2.3. Physical and Chemical Properties of Phenolic (Durite SC1008) Resin**

Boiling Point	98 °C
Vapor Pressure	28 mm of Hg
Vapor Density	2.1
Spec Gravity	1.07 - 1.10
pH value	> 7.9
Viscosity	180 - 300 cps
Solubility in Water	100%
Appearance and Odor	Clear amber liquid
% Volatiles by Volume	38

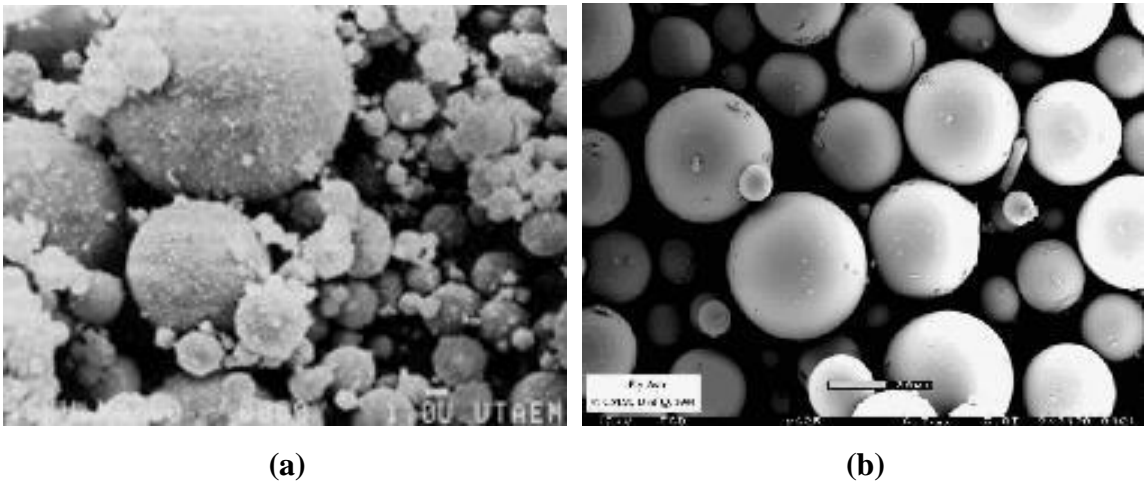


**Figure 2.1. Microscopic Structure of Cenosphere (a) As received (b) Surface washed**

### 2.3 Processing

A schematic of the processing is shown in Figure 2.2. The fly ash (Cenosphere) was treated to remove lime components by a dilute hydrochloric acid (pH ~ 4), and the heavier than water fraction of the ash was separated and removed by settling. The lighter floating fraction material was further washed with water approximately 3-4 times and was separated by filtration from the water. The floaters were scooped out and then they were thoroughly dried at 110°C in a convection oven. Subsequently, the treated fly ash was treated with a aminoalkyl triethoxysilane coupling agent. The Cenosphere after silane treatment was dried in an oven to attain a free-flowing material.

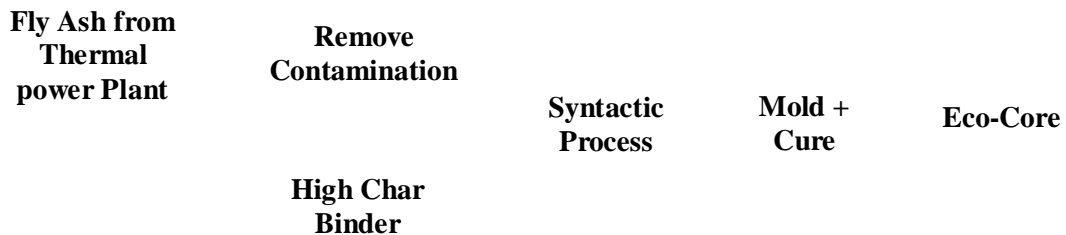


**Figure 2.2. Process Flow Diagram for Producing Eco-Core from Fly Ash**

The treated and dried fly ash was admixed with resole resin diluted with suitable solvents in a low-shear planetary motion mixer to uniformly coat the fly ash particles. The volatile solvents from the fly ash mixture were removed while mixing in a stream of warm air. The coated Cenosphere mix was subsequently charged into a wooden frame and then distributed uniformly using plastic rollers. Figure 2.3 shows the pre-compacted and uniformly distributed Cenosphere mix. The Cenosphere mix was preheated in a laboratory hot press at 82°C for 30 minutes without the application of any pressure. The pre-heated mix is shown in Figure 2.4. The pre-heated Cenosphere mix was subsequently transferred into a compression mold of 356 x 356 x 12.7 mm<sup>3</sup> (14 x 14 x 0.5 in<sup>3</sup>)

dimensions, compacted by a laboratory hot press and cured at 163°C for 30 minutes at a pressure of 20 tons on a high pressure gauge. The press pressure depends on the required density of the panel. Figure 2.5 shows a conventional laboratory hot press and its control panel. The temperature and pressure curing cycles for press molding is shown in Figure 2.6. To achieve reproducibility from sample to sample, the void fraction in the syntactic foam panels had to be controlled to as low a value as possible. The Eco-core panels were finally post cured in a circulating air oven at 163°C for 4-1/2 hours. The temperature cycle for post curing is given in Figure 2.7. The picture of the molded panel is shown in Figure 2.8. This process is considered as the base process and the specimens extracted from these panels were labeled as baseline Eco-Core. A typical microstructure of the base Eco-Core is shown in the Figure 2.9. The figure clearly shows a very thin coating of binder on the microbubbles.

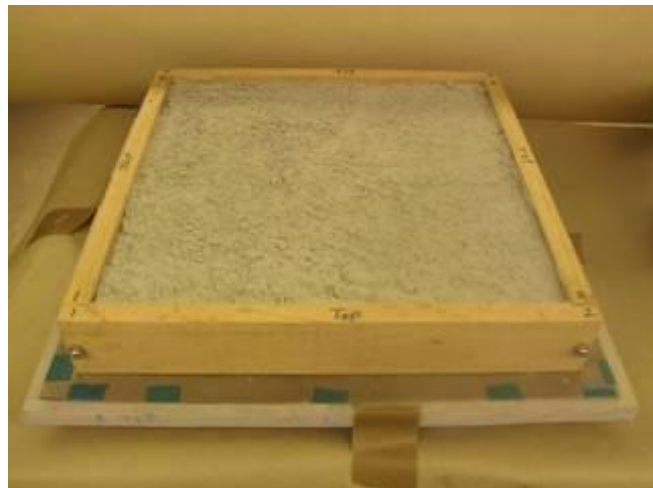


**Figure 2.3. Photograph of Pre-Compacted Cenosphere Mix**

In order to assess the quality of the fabricated panels, density and dimensional measurements were performed. Each panel was identified, and panel dimensions were measured and weighed. Table 2.4 records the dimensions and density of the Eco-Core

panels. The thickness of the panel was quite uniform with a variation from 12.8 to 12.9 mm. The dimensions such as length, width and thickness of the panel were measured at locations shown in Figure 2.10.

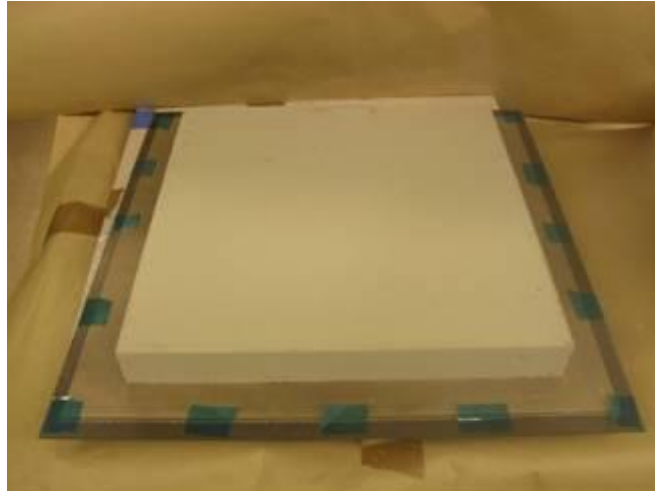


**Figure 2.4. Photograph of Pre-Heated Cenosphere Mix**



**Figure 2.5. Laboratory Hot Press and Control Panel**

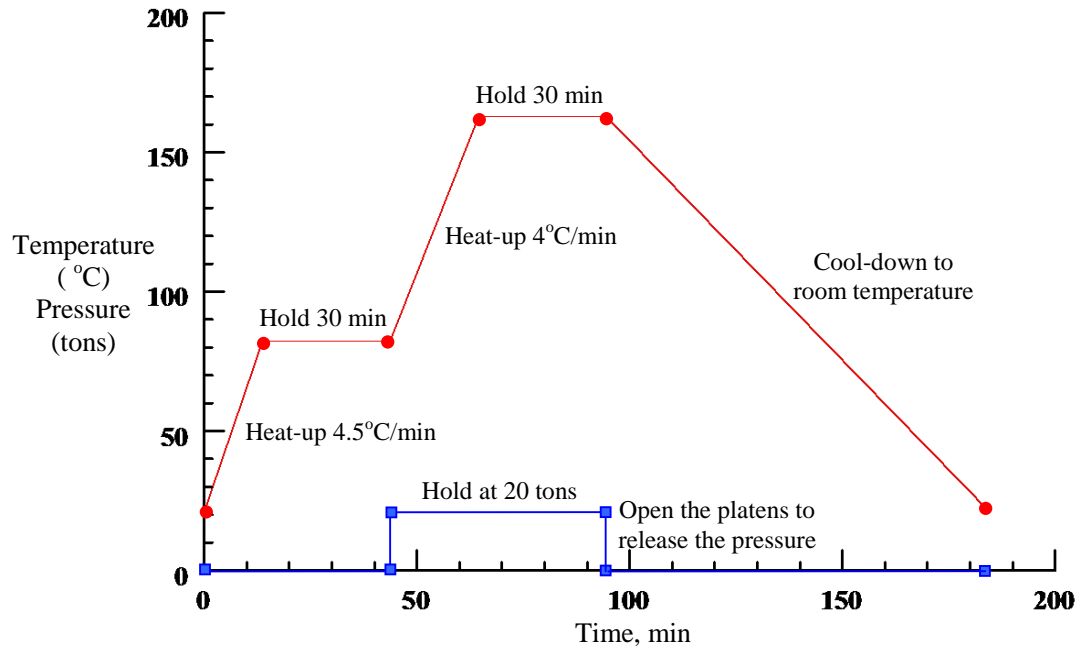


Figure 2.6. Press Curing Cycle

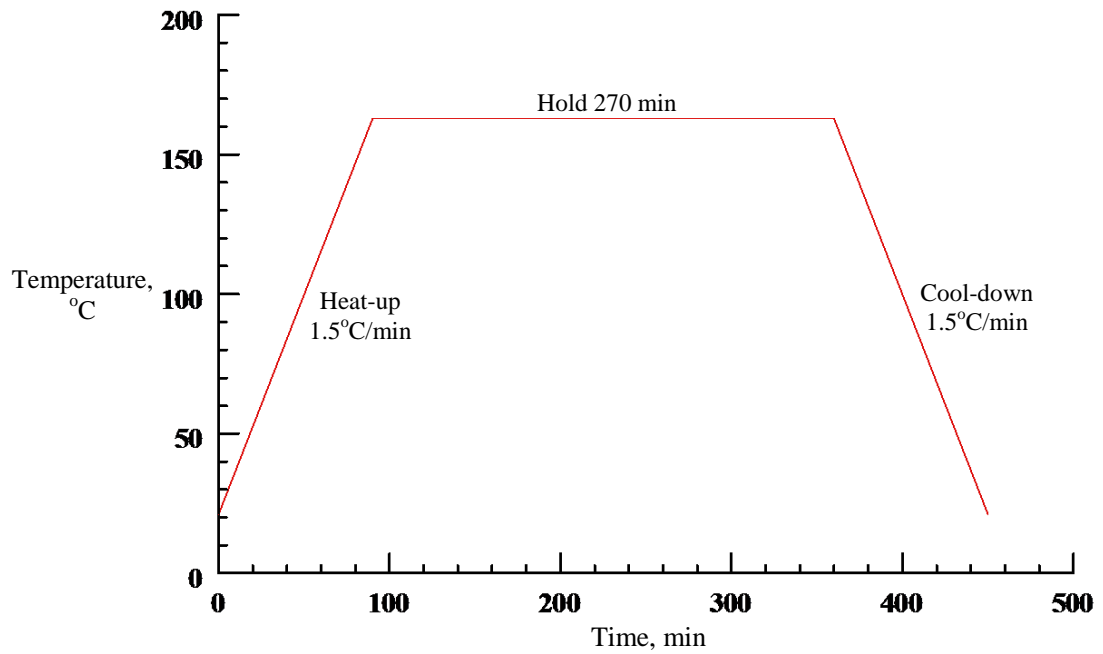
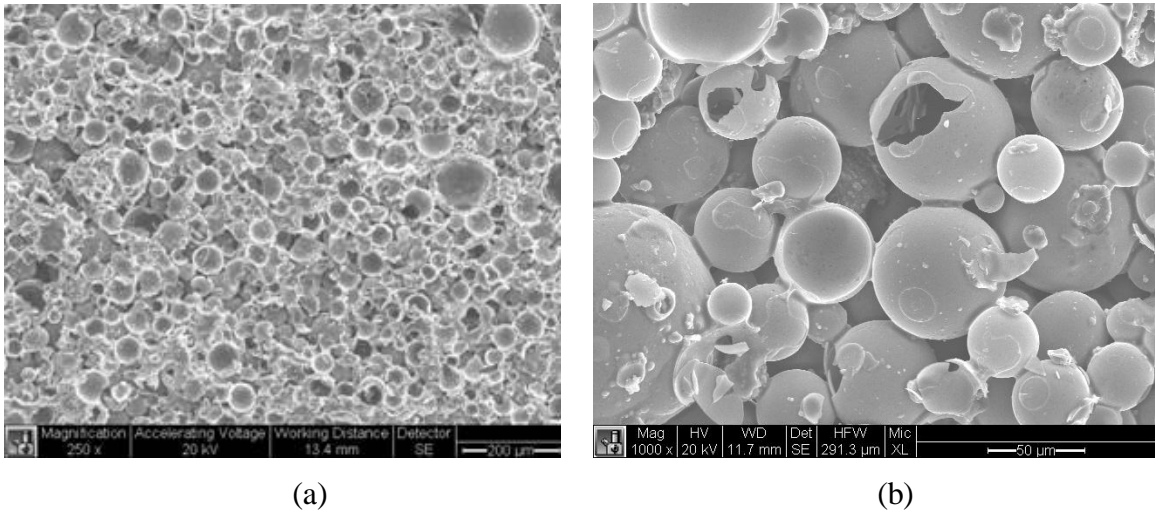


Figure 2.7. Post-Curing Cycle



**Figure 2.8. Photograph of the Molded Panel**



**Figure 2.9. SEM Micrograph of the base Eco-Core (a) 250x (b) 1000x**

Each specimen was identified and the density was measured by measuring the weight and volume of at least ten specimens of  $25.4 \times 25.4 \times 12.7 \text{ mm}^3$  ( $1 \times 1 \times 0.5 \text{ in}^3$ ) size. The measured densities of Eco-Core specimens are given in Table 2.5. The Eco-

Core density varied from 0.51 to 0.53 g/cc with an average value of 0.52 g/cc and a coefficient of variation of 1%, which is quite reasonable for lab manufactured material.

**Table 2.4. Density and Dimensions of Eco-Core Panels**

Panel #	Length, mm			Width, mm			Thickness, mm						Weight, g	Bulk Density, g/cc
	1	2	3	1	2	3	1	2	3	4	5	6		
MR01	304.5	304.7	304.6	304.6	304.7	304.6	12.81	12.83	12.85	12.87	12.90	12.87	620.04	0.520
R03	304.6	304.5	304.5	304.7	304.6	304.5	12.85	12.91	12.87	12.86	12.81	12.85	626.21	0.525

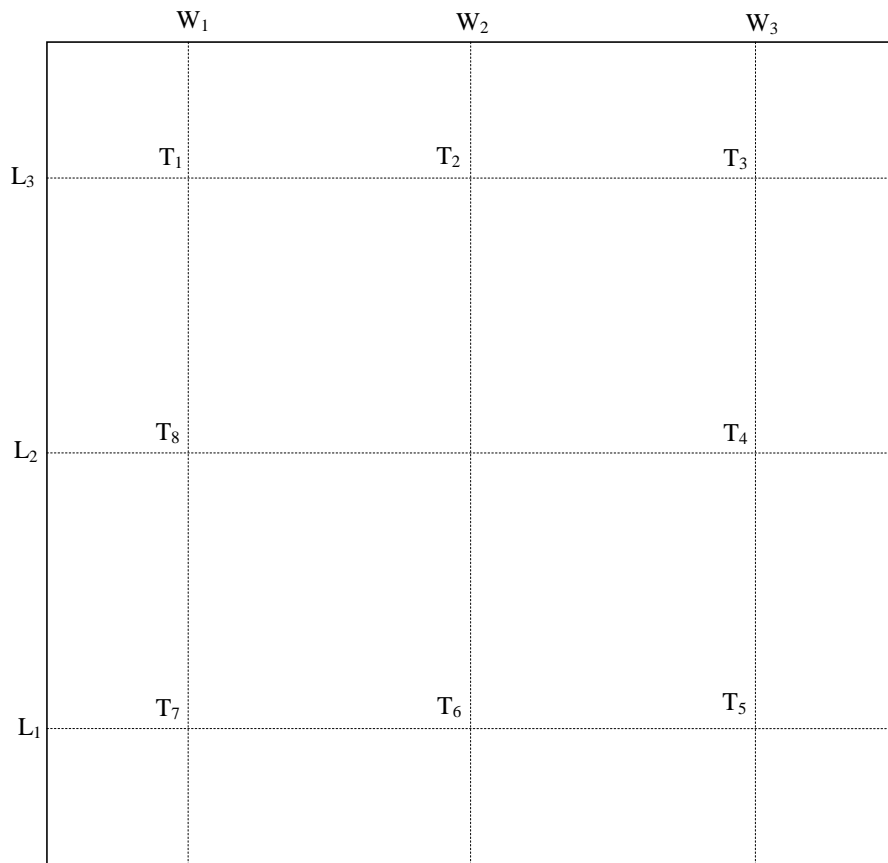


**Figure 2.10. Locations of Dimensional Measurement in a Panel**

**Table 2.5. Density of Eco-Core Specimens**

Panel #	Specimen #	Dimension, mm												Weight, g	Bulk Density, g/cc
		Length				Width				Thickness					
		1	2	3	Avg.	1	2	3	Avg.	1	2	3	Avg.		
R03	1	25.4	25.3	25.3	25.3	25.4	25.4	25.4	25.4	12.84	12.84	12.84	12.84	4.265	0.516
	2	25.3	25.4	25.4	25.4	25.3	25.4	25.3	25.3	12.88	12.87	12.88	12.88	4.367	0.528
	3	25.4	25.3	25.4	25.4	25.4	25.3	25.3	25.3	12.87	12.86	12.87	12.87	4.328	0.524
	4	25.3	25.3	25.3	25.3	25.3	25.4	25.4	25.4	12.82	12.82	12.82	12.82	4.316	0.525
	5	25.4	25.4	25.3	25.4	25.4	25.3	25.4	25.4	12.86	12.86	12.86	12.86	4.387	0.530
	6	25.5	25.4	25.3	25.4	25.4	25.4	25.3	25.4	12.81	12.80	12.81	12.81	4.254	0.516
	7	25.3	25.4	25.4	25.4	25.4	25.5	25.5	25.5	12.87	12.88	12.88	12.88	4.398	0.529
	8	25.4	25.4	25.4	25.4	25.4	25.3	25.4	25.4	12.81	12.80	12.81	12.81	4.287	0.520
	9	25.3	25.4	25.3	25.3	25.3	25.3	25.4	25.3	12.82	12.83	12.83	12.83	4.345	0.528
	10	25.4	25.3	25.3	25.3	25.4	25.4	25.3	25.4	12.80	12.82	12.81	12.81	4.332	0.526
R04	1	25.3	25.4	25.4	25.4	25.3	25.4	25.5	25.4	12.83	12.82	12.83	12.83	4.306	0.521
	2	25.4	25.3	25.4	25.4	25.5	25.4	25.3	25.4	12.80	12.81	12.81	12.81	4.312	0.523
	3	25.4	25.4	25.3	25.4	25.5	25.4	25.3	25.4	12.87	12.84	12.86	12.86	4.354	0.526
	4	25.4	25.5	25.5	25.5	25.3	25.4	25.4	25.4	12.85	12.85	12.85	12.85	4.323	0.521
	5	25.3	25.4	25.3	25.3	25.4	25.4	25.4	25.4	12.88	12.85	12.87	12.87	4.309	0.521
	6	25.4	25.3	25.3	25.3	25.3	25.4	25.4	25.4	12.87	12.85	12.86	12.86	4.212	0.510
	7	25.3	25.4	25.4	25.4	25.4	25.3	25.4	25.4	12.83	12.82	12.83	12.83	4.343	0.526
	8	25.5	25.4	25.3	25.4	25.4	25.4	25.3	25.4	12.83	12.82	12.83	12.83	4.296	0.520
	9	25.3	25.4	25.4	25.4	25.3	25.3	25.4	25.3	12.89	12.88	12.89	12.89	4.254	0.514
	10	25.4	25.3	25.4	25.4	25.4	25.4	25.3	25.4	12.88	12.88	12.88	12.88	4.276	0.516

## 2.4 Mechanical Characterization

Six types of mechanical tests were conducted, namely, unconfined and confined compression, tension, flexure, shear and fracture according to ASTM standards C-365, D-3574, D-790, D-5379 and E-399, respectively. There is no standard for the confined compression test; therefore the unconfined specimen inserted in a snug fit steel cylinder was used. The specimen configurations used for these tests are shown in Figure 2.11. The density measurements were completed on all the specimens used in the mechanical tests. Tensile, flexural, shear and fracture toughness specimens were prepared by machining Eco-Core panels as per test requirements using templates. Panels of size 305x305x12.7

mm were fabricated and compression, tension, flexure, shear and fracture specimens were machined respectively. Figures 2.12 and 2.13 show the specimen layout. All dimensions are in millimeter. Unconfined compression specimens were represented by UCs, confined compression specimens were represented by CCs, fracture specimens were represented by Fs, Flexure specimens were represented by Bs, Shear specimens were represented by ISs and tensile specimens were represented by Ts. The ASTM methods and the sample preparation for the characterization are described in more detail in the following sections. Five specimens were tested for each property.

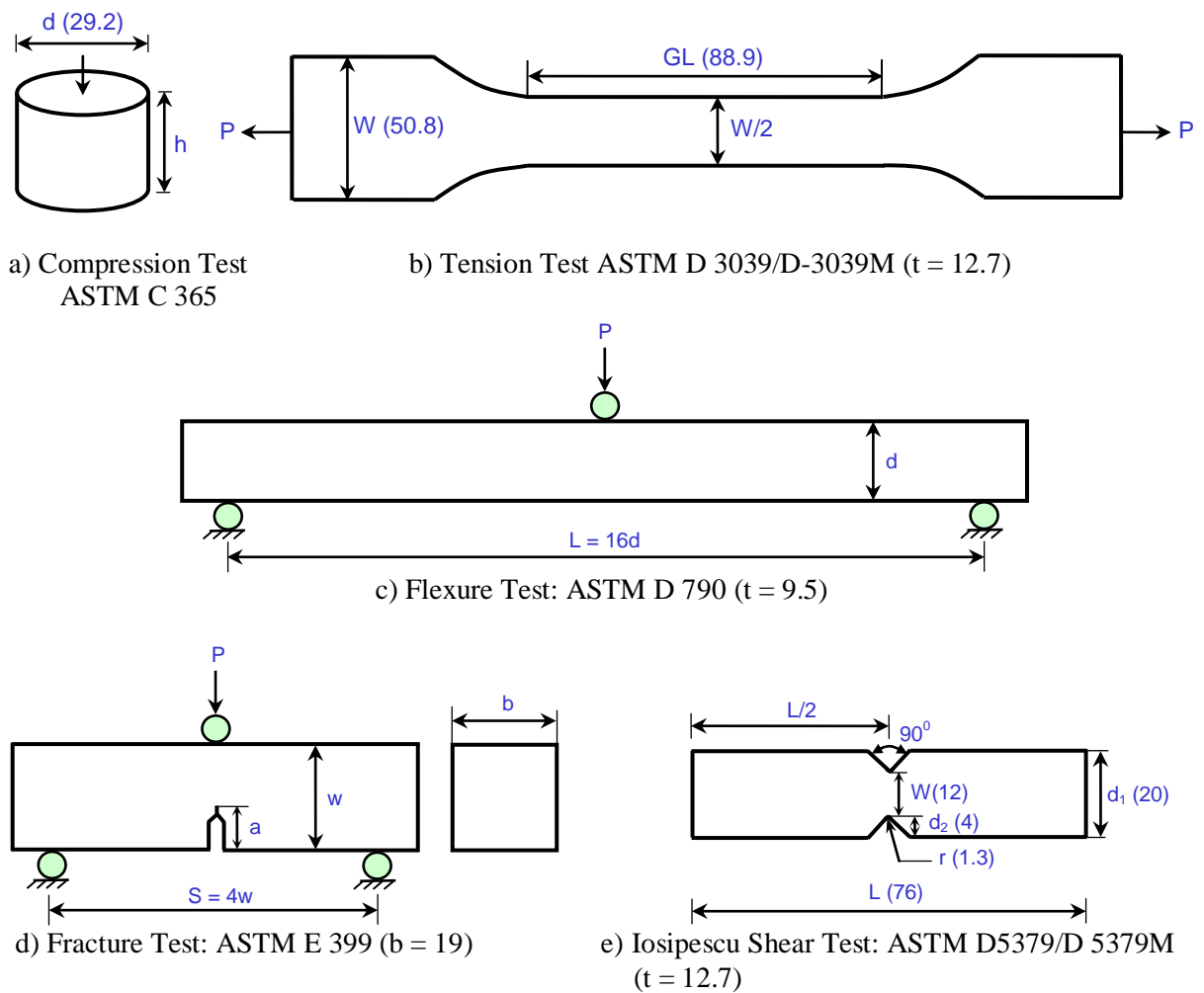


**Figure 2.11. Specimen Configurations**

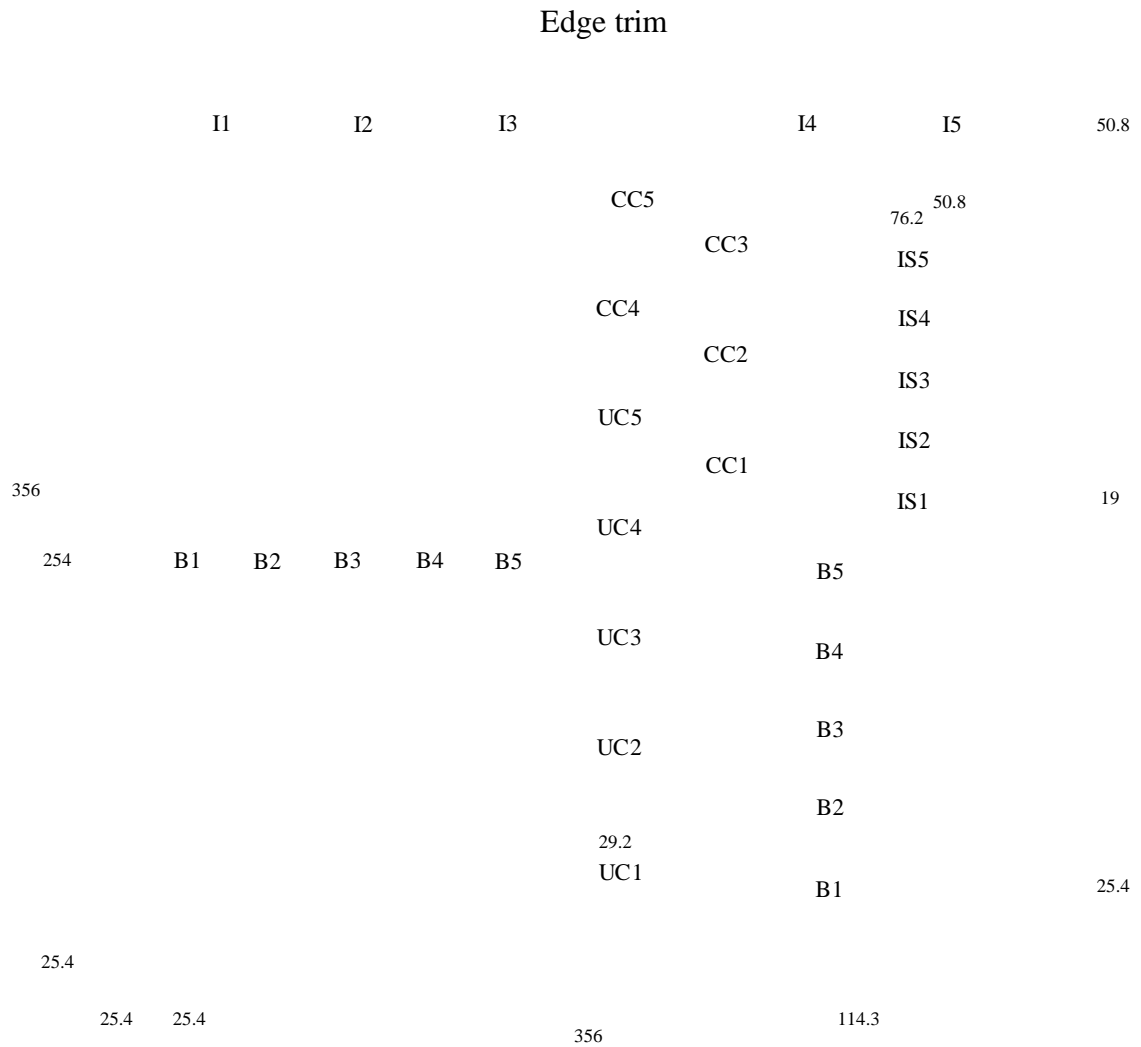


**Figure 2.12. Specimen Layout**

### ***2.4.1 Compression Test***

#### ***2.4.1.1 Unconfined***

The unconfined compression tests were performed according to ASTM C365 using an Instron 4204 electromechanical testing machine. The top and bottom face of each cylindrical specimen was coated with graphite fine powder to reduce the contact friction between the specimen and the platens. The specimen was compressed between two flat

## Edge trim

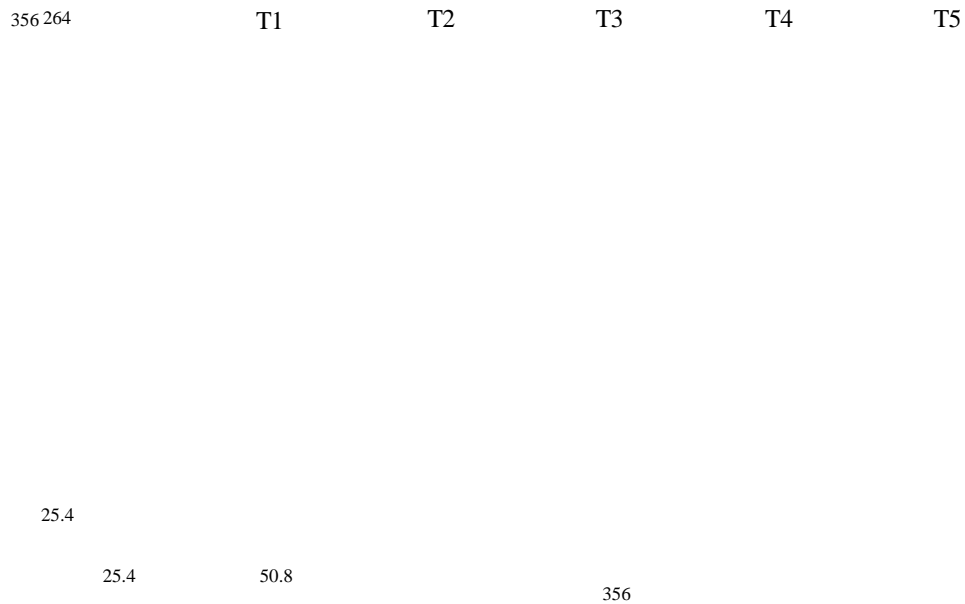


**Figure 2.13. Tensile Specimen Layout**

platens at a constant displacement rate of 1.27 mm/min while load and displacement were recorded every half second by a Vishay system 5000 scanner until the specimen fractured. Failure loads and failure modes were also recorded. Compressive stress and strain were calculated as load/area and displacement/initial height, respectively. Table 2.6 summarizes the density, compression strength, and compression modulus of Eco-Core samples.

**Table 2.6. Unconfined Compression Properties of Eco-Core**

Panel #	Specimen #	Dimension, mm						Weight, g	Density, g/cc	Maximum load, kN	Compression	
		Diameter			Thickness						Strength MPa	Modulus GPa
		1	2	3	1	2	3					
R03	1	29.79	29.85	29.82	12.93	12.92	12.93	4.87	0.540	14.1	20.1	1.01
	2	29.82	29.85	29.82	12.97	12.97	12.97	4.91	0.542	15.6	22.3	1.24
	3	29.79	29.90	29.79	12.97	12.95	12.95	5.01	0.554	14.9	21.3	1.03
	4	29.85	29.87	29.77	12.97	12.97	12.97	4.99	0.550	16.6	23.8	1.34
	5	29.82	29.87	29.82	12.97	12.98	12.98	5.01	0.553	15.2	21.7	1.11
Average (% CV)									0.548 (1.2)	15.3 (6.1)	21.9 (6.1)	1.15 (12)

#### 2.4.1.2 Confined

The purpose of the confined compression test was to measure the energy absorption potential of Eco-Core materials. The test setup is shown in Figure 2.14. The test fixture was a machined steel sleeve with an inner diameter of 30.2 mm, an outer diameter of 50.8 mm and a length of 88.9 mm. The compression load was applied using a plunger whose outer diameter was 29.5 mm and whose length was 114.3 mm. The specimen was compressed against the base plate with an outer diameter of 88.9 mm and a depth of 19.1 mm. The base plate had a cylindrical recess of depth 6.5 mm and diameter 51 mm to hold the steel sleeve in place. The dimensional tolerance for all parts was  $\pm 0.127$  mm. The load was applied by stroke control. The load and machine displacements were recorded continuously until the specimen loading rate became too high, indicating the full compression of specimen. From the data, stress and strain were calculated.

Figure 2.15 shows a confined compression stress-strain response of a typical cellular foam material including Eco-Core [72]. The critical parameters are compression strength ( $\sigma_c$ ), failure strain ( $\epsilon_c$ ), crushing strain ( $\epsilon_{crush}$ ) and the two moduli, namely, foam modulus  $E_{foam}$  and solid modulus  $E_{solid}$ . Critical points and associated failure in the diagram are compression strength, wherein the binder between the microbubbles fails. This process was followed by the crushing of the microbubbles in a confined volume, and then the bubbles consolidated as a solid, which is shown by a rising curve.  $E_{foam}$  was related through  $\sigma_c$  and  $\epsilon_c$  while  $E_{solid}$  had no role to perform in the energy absorption mechanism.

Energy absorption density was approximated by:

$$E_{EA} = \frac{1}{2} \sigma_c \varepsilon_c + \sigma_c \varepsilon_{crush} \quad (2.1)$$

and it was used for the comparison of different materials. The first part was the strain energy of the foam at failure and the second part was the crushing energies. As a first approximation, this equation could be written:

$$E_{EA} = \sigma_c \varepsilon_{crush} \quad \because \varepsilon_c \ll \varepsilon_{crush} \quad (2.2)$$

One can improve  $E_{EA}$  by increasing  $\sigma_c$  and  $\varepsilon_{crush}$ . The  $\varepsilon_{crush}$  depended on the void fraction of the foam while  $\sigma_c$  depended on the properties of the binder that encapsulated the microscopic voids and microbubbles. The parameters  $\sigma_c$  and  $\varepsilon_{crush}$  played an important role in the energy absorption mechanism. The  $\varepsilon_{crush}$  depended on the void fraction of the foam while  $\sigma_c$  depended on the properties of the binder that encapsulate the microscopic voids and microbubbles. Material developers have to weigh both parameters in the contest of application to design materials. Energy absorption density per unit volume was calculated from the area ABCD as shown in Figure 2.15. Table 2.7 summarizes the crushing strength, crushing strain and energy absorption density for the Eco-Core samples.

#### **2.4.2 Tensile test**

Tension tests were performed according to ASTM D 3574 on samples designed with a dog-bone shape to ensure failure away from the grips. Tests were run on an Instron 4204 electromechanical testing machine using mechanical (non-hydraulic) wedge grips and an extensometer for axial strain measurement. Rectangular specimens were carefully cut from panels using a diamond saw of the size specified in the standard. The rectangular specimens were clamped in a routing fixture and precisely machined to dumbbell-shape using a router. The load, displacement, and extensometer readings were recorded every half second by a Vishay system 5000 scanner until the specimen fractured.

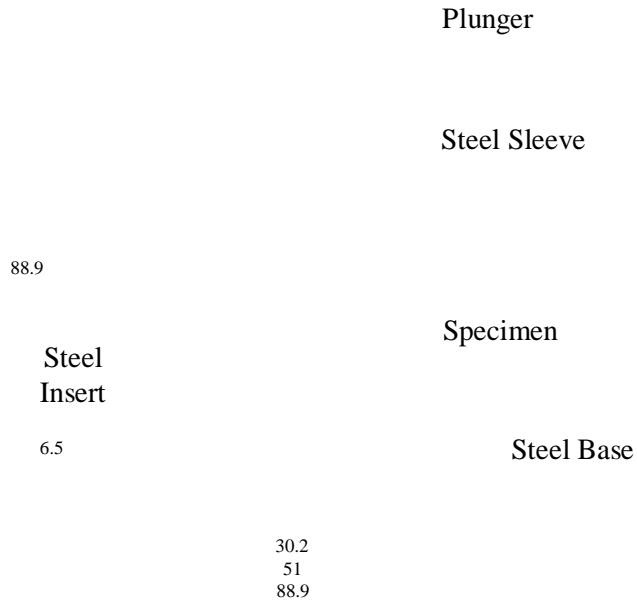


**Figure 2.14. Confined Compression Test Set-up**

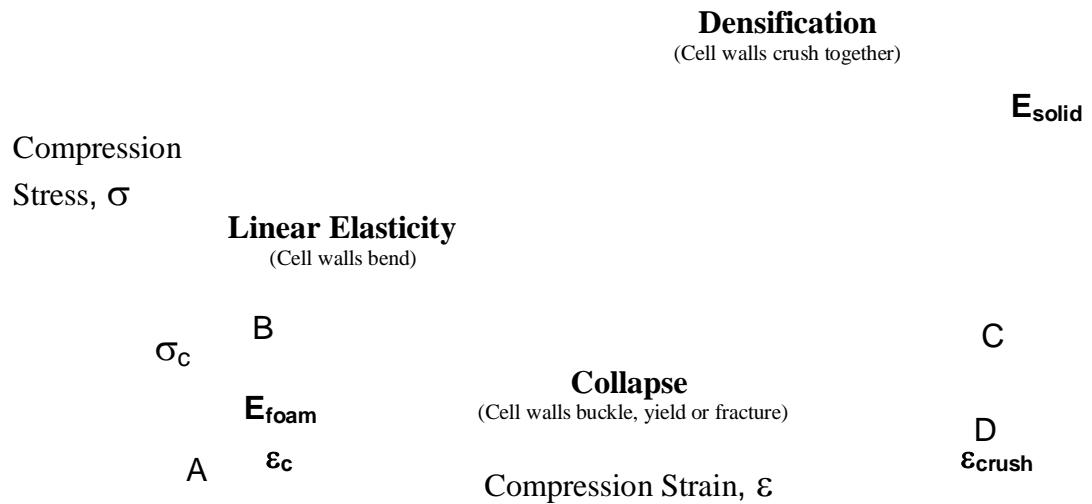


**Figure 2.15. Typical Compression Stress-Strain Response of Foam Material [72]**

**Table 2.7. Confined Compression Properties of Eco-Core**

Panel #	Specimen #	Dimension, mm						Weight, g	Density, g/cc	Maximum load, kN	Confined Compression		
		Diameter			Thickness						Failure strength, MPa	Crushing Strain, m/m	Energy Absorption Density, MPa
		1	2	3	1	2	3						
R03	1	29.82	29.87	29.95	12.93	12.93	12.93	4.90	0.541	14.2	20.3	0.467	9.1
	2	29.92	29.82	29.95	12.95	12.95	12.95	5.03	0.553	14.8	21.0	0.447	9.1
	3	29.85	29.87	29.92	12.99	13.00	13.00	5.07	0.556	15.2	21.7	0.449	9.4
	4	29.87	29.90	29.92	12.95	12.93	12.93	4.98	0.548	14.5	20.6	0.456	9.1
	5	29.82	29.90	29.95	12.97	12.97	12.97	4.99	0.548	15.1	21.6	0.451	9.5
Average (% CV)									0.549 (1.1)	14.8 (2.8)	21 (2.8)	0.454 (1.7)	9.3 (1.9)

A constant displacement rate of 1.27 mm/min was used during testing. The failure loads and modes were also recorded. From test data, the tensile modulus and strength were determined as per the ASTM standard. The average, standard deviation and % coefficient of variation (CV) were calculated and are listed in Table 2.8.

**Table 2.8. Tensile Properties of Eco-Core**

Panel #	Specimen #	Dimension, mm							Weight, g	Density, g/cc	Maximum load, kN	Tensile	
		Length	Width			Thickness						Strength, MPa	Modulus, GPa
			1	2	3	1	2	3					
MR01	1	265.4	25.62	25.60	25.62	12.90	12.89	12.88	90.2	0.54	1.59	4.8	2.54
	2	265.3	25.69	25.70	25.69	12.87	12.87	12.85	88.5	0.50	1.70	5.1	2.55
	3	265.2	25.65	25.65	25.62	12.87	12.89	12.89	90.8	0.54	1.57	4.8	2.70
	4	265.3	25.67	25.67	25.70	12.90	12.89	12.88	92.1	0.55	2.04	6.2	2.67
	5	265.4	25.68	25.64	25.68	12.79	12.80	12.81	92.7	0.53	-----	-----	-----
Average (% CV)									0.53 (3.2)	1.72 (12.6)	5.2 (12.5)	2.62 (3.2)	

### 2.4.3 Flexural test

The flexural tests were performed according to ASTM D 790. The tests were performed using a 3-point bend fixture by an Instron 4204 electromechanical testing machine. Rectangular specimens were carefully cut from panels using a diamond saw of

the size specified in the standard. The span of the support,  $S$ , was chosen to be 152 mm to achieve a span-to-depth ratio of 16, as recommended by the standard. A constant displacement rate of 1.27 mm/min was used while recording load and center deflection every half second. Flexural strength and modulus were calculated and are listed in Table 2.9.

**Table 2.9. Flexural Properties of Eco-Core**

Panel #	Specimen #	Dimension, mm						Weight, g	Density, g/cc	Maximum load, kN	Flexural		
		Length, h	Width			Thickness					Strength, MPa	Modulus, GPa	
			1	2	3	1	2						3
R03	1	254.0	25.32	25.50	25.53	12.95	12.95	12.88	45.03	0.54	0.17	12.1	2.94
	2	254.1	25.17	25.20	25.22	12.88	12.88	12.83	41.42	0.50	0.14	10.0	2.59
	3	254.2	25.27	25.15	25.25	12.95	12.95	12.90	45.05	0.54	0.17	12.1	3.00
	4	254.2	25.32	25.20	25.40	12.95	12.95	12.93	45.48	0.55	0.16	11.5	3.01
	5	254.0	25.15	25.27	25.32	12.90	12.93	12.88	44.07	0.53	0.16	11.7	2.89
Average (% CV)									0.53 (3.2)	0.16 (8.4)	11.5 (7.8)	2.89 (5.9)	

#### 2.4.4 Shear test

The shear tests were performed according to the Iosipescu or V-notched beam method, ASTM D 5379/D 5379M with the Instron 4204 electromechanical testing machine and a V-notched beam shear fixture. Specimen preparation was extremely important for this test. Rectangular specimens were carefully cut from panels using diamond saw cutter of the size specified in the standard. Final dimensions were obtained by precision grinding. In order to machine the V-notch, the specimens were stacked and clamped in a vise with a dummy specimen on the backside to prevent edge chipping. Notches were cut by precision milling. A constant displacement rate of 0.5 mm/min was used. The load and displacement readings were recorded every half second by a Vishay system 5000 scanner until the specimen fractured. Some specimens were strain gauged to measure the shear strain and to calculate the modulus. Shear strength was calculated by peak load divided by the cross-sectional area at the notch. Five specimens were tested

and the average, standard deviation and % coefficient of variation (CV) were calculated and are listed in Table 2.10.

**Table 2.10. Shear Properties of Eco-Core**

Panel #	Specimen #	Dimension, mm						Weight, g	Density, g/cc	Maximum load, kN	Shear		
		Width across notch	Width			Thickness					Strength, MPa	Modulus, GPa	
			1	2	3	1	2						3
R03	1	11.18	19.13	19.08	19.10	12.90	12.93	12.93	9.57	0.51	0.52	4.0	0.88
	2	10.74	19.08	19.05	19.05	12.93	12.95	12.88	9.75	0.52	----	----	----
	3	10.33	19.10	19.10	19.08	12.88	12.85	12.90	9.95	0.53	0.75	5.7	1.08
	4	10.50	19.08	19.05	19.05	12.95	12.93	12.93	9.82	0.52	0.69	5.2	1.02
	5	10.54	19.10	19.08	19.10	12.90	12.88	12.85	9.68	0.52	0.68	5.2	----
Average (% CV)									0.52 (1.5)	0.66 (14.6)	5.1 (14.3)	0.99 (10.3)	

#### 2.4.5 Fracture test

The fracture toughness tests were performed using a single-edge notched bend specimen according to ASTM E399. The crack starter notch of each sample was machined to a width of 2.3 mm and a depth of approximately 8.2 mm. A sharp crack was introduced using a sharp razor blade fixture mounted in a vise. This setup ensured that a sawing motion against the end of the starter notch would result in a fine crack extending from the center of the starter notch. These cracks were cut to about 1.3 mm beyond the machined notch, to a total crack length-to-width ratio of 0.5. The crack length,  $a$ , was selected such that  $0.45 < a/W < 0.55$ . The fracture specimens had a through-the-thickness crack (TC). The tests were conducted using a 3-point bend fixture by an Instron 4204 electromechanical testing machine at constant displacement rate of 0.25 mm/min while load and center displacement were recorded every half second. The critical stress intensity factor,  $K_{Ic}$ , was estimated from the peak load  $P_{max}$  using the following equations [73];

$$K_{Ic} = \frac{P_{max}}{BW^{1/2}} f\left(\frac{a}{W}\right) \quad (2.3)$$

$$f\left(\frac{a}{W}\right) = \frac{3\left(\frac{a}{W}\right)^{0.5}}{\left[2\left\{1+2\left(\frac{a}{W}\right)\right\}\left(1-\frac{a}{W}\right)^{0.5}\right]} \left[1.99 - \left(\frac{a}{W}\right)\left(1-\frac{a}{W}\right)\left\{2.15 - 3.93\left(\frac{a}{W}\right) + 2.7\left(\frac{a}{W}\right)^2\right\}\right] \quad (2.4)$$

where  $f(a/w)$  is a shape factor,  $P_{max}$  is the peak load at the onset of crack growth in a linear elastic fracture, and  $a$  is the crack length. In order to establish that the measured toughness was the plane strain fracture toughness, the test data was checked to satisfy the load criterion. Figure 2.16 shows a schematic of load-displacement plot in a fracture test. The line AB is the initial straight line portion of the plot, and line AB' is 95% of the slope of line AB. The intersection of the load-displacement curve and line AB' defined the apparent fracture load,  $P_Q$ . For the plane strain fracture toughness test to be valid,  $P_{max} \leq 1.1P_Q$ . Test results are listed in Table 2.11. From the test data, it was observed that the load criterion was satisfied.

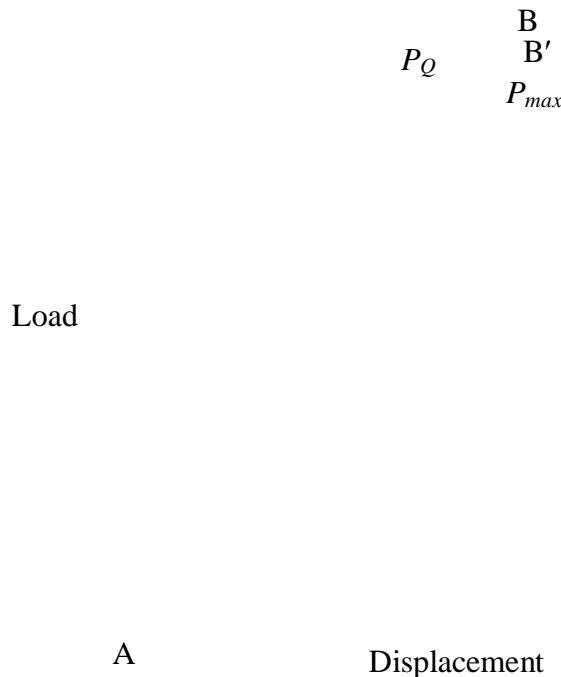


**Figure 2.16. Determination of  $P_Q$  as per Standard**

**Table 2.11. Fracture Properties of Eco-Core**

Panel #	Density, g/cc	Specimen #	W, mm	b, mm	a, mm	Span S, mm	P <sub>max</sub> , N	K <sub>Ic</sub> , kN/m <sup>3/2</sup>
		1	-----	-----	-----	-----	-----	-----
		2	25.5	12.9	12.1	101.6	74.0	349.2
R03	0.52	3	25.7	12.9	12.2	101.6	54.8	261.4
		4	25.5	12.9	12.2	101.6	69.2	333.8
		5	25.4	12.9	11.9	101.6	70.4	333.0
Average (% CV)							67.1 (12.6)	319.4 (12.3)

## 2.5 Results and Discussions

### 2.5.1 Unconfined Compression

Compression strength and modulus of Eco-Core samples are summarized in Table 2.6. The compression strength varied from 20 to 24 MPa with a co-efficient of variation of 6 % whereas the average compression modulus was 1.15 GPa with a co-efficient of variation of 12 %. The compression behavior of the Eco-Core samples as a function of binder material, binder content and density was investigated by Shivakumar and co-researchers and is reported in [14]. Shivakumar et al. also studied the effect of density and binder weight fraction on the compression properties of Eco-Coe. They found that the compression strength appeared to be a linear function of density and the density was also a nearly linear function of the binder weight percentage. Figure 2.17 exhibits uniaxial compression stress-strain behavior for five Eco-Core samples from the same panel. Figure 2.17 clearly shows that the all the curves were close to each other except for the specimen 1 thereby indicating that the results were repeatable. All the curves showed an initial linear elastic region until strain reaches approximately 2.5 %. As the peak stress crushed the top layers of the samples, the stress began decreasing and it crushed the hollow cenospheres upon displacement of the compression platens. This process continued until approximately 26% of the strain. The results of all specimens were nearly the same except for one specimen. A similar behavior was observed by N. Gupta, et al. for high

resin content (about 50% volume) syntactic foams made with epoxy resin and glass hollow microspheres [74].

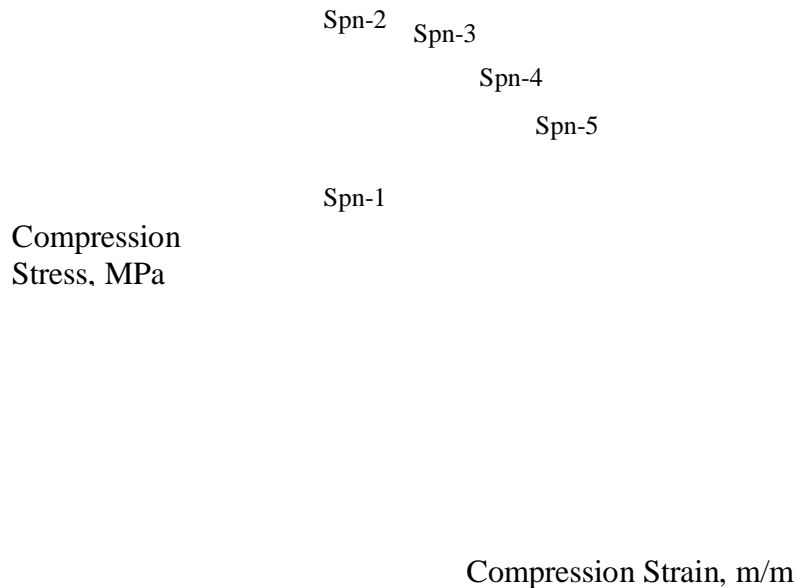


**Figure 2.17. Compression Stress vs. Strain Curve for Eco-Core**

### ***2.5.2 Confined Compression***

The confined compression stress-strain plot of Eco-Core samples is shown in Figure 2.18. The confined stress-strain response of Eco-Core samples matched well with that of the hypothesized foam, shown in Figure 2.15. From the Figure 2.18 it is clear that stress increased linearly with strain until approximately 2.8% and then stress remains plateau until approximately 45% strain. This constant stress behavior can be attributed to the binder breakage followed by a redistribution of the hollow cenospheres. Beyond 45% strain, the increased stress crushed the hollow cenospheres and compacted them to a solid state. This kind of stress-strain response shows the potential for the high energy absorbing capability of the Eco-Core. From Table 2.7 it is observed that the average failure strength is about 21 MPa, which compares well with that of the unconfined

compression strength (22 MPa). The crushing strain varied from 44.7% to 46.7% with sample to sample variation of 0.8% and the average energy absorption density of Eco-Core was 9.3 MPa with a CV of 1.7%.

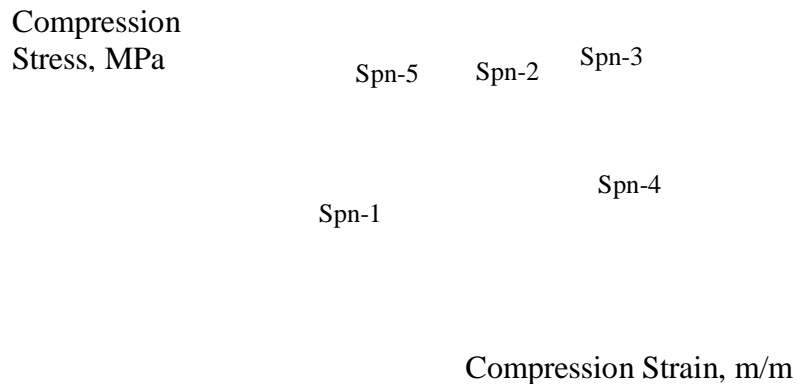


**Figure 2.18. Confined Compression Stress vs. Strain Curve for Eco-Core**

### **2.5.3 Tension**

The tensile stress-strain plot of Eco-Core samples is shown in Figure 2.19. From Figure 2.19 it is clear that the stress-strain response of Eco-Core is linear and is similar to that of a typical brittle material. Eco-Core showed a low fracture strain varying from 1.9% to 2.7%. The brittle nature of Eco-Core could be attributed to the brittleness of the phenolic resin matrix in a very thin layer form. All the Eco-Core samples showed a catastrophic brittle fracture across a plane perpendicular to the loading direction. Table 2.8 records the specimen dimensions, maximum load, tensile strength and tensile modulus data for the Eco-Core samples. The tensile strength of Eco-Core was approximately 5.2 MPa. Nevertheless, the overall standard deviation for the tensile

strength for all samples was within 13%, which is satisfactory for this lab manufactured material. Note that the tensile strength is nearly 1/4 times that of the compression strength (21.8 MPa). The average tensile modulus value of Eco-Core is 2.6 GPa with a percent coefficient of variation of under 5%. Note that the tensile modulus is twice that of the compression modulus (1.15 GPa). Also note that the consistency and minimal data scatter confirmed the quality of the panel fabrication, specimen preparation, testing, and data reduction.

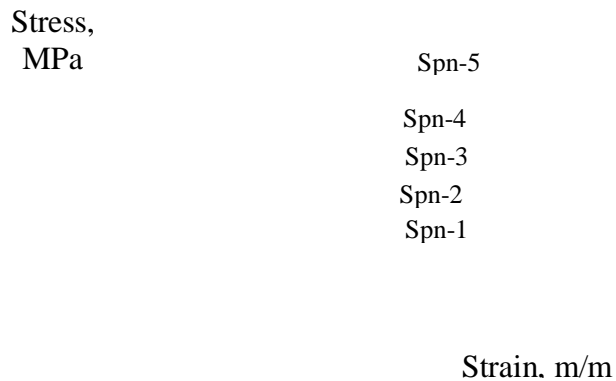


**Figure 2.19. Tensile Stress vs. Strain Curve for Eco-Core**

#### **2.5.4 Flexure**

The load-displacement curve under flexure for the Eco-Core samples is shown in Figure 2.20. The response was a linear elastic material and the specimen failed catastrophically like brittle fracture across a plane parallel to the loading direction. The displacement values corresponding to the peak loads varied from 2.05 to 2.25 mm. Indeed for all specimens, it was observed that the failure began in the form of crack

initiation on the tensile (bottom) side of the specimen as the displacement increased. This crack tended to grow towards the compression (top) side of the specimen like all brittle materials. Similar observations were reported by Gupta, et al. [75] for epoxy syntactic foams. Table 2.9 records the specimen dimensions, maximum load, flexural strength and flexural modulus. The average flexural strength of Eco-Core was 11.5 MPa with a sample to sample variation of 7.8% where as the average modulus was 2.89 GPa with a coefficient of variation of 5.9%. Note that the flexural modulus was nearly the same as the tensile modulus (2.62 GPa) or 9.6% higher. On the other hand, the flexural strength was nearly one-half of the compression strength and twice that of the tensile strength.

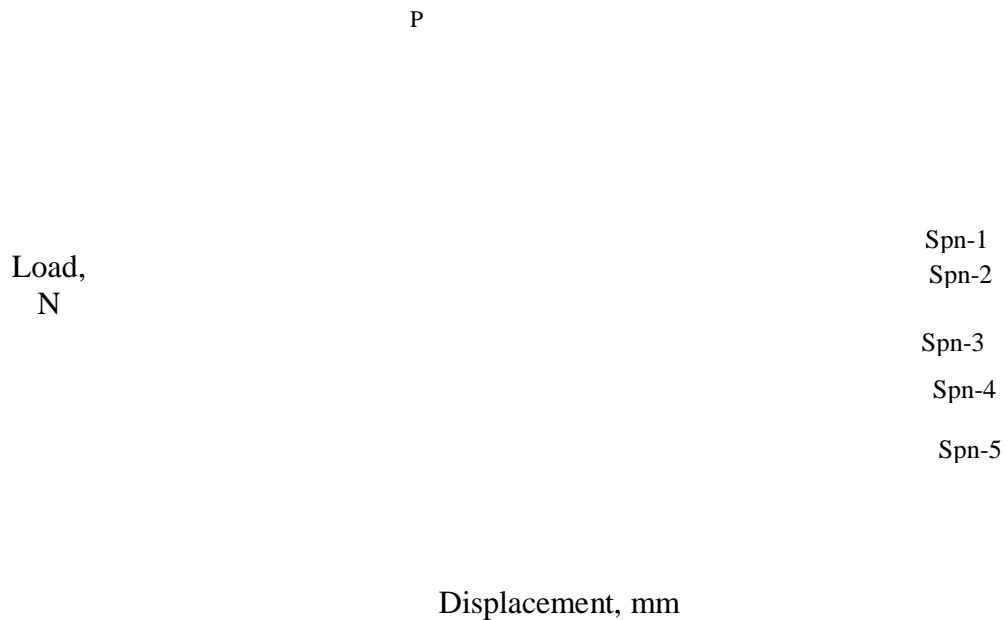


**Figure 2.20. Flexural Load vs. Displacement Curve for Eco-Core**

### **2.5.5 Shear**

The load-displacement curve under shear for Eco-Core samples is shown in Figure 2.21. Eco-Core behaved like a non-linear material when loaded to failure in shear. The considerable variation in the displacement values corresponding to the peak loads

was observed for all Eco-Core samples. The peak load values also showed a wide variation. Table 2.10 records specimen dimensions, maximum load, shear strength and shear modulus for Eco-Core. The shear strength variations from sample to sample were approximately 14% and the average shear strength was 5.1 MPa, which is in the higher range for this class of materials. Note that the shear strength was the same as the tensile strength (5.2 MPa). The shear modulus varied from 0.88 to 1.08 GPa with an average value of approximately 1 GPa. Note that the shear modulus was nearly the same as the compression modulus (1.15 GPa) or 13% lower.

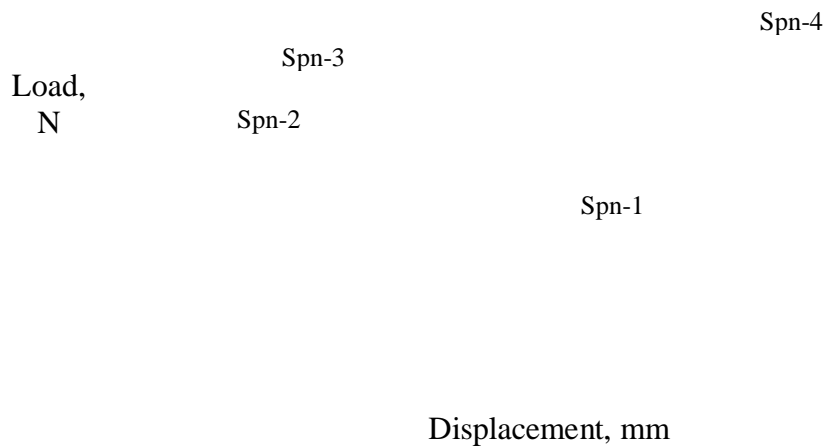


**Figure 2.21. Shear Load vs. Displacement Curve for Eco-Core**

### **2.5.6 Fracture**

The load-displacement curve under the SENB fracture for Eco-Core samples is shown in Figure 2.22. Eco-Core showed a non-linear load-displacement response when loaded to failure. A considerable variation in the peak load values was observed for all samples. Table 2.11 summarizes specimen dimensions, crack details, maximum load and

fracture toughness values for Eco-Core samples. The Eco-Core fracture toughness was in the range of 261 to 349 kPa-m<sup>1/2</sup>, which was considerably small. This measurement indicated that the Eco-Core was brittle in nature. The standard deviation for fracture toughness for all samples was within 13%, which is satisfactory for this lab manufactured material.

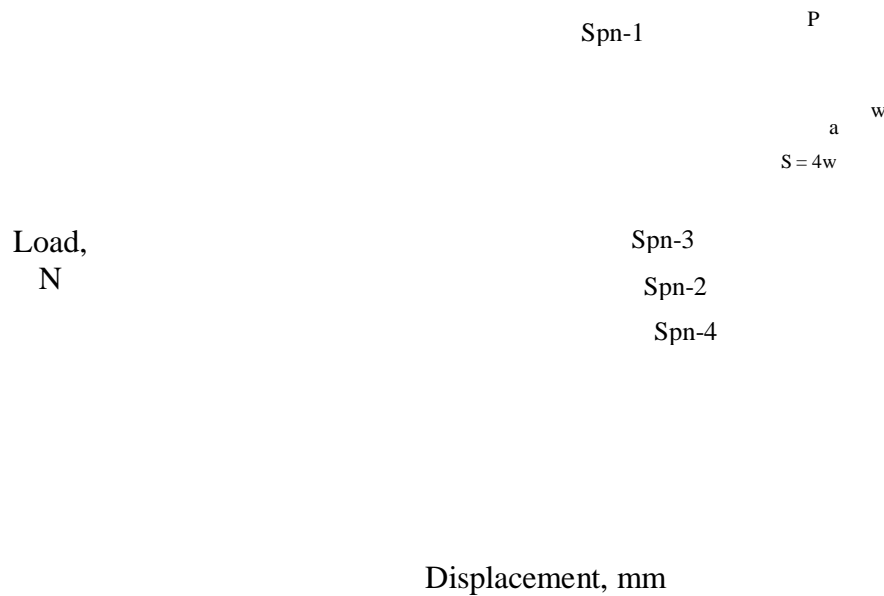


**Figure 2.22. Fracture Load vs. Displacement Curve for Eco-Core**

Table 2.12 compares the mechanical properties of the Eco-Core with the commercially available core materials such as balsa wood, PVC foam, carbon foam, and Alba core. It is very clear from Table 2.12 that the compression, tension, shear and fracture toughness data of the Eco-Core samples developed was very encouraging and compared favorably with other commercial core materials in the market.

**Table 2.12. Comparison of Mechanical Properties of Eco-Core with Other Commercially Available Core Materials**

Property	Balsa		PVC - Divinycell H		Alba Core	Cfoam	Eco-Core
	SB-100	SB-150	H100	H200			
<b>Density, g/cc</b>	0.15	0.24	0.10	0.20	0.20	0.40	0.53
<b>Compression</b>							
Strength, $F_c$ , MPa	12.7	25.8	2.0	4.8	3.7	15.0	21.8
Modulus, $E_c$ , MPa	3,921	7,840	135	240	330	550	1,145
<b>Tension</b>							
Strength, $F_t$ , MPa	13	23.18	3.5	7.1	2.1	3.5	5.2
Modulus, $E_t$ , MPa	3,518	5,688	130	250	230	550	2,622
<b>Shear</b>							
Strength, $F_s$ , MPa	2.9	4.9	1.6	3.5	2.8	2.1	5.1
Modulus, $G_s$ , MPa	157	302	35	85	-	-	1,000
<b>Flexural</b>							
Strength, $F_b$ , MPa	-	-	-	-	-	-	11.5
Modulus, $E_b$ , MPa	-	-	-	-	-	-	2,891
<b>Fracture toughness,</b> kPa-m <sup>1/2</sup>	-	-	-	-	-	-	319.4

## 2.6 Development of Constitutive Material Model

A constitutive model was required to represent the measured constitutive response in terms of simple equations. It was desirable to summarize the experimental results in the form of a simple material response model that could be used in numerical simulations of structural impact/shock responses and other design applications. To serve this purpose, the model should be simple in its form with few constants to be determined.

The stress-strain relationship for the Eco-Core material can be defined by a well known parabolic hardening rule, which is:

$$\frac{\sigma}{\sigma_c} = 1 + k\varepsilon^n \quad (2.5)$$

where  $\sigma_c$  = static compression strength of Eco-Core ( $\sigma_c = 20$  MPa), parameters  $k$ , and  $n$  are constant for a given initial density, and parameter  $k$  has units of stress. The equation (2.5) was fit to the experimental data as shown in Figure 2.18 and it was found that  $k = 45$  MPa and  $n = 5.4$ .

The Figure 2.23 compares the equation (2.5) with  $k = 45$  and  $n = 5.4$  with the experimental data. The equation agreed very well with experimental data. Therefore, the failure model for the Eco-Core was:

$$\frac{\sigma}{\sigma_c} = 1 + 45\varepsilon^{5.4} \quad (2.6)$$

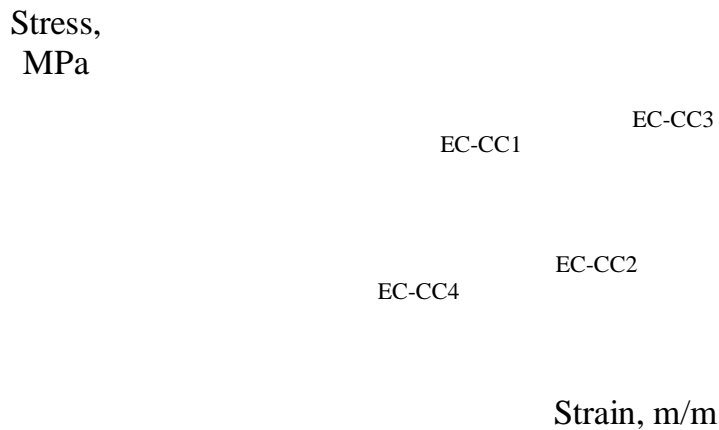


**Figure 2.23. Comparison of Compressive Stress-Strain Curves of Eco-Core from Experiments and from Model Description**

## **2.7 Summary**

Eco-Core was developed as a fire resistant core material for composite sandwich structures. It was made using a large volume of fly ash (Cenosphere) and a small volume of high char yield binder by a syntactic process. The cellular structure of the material offered potential for shock and blast mitigation applications. The compression, tension, shear and fracture toughness data of the Eco-Core were reasonably uniform, the process was repeatable, and the data compared favorably with other commercial core material. The compression strength of Eco-Core was nearly four times that of tensile strength and shear strength; and twice that of flexural strength. The compression modulus of Eco-Core was nearly one-half of the tensile modulus, 40% of the flexural modulus and nearly the same as that of the shear modulus. Fracture toughness studies showed that Eco-Core was brittle in nature. Therefore, there was scope to further modify the Eco-Core for improved toughness. A constitutive model was developed for Eco-Core.

## CHAPTER 3

# PROCESSING AND CHARACTERIZATION OF MODIFIED ECO-CORE

### 3.1 Introduction

This chapter describes the modification of baseline Eco-Core material by various routes with an aim to improve the energy absorption density of Eco-Core. Modification methods, testing and discussion of results are presented in this chapter. The first modification route was the surface confinement by coating with polyurea to different levels and the other modification to base Eco-Core was impregnation of Eco-Core with high-strain-to-fracture elastomeric materials such as polyurethane. This process was intended to enhance the compression strength ( $\sigma_c$ ) of Eco-Core; thus, improving its total energy absorption.

#### 3.1.1 Rationale for modification

- Recent studies have shown that applying a layer of polyurea backing to steel plates significantly enhances the resistance of the composite structure to impact and blast loading. Various tests showed that this improvement can change the response from full penetration of a projectile to fully eliminating fracturing [76]. Therefore surface coating of Eco-Core with polyurea provides an opportunity to enhance the shock mitigation potential of Eco-Core.
- Polyurethane elastomers have high strain to fracture and low viscosity, which can be readily impregnated with Eco-Core that has a high void content. The presence of elastomeric polyurethane in between microbubbles can absorb energy and help to increase the energy absorption capacity of Eco-Core. Therefore, the impregnation of Eco-Core with polyurethane is a potential route to increase the energy absorption potential of Eco-Core.

### 3.2 Materials and Processing

A class of fly ash known as Cenosphere of grade BIONIC BUBBLE–XL-150 obtained from Sphere Services Inc. was used in the formulation of the Eco-Core material. The binder resin was a phenol-formaldehyde resole resin, Durite SC 1008 supplied by Borden Chemical Co. Polyurea Aliphatic type RAP 1567 (manufactured and supplied by Stuart Smith of Engineered Polymers, International, LLC of Conyers, GA) was used to coat the Eco-Core panels. Smooth-On Clear Flex 95 aliphatic type unfilled-low viscosity polyurethane resin (manufactured and supplied by Smooth-On, Inc. of Easton, PA) was used to impregnate the Eco-Core panel. Typical physical properties of polyurea and polyurethane are given in Tables 3.1 and 3.2, respectively. Typical stress-strain responses of polyurea and polyurethane are given in Figures 3.1 and 3.2, respectively [77,78].

**Table 3.1. Typical Physical and Mechanical Properties of Polyurea Elastomers**

Shore A Hardness	60 – 100
Shore D Hardness	25 – 75
Tensile Strength	10- 30 MPa
Elongation	20 - 800 %
Angle Tear	50 - 125 N/mm
Trouser Tear	20 - 60 N/mm
Abrasion	150 - 500 mg
Cold Impact Resistance	50 – 100 kJ/m <sup>2</sup> at -20°C

**Table 3.2. Typical Physical and Mechanical Properties of Polyurethane Elastomers**

Specific Gravity	1.07 - 1.21
Shore Hardness	80A – 75D
Tensile Strength	20 - 62 MPa
100 % Modulus	3 -32 MPa
Elongation	270 - 800 %
Tear Strength Split	12 - 19 N/mm
Abrasion	110 - 435 mg

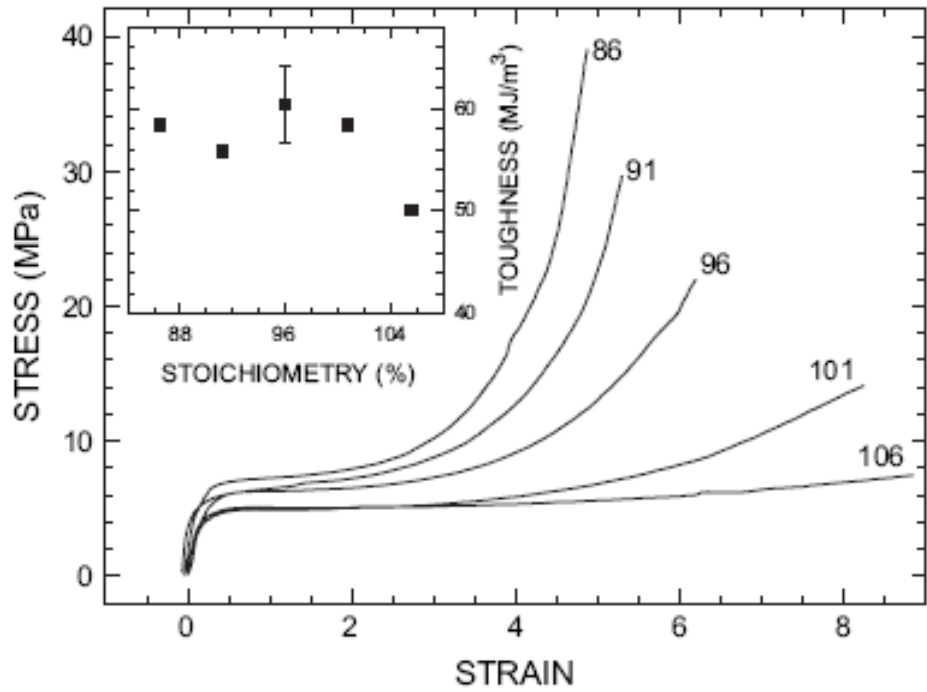


Figure 3.1. Typical Stress-Strain Graph of Polyurea [77]

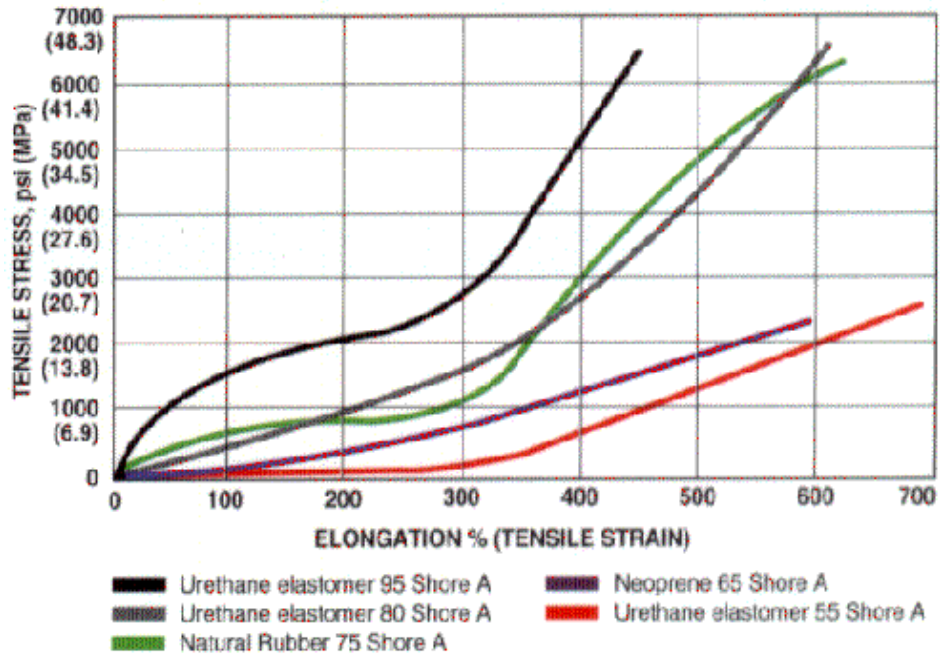


Figure 3.2. Typical Stress-Strain Graph of Polyurethane [78]

### 3.2.1 Coated Eco-Core

The Eco-Core panel was placed on a flat surface and the spacers of required thickness were positioned on edges of panel using adhesive tapes. Polyurea (PU) precursors (part A and part B) 1:1 by volume were mixed as per the manufacturer's procedure. The mix was then uniformly spread over the coating area using a brush and a doctor blade. The coating was allowed to cure at room temperature for 24 hours. The same procedure was followed for coating on the other side of the Eco-Core panel. In a similar manner, Eco-Core panels with near-zero, 10, 20 and 40 mil thick PU coating were prepared. Specimens extracted from these panel are marked as EPU0, EPU10, EPU20 and EPU40 for near-zero, 10 mil, 20 mil and 40 mil thick PU coating, respectively. The picture of the PU coated panels are shown in Figure 3.3.



**Figure 3.3. Photograph of Polyurea Coated Eco-Core Panels**

### ***3.2.2 Impregnated Eco-Core***

Eco-Core panels were impregnated with polyurethane (PUR) resin by three methods to check distribution of the resin through the thickness. The first method was by vacuum impregnation. The second method was by pressure impregnation and the third method was by both vacuum and pressure impregnation. In vacuum impregnation, polyurethane precursors (part A and part B) 1:1 by weight were mixed as per the manufacturer's procedure and the required quantity of mix was transferred to the aluminum tray. Then the Eco-Core panel was placed in the tray over which a dead weight was placed. The entire assembly was transferred to the vacuum chamber and 750mm of Hg vacuum was applied for about 20 minutes. After impregnation the panel was oven cured at approximately 71 °C for 1 hour. In pressure impregnation, the polyurethane soaked Eco-Core panel assembly was transferred to the pressure chamber and 0.048 MPa positive pressure was applied for about 20 minutes. Then the impregnated panel was oven cured at approximately 71°C for 1 hour. In vacuum-pressure impregnation, the polyurethane soaked Eco-Core panel assembly was first transferred to the vacuum chamber and 750mm of Hg vacuum was applied for about 5 minutes. Then the assembly was transferred to the pressure chamber and 0.048 MPa positive pressure was applied for about 15 minutes. After impregnation, the panel was oven cured at approximately 71°C for 1 hour.

Figure 3.4 shows the optical micrographs of the cross section of impregnated Eco-Core samples prepared by three impregnation methods. In the Figure 3.4, the lighter shade is the unimpregnated region where as the darker shade is polyurethane impregnated region. It is clear from the figures that the vacuum-pressure impregnation method showed uniform impregnation throughout the cross section whereas the other two methods showed partial impregnation. In both vacuum and pressure impregnation method, the applied pressure was insufficient to diffuse the polyurethane resin to the center. Therefore, the combination of both vacuum and positive pressure was used for processing the polyurethane impregnated panels. Specimens extracted from this panel were marked as EPUR.

(a)

(b)

(c)

**Figure 3.4. Optical Micrographs of PUR Impregnated Eco-Core (a) Vacuum method (40x) (b) Pressure Method (20x) and (c) Vacuum-Pressure Method (20x)**

In order to assess the quality of the fabricated panels, density and dimensional measurements were carried out. Each panel was identified, dimensionally measured and weighed out. Table 3.3 records the dimensions and density of the modified Eco-Core panels. The thickness of all panels was quite uniform with a co-efficient of variation under 0.5 %. The cylindrical test specimens were cut from the sheets with a hole saw mounted in a drill press. Each specimen was identified and the density is measured by measuring weight and volume of at least five specimens. Measured densities of modified Eco-Core specimens are given in Table 3.4. The density was uniform with a co-efficient of variation under 3 %.

**Table 3.3. Density and Dimensions of Modified Eco-Core Panels**

Panel #	Length, mm			Width, mm			Thickness, mm						Weight, g	Density, g/cc
	1	2	3	1	2	3	1	2	3	4	5	6		
Baseline	165.6	165.7	165.7	164.9	164.9	164.9	25.12	25.10	25.15	25.15	25.15	25.15	363.3	0.529
EPU0	140.7	140.4	140.2	156.6	153.8	153.4	25.15	25.12	25.15	25.17	25.17	25.17	312.3	0.572
EPU10	141.0	141.1	141.1	153.5	153.5	153.5	25.55	25.53	25.60	25.58	25.60	25.50	318.3	0.575
EPU20	141.0	141.1	141.3	153.4	153.4	153.4	26.09	26.11	26.14	26.11	26.14	26.06	322.1	0.570
EPU40	141.5	141.6	141.7	154.0	153.7	153.6	27.15	27.13	27.20	27.23	27.20	27.13	344.0	0.581
EPUR	139.8	129.5	139.9	139.7	139.9	139.9	25.49	25.48	25.47	25.51	25.54	25.58	384.2	0.789

### 3.3 Testing

Two types of tests were conducted, namely, unconfined and confined compression using a cylindrical specimens. The unconfined compression tests were conducted to measure the compression strength and failure modes. The confined compression test was to measure the compression strength ( $\sigma_c$ ), failure strain ( $\epsilon_c$ ) and energy absorption of the material. Density measurements were carried out on the cored specimens used in compression tests. The details of the specimen and testing method are described in chapter 2. Since the objective of the research is to study the energy absorption capacity of PU and PUR modified Eco-Core, confined and unconfined compression properties are tested and other mechanical properties are not characterized.

### 3.4 Discussion of Results

#### 3.4.1 Unconfined Compression

The typical compression stress-strain behavior of Eco-Core and modified Eco-Core is shown in Figure 3.5. The stress-strain curves of PU coated Eco-Core samples were similar to that of the stress-strain response of base Eco-Core but with a higher modulus. The peak compression stress of Eco-Core and PU coated Eco-Core were in the range of 19.4 – 24.6 MPa and the failure strains were in the range of 0.09 - 0.11. The PUR impregnated Eco-Core remained linearly elastic up to an axial strain of 4%. The PUR

**Table 3.4. Density and Dimensions of Modified Eco-Core Compression Specimens**

Panel #	Specimen #	Dimension, mm								Weight, g	Density, g/cc
		Diameter				Thickness					
		1	2	3	Avg.	1	2	3	Avg.		
Baseline	1	29.95	29.96	29.96	29.95	25.32	25.31	25.31	25.31	9.578	0.546
	2	30.01	29.98	30.04	30.01	25.28	25.28	25.30	25.29	9.433	0.536
	3	30.04	29.98	30.01	30.01	25.28	25.28	25.28	25.28	9.587	0.545
	4	30.01	29.98	30.01	30.00	25.30	25.30	25.28	25.29	9.527	0.542
	5	29.96	29.98	29.96	29.97	25.27	25.27	25.27	25.27	9.578	0.546
EPU0	1	29.78	29.75	29.74	29.76	25.31	25.31	25.32	25.31	10.112	0.584
	2	29.78	29.78	29.81	29.79	25.28	25.28	25.28	25.28	10.019	0.578
	3	29.74	29.75	29.78	29.76	25.30	25.31	25.32	25.31	10.174	0.588
	4	29.77	29.78	29.77	29.77	25.27	25.27	25.28	25.28	10.100	0.584
	5	29.75	29.77	29.78	29.77	25.28	25.28	25.28	25.28	9.940	0.574
EPU10	1	29.78	29.75	29.78	29.77	25.80	25.80	25.77	25.79	10.357	0.587
	2	29.78	29.77	29.78	29.78	25.77	25.74	25.77	25.76	10.424	0.591
	3	29.79	29.78	29.79	29.79	25.64	25.67	25.65	25.65	10.299	0.586
	4	29.77	29.79	29.81	29.79	25.64	25.65	25.65	25.65	10.207	0.580
	5	29.73	29.77	29.75	29.75	25.67	25.65	25.64	25.65	10.014	0.571
EPU20	1	29.77	29.77	29.77	29.77	26.34	26.36	26.33	26.34	10.777	0.598
	2	29.78	29.78	29.77	29.78	26.31	26.28	26.27	26.28	10.542	0.586
	3	29.78	29.78	29.81	29.79	26.23	26.23	26.22	26.23	10.365	0.577
	4	29.78	29.78	29.77	29.78	26.22	26.23	26.23	26.23	10.237	0.570
	5	29.77	29.77	29.77	29.77	26.18	26.20	26.19	26.19	9.864	0.550
EPU40	1	29.77	29.79	29.81	29.79	27.32	27.32	27.29	27.31	11.406	0.609
	2	29.77	29.81	29.82	29.80	27.35	27.35	27.39	27.37	11.102	0.591
	3	29.78	29.81	29.79	29.79	27.30	27.30	27.29	27.30	11.047	0.590
	4	29.78	29.81	29.78	29.79	27.28	27.28	27.29	27.28	10.883	0.582
	5	29.77	29.78	29.79	29.78	27.34	27.35	27.35	27.35	10.893	0.581
EPUR	1	29.83	30.07	30.14	30.01	25.80	25.83	25.82	25.82	14.081	0.784
	2	30.16	30.02	30.05	30.08	25.82	25.82	25.85	25.83	14.289	0.792
	3	30.10	30.01	29.88	30.00	25.77	25.74	25.74	25.75	14.342	0.801
	4	30.14	30.01	29.91	30.02	25.76	25.73	25.78	25.76	14.072	0.785
	5	30.15	30.05	30.07	30.09	25.74	25.80	25.77	25.77	14.412	0.800

impregnated Eco-Core showed a peak stress of 51 MPa at approximately 6% strain followed by an unstable zone where the stress decreased with increasing strain until the

strain reached a value of ~10%. Then the stress remained nearly constant with increasing strain until the strain reached ~27%.

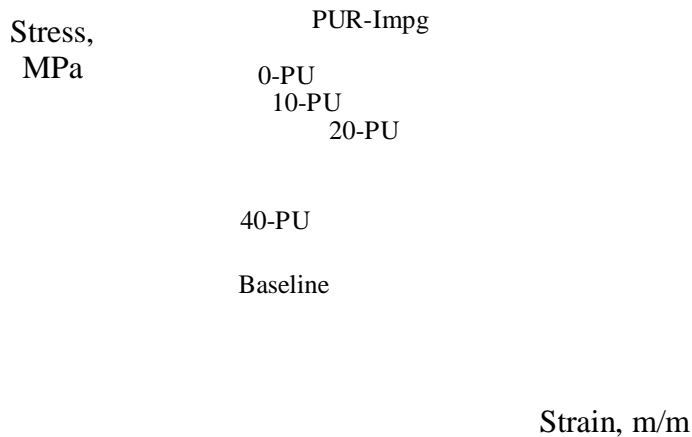


**Figure 3.5. Typical Compression Stress-Strain Plot for Modified Eco-Core**

Table 3.5 summarizes the density, compression strength, and compression modulus for baseline, PU coated and PUR impregnated Eco-Core. The density ranged from 0.54 g/cm<sup>3</sup> for baseline Eco-Core to 0.80 g/cm<sup>3</sup> for PUR impregnated specimens. These results are average of 5 tests. All PU coated Eco-Core samples showed enhancement of compression modulus. Zero-thickness and 10 mil thick PU coated Eco-Core showed 12% and 8% improvement in compression strength respectively. Among all, PUR impregnated eco-core samples showed very significant improvement of about 138% increase of compression strength in comparison with baseline Eco-Core but with a penalty of increased density. It is found that there is up to 12% improvement in

compression strength for PU coated Eco-Core samples. This indicates that the surface coating of PU and impregnation of PUR is beneficial in improving the compression strength. The thickness of PU coating appears to influence the compression properties. Compression strength and compression modulus measured as a function of thickness of PU coating are given in Figure 3.6 & 3.7. The first point in the Figure 3.6 & 3.7 represents the compression data for the 0-thickness PU coated Eco-Core panel and the solid symbol is for the baseline Eco-Core. The compression strength of PU coated Eco-Core samples decreases linearly with increase in PU coating thickness where as the compression modulus remained constant irrespective of the coating thickness. From the Figures 3.6 & 3.7 it is also observed that PU coating beyond 10 mil thick seems to have no effect on compression strength of baseline Eco-Core. All the PU coated Eco-Core's showed up to 64 % improvement in modulus. From the Table 3.5 it is clear that even a very thin PU coating on eco-core seems to improve compression strength by 14 % and compression modulus by 64 %. It also noted that PUR impregnated Eco-Core showed 32% reduction in modulus.

#### *3.4.1.1 Failure Modes*

Figure 3.8 shows the front view of the compression tested base and the modified Eco-Core samples. It is significant to observe from Figures 3.8a and 3.8b that the base Eco-Core and 0-PU specimens showed crushing at the top side layers followed by formation of vertical cracks in the direction of compression. From Figures 3.8c and 3.8d it is clear that both 10-PU and 20-PU specimens showed the crushing phenomenon at a location slightly below the top side and the formation of vertical cracks. It is evident from Figure 3.8e that 40-PU specimen showed crushing band at both top and bottom side layers followed by formation of multiple cracks in the direction of compression loading. Figure 3.8f shows the failure modes associated with polyurethane impregnated Eco-Core. The impregnated Eco-Core specimen showed bulging in the lateral direction followed by formation of multiple shear cracks along  $\sim 45^{\circ}$  direction to the loading axis. Similar observations were made by Gupta et al. [10] for the epoxy syntactic foams.

**Table 3.5. Unconfined Compression Test Results**

Panel	Specimen	Density, g/cc	Compression	
			Strength, MPa	Modulus, GPa
Baseline	1	0.55	21.8	1.38
	2	0.54	21.3	1.34
	3	0.54	22.2	1.39
	4	0.54	21.7	1.37
	5	0.52	19.4	1.55
Average (CV %)		0.54 (2.2)	21.3 (5.2)	1.40 (5.9)
EPU0	1	0.58	24.6	1.72
	2	0.58	23.7	2.38
	3	0.59	23.9	2.43
	4	0.58	23.1	2.31
	5	0.57	24.2	2.43
Average (CV %)		0.58 (0.9)	23.9 (2.4)	2.25 (13.4)
EPU10	1	0.59	22.1	2.27
	2	0.59	24.1	2.40
	3	0.59	24.0	2.41
	4	0.58	23.6	2.32
	5	0.57	22.1	2.45
Average (CV %)		0.58 (1.3)	23.2 (4.4)	2.37 (3.1)
EPU20	1	0.60	23.7	2.42
	2	0.59	23.2	2.36
	3	0.58	20.3	2.27
	4	0.57	21.2	2.26
	5	0.55	19.5	2.13
Average (CV %)		0.58 (3.1)	21.6 (8.4)	2.29 (4.8)
EPU40	1	0.61	20.9	2.52
	2	0.59	20.9	2.24
	3	0.59	20.9	2.18
	4	0.58	19.3	2.26
	5	0.58	20.1	2.45
Average (CV %)		0.59 (1.9)	20.4 (3.6)	2.33 (6.4)
EPUR	1	0.78	49.6	1.01
	2	0.79	52.1	0.98
	3	0.80	51.4	0.93
	4	0.78	50.8	0.96
	5	0.80	49.7	0.97
Average (CV %)		0.79 (0.9)	50.7 (2.2)	0.95 (10.9)

**Compression  
strength,  
MPa**

**Thickness of PU coating, mil**

**Figure 3.6. Variation of Compression Strength of Modified Eco-Core with Thickness of PU Coating**

**Compression  
Modulus,  
GPa**

**Thickness of PU coating, mil**

**Figure 3.7. Compression Modulus of Modified Eco-Core vs. Thickness of PU Coating**

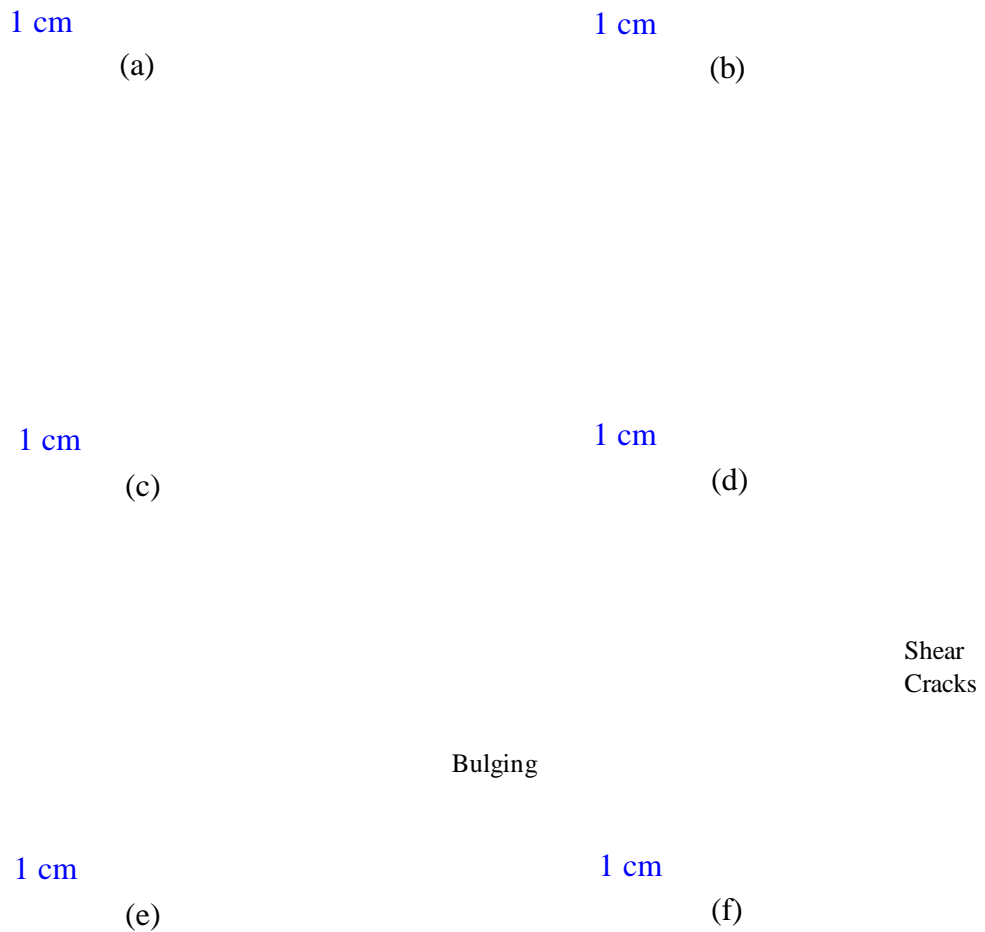


**Figure 3.8. Images of the damage/failure modes for (a) Base Eco-Core; (b) 0-PU; (c) 10-PU; (d) 20-PU; (e) 40-PU; and (f) PUR Impregnated Eco-Core**

### ***3.4.2 Confined Compression***

The typical confined compression stress-strain response of Eco-Core and modified Eco-Core is shown in Figure 3.9. The stress-strain curves of Eco-Core and PU

coated Eco-Core had the following three characteristics; an initial elastic region where stress was directly proportional to strain, a plateau region where the stress remained constant with strain due to breaking of bonds between microbubbles and its rearrangement (translation), followed by crushing of microbubbles, and finally a densification region shown by a rapid increase of stress as the crushed microbubble walls were compacted. The value of the plateau stress  $\sigma_{pl}$  (defined as the stress at 10% nominal axial strain) for baseline Eco-Core and PU coated Eco-Core was around 20 MPa. It is clear from Figure 3.9 that all the coated Eco-Core samples showed a shortened densification region when compared to that of baseline sample. From the Figure 3.9 it is clear that the PUR impregnated Eco-Core does not show much of the compressibility that is required for energy absorption. This finding indicated that the polyurethane had filled up the voids between the Cenosphere bubbles and beyond them, which in turn must have prevented the collapsing of the Cenosphere cells.

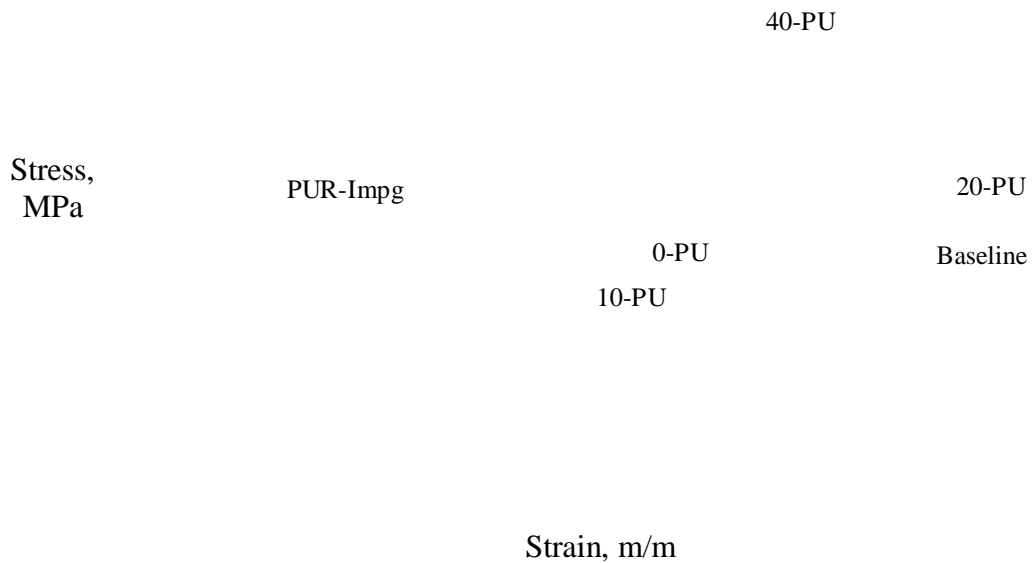


**Figure 3.9. Typical Confined Compression Stress-Strain Plot for Modified Eco-Core**

The energy absorption density of the materials was calculated using Eq. (2.2) for all material combination except for the PUR impregnated Eco-Core. Table 3.6 summarizes the compression strength, failure strain, crushing strain and energy absorption parameter for baseline and PU coated Eco-Core. The compression strength values of Eco-Core and PU coated Eco-Core were in the range of 18 to 24.6 MPa. The densification/crushing strain of all Eco-Core was between 0.48 and 0.56. Among all, 0-PU coated Eco-Core sample showed an improvement of approximately 14% increase of energy absorption density. Even a very thin coating of polyurea had improved the energy absorption density by 14%. Examining Table 3.6 reveals that the increase in energy absorption for 0-PU coated Eco-Core was due to an increased compression strength. The crushing strain was almost the same for all cases, which is evident from the foam formulation. Figure 3.10 shows the effect of thickness of PU coating on energy absorption density. It is evident that the energy absorption density decreased linearly with an increase in coating thickness.

**Energy  
Absorption  
Density ( $E_{EA}$ ),  
MPa**

**Thickness of PU coating, mil**

**Figure 3.10. Variation of Energy Absorption Density of Modified Eco-Core with Thickness of PU Coating**

**Table 3.6. Confined Compression Test Results**

Panel	Specimen	Density, g/cc	Compression Strength, MPa	Failure Strain, m/m	Crushing Strain, m/m	Energy Absorption Density, MPa/unit volume
Baseline	1	0.51	17.6	0.027	0.56	10.1
	2	0.54	20.9	0.028	0.55	11.9
	3	0.53	19.9	0.029	0.56	11.4
	4	0.55	21.1	0.027	0.54	11.7
	5	0.53	19.2	0.025	0.56	11.0
Average (CV %)		0.53 (2.8)	19.7 (7.1)	0.027 (4.7)	0.56 (1.5)	11.2 (6.1)
EPU0	1	0.59	25.1	0.027	0.52	13.3
	2	0.59	24.5	0.028	0.52	13.0
	3	0.58	24.9	0.024	0.49	12.5
	4	0.57	23.5	0.025	0.52	12.5
	5	0.57	23.7	0.026	0.52	12.7
Average (CV %)		0.58 (1.3)	24.3 (2.9)	0.026 (6.6)	0.51 (2.6)	12.8 (2.8)
EPU10	1	0.59	24.6	0.024	0.51	12.8
	2	0.60	24.2	0.023	0.46	11.5
	3	0.57	22.9	0.024	0.52	12.3
	4	0.57	20.8	0.022	0.54	11.4
	5	0.56	21.2	0.022	0.52	11.3
Average (CV %)		0.58 (2.7)	22.7 (7.5)	0.023 (3.9)	0.51 (5.6)	11.8 (5.4)
EPU20	1	0.59	23.4	0.025	0.51	12.1
	2	0.58	20.7	0.026	0.49	10.4
	3	0.58	22.8	0.024	0.50	11.7
	4	0.57	20.8	0.023	0.53	11.2
	5	0.56	20.5	0.023	0.53	11.1
Average (CV %)		0.58 (2.2)	21.6 (6.3)	0.024 (4.2)	0.51 (3.2)	11.3 (5.9)
EPU40	1	0.60	21.4	0.023	0.48	10.6
	2	0.60	21.4	0.026	0.49	10.8
	3	0.59	20.6	0.029	0.50	10.6
	4	0.58	19.0	0.027	0.51	9.9
	5	0.57	17.7	0.025	0.51	9.2
Average (CV %)		0.59 (2.2)	20.0 (8.1)	0.026 (7.6)	0.50 (1.8)	10.2 (6.7)

### 3.4.2.1 Comparison of Energy Absorption Density with Conventional Materials

Figure 3.11 shows a plot of compression energy absorption per unit volume of the material versus density for various foam materials tested (balsa, PVC, open cell

aluminum, polyimide, phenolic and Eco-Core). Among them, both balsa, Eco-Core and PU coated Eco-Core had high-energy absorption capability. Although balsa has lower density and similar energy absorption capability as Eco-Core, its energy absorption in the transverse direction is poor. In structures that are subjected to multi axial stress state balsa may be a poor choice for this reason. Therefore, alternative materials like Eco-Core are being developed because its properties can be tailored to increase  $\sigma_c$ ,  $\epsilon_c$ , and  $\epsilon_{crush}$ , as well as density. The Eco-Core material showed promise for further modifications to increase energy absorption capability as well as for decreasing of the density.

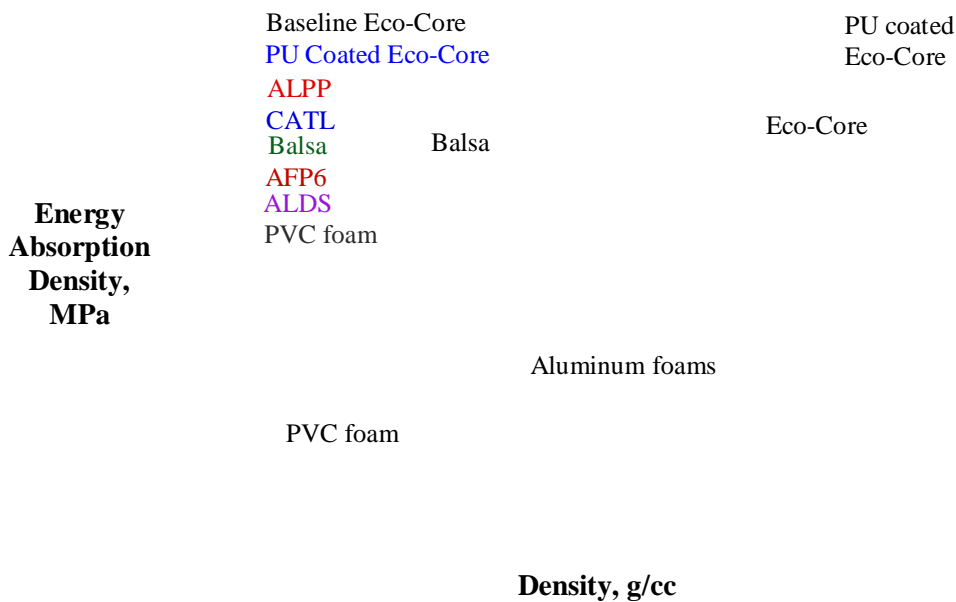


**Figure 3.11. Comparison of Energy Absorption Density vs. Density for Various Foams**

### 3.5 Summary

The cellular structure of Eco-Core offered potential for shock and blast mitigation applications. Through static confined and unconfined compression tests, Eco-Core's energy absorption density was evaluated. Both baseline and modified versions were

tested. The Eco-Core was modified by surface coating of polyurea and impregnation by polyurethane to improve the compression strength and the energy absorption density. Surface coating with PU resulted in an improvement in compression strength by 12%, compression modulus by 64% and the energy absorption density by 14%. For near-zero PU coated specimens, enhancement in energy absorption was due to an increase in compression strength. The impregnation of PUR enhanced the compression strength by 138% with a penalty of increased density and decreased modulus. Tests were also conducted on other core materials used in aerospace and marine applications. Among these materials, Eco-Core and balsa showed the best performance. Although Eco-Core had a higher density, it was fire resistant and had mechanical properties in the transverse directions superior to balsa.

## CHAPTER 4

### DEVELOPMENT OF SPLIT HOPKINSON PRESSURE BAR TEST FACILITY

#### 4.1 Introduction

This chapter explains the operating principles of Split Hopkinson Pressure Bar (SHPB) testing. The traditional one-dimensional stress wave theory behind SHPB testing is also described. The development and calibration of a SHPB test facility is presented. Various components of the SHPB test apparatus, specimen requirements, test procedure, data recording and analysis are described. The validation of the SHPB test facility with known material such as 6061-T651 aluminum and polycarbonate are discussed at the end of the chapter.

#### 4.2 Operating Principle of a Split Hopkinson Pressure Bar Test

A schematic of a traditional SHPB test apparatus used for high strain rate testing of materials is shown in Figure 4.1. In the SHPB test, a right-regular solid specimen with suitable dimensional tolerance is sandwiched between the incident/input bar ( $I_{\text{bar}}$ ) and the transmitter/output bar ( $T_{\text{bar}}$ ). The impact of a striker bar ( $S_{\text{bar}}$ ) on the impact end of the incident bar produces a compressive stress/strain pulse of geometric length twice that of the striker bar length [23]. The shape of the pulse in stress-time coordinates is almost rectangular. The strain pulse,  $\varepsilon_I(t)$ , in the incident bar is measured by the strain gauge on the bar and its amplitude is proportional to the impact velocity of the striker bar. The pulse propagates toward the incident bar-specimen ( $I_{\text{bar}}\text{-S}$ ) interface, while a part of the pulse transmits through the specimen and a part reflects back. The reflected pulse,  $\varepsilon_R(t)$ , is tensile (opposite to the incident pulse) and may be measured by the strain gage on the incident bar. The transmitted pulse,  $\varepsilon_T(t)$  may be measured by the strain gage mounted on

the transmitter bar. During the period of stress wave propagation through the specimen, the specimen undergoes deformation until its dynamic limit is reached.

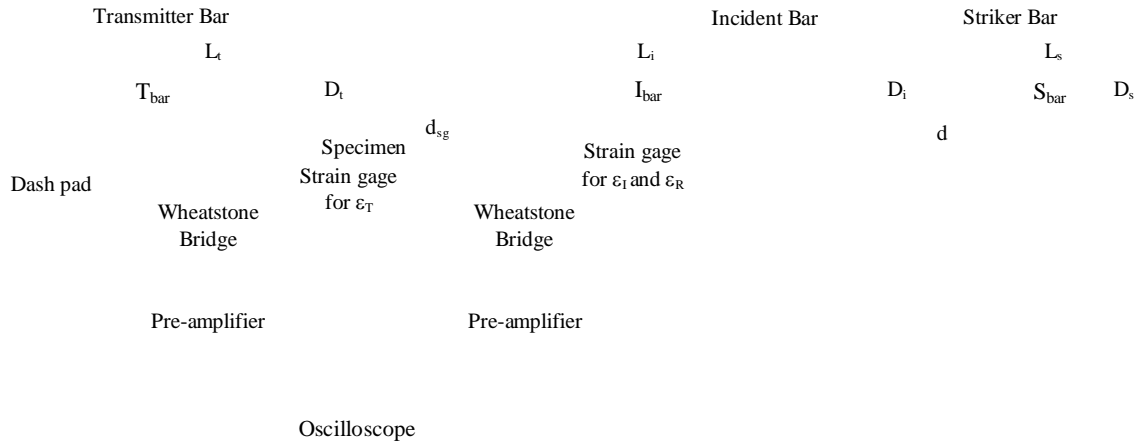


**Figure 4.1. Schematic of SHPB Test Apparatus**

A typical set of strain gage signals recorded by the digital oscilloscope from a SHPB experiment on aluminum specimen AL6061-T651-1 at the strain rate of 1350/s is shown in Figure 4.2. On a trace of strain gage signals, the sign of the transmitted pulse appears the same as the incident pulse, but opposite to that of the reflected pulse if the polarity of the recording devices is set similarly for both channels of strain gages on the incident and transmitter bar. By placing the center of the strain gages equidistant from the specimen-bar interfaces, a relative origin in time can be established for pressure bars made from the same material. The signal shown in Figure 4.2 is a conditioned and amplified signal, in which the incident and reflected pulses contain high frequency Pochhammer Modes, while the transmitted pulse contains almost none. It is believed that the viscoplastic deformation of the specimens damps out the high frequency contents of the transmitted signal. The properties of the bars such as the density, elastic modulus, longitudinal wave speed in the bar, diameter ( $\rho_b, E_b, c_b, D_b$ ) and the specimen dimensions

$(L_s, D_s)$  should be known prior to the data analysis from a SHPB test. The theory behind the SHPB test is explained in the next section.

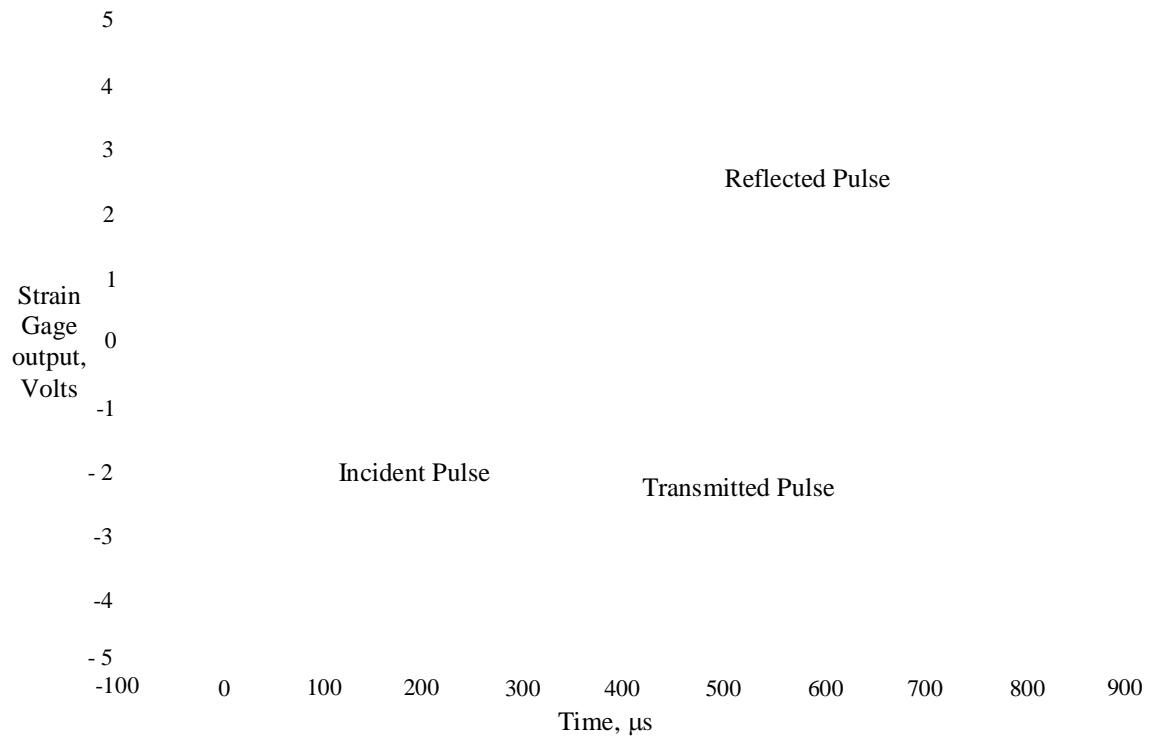


**Figure 4.2. Typical Strain Signal for Aluminum Specimen (Al 6061-T651-1) in a Split Hopkinson Pressure Bar Test**

### 4.3 Theory of SHPB Test

One-dimensional stress wave propagation theory in a thin, long rod is based on the following fundamental assumptions:

1. Stress wave propagation in the bar is one-dimensional. The conditions that satisfy this assumption are related to the material and geometric properties of the bar.

They are:

- a) The bar material is homogeneous and isotropic

- b) The cross-section of bars are uniform over the entire length and the centroidal axis of all bars are straight and co-linear
  - c) State of stress is elastic and uniform over the entire cross-section of the bar. According to Davies [28], use of the length/diameter of the bar must be greater than 20 to meet this criteria
  - d) No attenuation or dispersion of stress waves
2. The incident bar-specimen and specimen-transmitter bar interfaces remain plane and perpendicular to the axes throughout the test
  3. The specimen is in stress equilibrium after an initial “ringing-up” period
  4. Friction and inertia effects in the specimen are minimal and are neglected

*One-dimensional wave propagation analysis*

The determination of the stress-strain behavior of a material being tested in Hopkinson bar is based on the principles of one-dimensional elastic-wave propagation within the pressure loading bars as given by Gray III [24]. The SHPB test is schematically shown in Figure 4.3. The specimen is sandwiched between the incident and transmitter bars. During the entire test, all three units are in contact with each other. The deformation at the incident bar end and transmitter bar end of the specimen is  $u_1$  and  $u_2$ , respectively. The cross-sectional area of the specimen is  $A_s$  and the bars is  $A_b$ . The specimen length is  $l_s$  and the elastic modulus of the bars is  $E_b$ . The deformation of the specimen,  $u_s$ , is  $(u_1 - u_2)$ . The deformation of the of the pressure bars are given by  $u_I$ ,  $u_R$ , and  $u_T$ , respectively. The measured incident, reflected and transmitted strain pulses are  $\varepsilon_I(t)$ ,  $\varepsilon_R(t)$ , and  $\varepsilon_T(t)$ , respectively. The arrows show the direction of wave propagation.

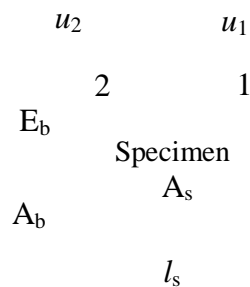


**Figure 4.3. One-Dimensional Wave Propagation Analysis in SHPB**

a) Wave analysis for incident bar

The deformation  $u_1$  is given by

$$u_1 = u_I + u_R \quad (4.1)$$

According to 1-D wave equation at the location  $I$  is

$$\frac{\partial^2 u_1}{\partial x^2} = \frac{1}{c_b^2} \frac{\partial^2 u_1}{\partial t^2} \quad (4.2)$$

where  $c_b$  is the wave speed in the bars and is given by

$$c_b = \sqrt{\frac{E_b}{\rho}} \quad (4.3)$$

where  $\rho$  is the mass density of the bar. At location  $I$ , the solution to the Eq. (4.2) using D'Alembert's principle is given by

$$u_1 = f(x - c_b t) + g(x + c_b t) = u_I + u_R \quad (4.4)$$

where  $f$  and  $g$  are functions describing the incident and reflected wave shapes.

The one-dimensional axial strain is given by

$$\varepsilon_1 = \frac{\partial u}{\partial x} \quad (4.5)$$

Substitute for  $u$  in Eq. 4.5 gives

$$\varepsilon_1 = \frac{\partial}{\partial x} f(x - c_b t) + \frac{\partial}{\partial x} g(x + c_b t) = \varepsilon_I(t) + \varepsilon_R(t) \quad (4.6)$$

Differentiating Eq. (4.4) with respect to time gives the particle velocity  $\left( \frac{\partial u_1}{\partial t} \right)$  at the incident bar-specimen interface as

$$\frac{\partial u_1}{\partial t} = \left( -c_b \frac{\partial}{\partial x} f(x - c_b t) + c_b \frac{\partial}{\partial x} g(x + c_b t) \right) = c_b (-\varepsilon_I(t) + \varepsilon_R(t)) \quad (4.7)$$

b) Wave analysis for transmitted bar

At location 2, the solution to a wave equation similar to the Eq. (4.2) using D'Alembert's principle is given by

$$u_2 = h(x - c_b t) = u_T \quad (4.8)$$

where  $h$  is the function describing the transmitted wave shape

Following the procedure similar to that of incident bar wave analysis, the particle velocity

$\left( \frac{\partial u_2}{\partial t} \right)$  at the specimen-transmitter bar interface is

$$\frac{\partial u_2}{\partial t} = c_b \left( \frac{\partial}{\partial x} h(x - c_b t) \right) = -c_b \varepsilon_T(t) \quad (4.9)$$

c) Specimen Strain, Strain rate and Stress

Displacement of the specimen,  $u_s$  is

$$u_s = u_1 - u_2 \quad (4.10)$$

The average axial strain in the specimen is

$$\varepsilon_s(t) = \frac{(u_1 - u_2)}{l_s} \quad (4.11)$$

Differentiating Eq. (4.11) with respect to time gives the specimen strain rate

$$\frac{\partial \varepsilon_s(t)}{\partial t} = \frac{\left( \frac{\partial u_1}{\partial t} - \frac{\partial u_2}{\partial t} \right)}{l_s} \quad (4.12)$$

Where  $l_s$  is the specimen length. Substituting Eqs. (4.7) and (4.9) in Eq. (4.12) gives

$$\dot{\varepsilon}_s(t) = \frac{c_b}{l_s} (-\varepsilon_I(t) + \varepsilon_R(t) + \varepsilon_T(t)) \quad (4.13)$$

Strain pulses  $\varepsilon_I(t)$ ,  $\varepsilon_R(t)$ , and  $\varepsilon_T(t)$  are measured from the strain gage signals of the incident and transmitter bars. By integrating Eq. (4.13) with respect to time, the specimen strain at any time,  $t$ , can be calculated and is given by

$$\varepsilon_s(t) = \frac{c_b}{l_s} \int_0^t (-\varepsilon_I(t) + \varepsilon_R(t) + \varepsilon_T(t)) dt \quad (4.14)$$

The forces at the specimen ends are

$$F_1 = A_b E_b (\varepsilon_I(t) + \varepsilon_R(t)) \quad (4.15)$$

and

$$F_2 = A_b E_b \varepsilon_T(t) \quad (4.16)$$

The average force is given by

$$F_{av} = \frac{A_b E_b}{2} (\varepsilon_I(t) + \varepsilon_R(t) + \varepsilon_T(t)) \quad (4.17)$$

After an initial “ringing-up period”, it is assumed that the specimen is in force equilibrium (i.e.  $F_1 = F_2$ ). Equating Eqs. (4.15) and (4.16) gives

$$\varepsilon_I(t) + \varepsilon_R(t) = \varepsilon_T(t) \quad (4.18)$$

Substituting Eq. (4.18) in Eqs. (4.13), (4.14), and (4.17) gives

$$\dot{\varepsilon}_s(t) = \frac{2c_b \varepsilon_R(t)}{l_s} \quad (4.19)$$

$$\varepsilon_s(t) = \int_0^t \dot{\varepsilon}_s(t) dt$$

$$\varepsilon_s(t) = \frac{2c_b}{l_s} \int_0^t \varepsilon_R(t) dt \quad (4.20)$$

$$F_{av} = A_b E_b \varepsilon_T(t) \quad (4.21)$$

The average engineering stress in the specimen is determined by dividing Eq. (4.21) by  $A_s$ , is the cross-sectional area of the specimen.

$$\sigma_s(t) = \frac{A_b E_b}{A_s} \varepsilon_T(t) \quad (4.22)$$

The calculation of average stress in the specimen using Eq. (4.21) is known as *1-wave* analysis. If Eq. (4.15) is used instead, which involves both incident and reflected strain signals, the analysis is known as *2-wave* analysis and the specimen stress is given by

$$\sigma_s(t) = \frac{A_b E_b}{A_s} (\varepsilon_I(t) + \varepsilon_R(t)) \quad (4.23)$$

If Eqs. (4.17) is used to find the algebraic average stress; the analysis is termed as *3-wave* analysis and the specimen stress is given by

$$\sigma(t) = \frac{AE}{2A_s} (\varepsilon_I(t) + \varepsilon_R(t) + \varepsilon_T(t)) \quad (4.24)$$

#### 4.4 Development of SHPB Test Facility

The SHPB test apparatus requires the following components and instruments:

- Bar assembly consisting of two long cylindrical bars with a uniform cross section (achieved by precision centerless grinding) of length to diameter ratio (L/D) in the

range 20 to 100 made from 7075 T6 aluminum. The commonly used bar materials are maraging steel, titanium, aluminum, magnesium and polymeric materials. The bar ends are machined orthogonal to the bar axis with high accuracy to ensure good contact between the specimen and the bar, and between the bar and the striker bar.

- A bearing and alignment fixture for correct alignment and satisfaction of the co-axiality to simulate one-dimensional wave propagation.
- A compressed gas launcher/gun to propel the striker bars made from same bar material.
- A strain measurement system consisting of strain gages mounted on the incident and transmitter bar to measure the strain pulse.
- The data acquisition system to control, record, and analyze the stress-wave data in the bars.

The Split Hopkinson Pressure Bar apparatus was built for the purpose of understanding the dynamic failure of materials at different strain rates. The materials of interest were composite materials that include fiber reinforced composites, Eco-Core, and other syntactic foams. The 7075 T6 aluminum bars were chosen because the impedance  $(A_b \sqrt{\rho_b E_b})$  of aluminum is lower than that of steel and is suitable for softer materials such as polymer composites and Eco-Core. The properties of 7075 T6 aluminum are listed in Table 4.1.

**Table 4.1. Properties of 7075 T6 Aluminum Pressure Bars**

Density	2.81 g/cc
Tensile Yield Strength	503 MPa
Elongation at Break	11%
Modulus of Elasticity	71.7 GPa
Poisson's Ratio	0.33
Wave Speed	5,051 m/s

The test facility had a striker bar with a capability of launching at 5 to 25 m/s to produce strain rates of 500 to 10,000/s. A number of safety features were included to operate the test facility in a safe manner. The section below explains the fabrication, calibration and validation of the SHPB test facility.

#### **4.4.1 SHPB Hardware**

##### **4.4.1.1 Components and Assemblies**

The split Hopkinson bar apparatus was designed to accommodate pressure bars of different sizes and material properties. The modular design concept was used for building the SHPB apparatus which allows one or more sub-assemblies to be modified independently as required. An AutoCAD model was designed and used to build the test apparatus. Figure 4.4 shows a photograph of the apparatus.

The apparatus consisted of four units: the bar assembly, gas gun assembly, control system and data acquisition system. Details of each of these units are provided in the sections below.



**Figure 4.4. Photograph of SHPB Test Apparatus**

##### **(a) Bar Assembly**

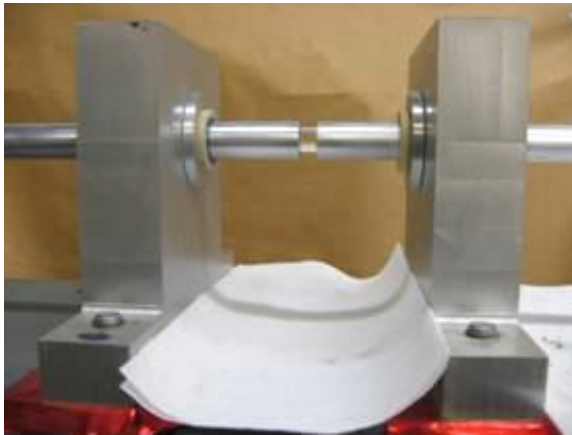
The Split Hopkinson Pressure Bar consisted of two I-beams: one of 6 m (20 ft) length for the incident and transmission bar assembly and the other 3 m (10 ft) length for the gun assembly with welded end plates for optional attachments. I-beams served as a

reference plane over which all the assemblies sat on except for the air compressor. Each I-beam was mounted on steel stands with casters for mobility. The stands were provided with leveling feet for alignment purposes. The incident bar was 19 mm (0.75”) in diameter and 3.66 m (12 ft) in length and was machined from 7075 T6 aluminum bar stock. The transmission bar was 19 mm (0.75”) diameter and 1.83 m (6 ft) in length, and was also machined from 7075 T6 aluminum bar. The incident bar and the transmission bar were supported on pillow blocks (Figure 4.5) at every 0.46 m (18”) intervals. Pillow blocks (Figure 4.6) were of a split horizontal design and fitted with dowel locating pins for easy assembly and removal of the bars. Each pillow block housed the pillow block insert, which contained the Teflon plain bushing through which the bars slide. This design concept allowed for a rapid change of incident and transmission bars of different diameters. Bars up to 38 mm (1.5”) diameter can be rapidly exchanged by simply changing the pillow block inserts (with pre-installed plain bushings) without the need of a complete realignment.

The momentum trap equipped with a low hardness urethane (Sorbothane) pad arrested the motion of the incident and transmission bars after impact and was mounted adjacent to the output end of transmission bar.

Transmitter bar      Specimen mounting area      Incident bar      Pillow blocks

**Figure 4.5. Incident and Transmission Bars Supported on Pillow Blocks**



(a)



(b)

**Figure 4.6. Pillow Block (a) Front View (b) Opened**

(b) Gas gun assembly

The gas gun was designed to maximize velocity and sensitivity. The two design constraints contradicted each other since achieving high velocities generally means large pistons that reduce the capability of providing a fine adjustment on the velocity. Since the velocity was controlled purely by the gas pressure in the reservoir, a slight increase in pressure for a larger piston would result in a much higher increase in velocity. To predict the acceleration of the piston, a simple static equilibrium analysis was used. Figure 4.7 shows the free body diagram of the striker bar resting inside the gun barrel.

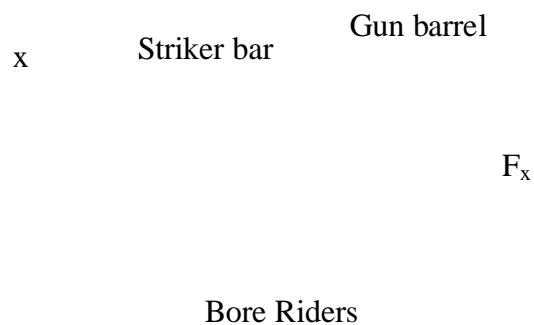


**Figure 4.7. Simple Free Body Diagram of the Striker Bar**

The force balance in the x-direction, neglecting kinetic and air friction gives

$$\sum F_x = ma_x = pA \quad (4.25)$$

where  $m$  was the mass of the striker bar and bore riders,  $A$  was the projected area of striker bar and bore rider, and  $p$  was the initial pressure of the compressed air reservoir. This equation ignored losses through the valve and pressure reduction in the reservoir as the striker bar moved. Based on the simple kinetics of rigid bodies ignoring friction, the striker bar velocity was given by

$$v_{sb} = \sqrt{2a_x d} \quad (4.26)$$

where  $d$  was the distance between the striker bar and the incident bar (see fig. 4.1). This simplified analysis does not represent the true dynamic behavior of the system, but does indicate the critical design parameters. Reducing friction in the gas gun was essential to control the repeatability of the tests.

The gas gun is shown in Figure 4.8. The gas gun functioned like a pneumatic actuator with the exception that the striker bar was launched at the end of the stroke. The gun assembly mainly consisted of a gun barrel, striker bars, a reservoir, a gun breech assembly, a gun pneumatic conditioner and controls. The gun barrel was 2 m (6.5 ft) in length with an inside diameter of 51mm (2") and its function was to fire the striker bar with compressed air. Vents were drilled into the muzzle end to allow pressure to vent behind the striker bar. The gun barrel was electro-less nickel coated to protect the surfaces from corrosion. The Striker Bars were of 0.41 m (16"), 0.61 m (24"), and 0.76m (30") length with 19 mm (0.75") diameter and were made of 7075 T6 aluminum. The striker bars were fitted with oil-filled nylon bore riders of 50.67 mm (1.995") diameter. The nylon bore riders were used to reduce friction and to increase durability. The gun breech assembly channeled compressed air through the gun and consisted of a Norgren pilot-operated poppet valve of high flow rate and rapid operation and a pipe union for the

breech and the pressure reservoir. The breech (Figure 4.9) allowed for a rapid changing of the striker bars without disturbance of the alignment of the gun. The gun pneumatic conditioner (Figure 4.10) and control assembly charged the pressure reservoir of the gun. The conditioner consisted of air filters plus a regulator pilot circuit, a rapid operating Norgren 3-way solenoid poppet valve, and a separate precision regulator with digital gauge to pressurize the gun reservoir. The gun could be fired remotely via an Omron one-shot digital timer relay (Figure 4.11) or it can be fired manually. Safety features were included to prevent inadvertent firing of the valves with a keyed interlock for the remote control as well as a manual lockout, which quietly vented the reservoir. A blinking light also alerted the operator when the reservoir was charged. A standard two gallon capacity air compressor was used to provide a compressed air supply to the pressure reservoir. The maximum operating pressure was 150 psi.

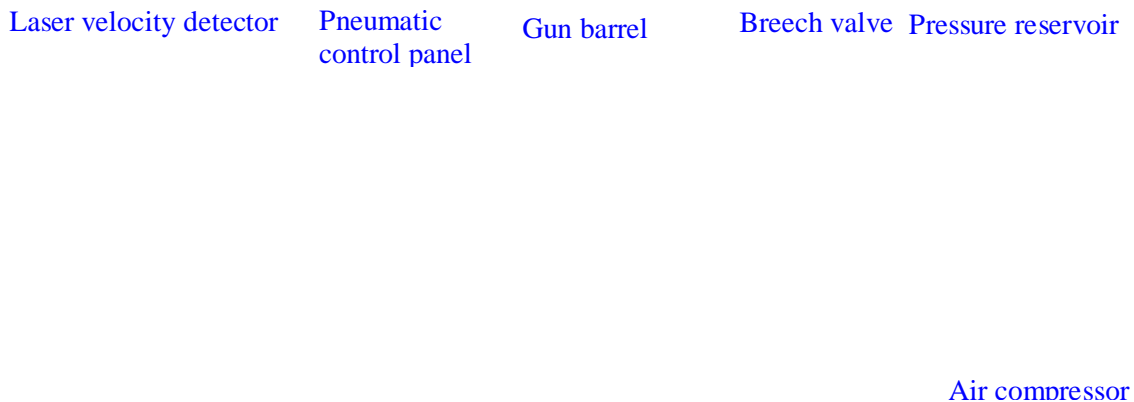


**Figure 4.8. Gas Gun Assembly**

(c) SHPB Control System (Sensors and Peripheral Equipments)

(i) *Velocity detector*

The ability to measure the striker velocity prior to impact provided an additional input condition when analyzing the results. In order to calibrate the velocity of the striker

bar a velocity detector was used. A schematic of the laser velocity detection system is shown in Figure 4.12. The system consisted of a custom circuit of four visible red diode lasers, four photo detectors and two frequency counters. The velocity detection system was mounted at the vented end of the gun. As the striker bar broke the first laser beam, the circuitry began a counter, which counted until the second beam was broken. Similarly, other counters timed the passage of the striker between each pair of lasers. For the configuration shown, three time measurements were made. Knowing the distances between the lasers and elapsed times, the instantaneous and the average velocity of the striker bar could be calculated. System pressure could be calibrated for desired striker velocity and strain rate.

**Figure 4.9. Top View of Breech Assembly**

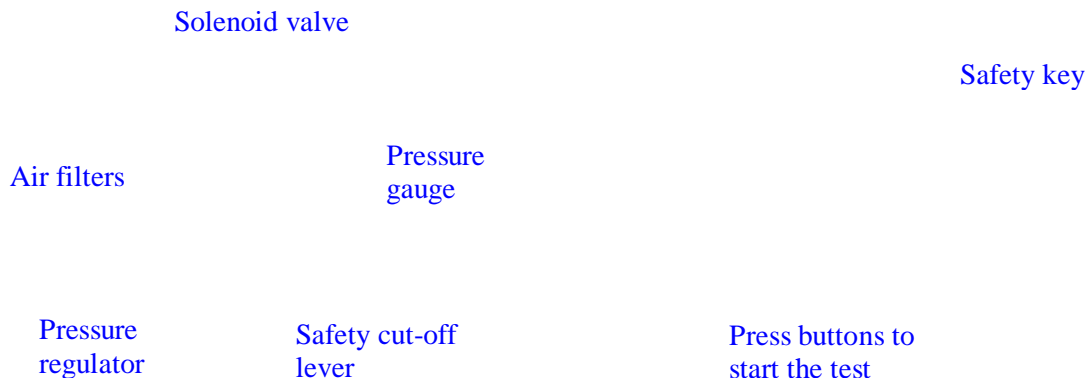


**Figure 4.10. Pneumatic Control Panel**

**Figure 4.11. Gas Gun Remote Control**

(ii) *Strain measurement system*

The split Hopkinson bar relied on the measurement of the strain-time history in the pressure bars to calculate stress, strain and strain rates. The strain measurement system consisted of strain gages connected in a half-bridge circuit configuration as shown in Figure 4.13 and a signal-conditioning amplifier. A pair of strain gages of 1000  $\Omega$  and

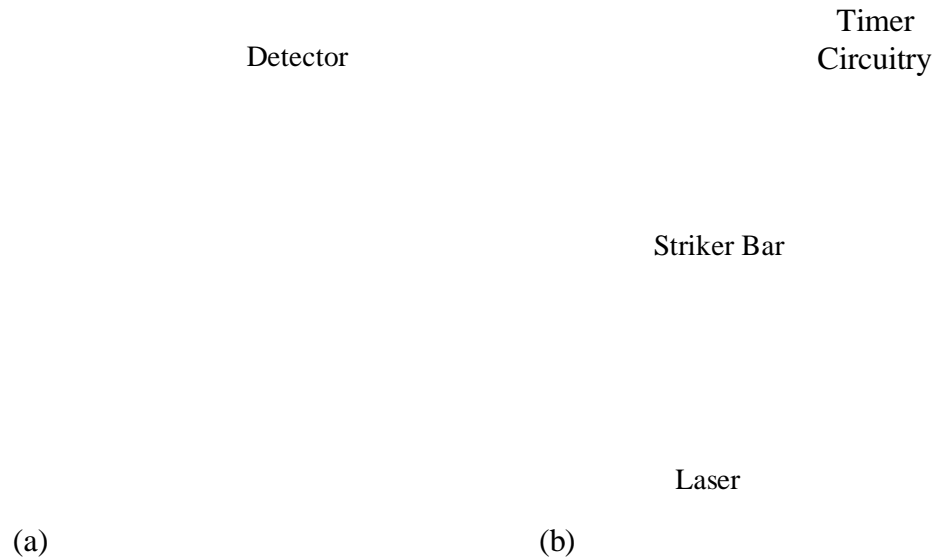


**Figure 4.12. Laser Velocity Detection System (a) Photograph (b) Schematic**

2.015 gage factor were mounted on incident and transmitter bars, respectively, at an equal distance of 0.91 m (3 ft) from incident-transmitter bar interface. Each pair of gages was mounted 180° apart on the bar in order to detect any asymmetry in the stress wave traveling through the length of the bar. The strain gages were connected to a signal bridge conditioner (Figure 4.14) which provided DC excitation voltage for four strain gages and amplified the signal. The signal conditioner was a modular system sourced from Validyne of custom model SG297A-2495 amp. This conditioner had a user adjustable

gain and could apply excitation voltage from 5 to 10V. The amplified signal from the strain gage signal conditioner was fed to the oscilloscope (Figure 4.15) for recording.

(d) Data Acquisition System

Dynamic compression strain pulses generated by impacts to the incident bar were acquired by a Yokogawa DL750 digital storage oscilloscope (Figure 4.16) and then transferred to a PC. The DL750 modular system was equipped with four (2-channel) 10 MHz 12 bit input modules that also had the capability to be remotely controlled via Ethernet or USB. The differential mode was used due to the presence of electronic noise

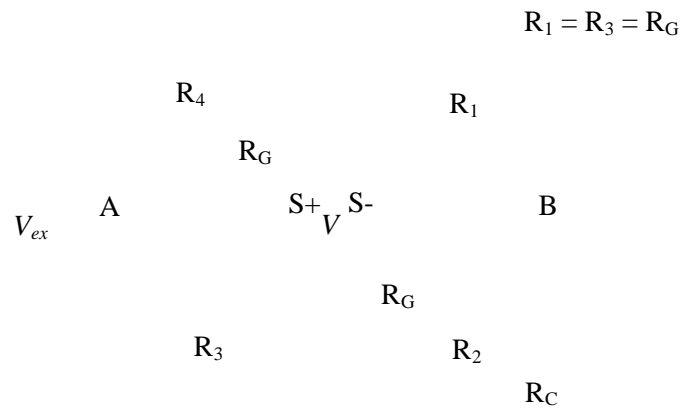


**Figure 4.13. Half-Bridge Circuit along with Shunt Calibration Resistor ( $R_c$ ) for SHPB Apparatus**

in the test area. The Yokogawa DS750 was capable of applying a high frequency filter to further reduce the effect of signal noise. X-Viewer software was provided to transfer waveform data files from the oscilloscope memory card to the PC for post-processing of waveform data.



**Figure 4.14. Strain Gage Signal Conditioner**



**Figure 4.15. Digital Storage Oscilloscope**

PC

Yokogawa DL750 Oscilloscope

**Figure 4.16. Strain Data Acquisition System**

## **4.5 Calibration of the SHPB System**

### *(a) Velocity calibration*

Velocity calibration of the striker bar was performed to relate the amount of breech pressure required to achieve the desired velocity. The pressure regulator was used to incrementally release a certain amount of gas to the solenoid valve. The SHPB test was performed using pressures ranging from 8 to 26 psi. Three SHPB test were performed at each pressure level without any specimen sandwiched between the incident and transmission bar

to check the repeatability of results. At breech pressure less than 13 psi, the striker bar barely touched the incident bar, generated negligible impact and the corresponding strain gauge signal was very weak. This situation may have been due to the heavy mass of the striker bar and the friction between the bore riders and the internal surface of the gun barrel. The maximum operating breech pressure was limited by the elastic strain limit of the incident pressure bar material. The experiments conducted at breech pressures beyond 26 psi frequently caused breakage of the soldering junction of the strain gage bonding terminals. Table 4.2 summarizes the details of breech pressure, travel time and velocity. The average velocity of the striker bar versus the breech pressure is plotted in Figure 4.17. This velocity-breech pressure calibration curve gives the best estimate of striker bar velocity for a given breech pressure.

**Table 4.2. Velocity-Pressure Calibration Test Data**

Experi ment #	Breech pressure, psi			Travel time, ms			Velocity of striker bar, m/s				
	1	2	3	1	2	3	1	2	3	Average	% CV
1	8	8	8	7.47	7.21	7.53	5.1	5.3	5.1	5.15	2.3
2	9	9	9	6.97	6.75	6.50	5.5	5.6	5.9	5.66	3.5
3	10	10	10	6.62	6.71	6.14	5.8	5.7	6.2	5.88	4.9
4	11	11	11	5.19	5.02	5.31	7.3	7.6	7.2	7.37	2.8
5	12	12	12	4.65	4.48	4.43	8.2	8.5	8.6	8.43	2.5
6	13	13	13	4.18	4.01	4.31	9.1	9.5	8.8	9.15	3.6
7	14	14	14	3.91	3.79	3.69	9.7	10.1	10.3	10.04	2.9
8	15	15	15	3.73	3.67	3.71	10.2	10.4	10.3	10.29	0.8
9	19	19	19	3.09	3.15	3.21	12.3	12.1	11.9	12.10	2.0
10	20	20	20	2.99	3.01	3.04	12.8	12.6	12.5	12.64	0.9
11	22	22	22	2.86	2.87	2.76	13.3	13.3	13.8	13.46	2.3
12	23	23	23	2.63	2.62	2.60	14.5	14.5	14.7	14.56	0.7
13	26	26	26	2.38	2.36	2.35	16.0	16.1	16.2	16.12	0.7

(b) *Dynamic calibration of strain gauges*

A dynamic calibration of the strain gauges was performed for the case of incident and transmitter bars made from 7075 T6 aluminum. The strain pulse generated by impact of the striker bar upon the incident bar was recorded by the strain gauges on the incident bar. From momentum considerations and wave theory [79], the amplitude of this strain pulse was given by

$$\varepsilon = \frac{v_{sb}}{2c_b} \quad (4.27)$$

where  $v_{sb}$  is the striker bar velocity and  $c_b$  is the longitudinal wave speed in the bar material.

The striker bar impact velocity,  $v_{sb}$  was measured by timing the passage of the striker bar between two light beams. The strain gauge calibration was checked dynamically using relation (4.27). The corresponding stress was calculated from

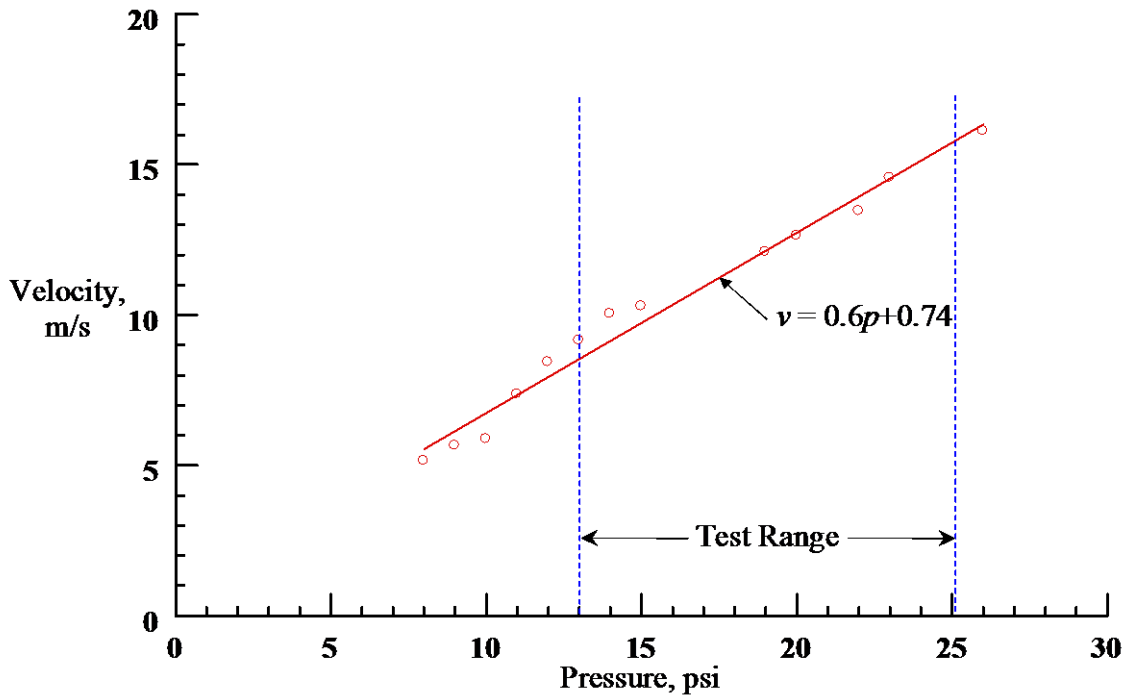


Figure 4.17. Velocity-Pressure Calibration Curve for the SHPB Apparatus

$$\sigma = E_b \varepsilon = \frac{\rho_b c_b v_{sb}}{2} \quad (4.28)$$

where  $E_b = \rho_b c_b^2$ , and  $\rho_b$  and  $E_b$  were material density and elastic modulus of the incident bar material. The calculated value of  $\varepsilon$  from equation (4.27) at a striker velocity of 15.2 m/s was 1495.7 micro strains. This value corresponded to a stress of 107.7 MPa. Two strain gauges on each bar were connected in a half-bridge circuit to record the axial strain (and to cancel any contribution from bending). The axial strain and stress in the incident bar were calculated from the strain bridge output and they were 1476 micro strain and 107.2 MPa, respectively. There was a very good agreement between the calculated and the measured data.

Equations (4.27) and (4.28) involved the constant,  $c_b$ , which was the longitudinal wave speed in the incident and transmission bars. The wave speed calculated from equation (4.3) was 5,051 m/s. In the SHPB experiment, the wave speed was measured by timing the passage of the incident and reflected pulses on the strain gauges mounted on the incident bar. Figure 4.18 shows the dynamic response from the strain gages mounted on the incident bar for the aluminum specimen (Al 6061-T651-1). The time elapsed between the incident pulse exiting the strain gage station and the reflected pulse entering strain gage station was measured ( $t = 385 \mu\text{s}$ ). The longitudinal wave speed was given by

$$c_b = \frac{2d_{sg}}{t} = 5,019 \text{ m/s} \quad (4.29)$$

where  $d_{sg} = 0.966\text{m}$ , was the distance between the strain gage mounting station and specimen end of the incident bar (see figure 4.1). There was a very good agreement between the calculated and the measured wave speed.

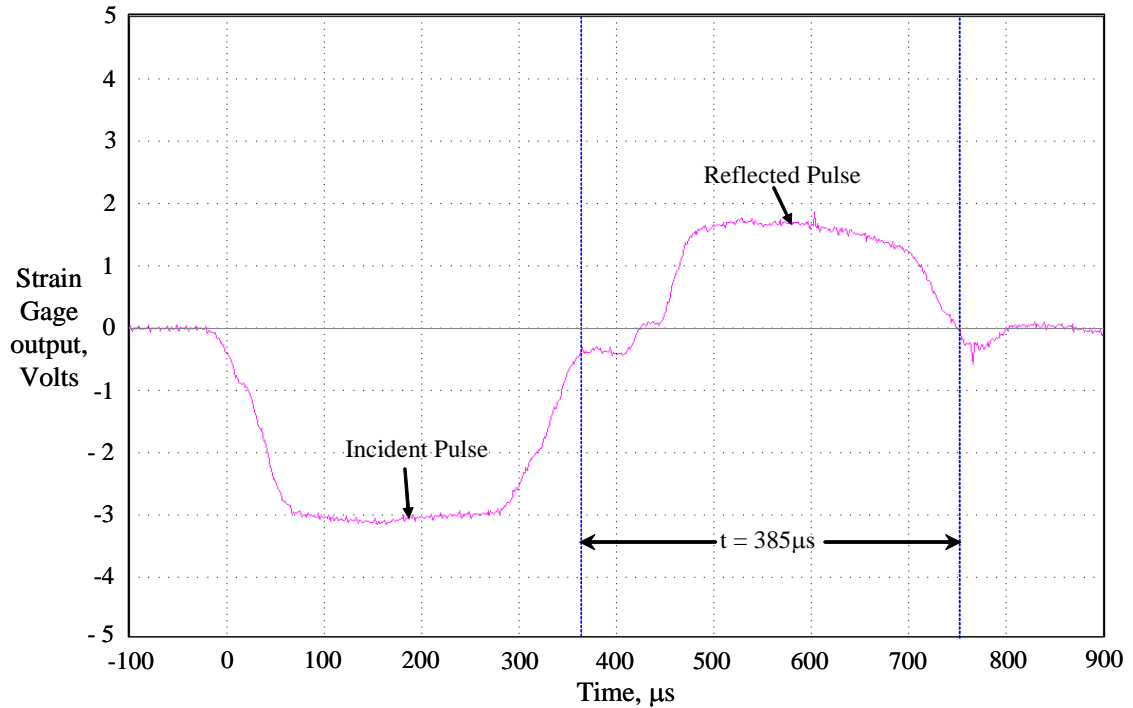


**Figure 4.18. Calculation of Wave Speed in a SHPB Experiment**

#### 4.6 Specimen Configuration and Requirements

The specimen size was selected so that it satisfied some of the assumptions made during analysis of the SHPB test (section 4.3). The specimen needed to satisfy the following assumptions: a) uniform deformation, b) dynamic stress equilibrium; and c) an uniaxial stress state. In addition, the sample size was selected so that a portion of the wave propagated into the transmitter bar. For metallic materials, the samples with a length to diameter (L/D) ratio between 0.5 and 1.0 were selected based on the guidelines of Gray III [43]. This allowed for homogenous deformation of the sample while preserving the equilibrium constraint. For soft materials, the samples having L/D ratio of 0.25 – 0.50 were selected in order to minimize wave attenuation [36]. This reduction in L/D ratio accommodated the reduced wave speed, which was proportional to  $(E/\rho)^{1/2}$ .

6061-T651 aluminum specimens (L = 6.35mm and D = 6.35mm) were fabricated for performing initial trial experiments and for validation of the SHPB test facility. The

cylindrical specimens of diameter 6.35 mm were carefully core drilled from plates of size 305 mm x 305mm (12”x 12”) using core a cutter. The specimens were polished using fine sand paper (grit #800) to remove the edge burrs.

## 4.7 SHPB test

### 4.7.1 Test Procedure

The 6061-T651 aluminum samples were tested in uniaxial compression at strain rates in the range of 990/s to 1,530/s using the SHPB apparatus shown in Figure 4.4. Prior to testing, based on the required strain rate, the striker bar velocity,  $v_{sb}$ , was calculated from

$$\dot{\epsilon} = \frac{v_{sb}}{l_s} \quad (4.30)$$

where  $l_s$  was the specimen length. Corresponding to this calculated striker bar velocity, the breech pressure was set based on the velocity-breech pressure calibration data. The SHPB test apparatus is shown in Figure 4.19, with critical sections marked by A, B, C and D. A typical procedure for performing SHPB test consisted of the following steps:

- a) Pre Firing/Test set up preparation
- b) Firing/Testing
- c) Post Firing/Data recording

D

B

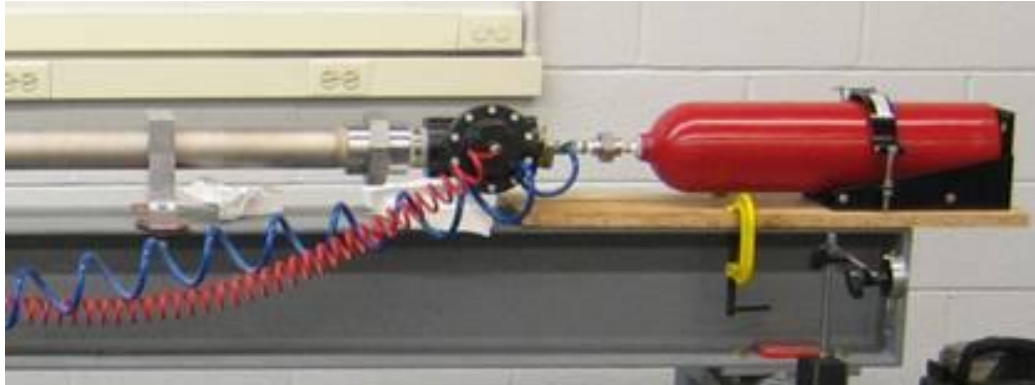
C

A

### Figure 4.19. SHPB Test Apparatus

#### (a) Pre Firing Test set up preparation

- Inspect and correct SHPB components for misalignment or damage. Ensure that there are no objects or personnel that may become pinched by firing of the striker bar.
- Depending on the pulse duration needed, select the required striker bar and insert into open the breech between the gun barrel and the firing valve as shown in Figure 4.20. Ensure pipe unions are secured between gun firing valve & pressure reservoir.



Gun barrel      Striker bar      Gun Breech assembly      Pressure reservoir

**Figure 4.20. Station A and Schematic of Assembly of Striker Bar into the Gun Barrel**

- Align incident and transmission bars so that the orientation marks on the bar ends are in line with each other as shown in Figure 4.21.

Transmission Bar

Incident Bar

Orientation marks

**Figure 4.21. Schematic of Aligning Incident Bar and Transmission Bar Prior to Testing**

- Check specimen dimensions carefully and apply a thin layer of molycoat on both ends and on each of the bar faces.
- Place the sample between the incident and transmitter bar using specimen alignment gauge as shown in Figure 4.22
- Place Lexan protective cover over test specimen location.
- Place the annealed C-11000 copper pulse shaper disk (diameter:4.8 mm and thickness:1.5 mm) as shown in Figure 4.23 on the striking end of the incident bar face using molycoat to precisely control the profile of the loading (incident) pulse so that the specimen deforms at a nearly constant strain rate under dynamic stress equilibrium, even at small strains.

Transmission Bar      Specimen      Incident Bar

Moly coat

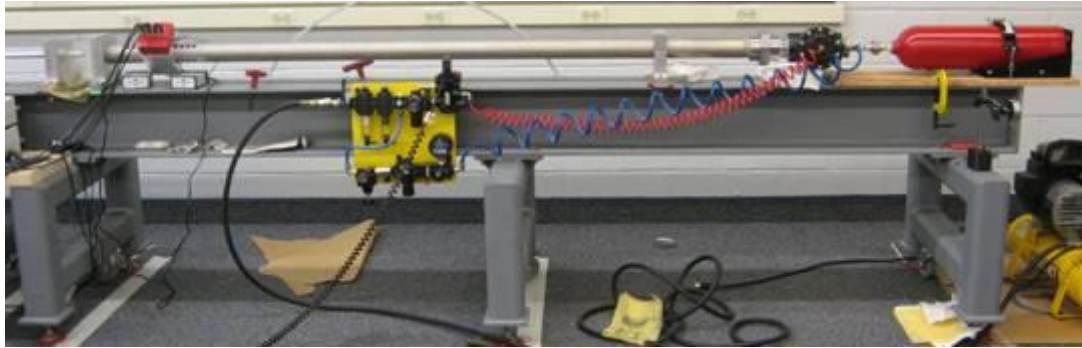
**Figure 4.22. Station D and Schematic of Placing the Specimen Between the Bars**

Incident Bar      Striker bar      Gun barrel

Copper pulse shaper      Bore Riders

**Figure 4.23. Station B and Schematic of Placing the Copper Pulse Shaper at the Incident Bar Face**

- Carefully insert 1.83 m (6 ft) long flexible plastic rod into muzzle end of gun barrel & push striker bar back into the breech as shown in Figure 4.24. A slight clunk should be heard as the bore rider contacts the breech, then stop. Carefully withdraw the plastic rod without disturbing the incident bar & stow rod on the gun's I-beam.



Incident Bar                      Gun barrel                      Striker bar      Gun Breech valve      Pressure reservoir

Flexible plastic rod

**Figure 4.24. Station C and Schematic of Placing the Striker Bar into the Firing Position using Flexible Plastic Rod**

- Turn ON the Data Acquisition System (Digital Storage Oscilloscope, Strain gauge signal conditioner, and PC etc).
- Connect air compressor to AC-mains & set maximum pressure to 0.7 – 0.9 MPa (100 – 125 psig).
- Connect compressor hose to Schrader quick-release air chuck.
- Open main air valve connected to Schrader fitting & set pilot control regulator to 80 – 100 psig.
- Set gun precision regulator to desired pressure. Unit has steady air bleed for fast response. For 19 mm (0.75”) aluminum bars, suggested range to prevent bar damage is 0.07 – 0.2 MPa (10 - 30 psig).
- Open valve between gun precision regulator, set pressure relief regulator to bleed air by turning CCW, & then turn slowly CW until air bleed stops.
- Press ON & lamp key on digital air pressure gage to precisely monitor air pressure. Push red safety cut-off lever upwards to connect gun air regulators to pressure reservoir. Readjust precision regulator to achieve desired pressure (+/-

0.1 psig). Close air valve between precision & relief regulator. At this point extreme caution must be observed since gun is pressurized and is ready to fire!

- Locate Remote Firing Control, ensure front panel firing key switch is OFF (CCW), & connect to AC-mains.
- Connect solenoid cable from gun's pneumatic panel to jack on rear panel of firing control (keyway in plug is orientated straight up @ 12:00).
- Locate main power switch on rear panel of firing control to activate the blue safety strobe.

*(b) Firing/Testing*

- Announce to participants & observers that they must wear their safety glasses & ear muffs. In addition, caution that the gun is ready for firing.
- Turn firing key switch to ON (CW) on firing control front panel, left-hand red push button will illuminate red.
- Press the START button on the digital storage oscilloscope.
- Press & hold the red button (right-hand button will illuminate yellow) and now press the right-hand button.

*(c) Post Firing/Data Collection*

- Save the waveform file using the file save button on the oscilloscope. Turn the firing control key switch OFF (CCW), & switch-off power (blue strobe will extinguish).
- Shut-off all air valves on gun's pneumatic panel including pushing red shut-off lever to down position to safely vent pressure reservoir.
- Remove the Lexan protective cover and remove test specimen from SHPB.
- Disconnect compressor hose to Schrader quick-release air chuck by twisting and pulling the hose connector, and then unplug the compressor from the AC-mains.
- Transfer the waveform data file stored in the PC card of digital storage oscilloscope to PC.
- Reduce the raw waveform data in Microsoft Excel sheet named "SHPB master"
- Plot the stress-strain curve to check validity of the test

- Plot the strain–time curve to calculate the strain rate obtained during SHPB test.

#### 4.7.2 Data Recording and Analysis

Processing of the Hopkinson bar signal into engineering data was not straightforward. Several operations were done prior to generating the dynamic stress-strain relations of the specimen. Figure 4.25 shows a typical progression through the data processing procedure.

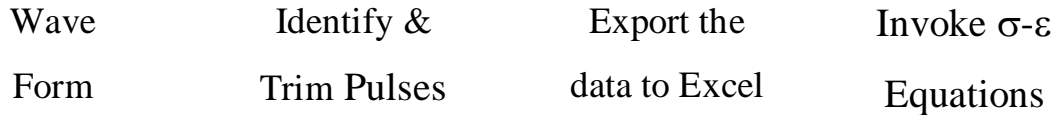


**Figure 4.25. Block Diagram of Typical Data Processing Procedure**

An example of the typical axial strain signal in the incident and transmitted bars for aluminum specimen Al6061-T651-1 is shown in Figure 4.2. The plateau in the reflected pulse shown in Figure 4.25 indicates that the aluminum specimen was deformed at a nearly constant strain rate for most of the time during specimen deformation. The strain rate for a given test varied as a function of time. Typically, it increased from zero to a maximum value in a short period of time, then fluctuated about a constant value and finally dropped to zero. This constant value of the strain rate was accounted for and was defined by an average strain rate and was used to characterize the specific experiment.

The waveform data was acquired by a high speed data acquisition card of DSO at a sampling rate of 1 MHz. The waveform file stored in DSO was converted into ASCII files and read by another signal processing software (Xviewer) for further analysis of the data. The raw waveform signals were oscillatory in nature due to noise. The waveforms were smoothed in Xviewer software using built-in mathematical filtering functions.

The unknown transit time through the greased joint and sample hindered the precise identification of the pulse start and end. Since the impact events had a short

duration (often only 100-200  $\mu$ s) small errors in aligning the two pulses together could yield large errors. The start of each pulse had to be identified properly and the two pulses needed to be synchronized correctly to enable an accurate construction of the dynamic stress-strain curve. The starting time was selected from the transmitted pulse at the instant when it began deviating from zero and the ending time was selected as the time when the transmitted pulse flattened out. The portion of the reflected pulse was chosen for the corresponding time range. The identified and trimmed pulses were converted to reflected  $\varepsilon_R(t)$  and transmitted  $\varepsilon_T(t)$  strains in the pressure bars using

$$\varepsilon = \left( \frac{-R_G}{F_G N (R_G + R_C)} \right) \frac{V}{V_{ex}} \quad (4.31)$$

where,  $V$  was output voltage from signal-conditioning amplifier,  $V_{ex}$  was bridge excitation voltage (10V),  $F_G$  was the gage factor and  $\varepsilon$  was the strain (compressive) simulated by shunting  $R_G$  with  $R_C$ ,  $R_G$  was the nominal resistance of the strain gage (1000 ohms),  $R_C$  was the shunt calibration resistance (49,000 ohms), and  $N$  was the number of active gages ( $N = 2$  for half-bridge configuration).

The specimen stress, strain, and strain rate were calculated from the pressure bar strain pulses. The strain rate and strain in the specimen were determined from the reflected pulse, and the specimen stress was determined from the transmitted pulse. A trapezoidal rule was used to integrate the strain rate to calculate the specimen strain. The equations (4.19), (4.20) and (4.22) were used for calculating specimen strain rate, strain, and stress, respectively. All the data analysis was performed using the MS Excel spreadsheet.

#### 4.8 Validation of SHPB Testing

Two materials were chosen to validate the operation of the SHPB test apparatus, the test procedure and data reduction. Thee materials were 6061-T651 aluminum and

polycarbonate. Results for these two materials are available in research literature for comparison purposes.

*(a) 6061-T651 Aluminum*

A cylindrical test specimen of 6.4 mm diameter and 6.4 mm length was prepared as explained before. The SHPB test was performed at strain rates of approximately 1,300/s on three different samples. The calculated strain rate, strain and stress using equations 4.19, 4.20 and 4.22, are shown in Figures 4.26 to 4.28, respectively. Parameters used in the calculation were  $l_s$ ,  $c_b$ ,  $A_b$ ,  $A_s$ , and  $E_b$  are 6.35 mm, 5,051 m/s, 285.02 mm<sup>2</sup>, 31.67 mm<sup>2</sup>, and 71.7 GPa, respectively. The  $\varepsilon_R(t)$  and  $\varepsilon_T(t)$  were responses from reflected and transmitted wave signals collected from the data acquisition system. Figure 4.29 shows the stress response calculated using equations 4.22 to 4.24. It was observed from the figure that all the three curves were close to each other after an initial “ringing-up” period (i.e. when the stress equilibrium was achieved in the specimen). This finding indicated that the results based on 1-wave, 2-wave and 3-wave analyses were similar to each other once the specimen attained stress equilibrium. The superposition of data in Figures 4.27 and 4.28 gave the transient stress-strain curve shown in Figure 4.30. Figure 4.30 also shows a dynamic stress-strain response of two other samples along with the quasi-static compression response of the same material. The average strain rate was determined from the slope of the strain-time plot up to maximum strain. The average strain rates were 1235/s, 1245/s, and 1264/s. All three tests showed nearly the same response. Current results were compared with Hall et al. [80] for the same material and at a strain rate of 1400/s. The current results were in very good agreement with Hall et al. Interestingly, the quasi-static compression test results were also in decent agreement with dynamic results in the plastic region.

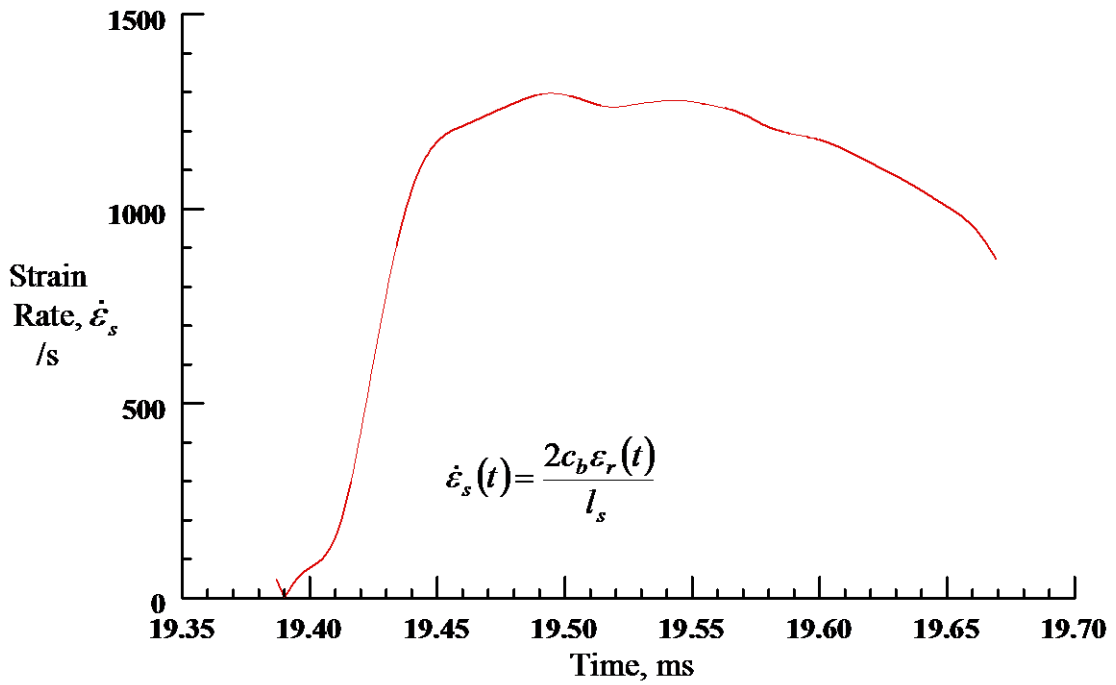


Figure 4.26. Strain Rate vs. Time Plot for 6061-T651 Aluminum

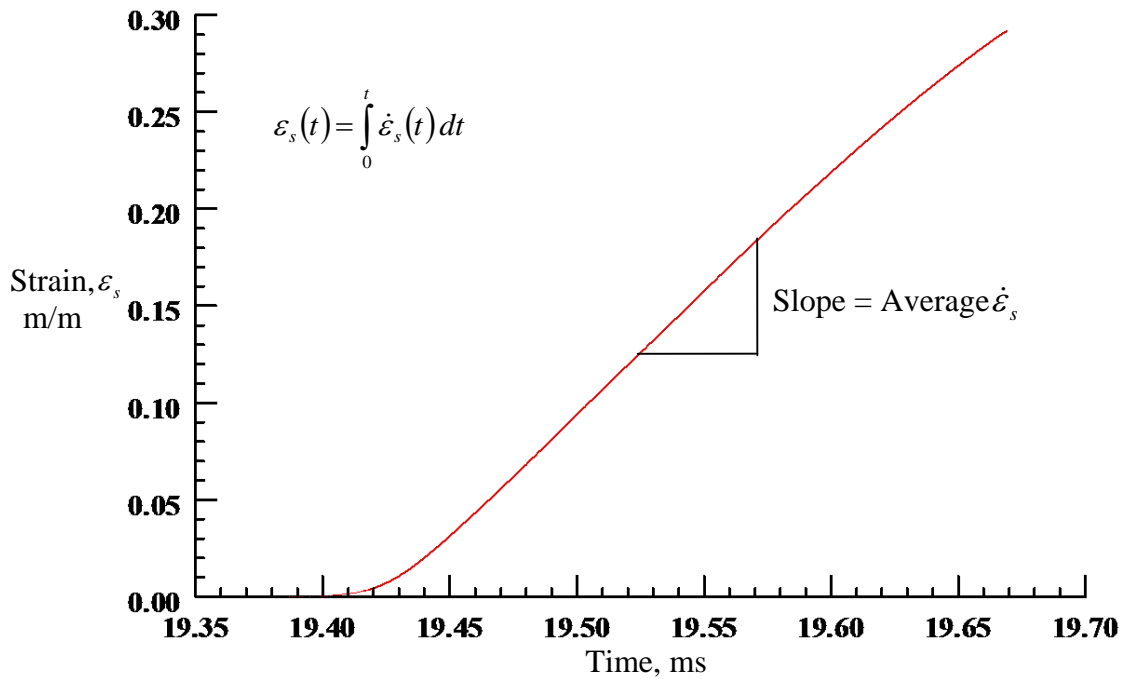


Figure 4.27. Strain vs. Time Plot for 6061-T651 Aluminum

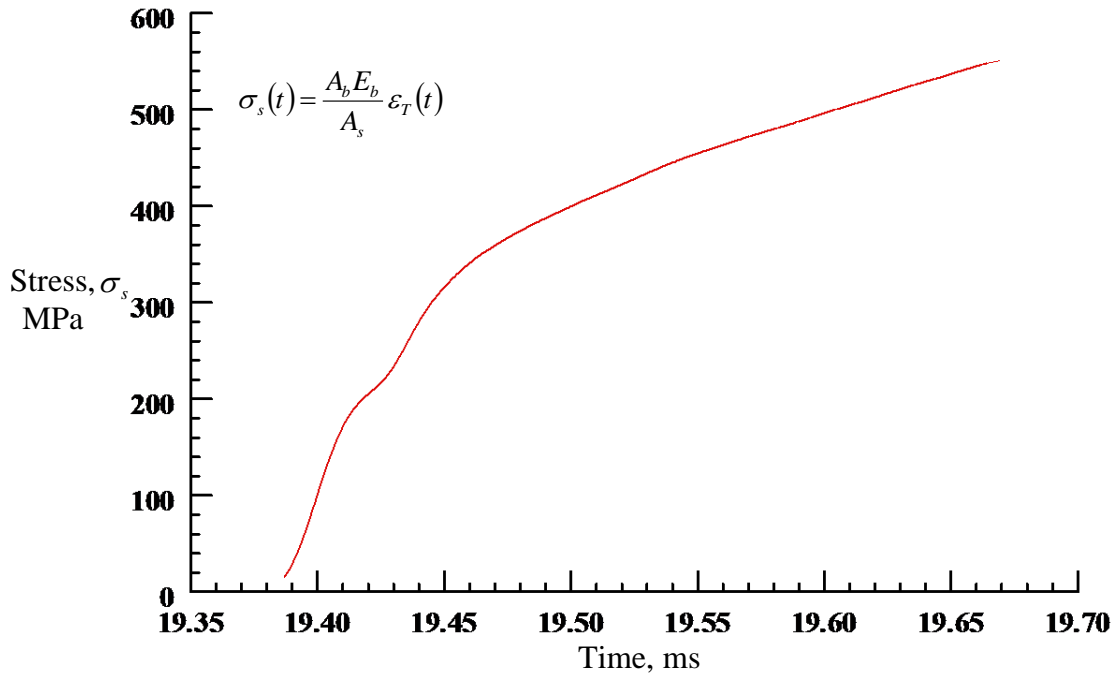


Figure 4.28. Stress vs. Time Plot for 6061-T651 Aluminum

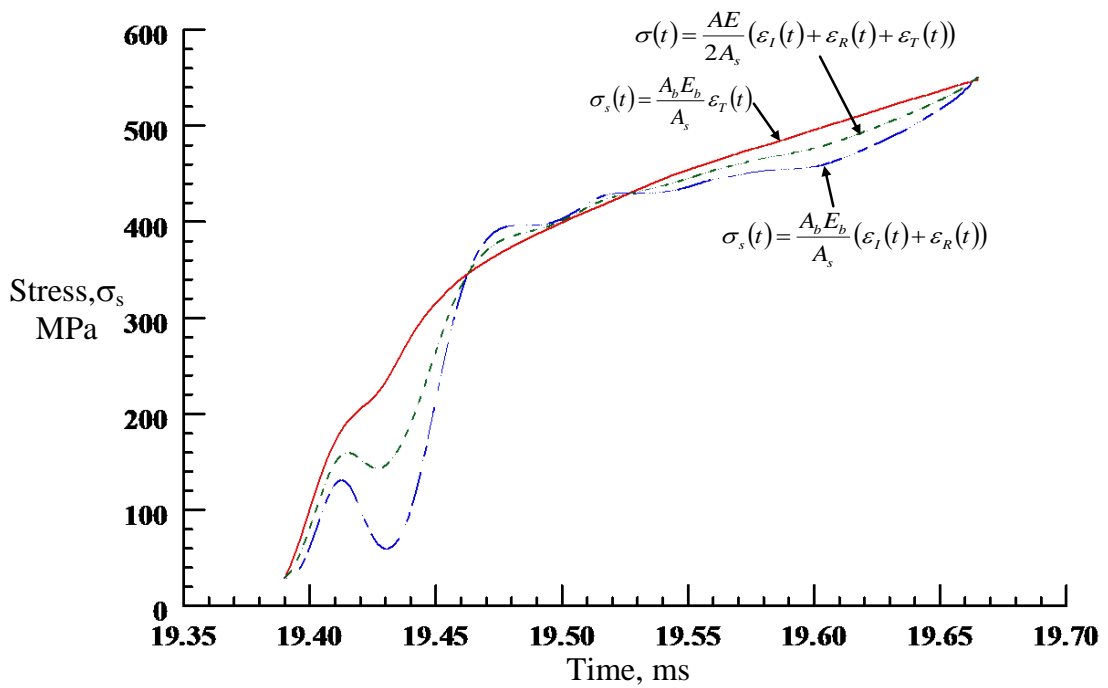
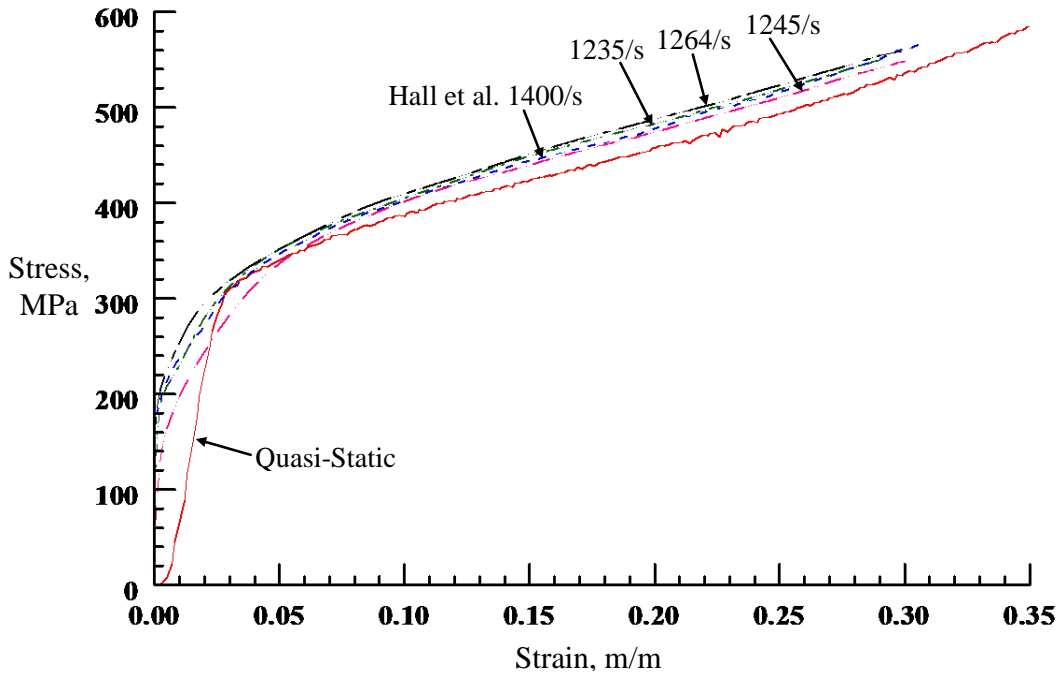


Figure 4.29. Stress vs. Time Plot for 6061-T651 Aluminum based on 1-wave, 2-wave

### and 3-wave Analysis



**Figure 4.30. Comparison of Dynamic Stress-Strain Plot for 6061-T651 Aluminum**  
*(b) Polycarbonate*

A cylindrical test specimen of 6.4 mm diameter and 6.4 mm length was prepared as explained before. The SHPB test was performed at strain rates of approximately 1,300/s on three different samples. The calculated strain rate, strain and stress using equations 4.19, 4.20 and 4.22, are shown in Figures 4.31 to 4.33, respectively. Parameters used in the calculation were  $l_s$ ,  $c_b$ ,  $A_b$ ,  $A_s$ , and  $E_b$  are 6.35 mm, 5,051 m/s, 285.02 mm<sup>2</sup>, 31.67 mm<sup>2</sup>, and 71.7 GPa, respectively. The  $\varepsilon_R(t)$  and  $\varepsilon_T(t)$  were responses from reflected and transmitted wave signal collected from the data acquisition system. Figure 4.34 shows the stress response calculated based on 1-wave, 2-wave and 3-wave analyses using equations 4.22 to 4.24. It was observed from the figure that the stress curves marginally separated from each other after an initial ringing-up period. This situation could have been due to the viscoelastic nature of the polycarbonate. The superposition of data in Figures 4.32 and 4.33 gives the transient stress-strain curve shown in Figure 4.35. Figure 4.35 also shows the dynamic stress-strain response of two other samples. The average strain rate was determined from the slope of

the strain-time plot up to maximum strain. The average strain rates were 1290, 1317, and 1329/s. All three tests showed nearly the same response. Current results were compared with Salisbury et al [81] for the same material and at a strain rate of 1,310/s. From Figure 4.33, it was observed that the slopes of the stress-strain curves were quite similar with the current results being little steeper than that in published data. The magnitude of the flow stress for Salisbury et al. was marginally higher than the current results. The higher flow stress from Salisbury et al. could be partially attributed to the difference in strain rates. The present results are in very good agreement with Salisbury et al.

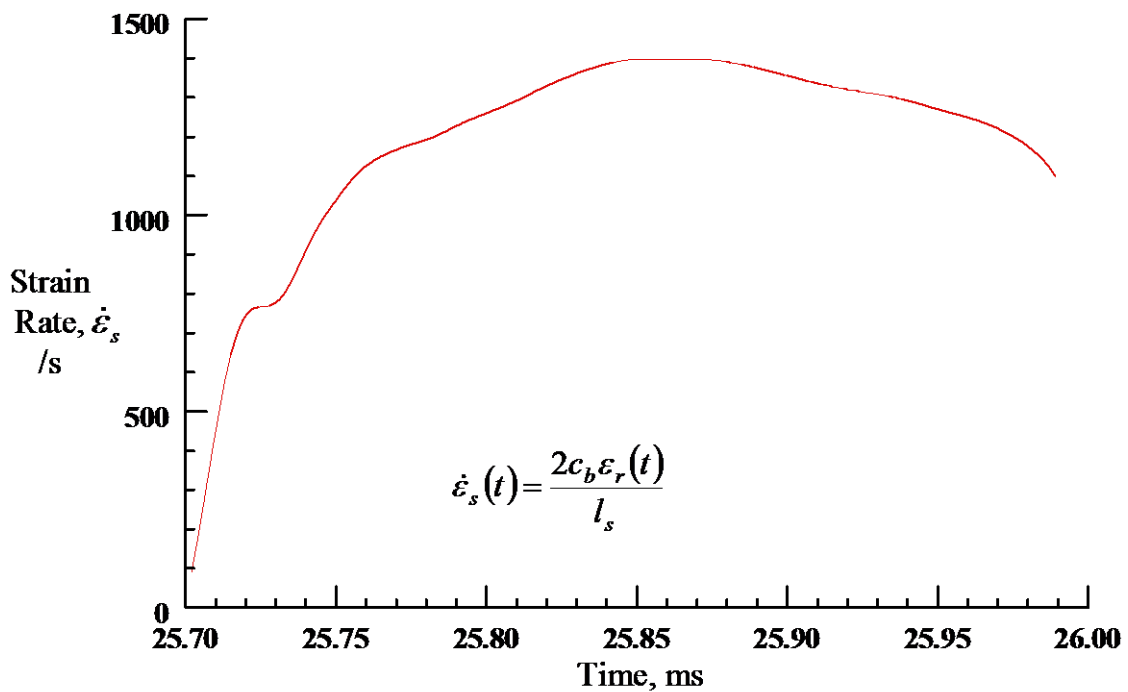


**Figure 4.31. Strain Rate vs. Time Plot for Polycarbonate**

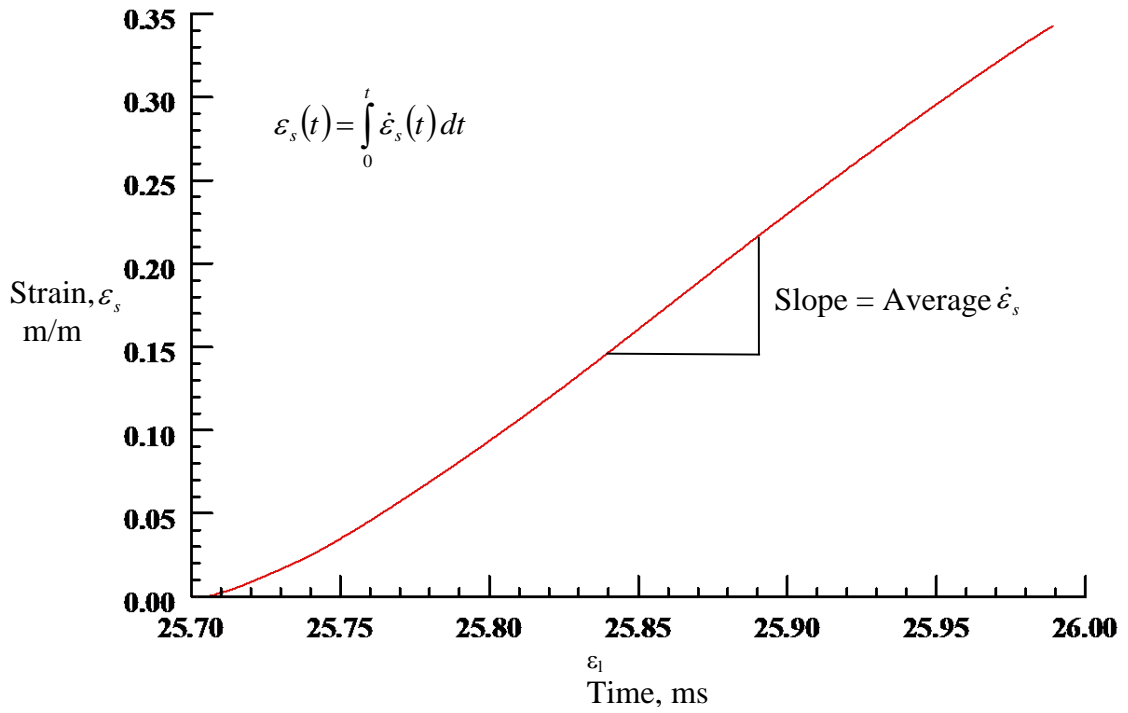


Figure 4.32. Strain vs. Time Plot for Polycarbonate

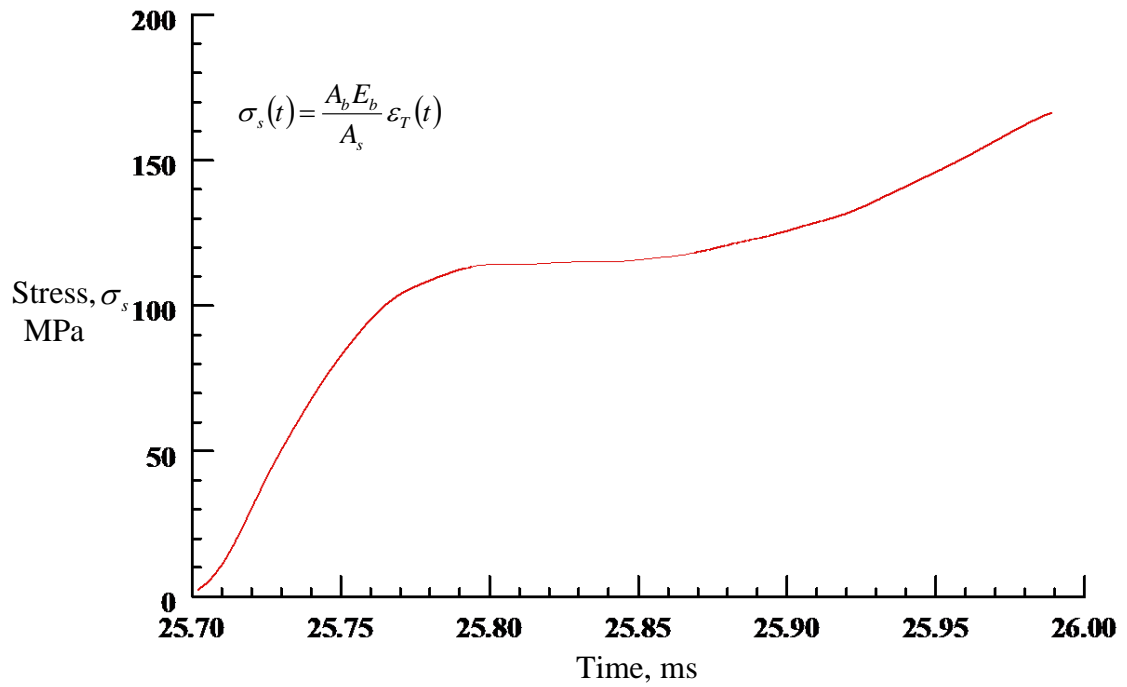


Figure 4.33. Stress vs. Time Plot for Polycarbonate

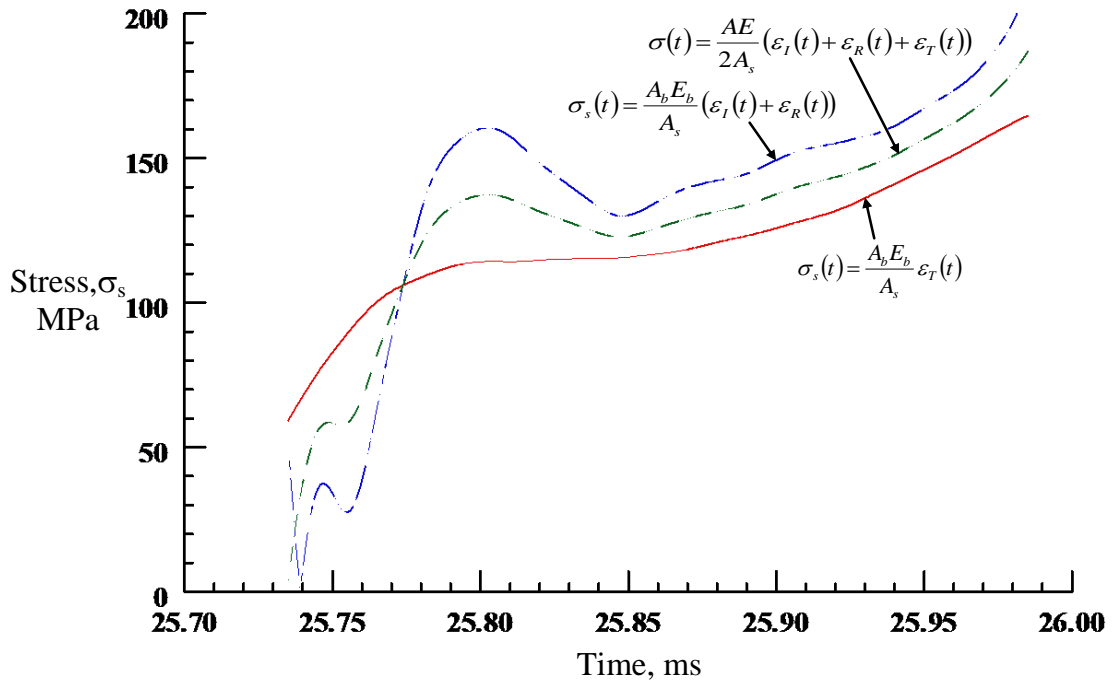


Figure 4.34. Stress vs. Time Plot for Polycarbonate based on 1-wave, 2-wave and 3-wave Analysis

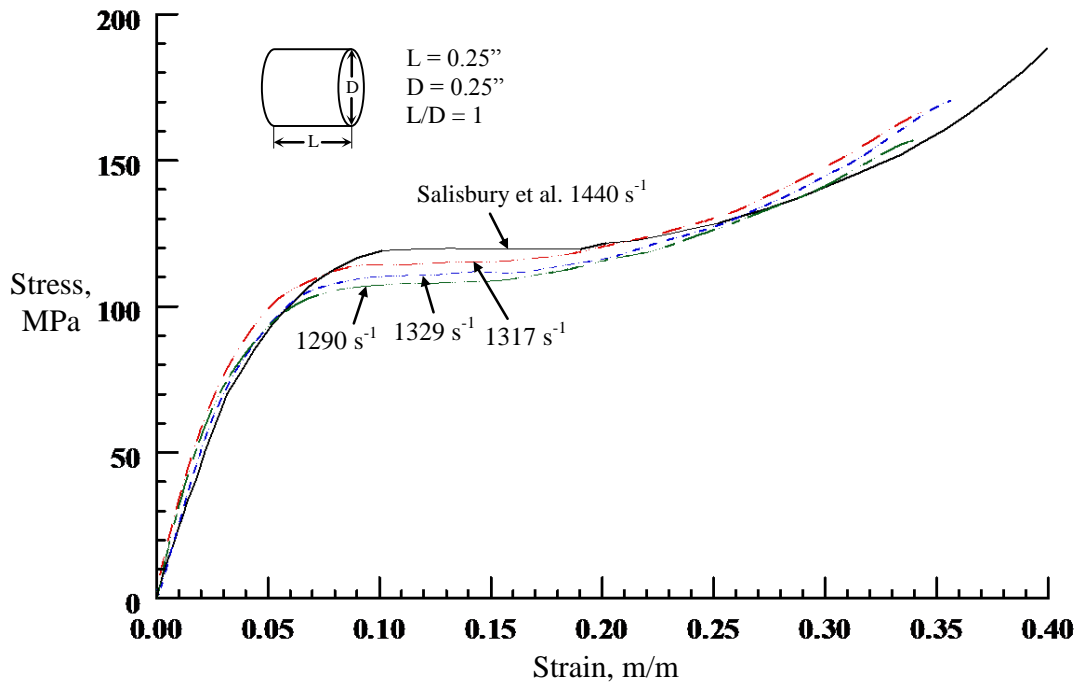


Figure 4.35. Comparison of Dynamic Stress-Strain Plot for Polycarbonate at 1,310/s

The above two tests validated the test apparatus, the test procedure and the data reduction.

#### **4.9 Summary**

The compression SHPB test apparatus with 7075 T6 aluminum pressure bars was successfully designed, fabricated, and developed for high strain rate testing of materials. The SHPB apparatus was calibrated for breech pressure and striker velocity. This will help in selecting breech pressure for the required impact velocity. The SHPB apparatus was verified for 6061-T651 aluminum and polycarbonate materials. SHPB Tests on 6061-T651 aluminum specimens were performed and compared with results from Hall et al. [80]. There was a good agreement with the published data. The SHPB apparatus was further validated by testing polycarbonate samples. The dynamic stress-strain response reported by Salisbury et al. [81] matched well with the present results.

## CHAPTER 5

# DYNAMIC CHARACTERIZATION OF ECO-CORE AND ITS MODIFICATIONS

### 5.1 Introduction

This chapter presents the dynamic characterization of Eco-Core and a discussion of the results of this characterization. First the baseline Eco-Core characterization and the development of constitutive model is presented. Then the test and analysis is extended to modified Eco-Core materials. The energy absorption capacity of the Eco-Core and its modification is analyzed and the results of each one are compared with each other.

### 5.2 Dynamic Characterization of Baseline Eco-Core

#### 5.2.1 Sample Preparation

The samples with a length to diameter (L/D) ratio between 0.25 and 0.50 were selected based on the guidelines of Chen et al. [43]. This reduction in ratio accommodated the reduced wave speed (proportional to  $(E/\rho)^{1/2}$ ) in the softer materials. Sample preparation for Eco-Core required a two-step operation: first, core drilling the rough sample; second, fine milling to the required size in a milling machine. Cylindrical specimens were carefully core drilled from panels of size 152 mm x 152mm (6"x 6") using a core cutter. The rim of the specimen was wrapped with thick masking tape before clamping in the machine vise to prevent local crushing. The specimen was then surface milled to the required thickness with a tolerance of  $\pm 0.02$  mm using a precision milling machine. The diameter of the specimen was not machined as the core drilling operation gave a finer surface with the required tolerance. Figures 5.1 and 5.2 show photographs of typical Eco-Core samples used in this research. The Eco-Core specimens without any

modification with a geometry of L = 0.125” and D = 0.5” were termed as baseline. The specimens were named with a set of characters/numbers following this definition:

- ECB-x : Baseline Eco-Core of L = 0.125 inch thick and D = 0.5 inch
- EC15-x : Eco-Core of L = 0.15 inch thick and D = 0.5 inch
- EC25-x : Eco-Core of L = 0.25 inch thick and D = 0.5 inch
- EC50-x : Eco-Core of L = 0.50 inch thick and D = 0.5 inch

In order to assess the quality of the fabricated specimens, density and dimensional measurements were performed. Table 5.1 records the dimensions and density of the baseline Eco-Core specimens used for the aspect ratio (L/D) study. The length of the specimens was quite uniform with a co-efficient of variation within 2%. The Eco-Core density varied from 0.53 to 0.56 g/cc with an average value of 0.55 g/cc and a co-efficient of variation of 2.2 %, which was quite reasonable for lab manufactured material. Measured densities of Eco-Core specimens used for strain rate studies are given in Table 5.2. The density varied from 0.54 to 0.56 g/cc with an average value of 0.55 g/cc and a co-efficient of variation of 1.3 %, which was quite uniform.

**Table 5.1. Density and Dimensions of Eco-Core Specimens of Various L/D Ratio**

Specimen #	Diameter (D), mm				Length (L), mm				Weight, g	Density, g/cc
	1	2	3	Avg.	1	2	3	Avg.		
ECB-7	12.32	12.32	12.33	12.32	3.14	3.14	3.12	3.13	0.205	0.549
ECB-8	12.32	12.32	12.33	12.32	3.12	3.16	3.18	3.15	0.206	0.548
ECB-9	12.34	12.34	12.36	12.35	3.18	3.19	3.19	3.18	0.208	0.546
ECB-26	18.50	18.50	18.52	18.51	3.18	3.20	3.20	3.19	0.453	0.528
ECB-27	18.50	18.50	18.49	18.50	3.20	3.20	3.19	3.20	0.457	0.532
ECB-29	18.48	18.50	18.49	18.49	3.18	3.15	3.18	3.17	0.447	0.526
EC15-17	12.59	12.59	12.60	12.59	3.81	3.82	3.81	3.81	0.267	0.562
EC15-21	12.55	12.55	12.55	12.55	3.81	3.81	3.81	3.81	0.266	0.565
EC15-26	12.52	12.53	12.52	12.53	3.78	3.78	3.78	3.78	0.263	0.564
EC25-1	12.31	12.32	12.31	12.31	6.34	6.34	6.35	6.34	0.419	0.555
EC25-2	12.33	12.33	12.34	12.34	6.36	6.35	6.36	6.36	0.417	0.549
EC25-3	12.29	12.29	12.31	12.30	6.35	6.35	6.36	6.35	0.418	0.554
EC50-2	12.31	12.31	12.29	12.30	13.08	13.09	13.08	13.09	0.841	0.541
EC50-3	12.29	12.29	12.31	12.30	13.06	13.06	13.06	13.06	0.849	0.547
EC50-4	12.29	12.32	12.29	12.30	13.02	13.03	13.02	13.02	0.842	0.544
Average (% CV)										0.547 (2.2)

**Table 5.2. Density and Dimensions of Baseline Eco-Core Specimens for Dynamic Failure Model Development**

Specimen #	Diameter (D), mm				Length (L), mm				Weight, g	Density, g/cc
	1	2	3	Avg.	1	2	3	Avg.		
ECB-1	12.31	12.29	12.31	12.30	3.18	3.18	3.14	3.16	0.208	0.553
ECB-2	12.40	12.40	12.38	12.39	3.18	3.18	3.16	3.17	0.209	0.547
ECB-3	12.29	12.29	12.29	12.29	3.14	3.14	3.14	3.14	0.204	0.548
ECB-4	12.29	12.31	12.32	12.31	3.18	3.20	3.21	3.20	0.206	0.542
ECB-5	12.29	12.29	12.29	12.29	3.12	3.14	3.15	3.14	0.208	0.559
ECB-6	12.31	12.31	12.31	12.31	3.19	3.20	3.19	3.19	0.207	0.545
ECB-10	12.33	12.33	12.34	12.34	3.12	3.12	3.12	3.12	0.209	0.560
ECB-11	12.33	12.33	12.33	12.33	3.21	3.23	3.21	3.22	0.208	0.541
ECB-12	12.33	12.34	12.36	12.34	3.14	3.15	3.15	3.15	0.209	0.555
Average (% CV)									0.550 (1.3)	



**Figure 5.1. Eco-Core Specimens of Various L/D Ratio's**



**Figure 5.2. Eco-Core Specimens for Dynamic Failure Model Development**

### **5.2.2 SHPB Test**

#### **5.2.2.1 Test Procedure**

The Eco-Core samples were tested in uniaxial compression at strain rates in the 1000/s to 3100/s range using the Split Hopkinson Pressure Bar (SHPB) apparatus. Testing at strain rates below 1000/s was difficult with the present setup. The apparatus was developed for measuring the dynamic compression response of low stiffness materials such as aluminum, composites and sandwich core materials. A striker bar of length 0.76 m (2.5 ft), and incident and transmitted bars of length 3.66 m (12 ft), 1.83 m (6 ft) respectively were used. All bars were made from 19 mm (0.75 in) diameter aluminum alloy 7075 T6 rods. The aluminum alloy was chosen to reduce the impedance (expresses the ratio of a driving force to the resulting velocity at a given point of the structure and is given by  $A(\rho E)^{1/2}$ ; where A,  $\rho$ , and E is the cross-sectional area, density, and elastic modulus of the incident bar, respectively) mismatch with the Eco-Core and other non-metallic samples to attain a high sensitivity in the stress measurement from the transmission signal. Annealed C-11000 copper discs (D = 4.8 mm and T = 1.5 mm) were

used as pulse shapers to improve dynamic equilibrium and to dampen the high frequency components in the stress pulses, thus reducing the dispersive effects. The complete operation, design details, test procedure and data analysis of split Hopkinson bar testing of materials is given in section 4.7 of Chapter 4. Some tests were coupled with a Phantom 650 high-speed digital camera to obtain high-speed images of specimens during the dynamic deformation. Figure 5.3 shows an example of the typical axial strain signal in the incident and transmitted bars for Eco-Core specimen ECB-12.

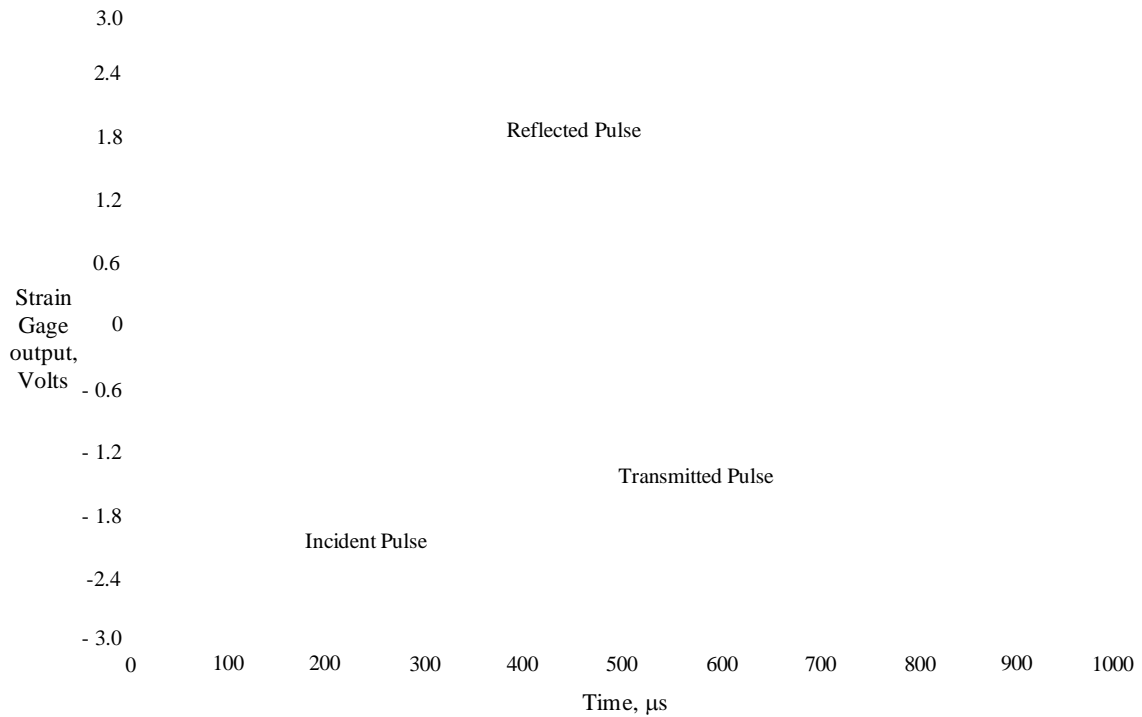


**Figure 5.3. Typical Dynamic Responses from the Strain Gages Mounted on the Incident and Transmission Bars for Eco-Core Specimen ECB-12**

#### 5.2.2.2 Test Matrix

Dynamic characterization of baseline Eco-Core samples was performed using a Split Hopkinson Pressure Bar set up (SHPB). An aspect ratio (L/D) of the specimen was

considered a parameter and it was varied from  $L/D = 0.17$  to 1. The effect of the  $L/D$  ratio on the dynamic stress equilibrium was studied at a constant breech pressure of around 19 psi. After finalizing the  $L/D$  ratio, the effect of strain rate on the compressive stress-strain response of Eco-Core is studied. Three specimens were tested for each category. The strain rate was varied by changing the breech pressure, which in turn changed the striker velocity. A range of strain rates (1,000/s to 3,100/s) were obtained by changing the breech pressure from 13 psi to 22 psi during SHPB tests. The lowest strain rate achievable in SHPB is around 200/s. The lowest possible strain rate achievable at the CCMR SHPB facility was approximately 1,000/s. At breech pressure less than 13 psi (corresponding to strain rates less than 1,000/s), the striker bar barely touched the incident bar and generated a negligible impact force. This situation may have been due to the heavy mass of the striker bar and the friction between the bore riders and the internal surface of the gun barrel. In addition, the captured strain gauge signal was very poor and noisy. The achievable high strain rate was limited by the elastic strain limit of the incident bar material. The velocity of the striker bar was limited to approximately 15 m/s (corresponds to a strain rate of about 3,500/s) in order to ensure that the aluminum alloy did not yield during testing. The experiments conducted at striker bar velocity beyond 15 m/s frequently caused breakage of the soldering junction of the strain gage bonding terminals. Therefore, the SHPB experiments for Eco-Core were conducted between strain rates of 1,000/s and 3,100/s.

### ***5.2.3 Results and Discussions – Baseline Eco-Core***

#### **(a) Typical dynamic stress-strain response**

The high strain rate compression test results for baseline Eco-Core is discussed in this section. Figure 5.4 shows a typical dynamic compressive stress-strain curve at a strain rate of 3,150/s for baseline Eco-Core. The curve has the following three characteristics typical of other core materials such as PVC foams [82]; an initial elastic region where stress is directly proportional to strain, a plateau region where the stress remains constant with strain due to breaking of bonds between microbubbles and its rearrangement (translation), and followed by crushing of microbubbles, densification shown by rapid increase of stress as the crushed

microbubble walls are compacted. The value of the plateau stress  $\sigma_{pl}$  (defined as the stress at 10% nominal axial strain) is around 20 MPa, which is about the same as static compression strength of the microbubble. The densification/crushing strain of Eco-Core is approximately 0.42. The shape of the dynamic compressive stress-strain curve is very similar to that of the static confined stress-strain curve given in chapter 2. In addition, the plateau stress and crushing strain values derived from the dynamic stress-strain curve is approximately the same as the quasi-static results. Following the same experimental procedure, dynamic experiments were performed on the Eco-Core at strain rates from 1000 to 3100/s. The strain rate effects are discussed in later sections.

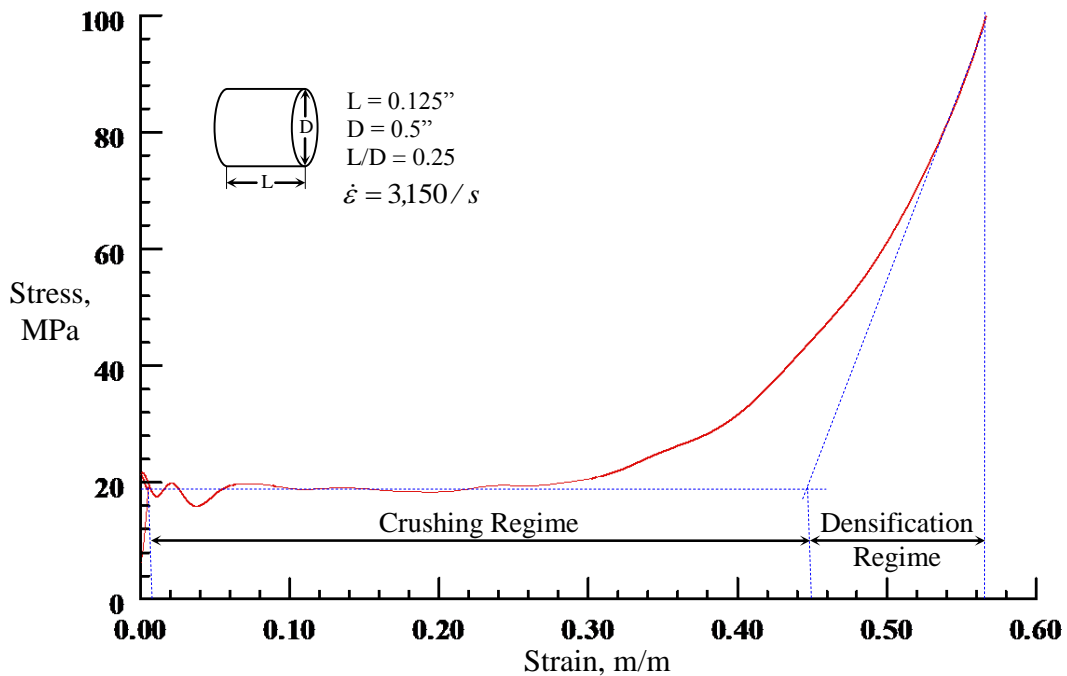


**Figure 5.4. Typical Dynamic Compressive Stress-Strain Curve of Eco-Core Specimen ECB-12 at the Strain Rate of 3,150/s**

(b) Image analysis of the dynamic phenomenon

A Phantom 650 high-speed digital camera was employed to image the side view of the SHPB test section at a rate of 45,000 frames per second. A series of images from the SHPB experiment are shown in Figure 5.5 at a time interval of 9.8  $\mu$ s. Time  $t = 0$  occurred just before the loading pulse arrived at the incident bar/specimen interface. In the images, the incident bar was moving from the right side of each image and pushed the specimen towards the left side. The Eco-Core specimen was observed to be compacted gradually from the transmitted bar/specimen end. The Eco-core deformed elastically for about 20 micro seconds and then the peak stress crushed the back side layers of the specimen (i.e, specimen side facing the transmitted bar). This situation is evident in Figure 5.5 where the bulging of the back side of the specimen is clearly observed. From the series of images given in Figure 5.5, it is clear that crushing of the Eco-Core specimen initiated at the transmitter bar/specimen end and propagated gradually towards the specimen/ incident bar end. It can also be observed that crushing of the Eco-Core layers continued for almost the entire length of the specimen. The crushing phenomena continued for about 225  $\mu$ s; thereafter rapid lateral ejection of the crushed Eco-Core particles was observed. The photograph of the crushed specimen after dynamic loading is shown in Figure 5.6. The samples of crushed specimens were collected to analyze by Scanning Electron Microscope (SEM).

Figure 5.7 shows the SEM micrograph of the samples collected after testing at four different strain rates. At the strain rate of approximately 1,000/s the crushing strain attained was 0.21, and the SEM image showed few broken cenosphere bubbles. As the strain rate increased, the Eco-Core specimen underwent a higher crushing strain that led to more crushing of the cenosphere bubbles. From Figure 5.7, it is evident that the amount of crushed micro balloons increased with an increasing strain rate. It is clear from the SEM micrograph of the Eco-Core sample tested at a strain rate of 3,139/s (see Figure 5.7d) that all the cenosphere bubbles crushed extensively as debris of crushed cenospheres are observed all over the micrograph. Therefore, SEM studies proved that Eco-Core undergoes a crushing mode of failure at high strain rates and shows the capability to absorb energy.

t = 0  $\mu$ s      t = 9.8 $\mu$ s      t = 19.6 $\mu$ s      t = 29.4 $\mu$ s      t = 39.2 $\mu$ s

t = 49.0 $\mu$ s      t = 58.8 $\mu$ s      t = 68.6 $\mu$ s      t = 78.4 $\mu$ s      t = 88.2 $\mu$ s

t = 98.0 $\mu$ s      t = 107.8 $\mu$ s      t = 117.6 $\mu$ s      t = 127.4 $\mu$ s      t = 225.4 $\mu$ s

**Figure 5.5. Images of the Eco-Core Specimen (L/D = 0.25) Deformation in a Dynamic Test (time interval: 9.8 $\mu$ s)**



**Figure 5.6 Eco-Core Specimen after Dynamic Testing**

(a)

(b)

(c)

(d)

**Figure 5.7. SEM Micrograph of Eco-Core Specimens after Testing at a Strain Rate of (a) 989/s (b) 1,600/s (c) 2,574/s and (d) 3,139/s**

#### *5.2.3.1 Effect of Specimen Geometry (L/D ratio)*

Specimens with different aspect ratios (L/D) of 0.17, 0.25, 0.3, 0.5, and 1 were used to investigate the effect of aspect ratio on the dynamic compressive properties of baseline Eco-Core. Since the specimen length in dynamic experiments was limited by the dynamic force equilibrium, the effects of specimen length on the mechanical properties obtained from these specimens required examination. The details of the specimen geometry and aspect ratios considered for dynamic experiments are given in Table 5.3.

**Table 5.3 Test Plan for Investigating the Effect of Specimen Aspect Ratio**

Sl. No.	Specimen Length, in	Specimen Diameter, in	L/D ratio
1	0.125	0.73	0.17
2	0.125	0.50	0.25
3	0.150	0.50	0.30
4	0.250	0.50	0.50
5	0.500	0.50	1.00

Figure 5.8 shows a confined compression stress-strain response of a typical cellular foam material including Eco-Core [72]. The critical parameters are compression strength ( $\sigma_c$ ), failure strain ( $\varepsilon_c$ ), plateau strain ( $\varepsilon_p$ ), crushing strain ( $\varepsilon_{crush}$ ) and the two moduli, namely, foam modulus  $E_{foam}$  and solid modulus  $E_{solid}$ . Critical point and associated failure in the diagram are compression strength, wherein the binder between the microbubbles fails. This incident is followed by the crushing of the microbubbles (shown by the flat curve) in a confined volume, and then the bubbles consolidate as a solid, which is shown by the rising curve.  $E_{foam}$  is related through  $\sigma_c$  and  $\varepsilon_c$  while  $E_{solid}$  has no role to perform in the energy absorption mechanism. Energy absorption density was approximated by:

$$E_{EA} = \frac{1}{2} \sigma_c \varepsilon_c + \sigma_c \varepsilon_{crush} \quad (5.1)$$

and was used for comparison of different materials. The first part of the approximation was the strain energy of the foam at failure and the second part was the crushing energy. As a first approximation, it can written:

$$E_{EA} = \sigma_c \varepsilon_{crush}; \text{ Because } \varepsilon_c \ll \varepsilon_{crush} \quad (5.2)$$

$E_{EA}$  can be improved by increasing  $\sigma_c$  and  $\varepsilon_{crush}$ . The  $\varepsilon_{crush}$  depended on the void fraction of the foam while  $\sigma_c$  depended on the properties of the binder that encapsulated the

microscopic voids and microbubbles. The parameters  $\sigma_c$  and  $\epsilon_{crush}$  played an important role in the energy absorption mechanism.

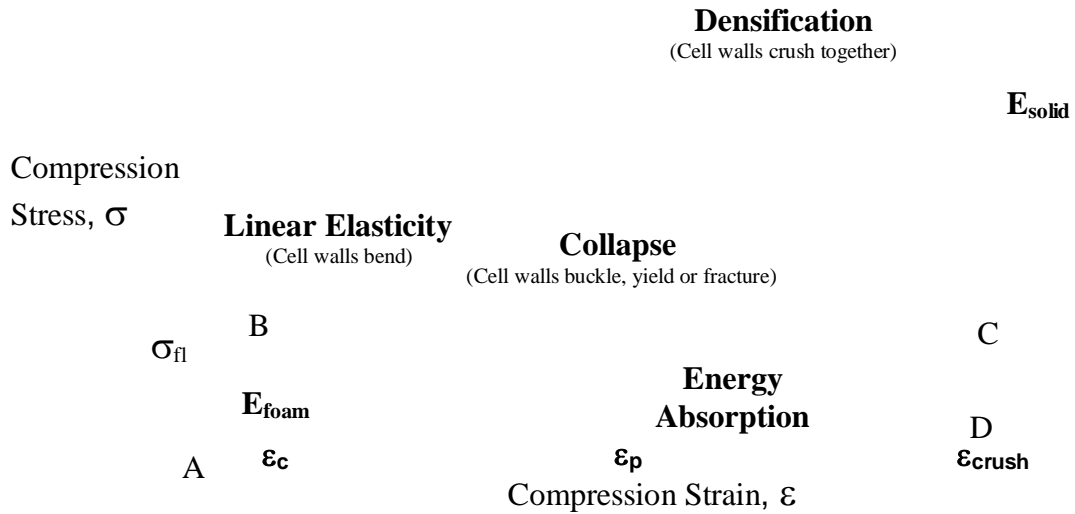


**Figure 5.8. Typical Compressive Stress-Strain Response of Core Material [72]**

#### 5.2.3.1.1 Dynamic test for different L/D Specimens

All the experiments at various aspect ratios were repeated on carefully grouped specimens according to their densities. Figures 5.9 to 5.13 show the dynamic compressive stress-strain curves for Eco-Core specimens having L/D ratios of 0.17, 0.25, 0.3, 0.5 and 1, respectively. Three experiments were conducted for each L/D ratio. From Figures 5.9 through 5.13 it is clear that the experimental results were repeatable under the exact same test conditions (i.e. strain rates). The values in the parenthesis were the velocity of the striker bar. It can be seen from the appearance of the stress-strain curve shown in Figure 5.9 that the Eco-Core specimen with L/D = 0.17 exhibited a response that is similar to the elastic-plastic response of metals. The plateau stress value was nearly the same for all the three specimens and was approximately 20.5 MPa. The specimens failed by breakage of bonds between the

microbubbles at peak load, crushing of microbubbles and then solidification, which is a typical response of foam materials. After peak stress, a plastic plateau region existed where the stress was constant or mildly increased with the applied strain. The plateau region for all specimens extended to about 35% strain without any further decrease in stress. After the plateau phase, all three specimens exhibited densification behavior.

Figure 5.10 shows the dynamic stress-strain curves for the Eco-Core specimen with  $L/D = 0.25$ . All the three specimens tested show the similar initial elastic phase, plastic plateau phase and final densification stage. The plateau stress for all specimens was approximately 20 MPa. The plateau region was observed until approximately 26% strain. All specimens showed a well defined densification region. During the SHPB experiment, the entire volume of the specimen was crushed in a single hit loading. Figure 5.11 presents the dynamic compression stress-strain behavior for Eco-Core specimen having  $L/D = 0.3$ . The stress-strain response of all three specimens exhibited a linear elastic region, a plastic plateau phase and a final densification phase, which were similar to that of specimens with  $L/D = 0.25$ . The plateau stress was around 17.5 MPa and the plateau stress region extended until approximately 26% strain. The dynamic compressive stress-strain curve for Eco-Core specimen having  $L/D = 0.5$  are shown in Figure 5.12. The dynamic stress-strain behavior of all three specimens was oscillatory in nature and showed only an elastic region and a plastic plateau region and no densification stage. The plateau stress value was approximately 18 MPa and the plateau region continues until approximately 26% strain. It was observed during the SHPB test that the specimen failed partially in a single hit loading and underwent complete crushing under repeated multiple hits. The strain rate ranged from 1,100 to 1,400/s.

Figure 5.13 shows the dynamic stress-strain curves of Eco-Core having  $L/D = 1$ . The peak strength value for all three specimens was around 25 MPa. It is evident from Figure 5.13 that the stress decayed rapidly with increasing strain. The dynamic stress-strain curve for all three specimens showed large oscillations. The plateau stress value was around 6 MPa. All specimens crushed completely under a failure strain of 14%. It was observed during the SHPB experiment that the specimen did not fail in a single hit loading and it took multiple hits to undergo complete crushing failure. The strain rate was about 800/s.

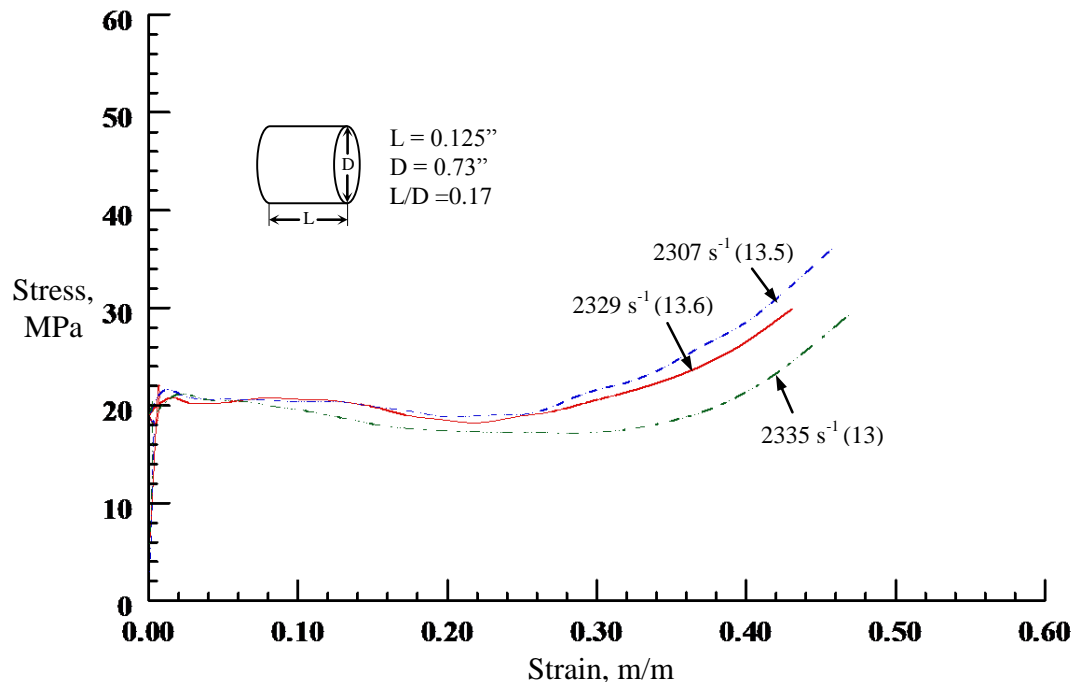


Figure 5.9. High Strain Rate Compressive Stress-Strain Response of Eco-Core Specimen with  $L/D = 0.17$

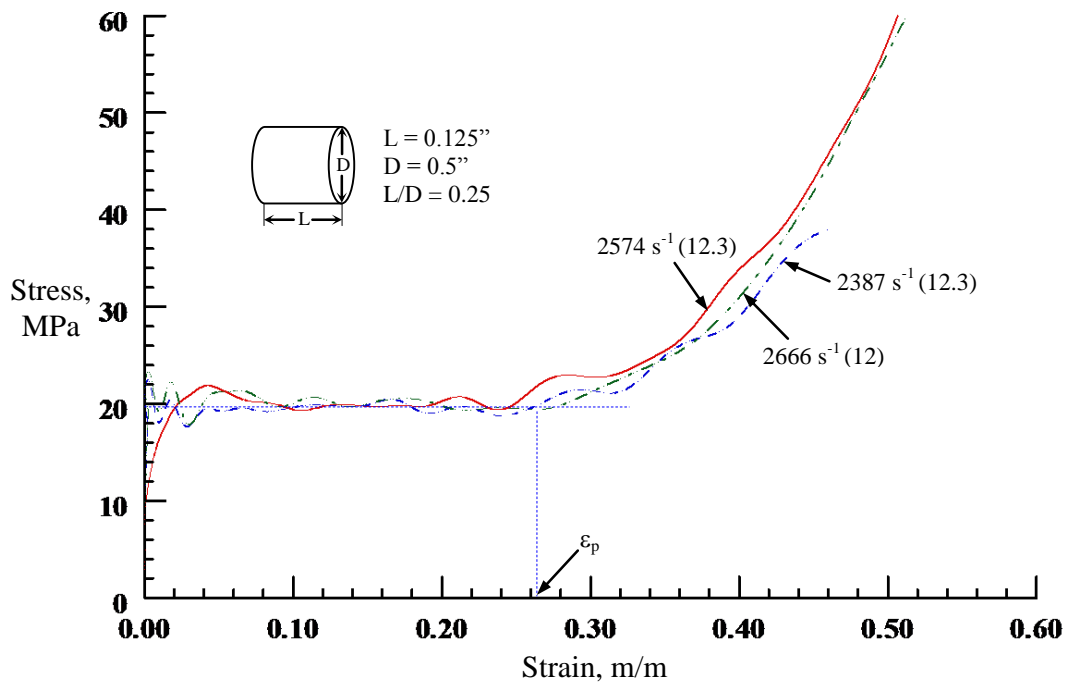
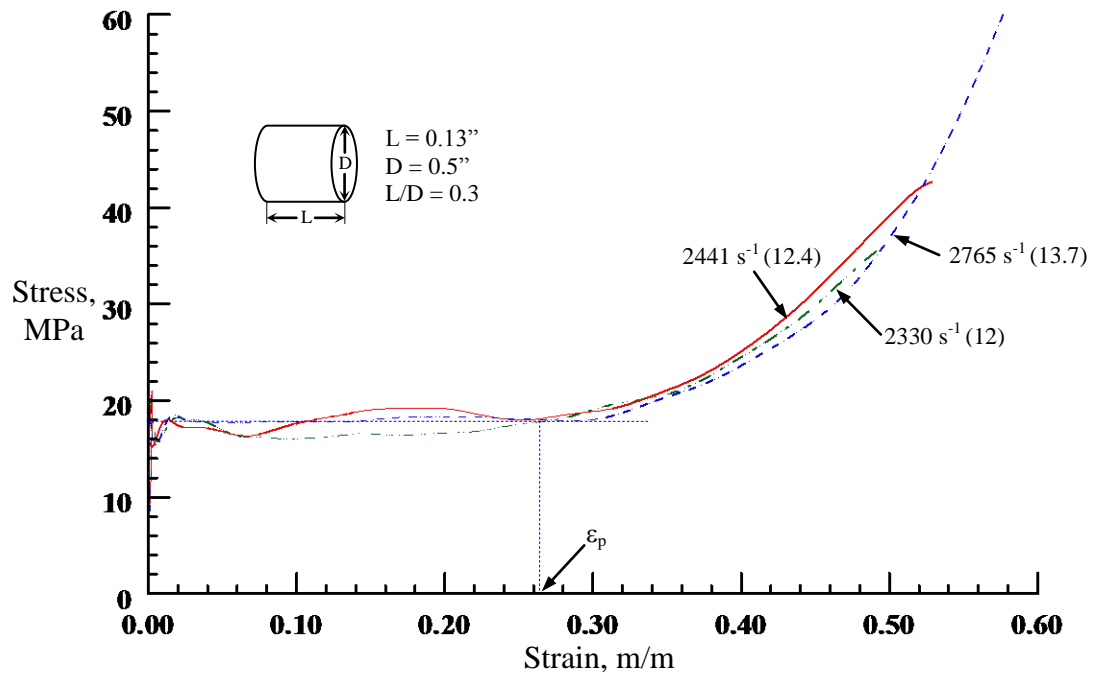
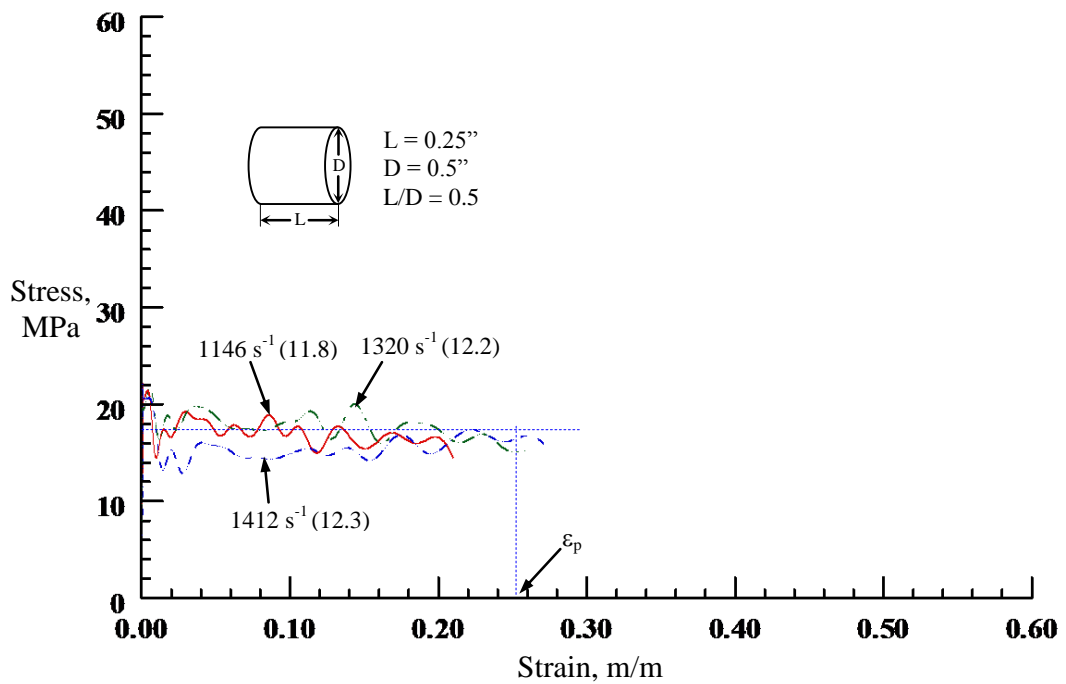


Figure 5.10. High Strain Rate Compressive Stress-Strain Response of Eco-Core Specimen with  $L/D = 0.25$



**Figure 5.11. High Strain Rate Compressive Stress-Strain Response of Eco-Core Specimen with  $L/D = 0.3$**



**Figure 5.12. High Strain Rate Compressive Stress-Strain Response of Eco-Core Specimen with  $L/D = 0.5$**

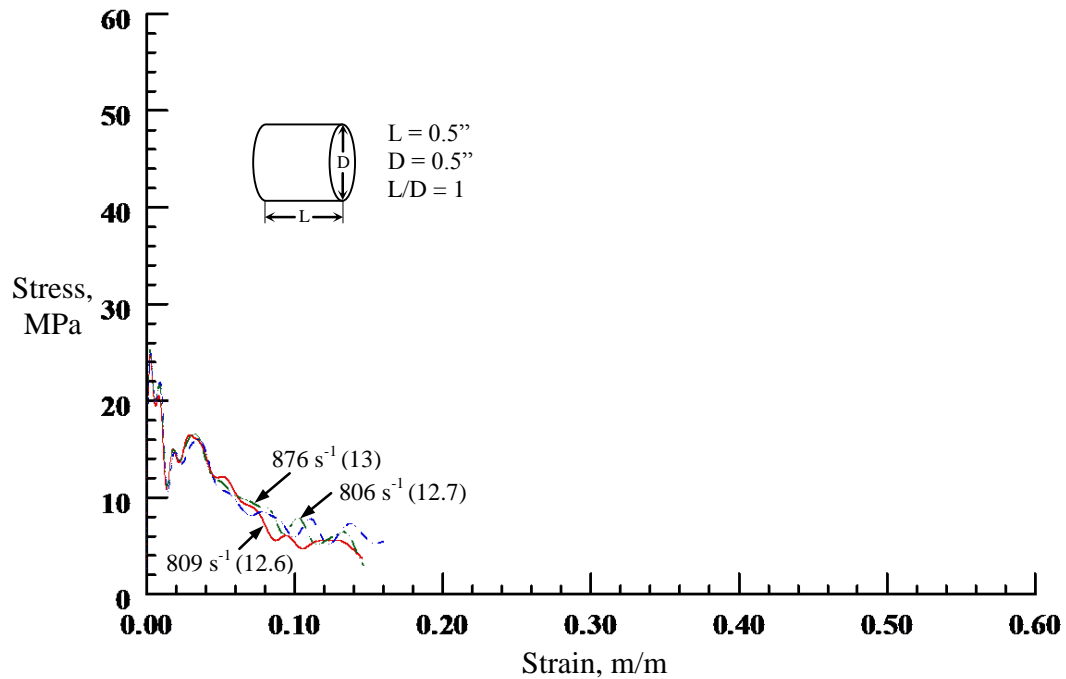


**Figure 5.13. High Strain Rate Compressive Stress-Strain Response of Eco-Core Specimen with  $L/D = 1$**

It is clear from Figures 5.9 through 5.13 that the experiment results are repeatable under same test conditions. In addition, the effects of materials inhomogeneity may be accounted through averaging the results of the experiments under the same testing conditions. The resultant stress-strain curves under the same testing conditions were averaged to account for the slight differences in the results possibly due to the materials inhomogeneity. Figure 5.14 summarizes the effect of  $L/D$  ratio on the stress-strain behavior of Eco-Core specimens. It is evident from Figure 5.14 that the Eco-Core specimens having  $L/D$  ratio  $\leq 0.3$  exhibited a clear elastic phase, a plastic plateau region and a densification region, typical to the static confined compression results of Eco-Core as explained in chapter 2 (Figure 2.18). The Eco-Core specimens with  $L/D$  ratio  $> 0.3$  exhibited oscillations in the stress-strain curves and a reduction of 10 to 15% in plateau stress values. The specimens with  $L/D = 0.17$  and  $0.25$  (having same length but different diameter) exhibited similar stress-strain behavior. The dynamic stress-strain curves with  $L/D \leq 0.3$  were smooth with minimum oscillations.

Therefore, the Eco-Core specimen configuration suitable for dynamic testing was  $L/D \leq 0.3$ , and  $L/D = 0.25$  was chosen for all other studies.

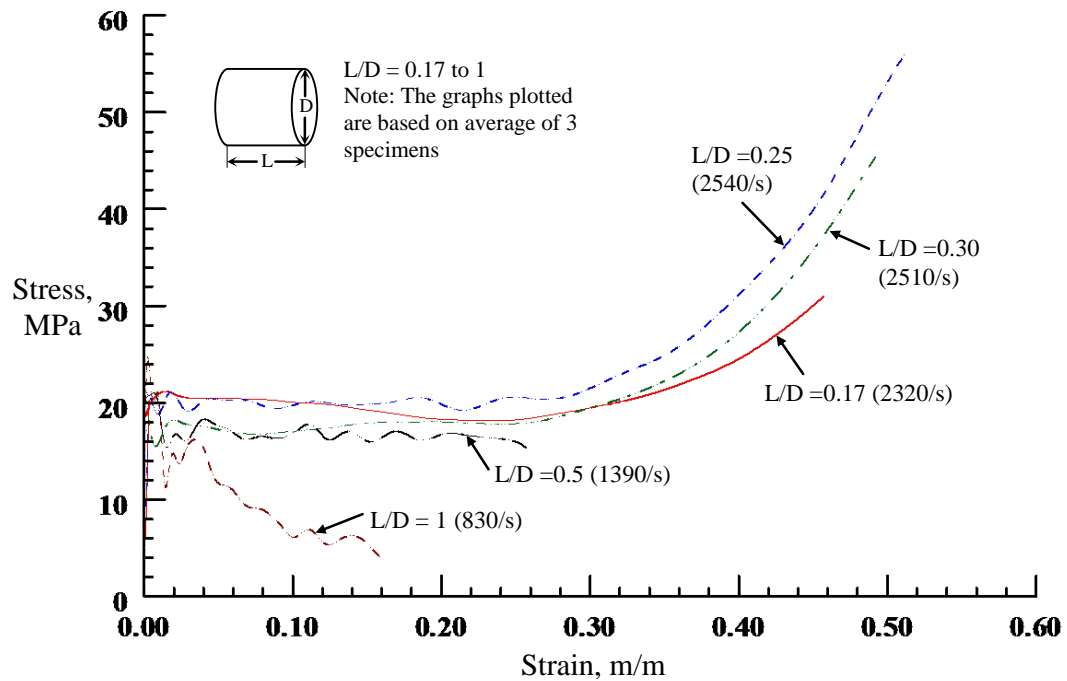


**Figure 5.14. Dynamic Compressive Stress-Strain Curves of Eco-Core Specimens with Aspect Ratio from 0.17 to 1**

#### 5.2.3.1.2 Selection of Specimen $L/D$ based on the Dynamic Force Equilibrium

Since the dynamic stress equilibrium is one of the basic assumptions in a valid SHPB experiment, it is necessary to ensure the dynamic stress equilibrium in a specimen to obtain valid results. Figures 5.15 to 5.19 present the variation of the axial forces in the incident and transmission bars with time for specimens having  $L/D$  of 0.17, 0.25, 0.3, 0.5 and 1, respectively, tested at a striker velocity of 12 – 13 m/s. The associated strain rate was approximately 2,500/s for  $L/D = 0.17$  to 0.3, ranged 1,100 – 1,400/s for  $L/D = 0.5$  and approximately 830/s for  $L/D = 1$ . The  $F_1$  corresponded to the force at the front end of the specimen calculated through the difference between the incident and reflected pulses;

whereas  $F_2$  was the force at the back (facing the transmission bar) end of the specimen, which was calculated through the transmitted pulse. The axial forces on the incident and transmission end of the specimen were given by equations (5.3) and (5.4) respectively.

$$F_1 = EA[\varepsilon_I(t) + \varepsilon_T(t)] \quad (5.3)$$

$$F_2 = EA\varepsilon_T(t) \quad (5.4)$$

Where  $E$  and  $A$  were elastic modulus and cross-section of the incident and transmission bars. From Figure 5.15 it is clear that the force histories nearly overlapped each other over almost the entire duration of the experiment, indicating that the specimen was under dynamic stress equilibrium during the whole experiment. In addition, Figure 5.16 shows that the forces  $F_1$  and  $F_2$  were equal for most of the dynamic test; thereby, satisfying the dynamic stress equilibrium. From Figure 5.17, it is observed that the force curves were quite apart indicating the two forces were not equal and the dynamic stress equilibrium was not satisfied for the specimen having  $L/D = 0.3$ . Figure 5.18 clearly shows that the forces  $F_1$  and  $F_2$  were not equal initially, but approached each other after 120  $\mu$ s. The forces were equal only for short duration of around 30  $\mu$ s. It is evident from the Figure 5.19 that the force curves did not overlap each other; thereby, they did not satisfy the dynamic stress equilibrium condition. Among various aspect ratio considered for Eco-Core specimens, only  $L/D = 0.17$  and  $0.25$  satisfied the dynamic stress equilibrium conditions. Therefore, specimen geometry with  $L/D = 0.17$  and  $0.25$  were selected for the dynamic tests. Further, the specimen having  $L/D = 0.25$  ( $L = 0.125$  and  $D = 0.5$ ) was selected against  $L/D = 0.17$  ( $L = 0.125$  and  $D = 0.73$ ) for all the dynamic tests because of the ease of its preparation and enough number of microbubbles included within the thickness to homogenize the material as isotropic.

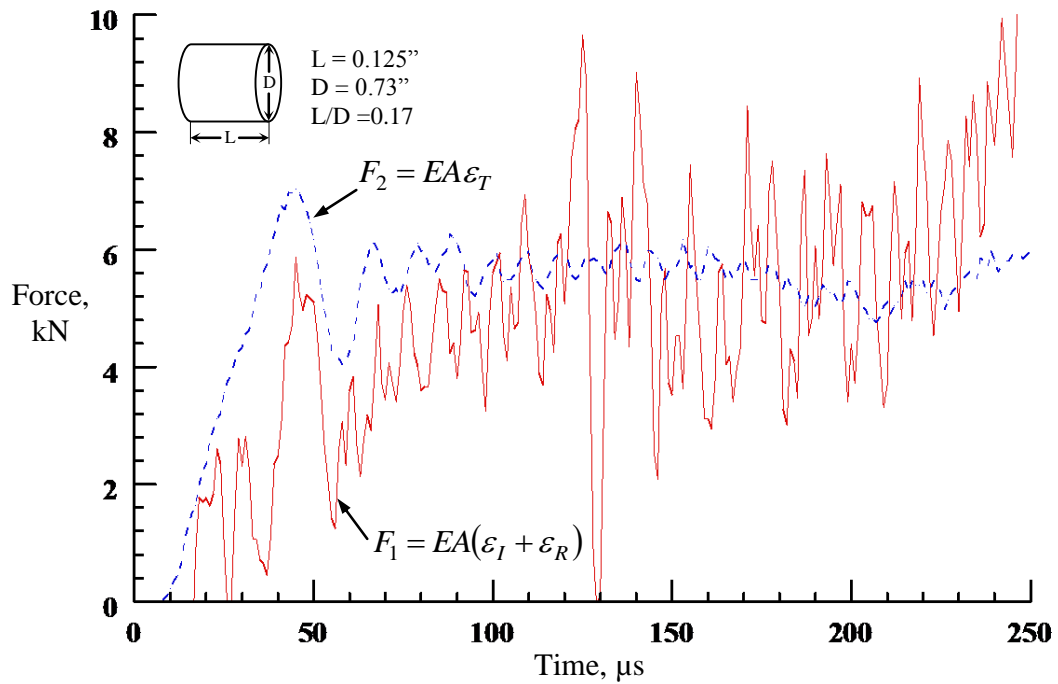


Figure 5.15. The Time History of the Force on the Incident and Transmitted Ends of Eco-Core Specimen Having  $L/D = 0.17$

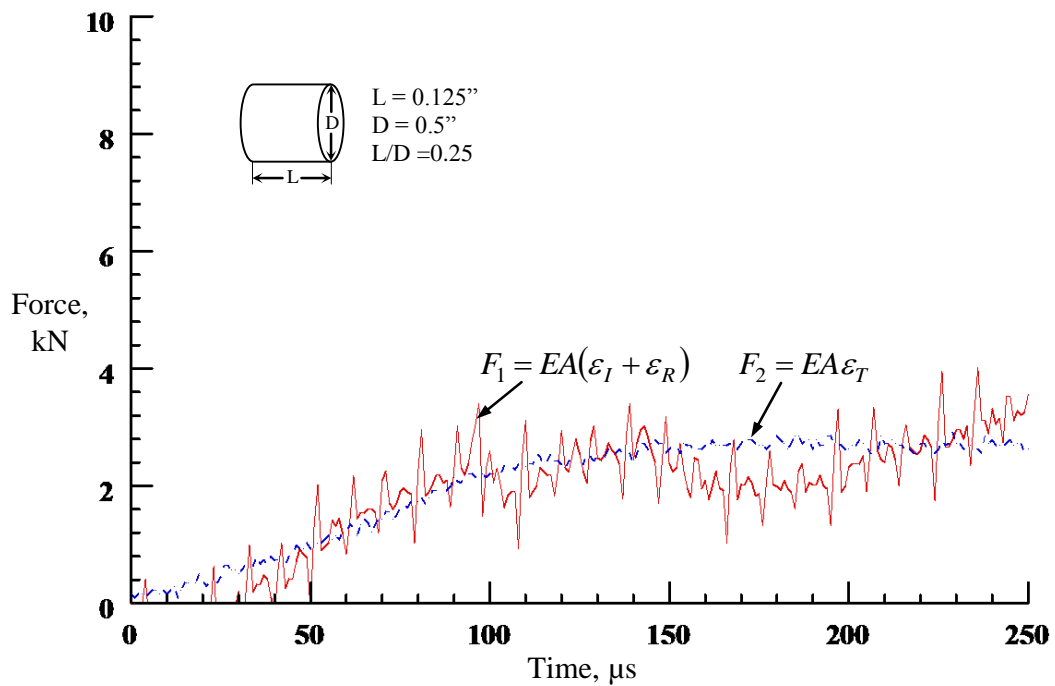


Figure 5.16. Time History of the Force on the Incident and Transmitted Ends of Eco-Core Specimen Having  $L/D = 0.25$

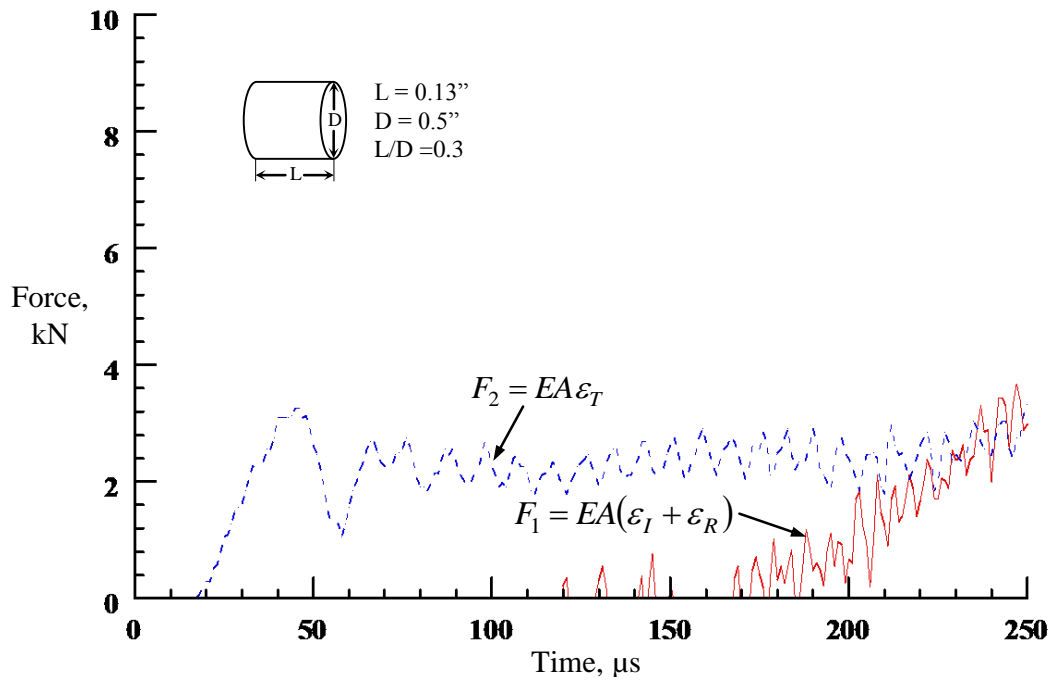


Figure 5.17. Time History of the Force on the Incident and Transmitted Ends of Eco-Core Specimen Having  $L/D = 0.3$

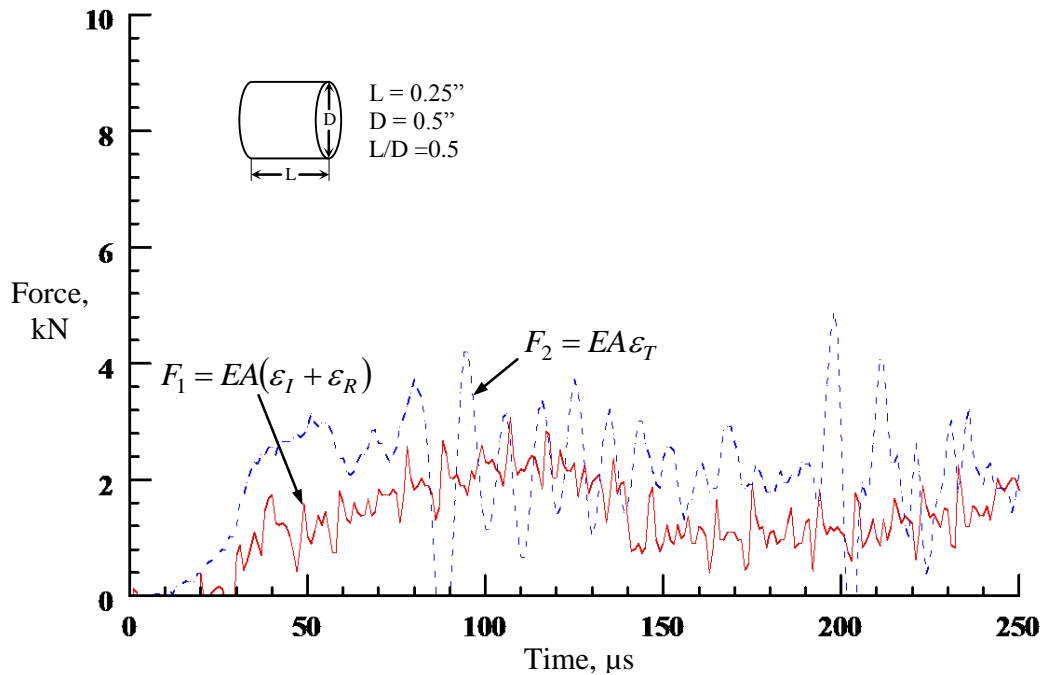
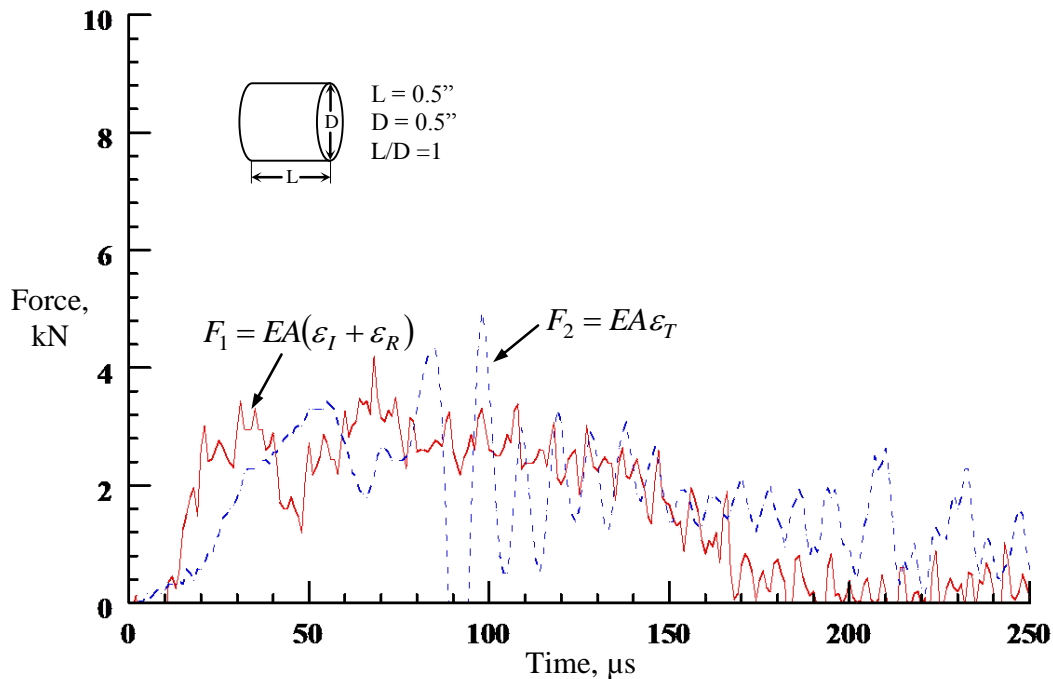


Figure 5.18. Time History of the Force on the Incident and Transmitted Ends of Eco-Core Specimen Having  $L/D = 0.5$



**Figure 5.19. Time History of the Force on the Incident and Transmitted Ends of Eco-Core Specimen Having  $L/D = 1$**

### 5.2.3.2 Effect of Strain Rate

The high strain rate behavior of the baseline Eco-Core was measured using the SHPB apparatus at strain rates in the range of 1,000/s to 3,100/s. Three experiments were conducted at each strain rate level to account for variations in specimen density and microstructure. Figure 5.20 illustrates the dynamic compressive stress-strain response of Eco-Core at strain rates of approximately 1,000/s. The stress-strain curves are plotted in measures of engineering stress and engineering strain. All the dynamic compressive stress-strain curves show very similar response and are nearly identical; therefore, the results were repeatable. There existed a nearly linear elastic region where the axial strain was less than 0.5%. After 0.5% axial strain, the curves showed little oscillations until approximately 4% strain. Then the stress remained nearly constant with increasing strain until the strain reached 18%. The peak dynamic compression strength was around 24 MPa and the dynamic plateau (cell collapse stress) stress was around 20 MPa.

Figure 5.21 presents the dynamic compressive stress-strain response of Eco-Core at strain rates over the range of 1,400/s to 2,200/s. Dynamic compressive experiments on the Eco-Core showed constitutive behaviors very similar to the stress-strain curves in Figure 5.21, except for the strain levels. The peak dynamic compression strength was around 22 MPa and the cell collapse stress was approximately 20 MPa. Figure 5.21 reveals a linear elastic portion till about 0.5% strain and then the curves gradually enter a nearly flat region after the strain reaches a value of 4%. The flat region extends to a strain of 28%, where a densification stage appears to begin. All the stress–strain curves nearly overlapped each other regardless of strain rates.

Figure 5.22 summarizes the dynamic compressive stress-strain curves for the Eco-Core at strain rates near 2,500/s. The strain rate range was from 2,387/s to 2,666/s. Figure 5.22 again shows similar stress-strain curves except for the densification stage. The peak dynamic compression strength was around 23 MPa and the cell collapse stress was around 20 MPa. There existed a nearly linear elastic region within the axial strain less than 0.5%. After 0.5% axial strain, the curves showed little oscillations till about 4% strain. Then, the curves gradually entered a nearly flat region, until the densification stage began at a strain of 38%. Furthermore, all the dynamic stress-strain curves also nearly overlapped each other until the strain exceeded 26%, when the Eco-Core was considerably compacted. The stress-strain curves exhibited densification behavior when the strain exceeded 38%. When the strain rate was below 2,500/s, this densification region was absent as shown in Figures 5.20 and 5.21 because the Eco-Core specimens deformed only slightly beyond 20% of strain. During the SHPB experiments at lower strain rates, the striking velocity of the striker bar was lowered to achieve a lower strain rate in the specimen, resulting in a smaller input energy to deform the specimen and, consequently, a smaller strain. Unlike the overlapping linear elastic and the cell-wall collapse region in the dynamic stress–strain curves, the densification behavior was less consistent. When the densification occurs, the constitutive behavior of the Eco-Core specimen is closer to that of the solid cenospheres.

Figure 5.23 presents the dynamic compressive stress-strain response of the Eco-Core at a strain rate near 3,100/s. The strain rate range was from 3,002/s to 3,150/s. Figure 5.23 again shows similar stress-strain curves as that of the Eco-Core specimens tested at strain rate 2,000/s but with a prominent densification stage. All the dynamic compressive stress-strain curves showed very similar characteristics. The peak dynamic compression strength was around 21 MPa and the cell collapse stress was around 20 MPa. After the peak stress, the curve passed through a short unstable range where the stress showed some oscillations with increasing strain until the strain reached a value of 4%. Then the stress remained nearly constant with an increasing strain until the strain reached 26%, where the slope of the stress-strain curve became positive. The stress-strain curve then rose monotonically until unloading. The nominal crushing strain of Eco-Core was about 44%. The dynamic compressive stress-strain curves shown in Figure 5.23 are very similar to typical curves obtained under quasi-static loading conditions (Figure 2.18 in chapter 2), where the initial linear stress-strain response was considered to be the elastic response. The plateau on a compressive stress-strain curve was associated with breakage of cell walls followed by crushing of cells, and further strain compresses the solid cenospheres itself, resulting in a rapid rising in the stress-strain curve. The dynamic experiments were conducted under carefully controlled conditions where the specimens were at the dynamic stress equilibrium. The strain rate was also controlled to be as constant as necessary, so that the inertia effects associated with axial compression could be neglected.

Figure 5.24 summarizes the dynamic compressive stress-strain curves at strain rates from 1,000 to 3,100/s for Eco-Core. The stress-strain curves presented in Figure 5.24 are average curves of the repeatable data at each strain rate. Within the dynamic strain rate range achieved in SHPB experiments (1,000 – 3,100/s), all the dynamic compressive stress-strain curves nearly passed the same peak point (0.5% strain and 22 MPa stress) and showed a compressive failure stress of about 20 MPa. Furthermore, all the dynamic stress-strain curves also nearly overlapped each other until the strain exceeded 26%, when the Eco-Core was compacted considerably. This situation indicated

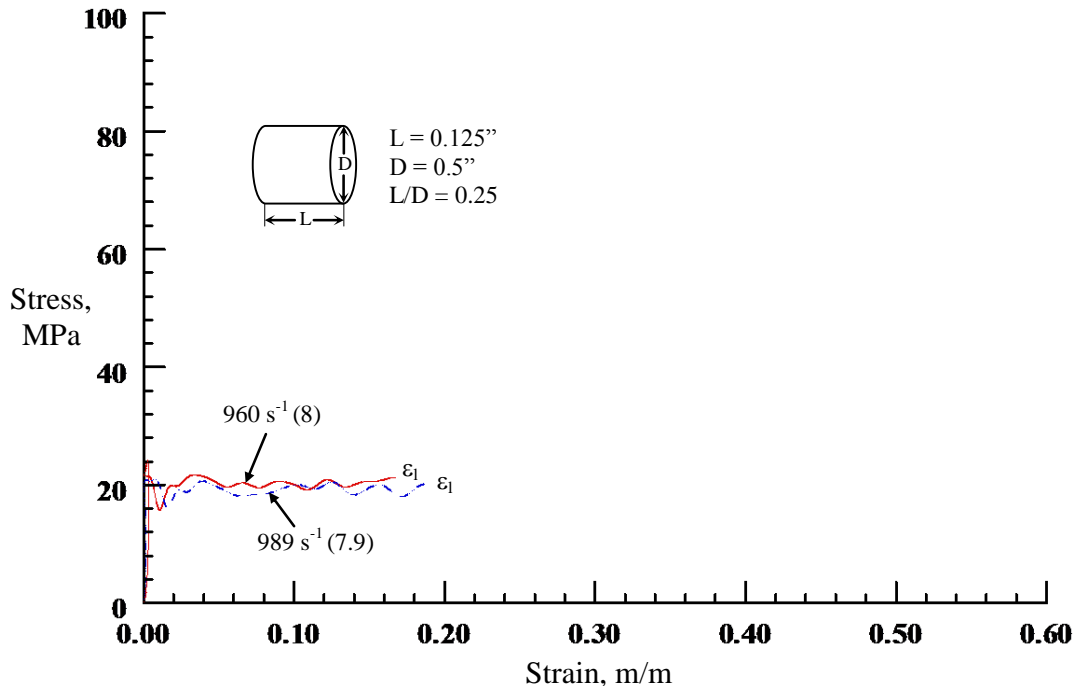


Figure 5.20. Dynamic Compressive Stress-Strain Curves for Eco-Core at a Strain Rate  $\sim 1,000/s$

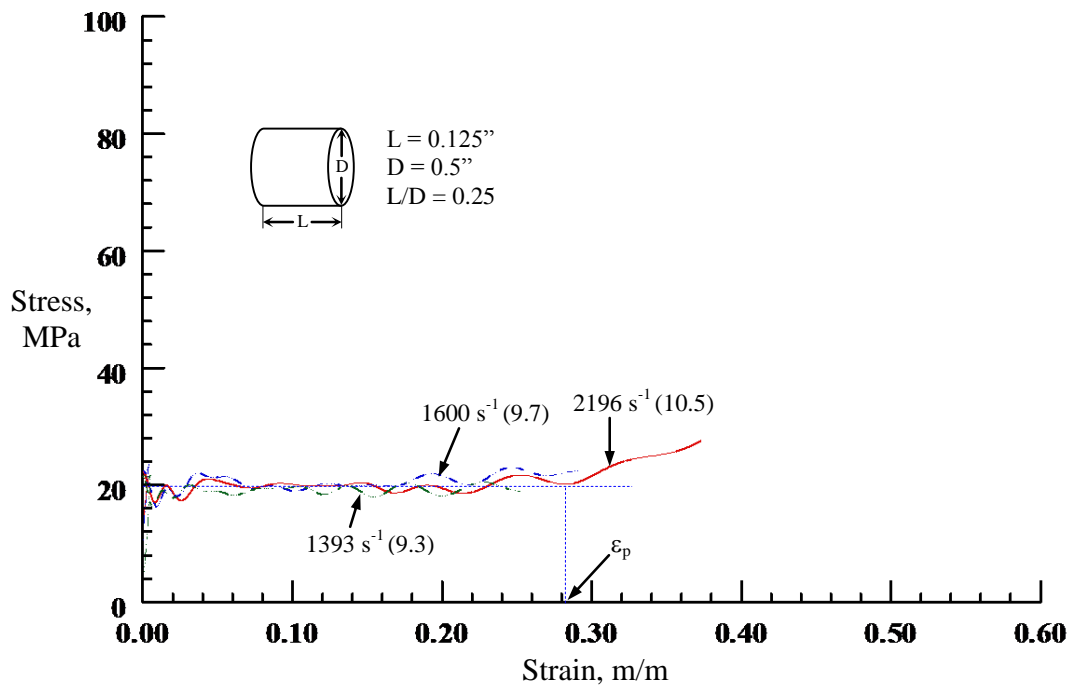


Figure 5.21. Dynamic Compressive Stress-Strain Curves for Eco-Core at a Strain Rate  $\sim 1,700/s$

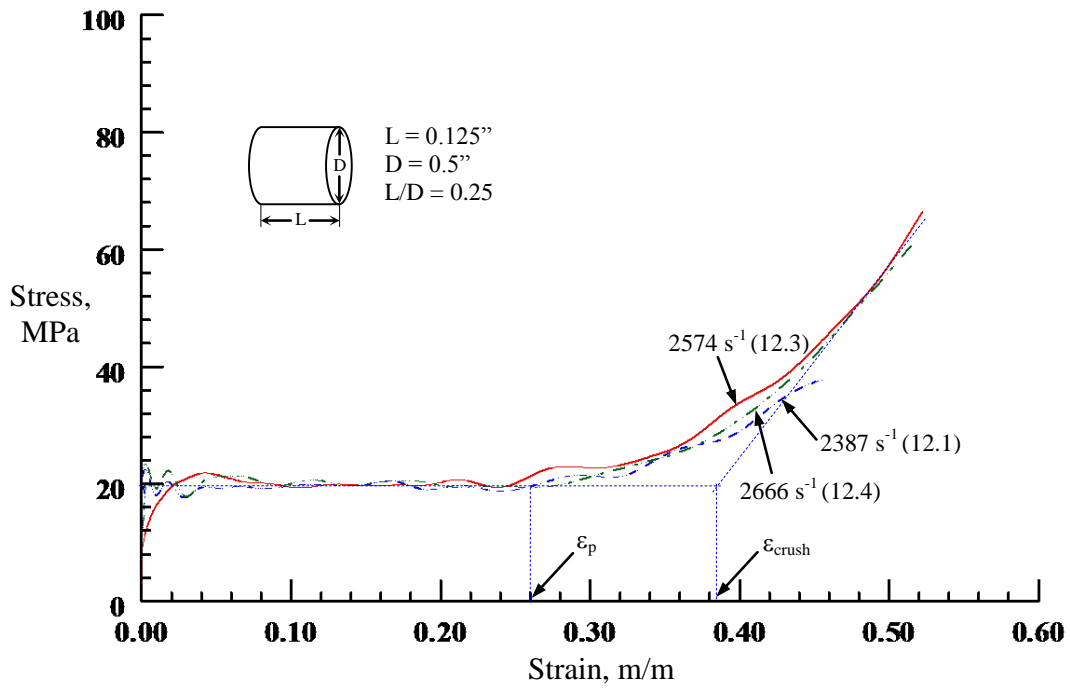


Figure 5.22. Dynamic Compressive Stress-Strain Curves for Eco-Core at a Strain Rate  $\sim 2,500/s$

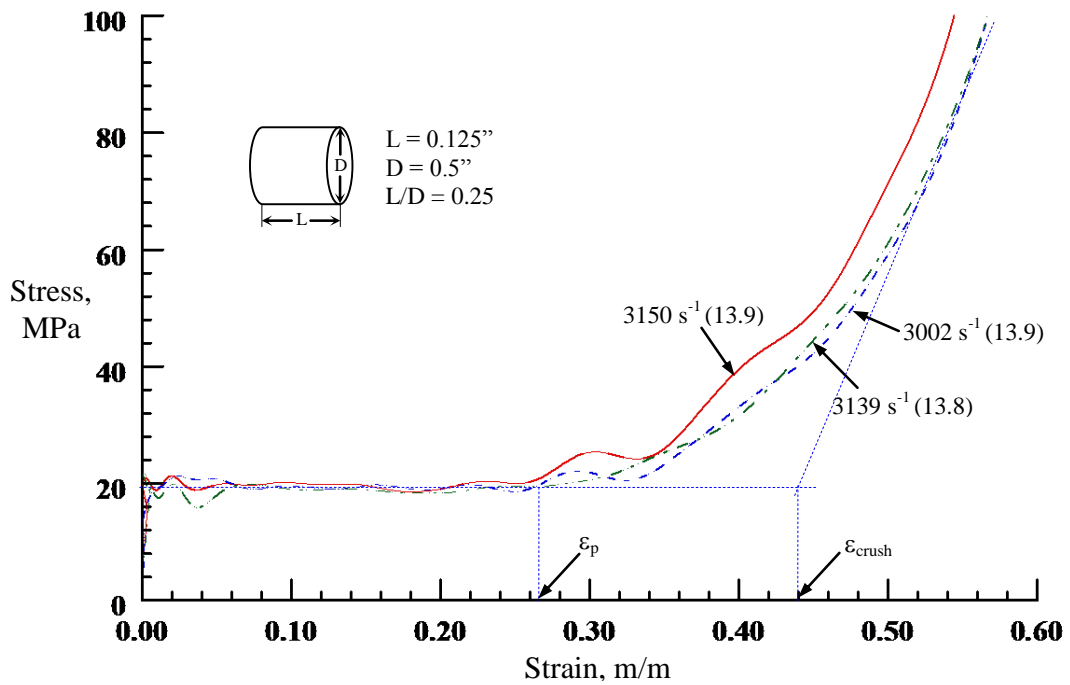
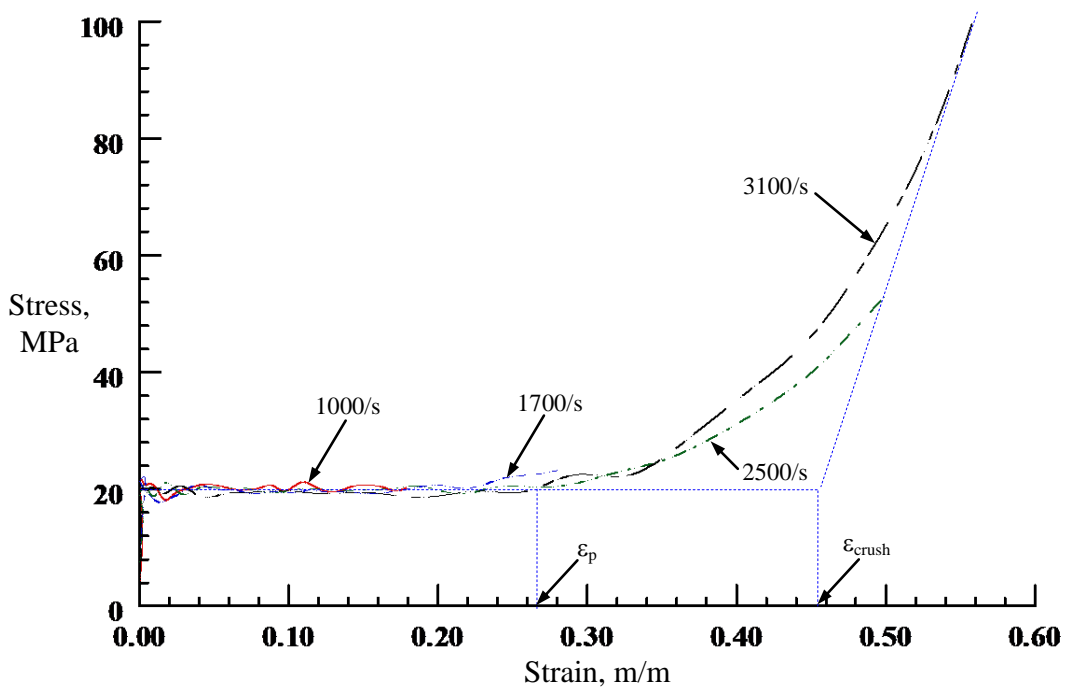


Figure 5.23. Dynamic Compressive Stress-Strain Curves for Eco-Core at a Strain Rate  $\sim 3,100/s$

that the dynamic compressive response of the Eco-Core at this density was *not sensitive to strain rates* in the dynamic strain rate range studied. In general, at strain rates below 2,500/s, Eco-Core exhibited an initial elastic regime followed by a flat cell collapse phase whereas at strain rates above 2,500/s, the Eco-Core exhibited densification as an additional mode of failure. The plateau region extended to a strain of 26%, where densification initiated. The Eco-Core specimen tested at a strain rate near 3,100/s had a nominal crushing strain of approximately 46%.



**Figure 5.24. Dynamic Compressive Stress-Strain Curves for Eco-Core at Strain Rates from 1,000/s to 3,100/s**

The strain rate and strain limit data for Eco-Core specimens tested at various strain rates were listed in Table 5.4. For samples tested at strain rates below 1,700/s, the strain limit,  $\epsilon_l$ , is the as failure strain of the specimen as shown in the Figure 5.20. Whereas for samples tested at strain rates above 1,700/s, the strain limit was taken as  $\epsilon_{crush}$  (see for example figure

5.22). The average strain limits were 0.21, 0.31, 0.40, and 0.48 for strain rates of 975, 1730, 2542, and 3097/s, respectively.

**Table 5.4. Strain Rate and Strain Limit Data from Eco-Core SHPB Tests**

Specimen #	Density, g/cc	Strain rate ( $\dot{\epsilon}$ ), s <sup>-1</sup>	Strain limit ( $\epsilon_l$ ), m/m
ECB-1	0.553	---	---
ECB-2	0.547	960	0.17
ECB-3	0.548	989	0.19
Average (CV %)	0.549 (0.7)	975 (2.1)	0.21 (29.9)
ECB-4	0.542	2,196	0.37
ECB-5	0.559	1,600	0.29
ECB-6	0.545	1,393	0.25
Average (CV %)	0.549 (1.6)	1730 (24.1)	0.31 (20.2)
ECB-7	0.549	2,574	0.41
ECB-8	0.548	2,387	0.40
ECB-9	0.546	2,666	0.38
Average (CV %)	0.547 (0.3)	2542 (5.6)	0.40 (3.7)
ECB-10	0.560	3,150	0.47
ECB-11	0.541	3,002	0.48
ECB-12	0.555	3,139	0.49
Average (CV %)	0.552 (1.7)	3097 (2.7)	0.48 (2.4)

### 5.2.3.3 Development of phenomenological constitutive material model

A constitutive model was required to summarize the effect of strain rate upon the measured constitutive response. It was desirable to summarize the experimental results in the form of a simple material response model that could be used in numerical simulations of structural impact/shock responses and other design applications. To serve this purpose, the model had to be simple in its form with few constants to be determined. The constitutive model for Eco-Core or similar syntactic foam materials with strain-rate was not available in the literature due to the scarcity of reliable experimental data, especially from dynamic experiments. However, the strain-rate dependent constitutive models for metals [83], alloys [84], and composites [85-88] had recently been developed and studied.

The goal of this study was to develop a phenomenological material model to describe the strain rate effects on the compressive stress-strain behavior of Eco-Core. From a strict sense of material constitutive modeling, a phenomenological model could not be very accurate in describing the experimental conditions and results because of complicated mechanisms of deformation and failure. A deformation mechanism based material model inevitably becomes very complicated, creating difficulties in the application of the experimental results in practice. Furthermore, the deformation mechanisms at the microbubble cell level were not considered in the modeling of stress-strain response of the specimen.

The most complex rate dependant models defined the yield stress as a function strain, strain rate, and temperature. These models are usually classified as empirical or physically based, depending on their basic assumptions. Today, the tendency is to develop more physically based models that will enable application of the model to a broader range of strains, opposite the restriction to a specific strain range when using the less physically sound models. There are many constitutive equations that have been proposed by different investigators. Among them the most widely used models for metals is the Johnson-Cook (JC) material model [89].

The Johnson-Cook constitutive model is a phenomenological model, (i.e. it is not based on traditional plasticity theory that reproduces several important material responses observed in impact and penetration of metals). The three key material responses are strain hardening, strain rate effects and thermal softening. These three effects are expressed in a simple separation of variable form as follows:

$$\sigma = \left[ A + B(\varepsilon)^n \right] \left[ 1 + C \ln(\dot{\varepsilon}^*) \right] \left[ 1 - (T^*)^m \right] \quad (5.5)$$

Here A, B, C, n and m are material constants, which are experimentally determined. The expression in the first set of brackets gives the static response that is similar to Ramberg-Osgood equation for metals. The second and third part are strain rate and temperature effect parameters.

The term  $T^*$ , homologous temperature, is the ratio of the current temperature  $T$  to the melting temperature  $T_m$ :

$$T^* = \frac{T - T_r}{T_m - T_r} \quad (5.6)$$

where  $T_r$  is the reference temperature at which yield stress,  $\sigma_0$  is measured.

The dimensionless strain rate  $\dot{\varepsilon}^*$  is given as

$$\dot{\varepsilon}^* = \frac{\dot{\varepsilon}}{\dot{\varepsilon}_0} \quad (5.7)$$

where  $\dot{\varepsilon}$  is the effective plastic strain rate,  $\dot{\varepsilon}_0$  is the reference strain rate, which can be made equal to 1 ( $\dot{\varepsilon}_0 = 1.0 \text{ s}^{-1}$ ).

One of the problems with this constitutive equation is that strain rate and temperature effects on the flow stress are uncoupled. This implies that the strain rate sensitivity is independent of temperature, which has not been generally observed for most metals. Because the empirical constitutive equations are basically a curve-fitting procedure, they are easy to calibrate with a minimum of experimental data in the form of a few stress-strain curves at several strain rates and temperatures.

For tests conducted at ambient temperature, where the material temperature is not altered much, one can drop the temperature effect. Furthermore, as explained by the experimental data trend Eco-Core is not a strain rate dependent material. Therefore, the JC equation for Eco-Core reduces to:

$$\sigma = \left[ A + B(\varepsilon)^n \right] \quad (5.8)$$

Alternatively, the stress-strain relationship for the Eco-Core material can be defined by a well known parabolic hardening rule, which is:

$$\frac{\sigma}{\sigma_c} = 1 + k\varepsilon^n \quad (5.9)$$

where  $\sigma_c$  = static compression strength of Eco-Core ( $\sigma_c = 20$  MPa), parameters  $k$ , and  $n$  are constant for a given initial density and strain rate, and parameter  $k$  has units of stress. This function is continuously differentiable. The parameters  $k$  and  $n$  capture rapid densification behavior and control onset and rate of densification. The variation of  $n$  implies stretching or shrinking of the curve on the strain axis without altering the origin of the plot. The proposed equation (5.9) describes a plastic like plateau regime and a rapid densification phase of the Eco-Core except for the initial linear elastic regime. In order to describe the initial linear elastic region, the modulus of elasticity ( $E$ ) obtained from the quasi-static test results of the Eco-Core was used. Therefore, the generalized function given in equation (5.9) could be used to describe the whole family of stress-strain characteristics of Eco-Core, i.e., stretching/shrinking (strain due to cell collapse or crushing) and subsequent accumulation of large strain, and rapid densification where the stress rises sharply.

The equation (5.9) was fit to the experimental data as shown in Figure 5.24 and it was found that  $k = 90$  MPa and  $n = 5.43$ . The sensitivity of the constants  $k$  and  $n$  were performed for a range of values of  $k$  and  $n$ . Figure 5.25 compares results for  $k = 89, 90$  and  $91$ . Within a 1 % change in  $k$ , there was very little change in the results. Figure 5.26 illustrates the influence of index  $n$  over a range of 5.4 to 5.5. The index  $n$  varied from 5.4 to 5.5. The variation of  $n$  implied mild stretching or shrinking of the curve on the strain axis, without altering the origin of the plot. As the value of  $n$  increased the curve tended to marginally stretch outwards to the right side on the strain axis.

Figure 5.27 compares the equation with  $k = 90$  and  $n = 5.4$  with the experimental data for strain rate range of 1,000 to 3,000/s. The equation agreed very well with experimental data for all strain rates. Therefore, the failure model for Eco-Core is:

$$\frac{\sigma}{\sigma_c} = 1 + 90\varepsilon^{5.4} \quad (5.10)$$

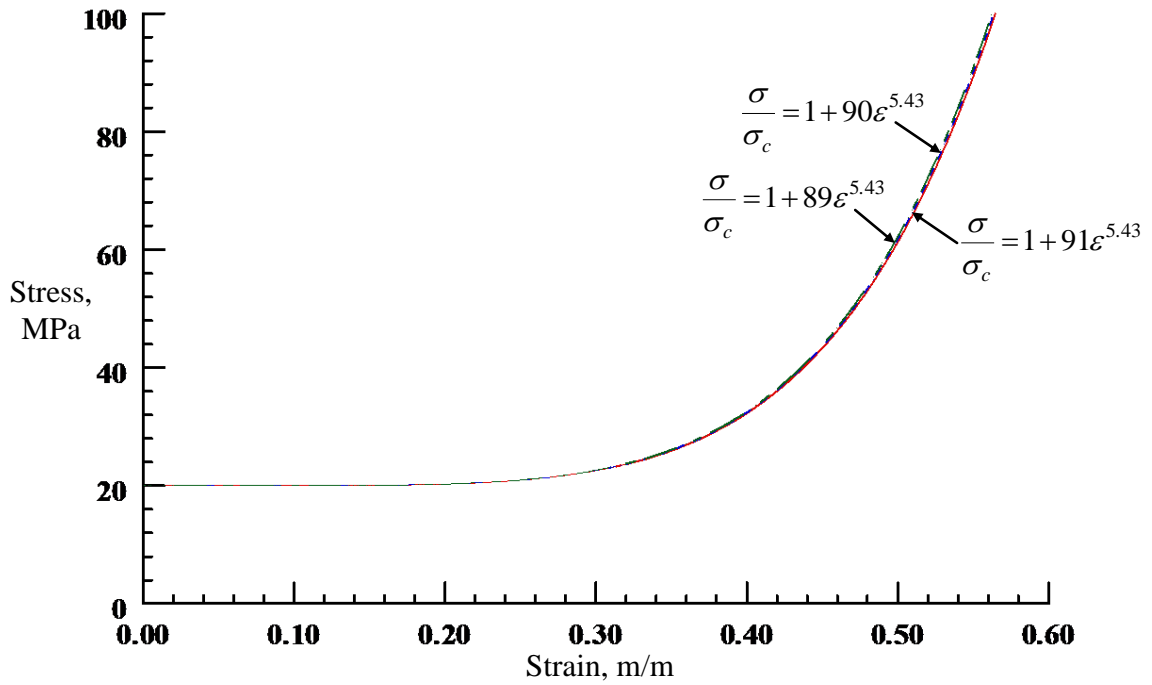


Figure 5.25. Illustration of the Influence of Model Parameter  $k$

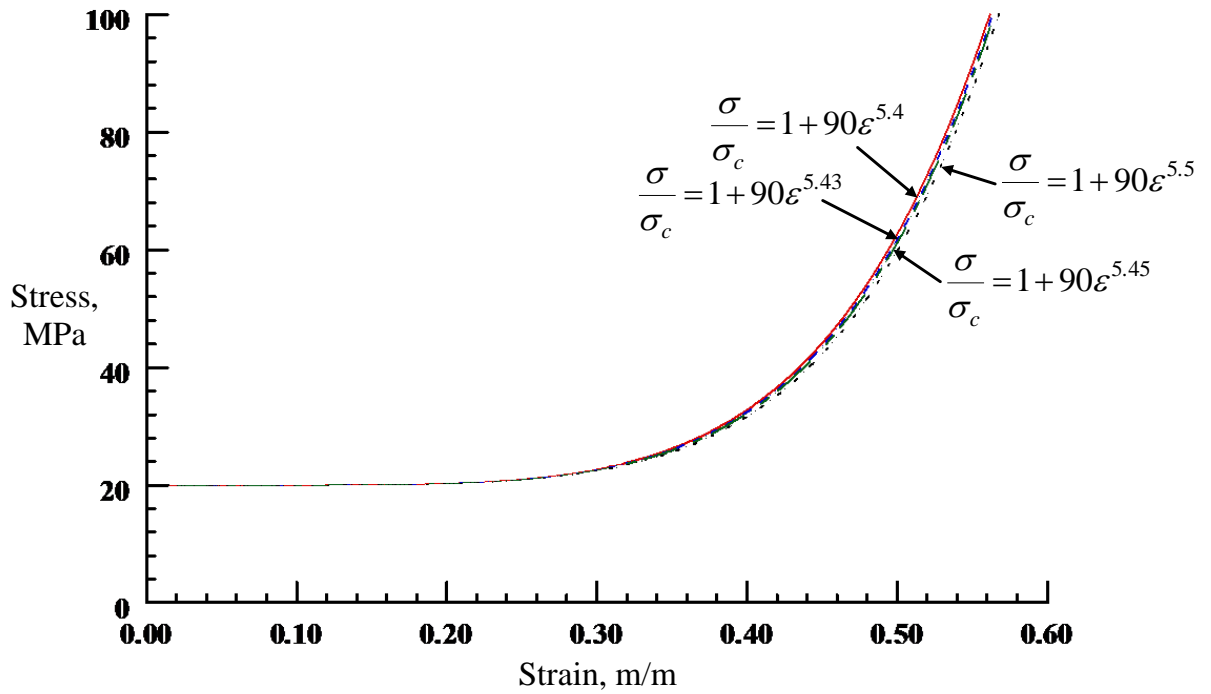


Figure 5.26. Illustration of the Influence of Model Parameter  $n$

The material model is valid for 16% and 28% strains for strain rates of 1,000 and 1,700/s respectively, and >50% strains for strain rates > 2,500/s.

The material model for Eco-Core under quasi static confined compression (equation (2.6) in chapter 2) is:

$$\frac{\sigma}{\sigma_c} = 1 + 45\varepsilon^{5.4}$$

The comparison of equations (5.10) and (2.6) revealed that the value of model parameter  $k$  for a dynamic model was twice that of the  $k$  value of the quasi-static model. Therefore, the dynamic characteristics of Eco-Core can easily be obtained from the quasi static test results without having to conduct the SHPB test for Eco-Core at a high strain rate.

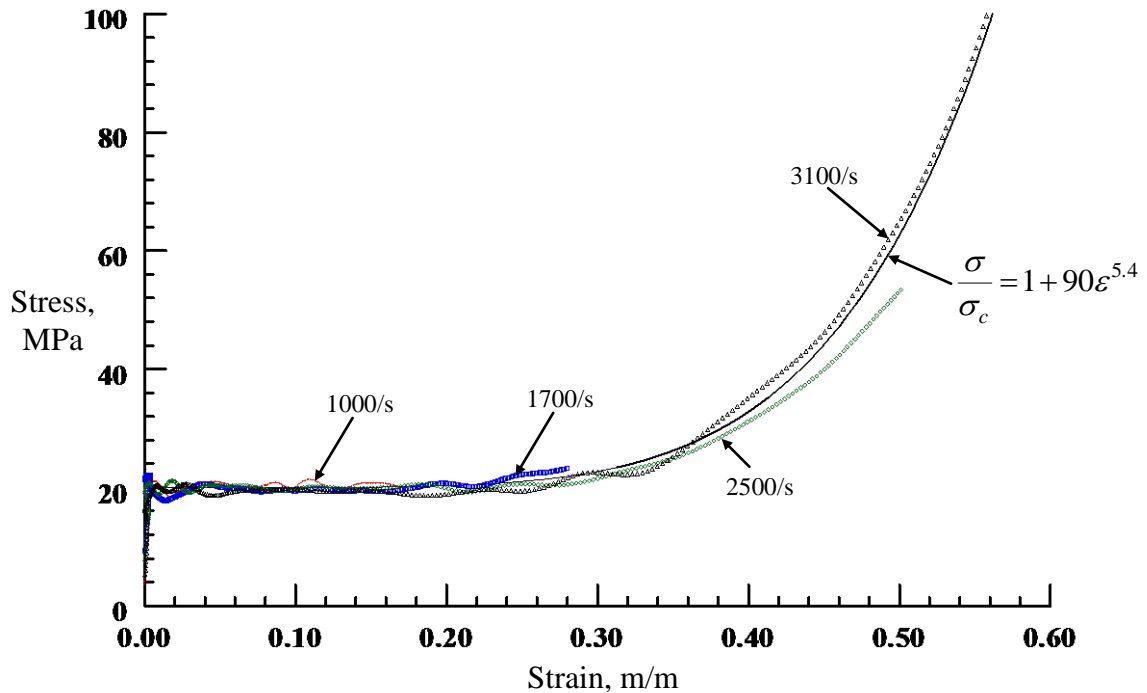


**Figure 5.27. Comparison of Dynamic Stress-Strain Curves of Eco-Core from Experiments and from Model Description over Strain Rate 1,000/s–3,100/s**

#### 5.2.3.4 Energy Absorption

The cellular structure of the Eco-Core enabled them to undergo large deformations in compression, there by absorbing considerable amounts of energy [90]. Energy absorption in Eco-Core was due to various sources such as cenosphere cell fracture, cell collapse and crushing. Additionally, friction in relative and rotational movements of the broken pieces of cenospheres during deformation process consumes energy. The energy absorption was calculated from two methods. The approximate (Eq. 5.2) method and the other was the area method, which is the area under the stress-strain curve. The simple method is an approximation where as the area method is more accurate. For Eco-Core samples the energy absorption can be predicted by the integrating the equation 5.10 between the required strain limits.

An energy absorption density defined by equation (5.2) is referred as an *approximate method*, and it was used for comparison of different materials. The first part was the elastic part and the second part was the crushing energy. Elastic part of the strain energy is small and it is ignored. Only crushing part of the energy is important and the critical parameters were compression strength ( $\sigma_c$ ) and crushing strain ( $\epsilon_{crush}$ ). When all the foam cell walls are collapsed, modulus of the solid material is  $E_{solid}$  and  $E_{solid}$  has no role in the energy absorption. The compression strength ( $\sigma_c$ ) is taken as the stress at the onset of plateau region in the stress-strain curve. The  $\epsilon_{crush}$  depends on the void fraction of the foam while  $\sigma_c$  depends on the properties of the binder that encapsulates the microscopic voids and microbubbles.

Compression strength ( $\sigma_c$ ) and crushing strain ( $\epsilon_{crush}$ ) were measured for all Eco-Core samples and are listed in Table 5.5. Eco-Core samples did not showed a densification region at strain rates below 2500/s, hence, for these materials area under the stress-strain curve till fracture was measured. Table 5.5 summarizes the energy absorption density values for Eco-Core.

The area under the stress-strain curve up to a given value of strain is the total mechanical energy per unit volume consumed by the material in straining it to that value. This can be expressed by the equation

$$U_0 = \int_0^{\varepsilon} \sigma(\varepsilon) d\varepsilon \quad (5.11)$$

where  $\sigma(\varepsilon)$  denotes uniaxial stress as a function of strain and  $\varepsilon$  is the axial strain. In the absence of molecular slip and other mechanisms for energy dissipation, this mechanical energy is stored within the material as strain energy  $U_0$ .

The Eq. (5.11) can be integrated numerically or using the stress-strain data generated till the failure or  $\varepsilon_{crush}$ , whichever is the largest. These results were referred as the *area method* and these results are listed in Table 5.5. Alternatively, the Eq. (5.11) can be integrated using the  $\sigma(\varepsilon)$  expression developed in Eq. (5.10), this method is termed the *integral method*. The energy absorption density equation is given by

$$\sigma(\varepsilon) = \sigma_c \left(1 + k\varepsilon_l^n\right)$$

$$U_0 = \sigma_c \varepsilon_l \left(1 + \frac{k\varepsilon_l^n}{n+1}\right) \quad (5.12)$$

where  $k = 90$  and  $n = 5.4$ . For the strain limits, the guidelines used in the area method is used.

From the Table 5.5 it is observed that the energy absorption density calculated from integral method (Eq. 5.12) was in very good agreement (within 4%) with that of energy absorption density calculated from the area method. At strain rates  $\leq 2,500/s$ , the energy absorption density values calculated from the approximate and the area method were very close to each other (within 5%). Whereas, at strain rates near 3,100/s, the energy absorption density calculated from the area method was 26% higher than the energy absorption density calculated from the approximate method. This was due to the reason that the approximate method ignores the part of the area above the  $\sigma_c = \text{constant}$  line near the transition region.

**Table 5.5. Energy Absorption Density of Baseline Eco-Core at Various Strain Rates**

Strain rate	Specime n #	Density, g/cc	Strength, $\sigma_c$ , MPa	Strain limit, $\epsilon_i$ , m/m	Energy Absorption Density, MPa		
					Approximate Mehod (Eq. 5.2)	Area Method	Integral Method (Eq. 5.12)
	ECB-1	0.553	---	---	---	---	---
~1000	ECB-2	0.547	19.9	0.17	3.3	3.3	3.4
	ECB-3	0.548	19.3	0.19	3.6	3.6	3.8
	Average (CV%)	0.549 (0.7)	20.2 (5.6)	0.21 (29.9)	3.5 (6.1)	3.5 (5.6)	3.6 (8.1)
	ECB-4	0.542	19.9	0.37	7.40	7.7	8.0
~1700	ECB-5	0.559	20.2	0.29	5.9	6.0	5.9
	ECB-6	0.545	19.3	0.25	4.87	4.8	5.1
	Average (CV%)	0.549 (1.6)	19.8 (2.3)	0.31 (20.2)	6.1 (21.1)	6.2 (24.3)	6.3 (23.5)
	ECB-7	0.549	19.9	0.41	8.2	9.0	9.1
~2500	ECB-8	0.548	19.9	0.40	7.9	8.3	8.7
	ECB-9	0.546	20.6	0.38	7.8	8.0	8.2
	Average (CV%)	0.547 (0.3)	20.1 (1.9)	0.40 (3.7)	8.0 (2.3)	8.4 (6.6)	8.7 (5.4)
	ECB-10	0.560	19.9	0.47	9.31	12.2	11.5
~3100	ECB-11	0.541	19.7	0.48	9.5	11.6	12.2
	ECB-12	0.555	19.8	0.49	9.7	12.1	12.8
	Average (CV%)	0.552 (1.7)	19.8 (0.5)	0.48 (2.4)	9.5 (2.1)	12 (2.4)	12.2 (5.1)

Figure 5.28 shows the energy absorbed by Eco-Core as a function of strain rate. With increase in the strain rate, the energy absorption density was found to be increasing linearly. This is because crushing strain increases with strain rate, hence the energy absorption density. Both the area and the integral method agreed very well (within 4%), this also indicated that the  $\sigma$ - $\epsilon$  equation (5.10) is a good representation of the constitutive equation for Eco-Core. The approximate method (Eq. 5.2) differed from the area and the integral method at high strain rates because of not including the partial densification. Figure 5.28 also includes the energy absorption density from the quasi-static test up to the limit of crushing strain (0.48). This value compared well with the upper limit from the dynamic test.

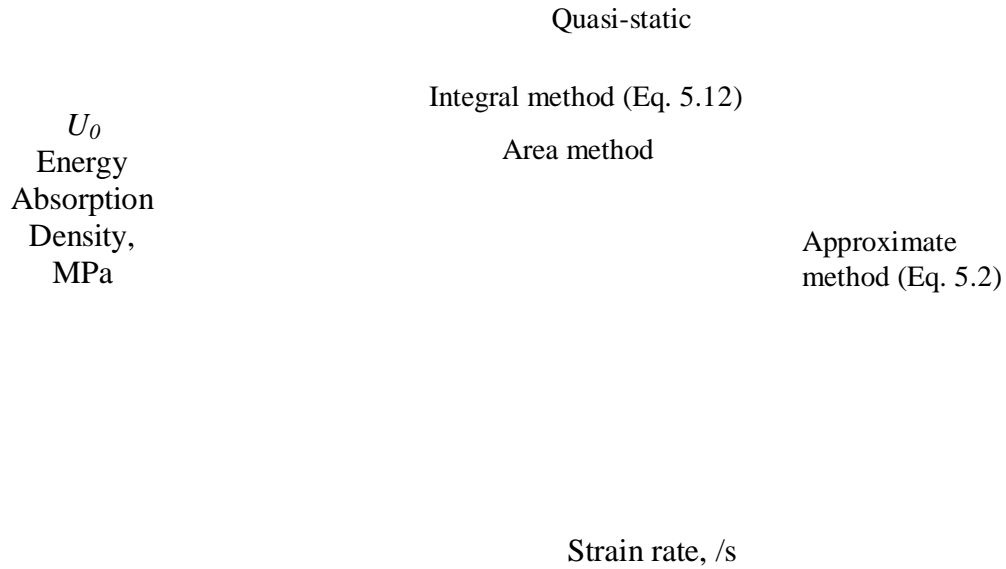


**Figure 5.28. Energy Absorption Density of Eco-Core as a Function of Strain Rate**

### **5.3 Dynamic Characterization of Modified Eco-Core**

#### **5.3.1 Polyurea Coated Eco-Core**

##### **5.3.1.1 Sample Preparation**

Details of preparation of polyurea coated samples and the reason for this study was explained in section 3.3.2.1. The dynamic testing of 0-thickness coated (0-PU) and 10 mil coated (10-PU) Eco-Core samples were performed. The additional details of specimen preparation for the dynamic test were explained in section 5.2.1. The 0-PU coating is defined as the near-zero thick coating obtained by smearing of polyurea on Eco-Core panel using doctor blade. For ease of reading and referencing the specimen following nomenclature is used.

- EPU0F-x : Eco-Core coated with ~ 0 mil thick polyurea on front side
- EPU10F-x : Eco-Core coated with 10 mil thick polyurea on front side
- EPU0B-x : Eco-Core coated with ~ 0 mil thick polyurea on back side
- EPU10B-x : Eco-Core coated with 10 mil thick polyurea on back side

- EPU0FB-x : Eco-Core coated with ~ 0 mil thick polyurea on front and back side
- EPU10FB-x : Eco-Core coated with 10 mil thick polyurea on front and back side

The 0-PU specimen dimensions and density are listed in Table 5.6. From the Table 5.6 it is clear that the thickness of all the coated Eco-Core specimens were quite uniform with a co-efficient of variation of less than 3%. The co-efficient of variation for density is below 5%. Table 5.7 lists the dimensions and density of 10-PU specimens. The table clearly shows that the thickness of the coated Eco-Core specimens was quite uniform with a co-efficient of variation below 3%. The co-efficient of variation for density is below 7%, which is quite reasonable for the lab manufactured material. Figures 5.29 and 5.30 show photographs of specimens used in the current study.

**Table 5.6. Density and Dimensions of 0-PU Coated Eco-Core Specimens**

Specimen #	Diameter (D), mm				Length (L), mm				Weight, g	Density, g/cc
	1	2	3	Avg.	1	2	3	Avg.		
EPU0F-4	12.24	12.27	12.24	12.25	3.20	3.18	3.20	3.19	0.198	0.526
EPU0F-5	12.24	12.27	12.24	12.25	3.12	3.12	3.12	3.12	0.199	0.540
EPU0F-6	12.24	12.27	12.24	12.25	3.18	3.18	3.20	3.18	0.199	0.530
EPU0F-7	12.27	12.32	12.24	12.28	3.18	3.16	3.18	3.17	0.201	0.536
EPU0F-8	12.24	12.22	12.22	12.23	3.20	3.18	3.20	3.19	0.204	0.544
EPU0F-10	12.24	12.22	12.22	12.23	3.18	3.18	3.18	3.18	0.205	0.550
EPU0B-4	12.19	12.19	12.19	12.19	3.18	3.18	3.18	3.18	0.192	0.518
EPU0B-5	12.19	12.22	12.22	12.21	3.18	3.18	3.18	3.18	0.194	0.522
EPU0B-6	12.19	12.19	12.19	12.19	3.15	3.15	3.15	3.15	0.196	0.533
EPU0B-7	12.22	12.22	12.22	12.22	3.18	3.18	3.18	3.18	0.197	0.529
EPU0B-8	12.19	12.19	12.19	12.19	3.18	3.18	3.20	3.18	0.202	0.544
EPU0B-9	12.19	12.22	12.19	12.20	3.18	3.18	3.18	3.18	0.202	0.544
EPU0FB-4	12.34	12.32	12.29	12.32	3.20	3.20	3.18	3.19	0.212	0.557
EPU0FB-5	12.34	12.29	12.27	12.30	3.18	3.18	3.20	3.18	0.213	0.563
EPU0FB-6	12.32	12.29	12.34	12.32	3.20	3.20	3.20	3.20	0.213	0.558
EPU0FB-7	12.24	12.34	12.29	12.29	3.20	3.20	3.20	3.20	0.213	0.561
EPU0FB-8	12.24	12.24	12.24	12.24	3.15	3.15	3.15	3.15	0.216	0.583
EPU0FB-9	12.24	12.27	12.24	12.25	3.20	3.20	3.20	3.20	0.213	0.565

**Table 5.7. Density and Dimensions of 10-PU Coated Eco-Core Specimens**

Specimen #	Diameter (D), mm				Length (L), mm				Weight, g	Density, g/cc
	1	2	3	Avg.	1	2	3	Avg.		
EPU10F-7	12.42	12.40	12.40	12.40	3.38	3.38	3.38	3.38	0.245	0.600
EPU10F-8	12.34	12.34	12.32	12.34	3.43	3.43	3.43	3.43	0.246	0.600
EPU10F-9	12.32	12.32	12.32	12.32	3.42	3.40	3.40	3.41	0.247	0.608
EPU10F-3	12.34	12.34	12.34	12.34	3.45	3.43	3.43	3.44	0.231	0.561
EPU10F-10	12.40	12.34	12.37	12.37	3.45	3.45	3.45	3.45	0.247	0.595
EPU10F-11	12.40	12.37	12.37	12.38	3.43	3.43	3.43	3.43	0.248	0.601
EPU10B-4	12.32	12.32	12.29	12.31	3.45	3.45	3.45	3.45	0.239	0.581
EPU10B-5	12.40	12.40	12.42	12.40	3.45	3.45	3.45	3.45	0.241	0.577
EPU10B-6	12.29	12.29	12.29	12.29	3.43	3.43	3.44	3.43	0.241	0.591
EPU10B-7	12.42	12.40	12.34	12.39	3.43	3.43	3.43	3.43	0.248	0.600
EPU10B-8	12.37	12.37	12.32	12.35	3.45	3.45	3.44	3.45	0.249	0.602
EPU10B-9	12.40	12.40	12.42	12.40	3.44	3.45	3.44	3.45	0.249	0.598
EPU10FB-4	12.42	12.45	12.42	12.43	3.68	3.68	3.68	3.68	0.298	0.667
EPU10FB-6	12.34	12.34	12.34	12.34	3.84	3.86	3.81	3.84	0.303	0.660
EPU10FB-14	12.37	12.40	12.40	12.39	3.71	3.70	3.71	3.70	0.295	0.661
EPU10FB-7	12.42	12.42	12.40	12.41	3.63	3.61	3.70	3.64	0.304	0.689
EPU10FB-8	12.37	12.40	12.34	12.37	3.70	3.71	3.71	3.70	0.305	0.685
EPU10FB-9	12.45	12.40	12.45	12.43	3.81	3.81	3.84	3.82	0.308	0.665



**Figure 5.29. 0-PU Coated Eco-Core Specimens**



**Figure 5.30. 10-PU Coated Eco-Core Specimens**

The dynamic characterization of polyurea coated Eco-Core samples were performed using the Split Hopkinson Pressure Bar test by following the test procedure, the data recording and the analysis as outlined in section 4.7.

*5.3.1.2 Test Matrix*

The Eco-Core samples coated with polyurea in different arrangements were tested at two strain rates near 3,000/s and 4,000/s. Eco-Core panels were coated with polyurea as per the plan (front side, back side and two-side). The Table 5.8 represents test matrix used. All tests were conducted in the ambient conditions. Three specimens are tested for each case.

**Table 5.8. Dynamic Test Matrix for Polyurea Coated Eco-Core**

Test Case	Strain Rate, s <sup>-1</sup>		
	1	2	
Polyurea coated Eco-Core	~0 thick front	~ 3000	~ 4000
	10 mil thick front	~ 3000	~ 3600
	~0 thick front	~ 3000	~ 4000
	10 mil thick front	~ 3000	~ 3600
	~0 thick front & back	~ 3000	~ 4000
	10 mil thick front & back	~ 3000	~ 3600

### *5.3.1.3 Results and Discussions – Polyurea Coated Eco-Core*

#### *5.3.1.3.1 Front Face Coated Eco-Core*

##### (a) Dynamic Stress-Strain Response

###### *0-thickness coating (0-PU)*

The uniaxial compressive stress-strain curves for front coated Eco-Core tested at breech pressures of 22 psi and 26.5 psi were presented in Figures 5.31 and 5.32, respectively. The strain rate attained at breech pressure of 22 psi varied from 2,722/s to 2,917/s. It was observed from Figure 5.31 that all the three curves showed very similar characteristics thereby indicating that the results were repeatable. All the curves show plateau stress regime where stress remained nearly constant with increasing strain until the strain reaches around 26% followed by a densification region where stress rose rapidly with strain. The dynamic plateau stress was between 18 to 20 MPa. The strain rate achievable at breech pressure of 26.5 psi varied from 3,111/s to 3,848/s. Figure 5.32 clearly shows that all the stress-strain curves exhibited the stress plateau and the densification region. The sample tested at strain rate 3,566/s showed an early onset of densification. The dynamic plateau stress was between 18 to 21 MPa.

Figure 5.33 summarizes the dynamic compressive stress-strain curves of 0-PU specimens tested at breech pressures of 22 psi and 26.5 psi. It was clear from Figure 5.33 that all the stress-strain curves were close to each other until the onset of densification irrespective of the strain rate. All the stress-strain curves marginally differed from each other in the densification zone except for the specimen tested at strain rate of 3,566/s which showed early onset of solidification.

###### *Ten mil thick coating (10-PU)*

The uniaxial compressive stress-strain curves for front 10-PU coated specimens tested at breech pressures of 22 psi and 26.5 psi were presented in Figures 5.34 and 5.35, respectively. The strain rate attained at breech pressure of 22 psi varied from 2,666/s to 2,919/s. Figure 5.34 clearly shows that the two curves overlapped each other over the entire strain range thereby indicating that the results were repeatable. Both the curves exhibited the stress plateau regime, the linear transition region between strains of 0.26 and 0.44,

followed by the densification region. This response may be related to wave reflections from front and back surface of the coating. This phenomenon was not noticed for 0-PU specimens because of very small thickness of coating. The dynamic plateau strength was approximately 20 MPa. The strain rate attained at breach pressure of 26.5 psi varied from 3,401/s to 3,649/s. Figure 5.35 again shows the similar stress-strain response consisting of the stress plateau regime, the linear transition region between strains of 0.27 and 0.48 followed by the densification region. The stress-strain curves separated from each other in the densification zone. The dynamic plateau strength was between 17 and 21 MPa.

Figure 5.36 summarizes the dynamic compressive stress-strain curves of 10-PU specimens tested at breach pressures of 22 psi and 26.5 psi. Figure 5.36 clearly shows that all the stress-strain curves were close to each other until the onset of densification irrespective of the strain rate and the curves separated from each other in the densification region. It is evident from Figures 5.33 and 5.36 that the 10-PU specimens showed a linear transition zone between strain values 0.26 and 0.44 whereas the 0-PU specimens showed a typical curvilinear transition region.

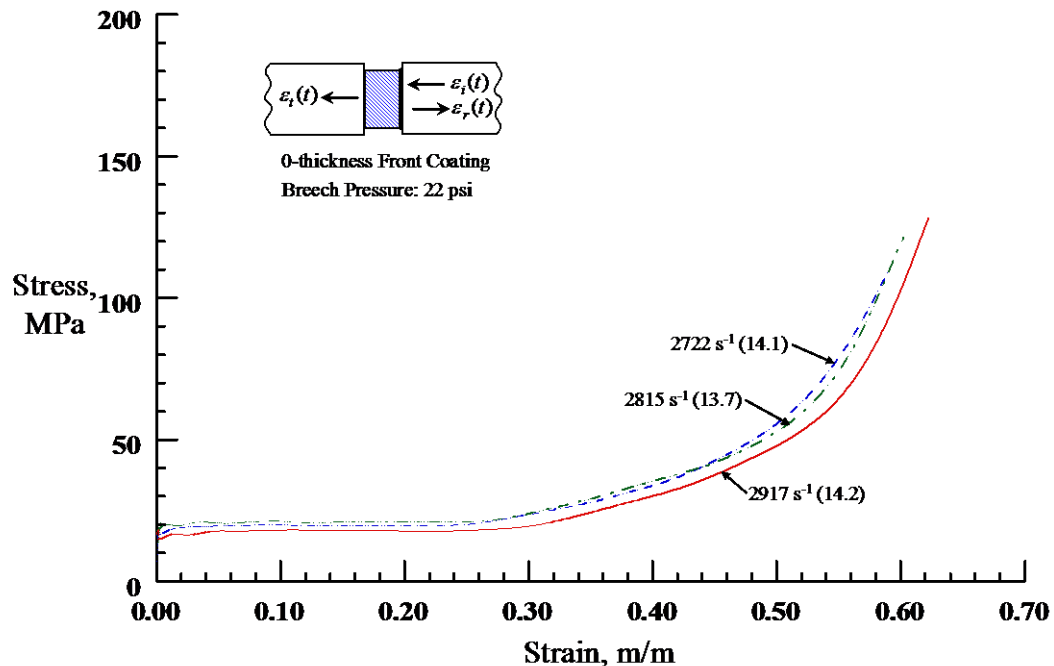


**Figure 5.31. Dynamic Compressive Stress-Strain Curves for 0-PU Front Coated Eco-Core at Breach Pressure of 22 psi**

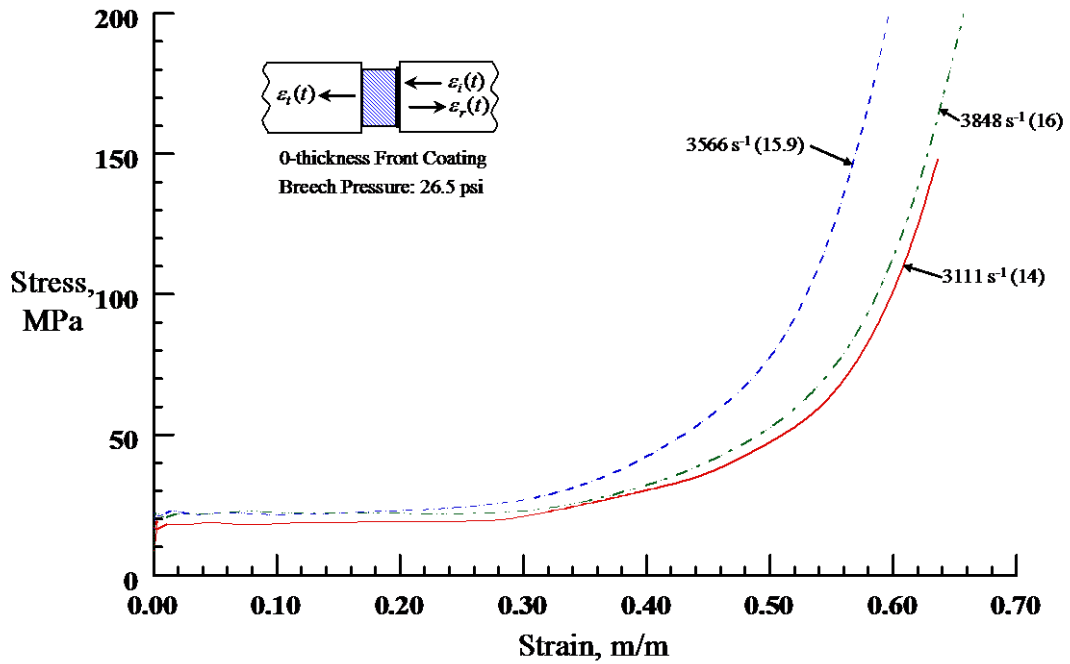


Figure 5.32. Dynamic Compressive Stress-Strain Curves for 0-PU Front Coated Eco-Core at Breach Pressure of 26.5 psi

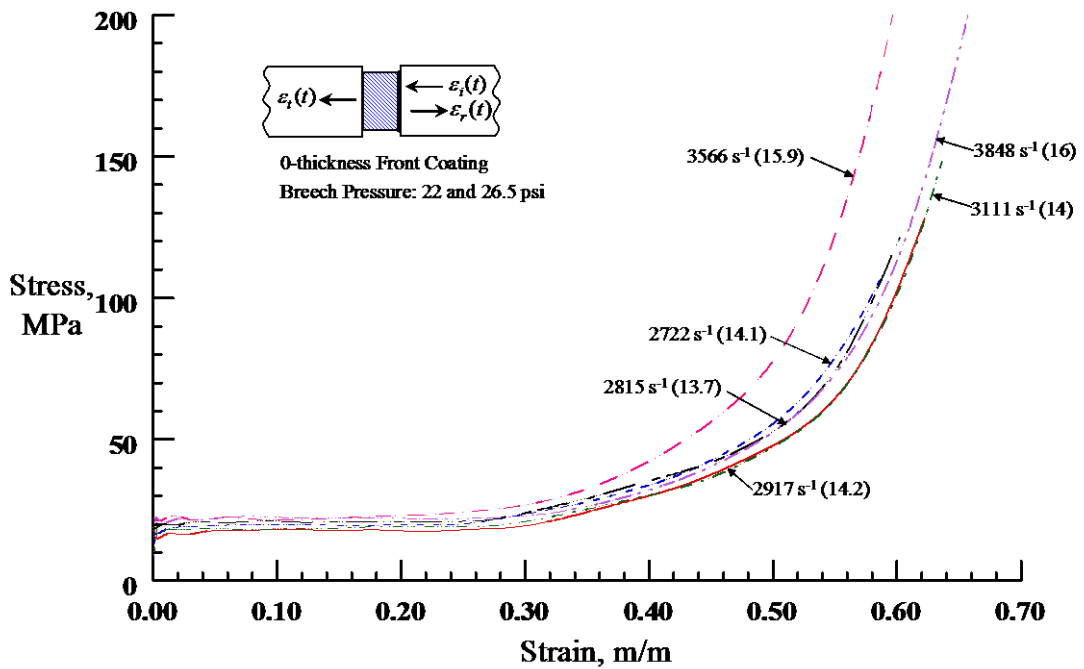


Figure 5.33. Dynamic Compressive Stress-Strain Curves for 0-PU Front Coated Eco-Core at Breach Pressure of 22 and 26.5 psi

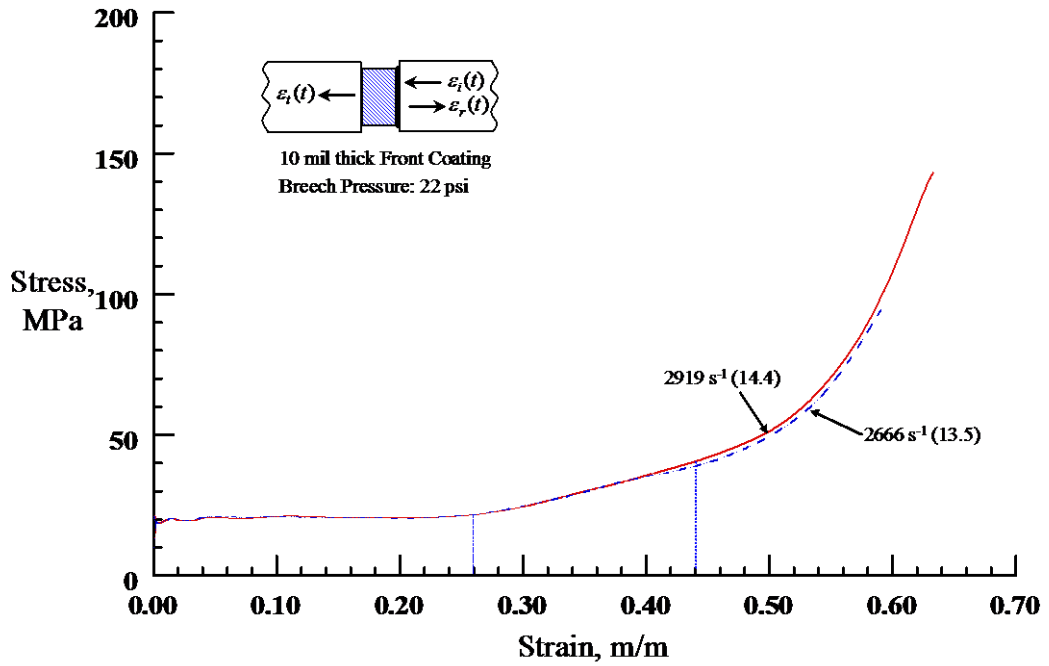


Figure 5.34. Dynamic Compressive Stress-Strain Curves for 10-PU Front Coated Eco-Core at Breach Pressure of 22 psi

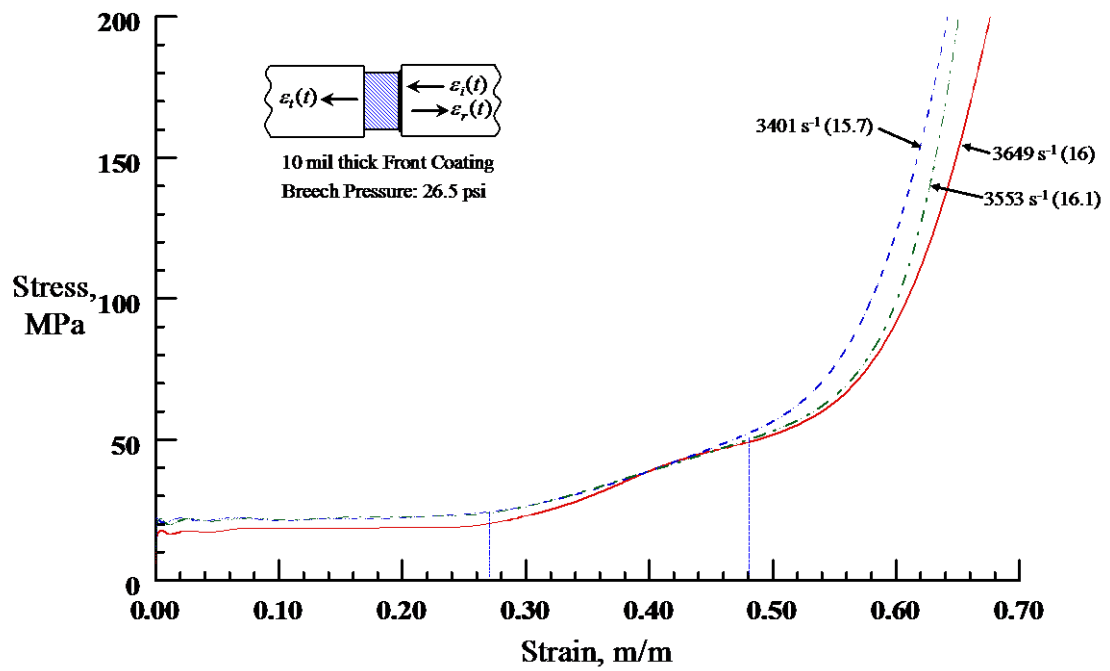
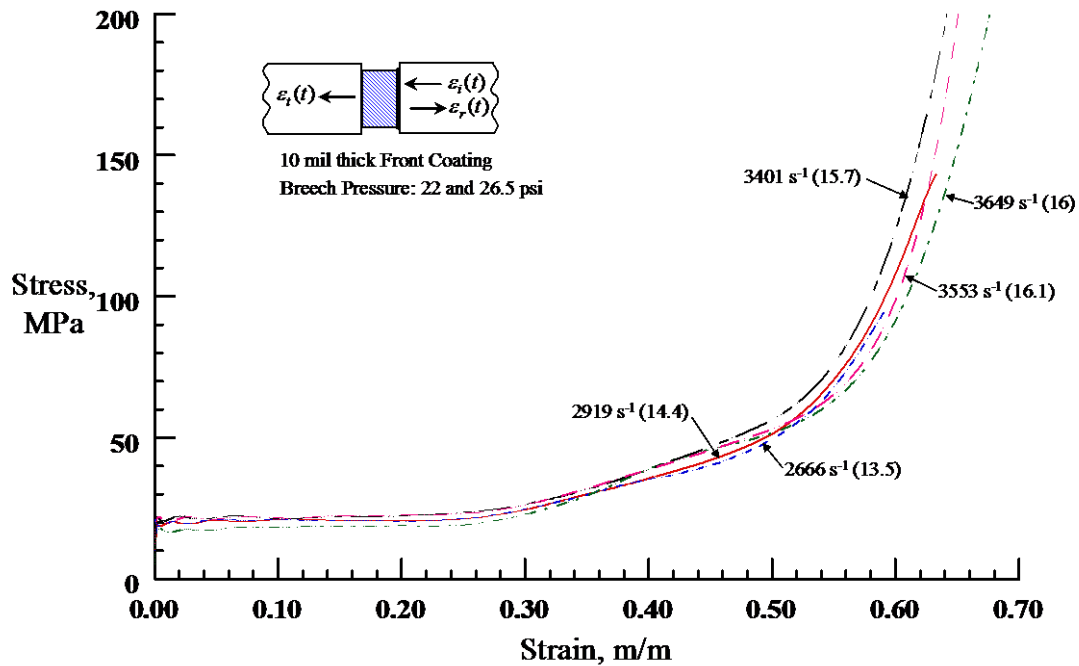


Figure 5.35. Dynamic Compressive Stress-Strain Curves for 10-PU Front Coated Eco-Core at Breach Pressure of 26.5 psi



**Figure 5.36. Dynamic Compressive Stress-Strain Curves for 10-PU Front Coated Eco-Core at Breech Pressure of 22 and 26.5 psi**

(b) High Speed Image Analysis of the Dynamic Phenomenon

Figure 5.37 shows a series of images at a time interval of  $30.8 \mu\text{s}$  during a SHPB test on 0-PU front coated Eco-Core sample at a strain rate of  $\sim 3,000/\text{s}$ . The coated Eco-Core specimen was observed to be compacted gradually from the incident bar/specimen end. The Eco-core deformed elastically for approximately  $30 \mu\text{s}$  and then the peak stress started crushing the front-side layers of the specimen (i.e, specimen side facing the incident bar). This is evident from Figure 5.37 where it was clearly observed bulging of front-side of the specimen. From the series of images given in Figure 5.37 it was clear that crushing of the Eco-Core specimen initiated at the incident bar/specimen end and propagated gradually towards the transmitted bar/specimen end. After  $154 \mu\text{s}$ , a straight crack plane was initiated at transmission end of the specimen and causes vertical spitting of the specimen. The crushing of broken pieces of the specimen continued over the remaining strain history until approximately  $277 \mu\text{s}$  and there afterwards rapid lateral

ejection of the crushed debris was observed. Figure 5.33 shows the representative high speed photographs captured during a high rate test on 10-PU front coated Eco-Core sample at a strain rate of  $\sim 3,000/s$ . Here, the sample deformed elastically until approximately  $31 \mu s$  and then crushing started at the transmission end of the specimen. Unlike in the case of 0-thickness front coated Eco-Core sample, no cleavage like tensile crack planes were observed. It is clear from the Figure 5.38 that crushing of the layers initiated at the transmission end of the specimen propagated gradually towards the specimen/incident bar end. It was also observed that crushing of the Eco-Core layers continued over the entire strain history.

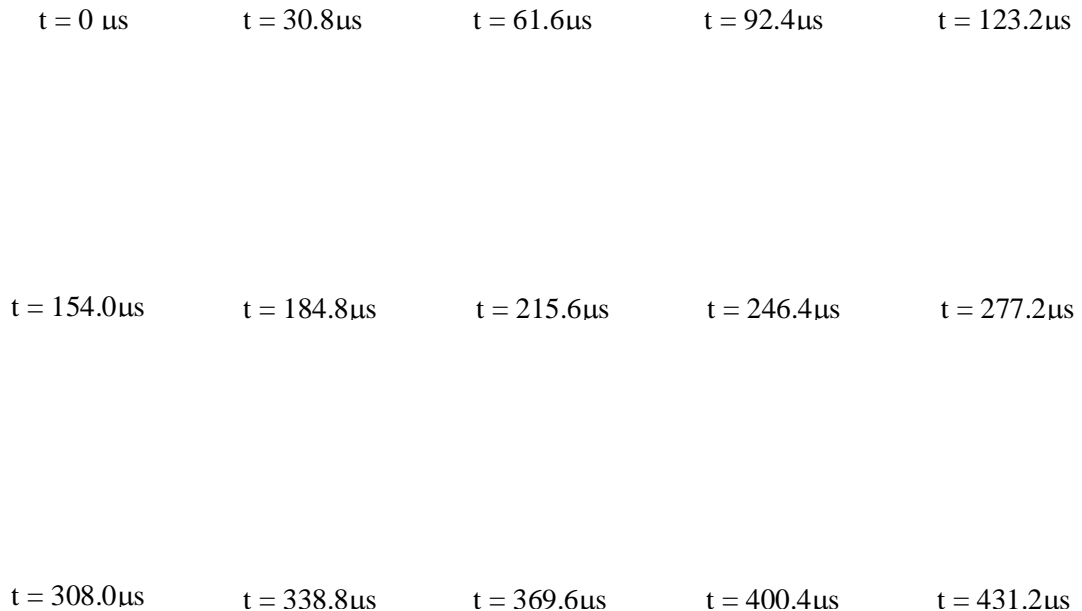


**Figure 5.37. Photographs Recorded During a High Strain Rate Compression Test on 0-PU Front Coated Eco-Core Specimen at a Strain Rate  $\sim 2,900/s$  (Time Interval:  $30.8\mu s$ )**

$t = 0 \mu\text{s}$        $t = 30.8 \mu\text{s}$        $t = 61.6 \mu\text{s}$        $t = 92.4 \mu\text{s}$        $t = 123.2 \mu\text{s}$

$t = 154.0 \mu\text{s}$        $t = 184.8 \mu\text{s}$        $t = 215.6 \mu\text{s}$        $t = 246.4 \mu\text{s}$        $t = 277.2 \mu\text{s}$

$t = 308.0 \mu\text{s}$        $t = 338.8 \mu\text{s}$        $t = 369.6 \mu\text{s}$        $t = 400.4 \mu\text{s}$        $t = 431.2 \mu\text{s}$

**Figure 5.38. Photographs Recorded During a High Strain Rate Compression Test on 10-PU Front Coated Eco-Core specimen at a Strain Rate ~ 3,000/s (Time Interval: 30.8 $\mu\text{s}$ )**

#### 5.3.1.3.2 Back Face Coated Eco-Core

##### *0-thickness coating*

Figures 5.39 and 5.40 shows the dynamic compressive stress-strain curves for 0-PU specimens tested at breech pressures of 22 and 26.5 psi, respectively. The strain rate attained at breech pressure of 22 psi varied from 2,747/s to 2,958/s. Figure 5.39 clearly shows that all the curves overlapped each other over the entire strain range thereby indicating that the results were repeatable. All curves exhibited the stress plateau regime followed by the densification region. The dynamic plateau stress was around 18 MPa. The strain rate obtained at breech pressure 26.5 psi ranged from 3,887/s to 4,036/s. Figure 5.40 shows

stress-strain response similar to that of specimens tested at 22 psi but with a higher stress levels. The dynamic stress plateau was around 20 MPa.

Figure 5.41 summarizes the dynamic compressive stress-strain response of 0-PU specimens tested at breech pressures of 22 psi and 26.5 psi. It is evident from Figure 5.41 that the stress-strain curves were close to each other until the onset of densification irrespective of the strain rates. The specimens tested at strain rate range of 3,887/s – 4,036/s showed higher rate of densification when compared to specimens tested at strain rate range 2,747/s - 2,958/s.

*Ten mil thick coating*

The dynamic compressive stress-strain curves for 10-PU specimens tested at breech pressure of 22 psi and 26.5 psi were presented in Figures 5.42 and 5.43, respectively. The strain rate attained at breech pressure of 22 psi varied from 2,327/s to 2,928/s. Figure 5.42 clearly shows that the two curves overlapped each other over the entire strain range thereby indicating that the results were repeatable. Two of the specimen exhibited the stress plateau regime, the linear transition region between strains of 0.26 and 0.47, followed by the densification region. But one of the specimen tested at a strain rate of 2,327/s showed only the stress plateau region and the linear transition region. This was due to the lower velocity of the striker bar which limited the failure strain to 0.5. The dynamic plateau stress was approximately 18 MPa. The strain rate attained at breech pressure of 26.5 psi varied from 3591/s to 3640/s. Figure 5.43 again shows the similar stress-stain response consisting of the stress plateau regime, linear transition region between strains of 0.24 and 0.48 followed by densification region. The dynamic plateau stress is around 20 MPa.

Figure 5.44 summarizes the dynamic compressive stress-strain curves of 10-PU specimens at breech pressures of 22 psi and 26.5 psi. Figure 5.44 clearly shows that all the stress-strain curves are close to each other till the onset of densification irrespective of the strain rate and the curves marginally separate from each other in the densification region. Comparison of Figures 5.41 and 5.44 reveals that the 10-PU specimens showed a linear transition zone between strain values 0.24 and 0.47 where as the 0-PU specimens showed a typical curvilinear transition region.

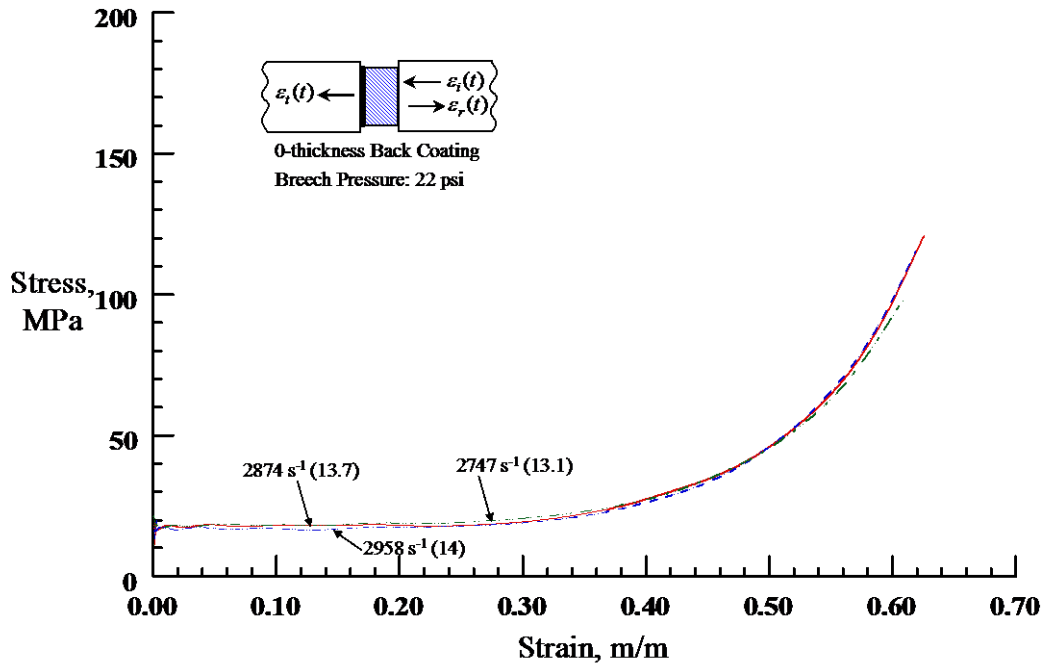


Figure 5.39. Dynamic Compressive Stress-Strain Curves for 0-PU Back Coated Eco-Core at Breach Pressure of 22 psi

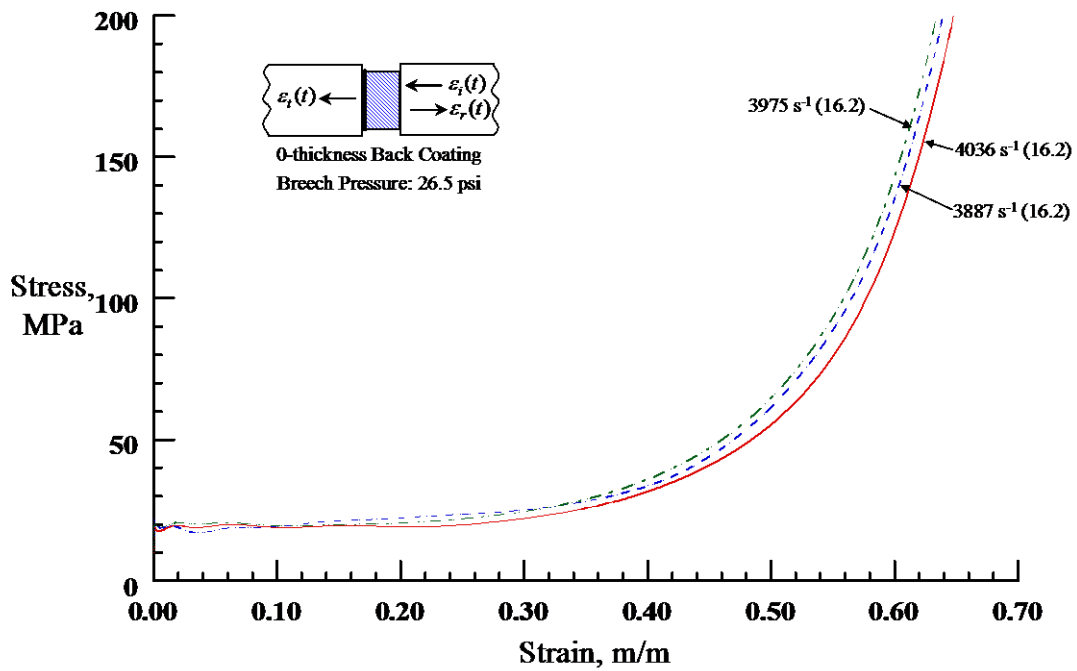


Figure 5.40. Dynamic Compressive Stress-Strain Curves for 0-PU Back Coated Eco-Core at Breach Pressure of 26.5 psi

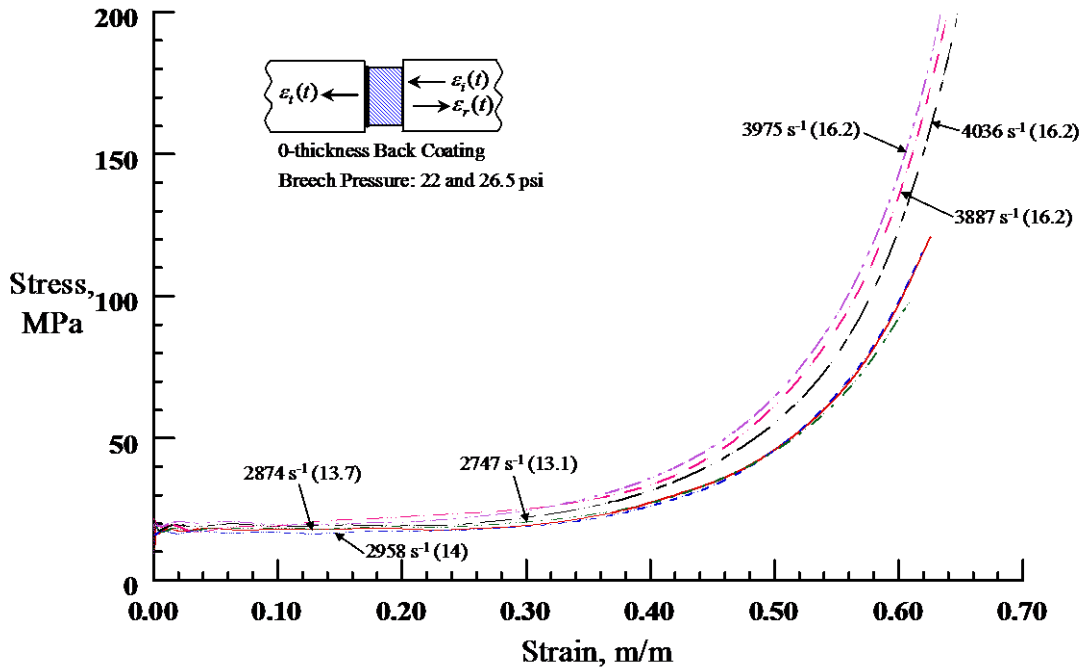


Figure 5.41. Dynamic Compressive Stress-Strain Curves for 0-PU Back Coated Eco-Core at Breech Pressures of 22 and 26.5 psi

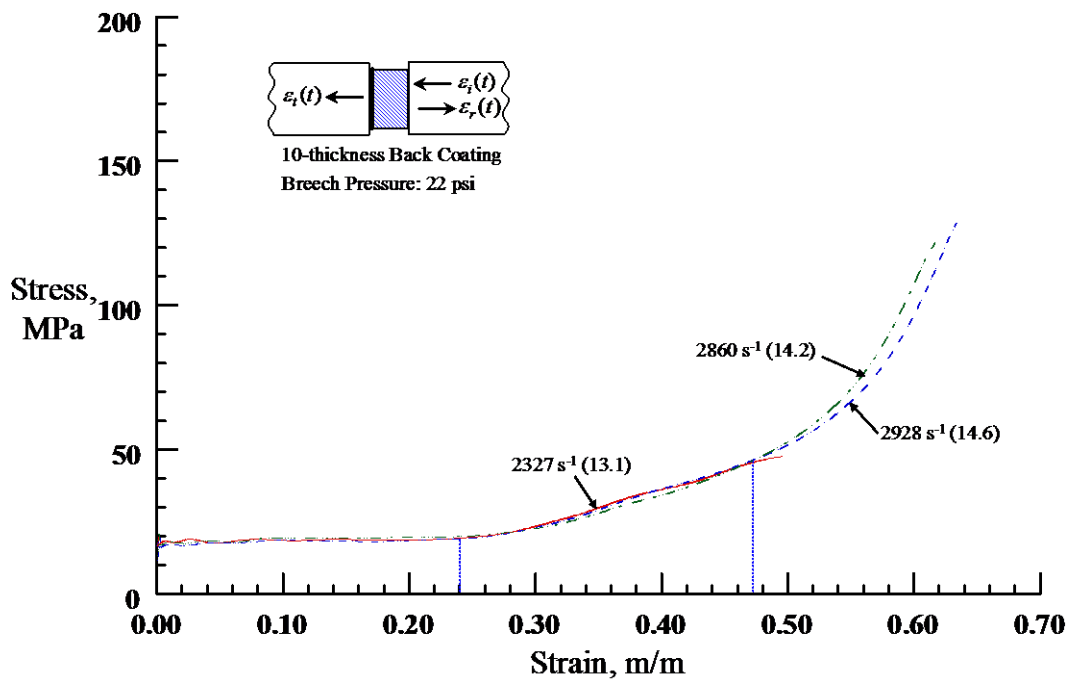


Figure 5.42. Dynamic Compressive Stress-Strain Curves for 10-PU Back Coated Eco-Core at Breech Pressure of 22 psi

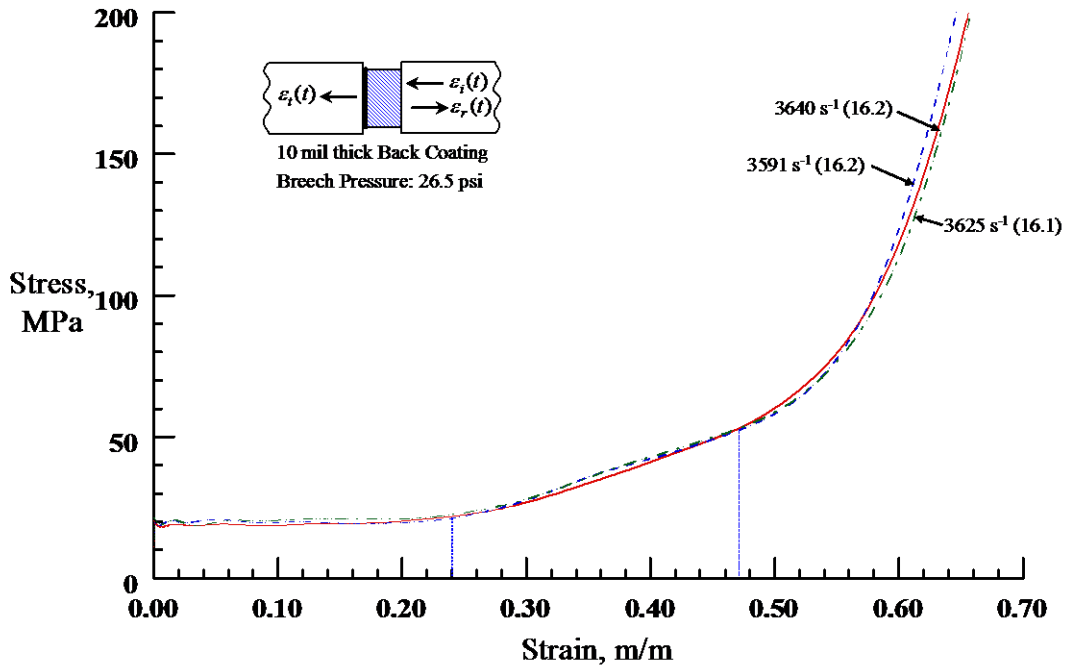


Figure 5.43. Dynamic Compressive Stress-Strain Curves for 10-PU Back Coated Eco-Core at Breech Pressure of 26.5 psi

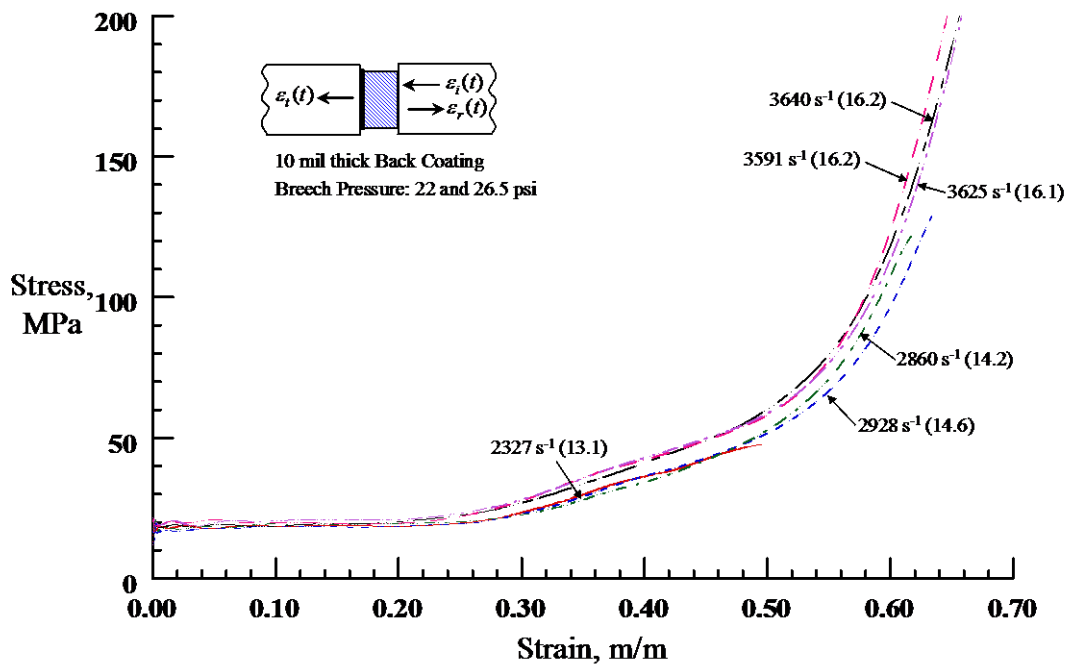


Figure 5.44. Dynamic Compressive Stress-Strain Curves for 10-PU Back Coated Eco-Core at Breech Pressures of 22 and 26.5 psi

### 5.3.1.3.3 Front-Back Face (Two-Side) Coated Eco-Core

#### (a) Dynamic stress-strain response

##### *0-thickness coating*

The dynamic compressive stress-strain curves of 0-PU specimens tested at breech pressures of 22 psi and 26.5 psi were presented in Figures 5.45 and 5.46, respectively. The strain rate attained at breech pressure of 22 psi varied from 3,040/s to 3,247/s. It was observed from Figure 5.45 that all the three curves showed very similar characteristics thereby indicating that the results were repeatable. All the curves show plateau stress regime where stress remained nearly constant with increasing strain until the strain reaches around 28% followed by a densification region where stress rose rapidly with strain. The dynamic plateau stress was around 18 MPa. The strain rate achievable at breech pressure of 26.5 psi varied from 3,844/s to 3,925/s. Figure 5.46 clearly shows that all the stress-strain curves exhibited the stress plateau and a prominent densification region. One of the sample tested at strain rate of 3,925/s showed little prolonged densification region. The dynamic plateau stress was around 18 MPa.

Figure 5.47 summarizes the dynamic compressive stress-strain curves of 0-PU specimens tested at breech pressures of 22 psi and 26.5 psi. It is clear from the Figure 5.47 that all the stress-strain curves were close to each other until the onset of densification irrespective of the strain rate. All the stress-strain curves marginally differed from each other in the densification region. The specimens tested at strain rates between 3,040/s and 3,247/s showed more prolonged densification region than specimens tested at strain rate range 3,844 -3,925/s.

##### *Ten mil thick coating*

The dynamic compressive stress-strain curves of 10-PU specimens tested at breech pressures of 22 psi and 26.5 psi were presented in Figures 5.48 and 5.49, respectively. The strain rate attained at breech pressure of 22 psi varied from 2,249/s to 2,761/s. Figure 5.48 clearly shows that all the samples exhibited similar stress-strain response thereby indicating that the results were repeatable. All the curves exhibited stress plateau regime until 18% strain, a prominent stress peak at strain levels of 0.18 - 0.47, followed by a less consistent

densification region. The stress peak may be due to the complex multiple reflections of the stress waves at the Eco-Core/PU interface. The dynamic plateau stress was between 17 and 20 MPa. The strain rate attained at breach pressure of 26.5 psi varied from 3,478/s to 3,572/s. Figure 5.49 again shows the similar stress-strain response consisting of the stress plateau regime, a prominent stress peak at strain levels of 0.14 - 0.44, followed by a prominent densification region. The stress-strain curves separated from each other in the densification zone. The dynamic plateau stress was around 20 MPa.

Figure 5.50 summarizes the dynamic compressive stress-strain curves of 10-PU specimens tested at breach pressures of 22 psi and 26.5 psi. Figure 5.50 clearly shows that all the stress-strain curves exhibited similar characteristics until the onset of densification irrespective of the strain rate. The specimens tested at strain rate range of 3,478/s – 3,572/s showed 10% higher plateau stress than those of the specimens tested at strain rates of 2,249/s – 2,761/s. In addition, the specimens tested at strain rate range of 3,478/s – 3,572/s showed an early onset of densification and their densification region was more prominent than those of the specimens tested at strain rates of 2,249/s – 2,761/s.

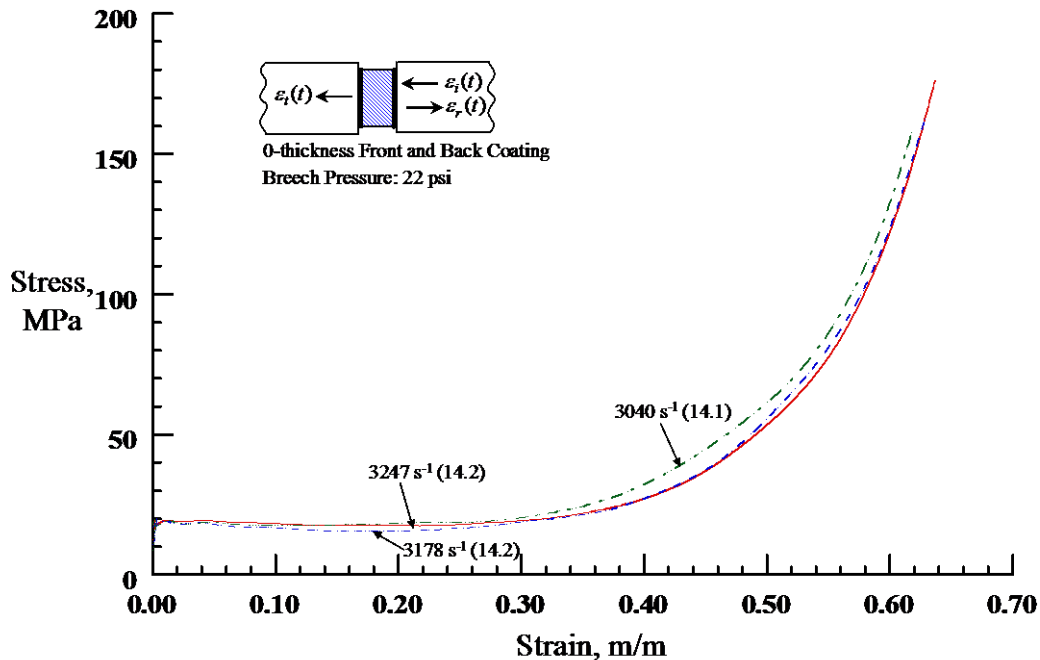


**Figure 5.45. Dynamic Compressive Stress-Strain Curves for 0-PU Front-Back Coated Eco-Core at Breach Pressure of 22 psi**

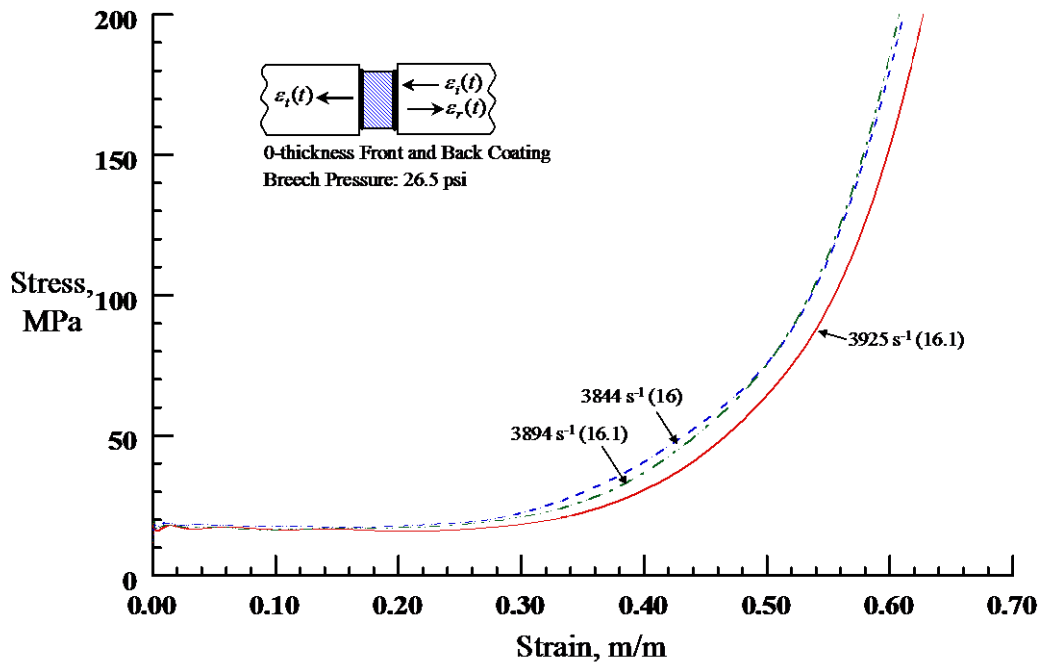


Figure 5.46. Dynamic Compressive Stress-Strain Curves for 0-PU Front-Back Coated Eco-Core at Breach Pressure of 26.5 psi

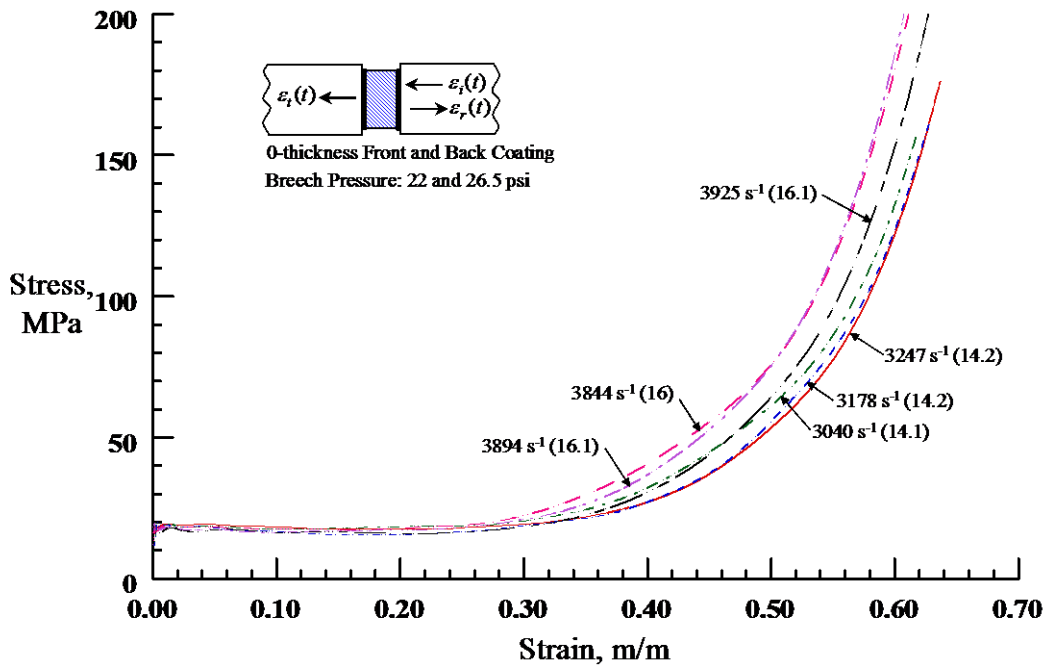


Figure 5.47. Dynamic Compressive Stress-Strain Curves for 0-PU Front-Back Coated Eco-Core at Breach Pressures of 22 and 26.5 psi

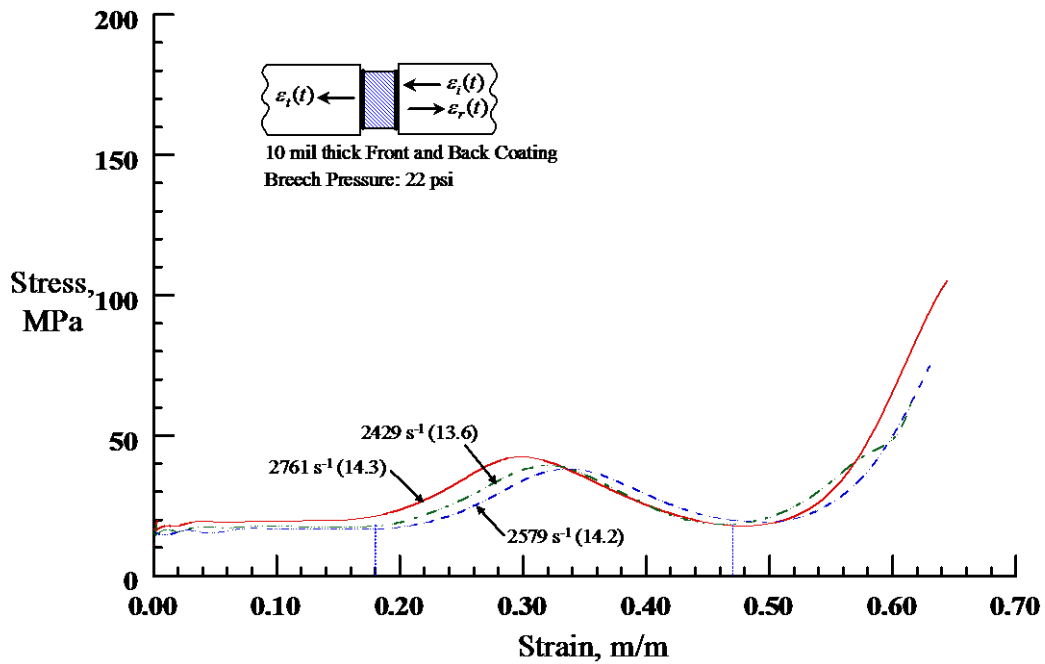


Figure 5.48. Dynamic Compressive Stress-Strain Curves for 10-PU Front-Back Coated Eco-Core at Breech Pressure of 22 psi

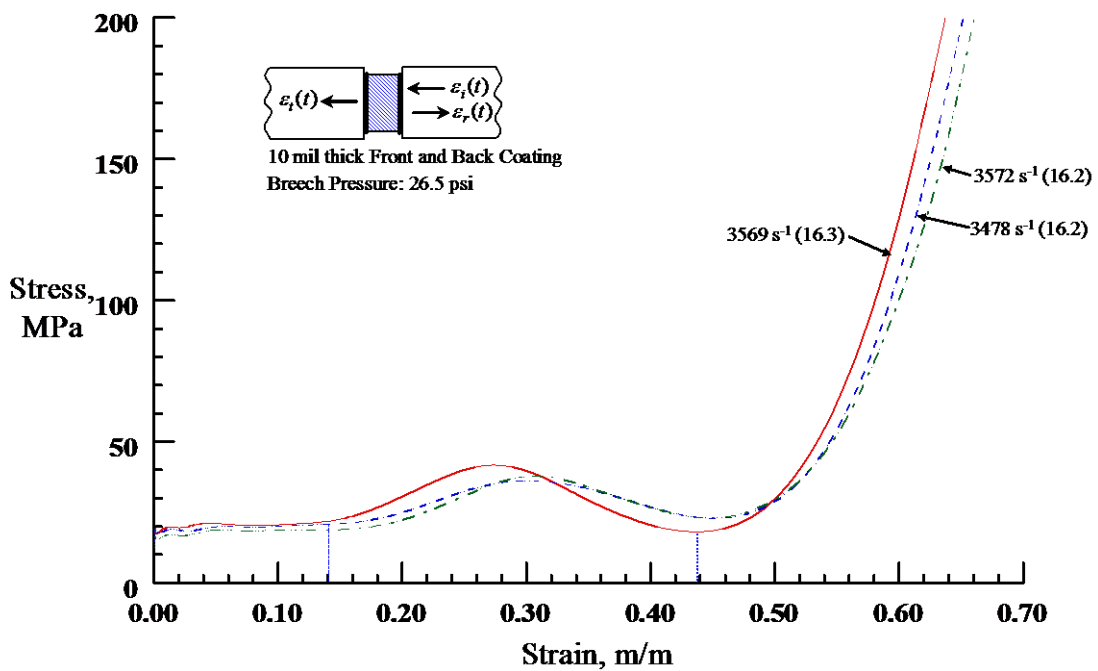
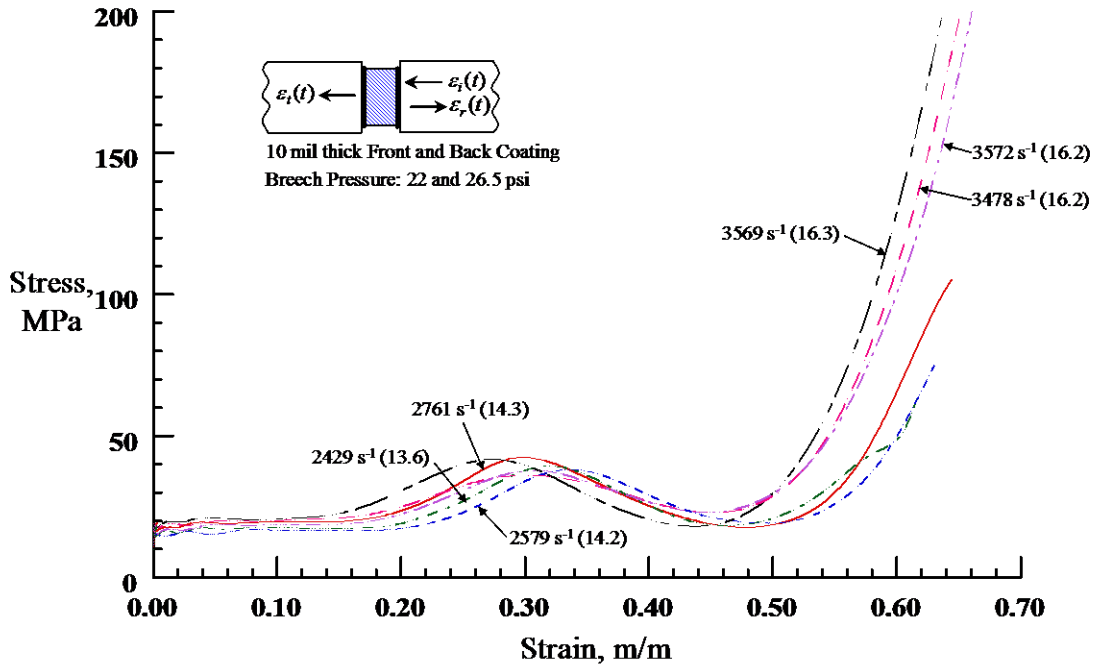


Figure 5.49. Dynamic Compressive Stress-Strain Curves for 10-PU Front-Back Coated Eco-Core at Breech Pressure of 26.5 psi



**Figure 5.50. Dynamic Compressive Stress-Strain Curves for 10-PU Front-Back Coated Eco-Core at Breach Pressures of 22 and 26.5 psi**

(b) High Speed Image analysis of the Dynamic Phenomenon

A Phantom 650 high-speed digital camera was employed to obtain high speed images of specimens during the dynamic deformation. Figure 5.51 shows the representative high speed photographs captured during a high rate test on 0-PU front-back coated Eco-Core sample at a strain rate of  $\sim 3,000/s$ . Time  $t = 0$  occurred just before the loading pulse arrives at the incident bar/specimen interface. The sample was seen to deform uniformly until approximately  $62 \mu s$  and then the peak stress crushed the back side layers of the specimen (i.e. specimen side facing the transmitted bar). From the series of images given in Figure 5.51 it was clear that crushing of the specimen initiated at the transmitter bar/specimen end and propagated gradually towards the specimen/incident bar end. After approximately  $123 \mu s$ , straight crack planes initiated at both incident and transmission end of the specimen and caused vertical spitting. The crushing of broken pieces of the specimen continued over the remaining strain history.

The crushing phenomena continued for approximately 216  $\mu\text{s}$  and thereafter rapid lateral ejection of the crushed debris was observed. Figure 5.52 shows a series of images at a time interval of 30.8  $\mu\text{s}$  during a SHPB test on 10-PU front-back coated Eco-Core sample coating at a strain rate of  $\sim 3,000/\text{s}$ . Here, the sample deformed elastically until approximately 62  $\mu\text{s}$  and then crushing started at the transmission end of the specimen. It can be observed from the Figure 5.52 that after approximately 154  $\mu\text{s}$ , multiple straight cleavages like tensile crack planes initiated at incident end of the specimen in the direction of loading, which eventually propagated to the transmitted end causing vertical splitting of the specimen into several fragments. All of the broken fragments crushed over the remaining test duration.

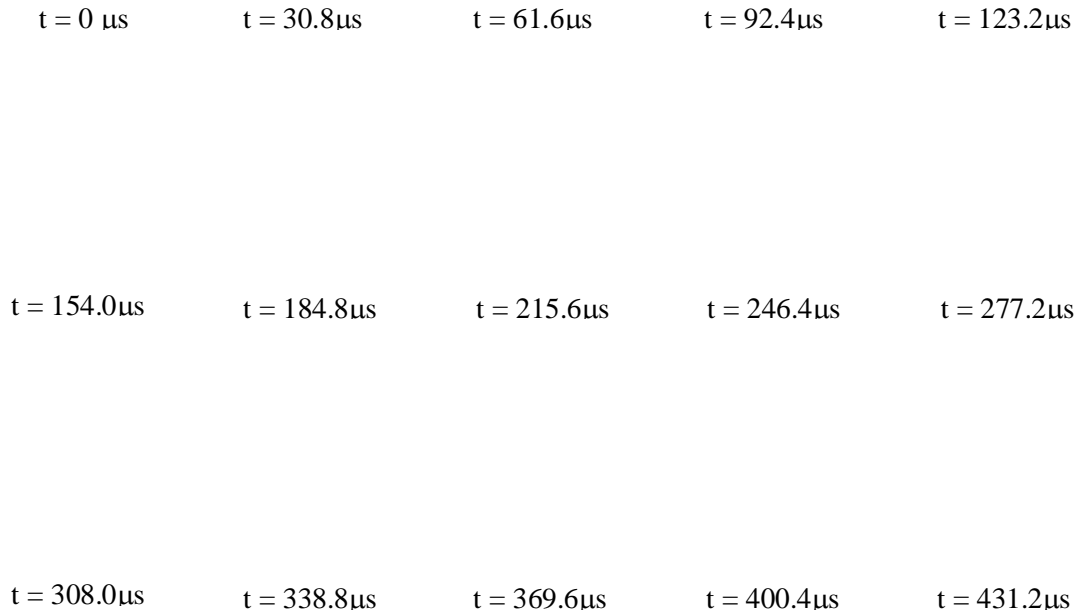


**Figure 5.51. Photographs Recorded During a High Strain Rate Compression Test on 0-PU Front-Back Coated Eco-Core Specimen at a Strain Rate  $\sim 3,000/\text{s}$  (Time Interval: 30.8 $\mu\text{s}$ )**

$t = 0 \mu\text{s}$        $t = 30.8 \mu\text{s}$        $t = 61.6 \mu\text{s}$        $t = 92.4 \mu\text{s}$        $t = 123.2 \mu\text{s}$

$t = 154.0 \mu\text{s}$        $t = 184.8 \mu\text{s}$        $t = 215.6 \mu\text{s}$        $t = 246.4 \mu\text{s}$        $t = 277.2 \mu\text{s}$

$t = 308.0 \mu\text{s}$        $t = 338.8 \mu\text{s}$        $t = 369.6 \mu\text{s}$        $t = 400.4 \mu\text{s}$        $t = 431.2 \mu\text{s}$

**Figure 5.52. Photographs Recorded During a High Strain Rate Compression Test on 10-PU Front-Back Coated Eco-Core Specimen at a Strain Rate  $\sim 3,000/\text{s}$  (Time Interval:  $30.8 \mu\text{s}$ )**

*5.3.1.3.4 Effect of Coating Thickness on Polyurea Coated Eco-Core*

The dynamic compressive stress-strain response of Eco-Core samples with 0-PU coating in different arrangements at strain rates between 2,900 and 3,900/s is summarized in Figure 5.53. Figure 5.53 clearly shows that all the stress-strain curves showed similar characteristics until the onset of densification irrespective of the strain rate and the coating arrangement. The effect of coating arrangement and strain rates affected only the densification region of the stress-strain response. Front-back coated specimen densified earlier than the front coated specimen. For all the coating arrangements, the specimens tested at strain rates near 2,900/s showed prolonged densification region than the specimen tested at

strain rates near 3,900/s. This implied that specimen tested at higher strain rates shows early densification process.

Figure 5.54 shows the dynamic compressive stress-strain response of Eco-Core samples with 10-PU coating in different arrangements at strain rates from 2,800 to 3,600/s. For back and front-back coating arrangements, the specimens tested at strain rates near 2,800/s showed prolonged densification region than the specimen tested at strain rates near 3,600/s. Whereas an opposite trend was observed for front coated specimens. Both front and back coated Eco-Core specimens showed a linear transition region between strain levels 0.26 and 0.46 whereas, front-back coated Eco-Core specimens showed a prominent stress peak at strain levels of 0.18 - 0.46.

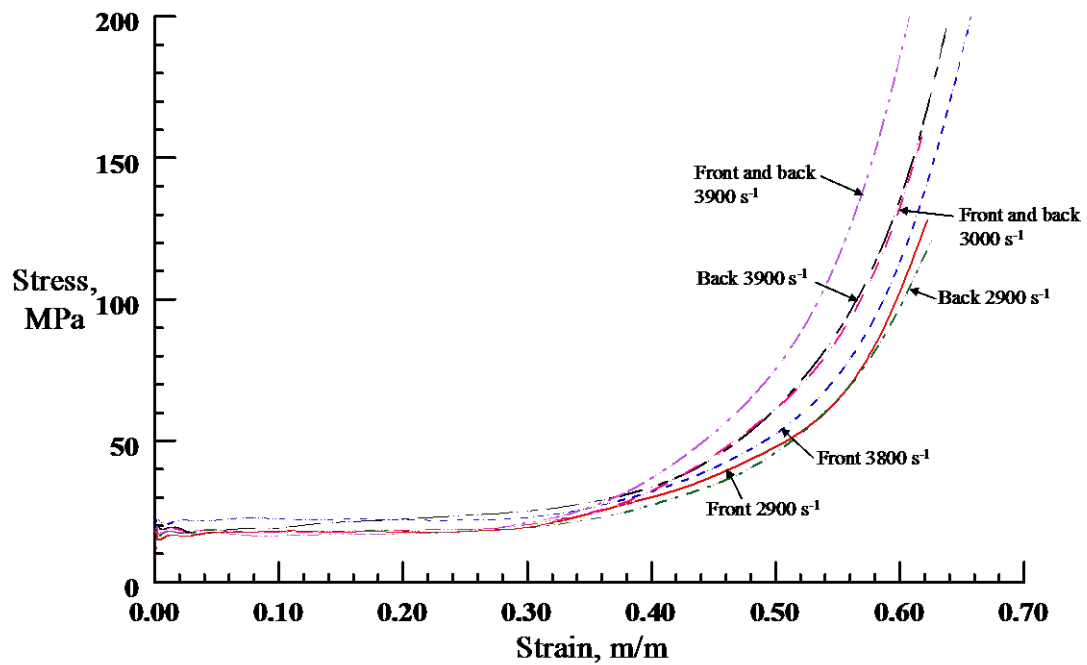
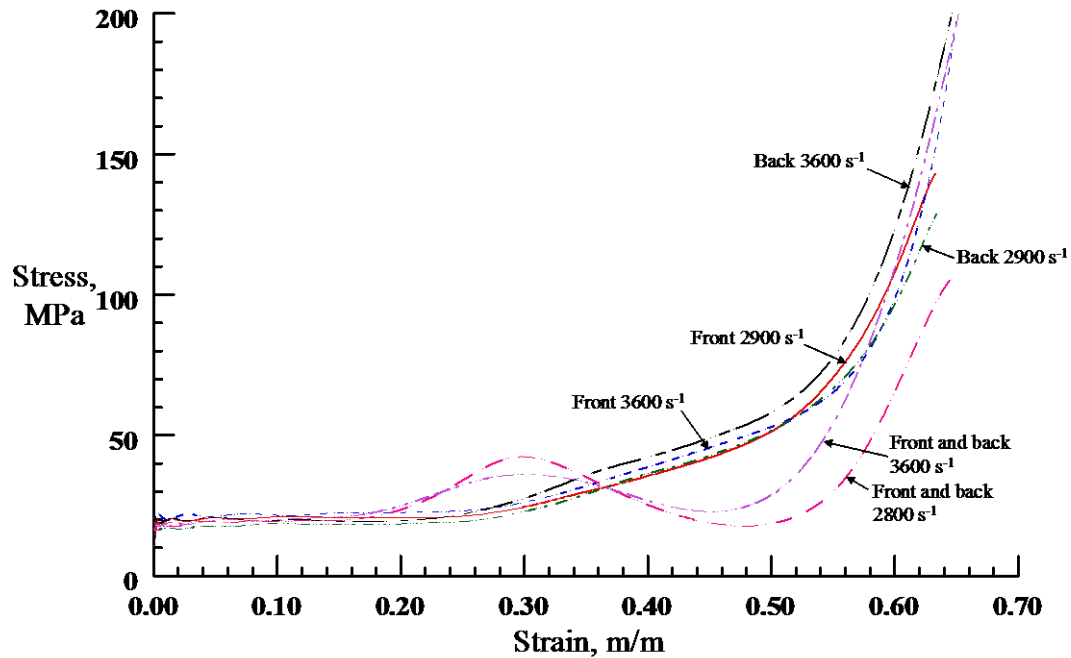


Figure 5.53. Dynamic Compressive Stress-Strain Curves for 0-PU Coated Eco-Core



**Figure 5.54. Dynamic Compressive Stress-Strain Curves for 10-PU Coated Eco-Core**

#### 5.3.1.3.5 Effect of Strain Rate on Polyurea Coated Eco-Core

The dynamic compressive stress-strain response of Eco-Core samples coated with polyurea in different arrangements at strain rate near 2,900/s is summarized in Figure 5.55. It is clear from the Figure 5.55 that all the stress-strain curves nearly overlapped each other until the onset of densification. The plateau stress of all the coated Eco-Core samples was very close to that of the Eco-Core (20 MPa). It is evident from the Figure 5.55 that the densification region of all the coated Eco-Core samples lies beyond that of the Eco-Core except for the 0-PU front-back coated specimen. The densification region of 0-PU front-back coated specimen overlapped with that of the Eco-Core. The 10-PU front-back coated specimen showed a stress peak at strain level of 0.18 to 0.46 and less consistent densification region.

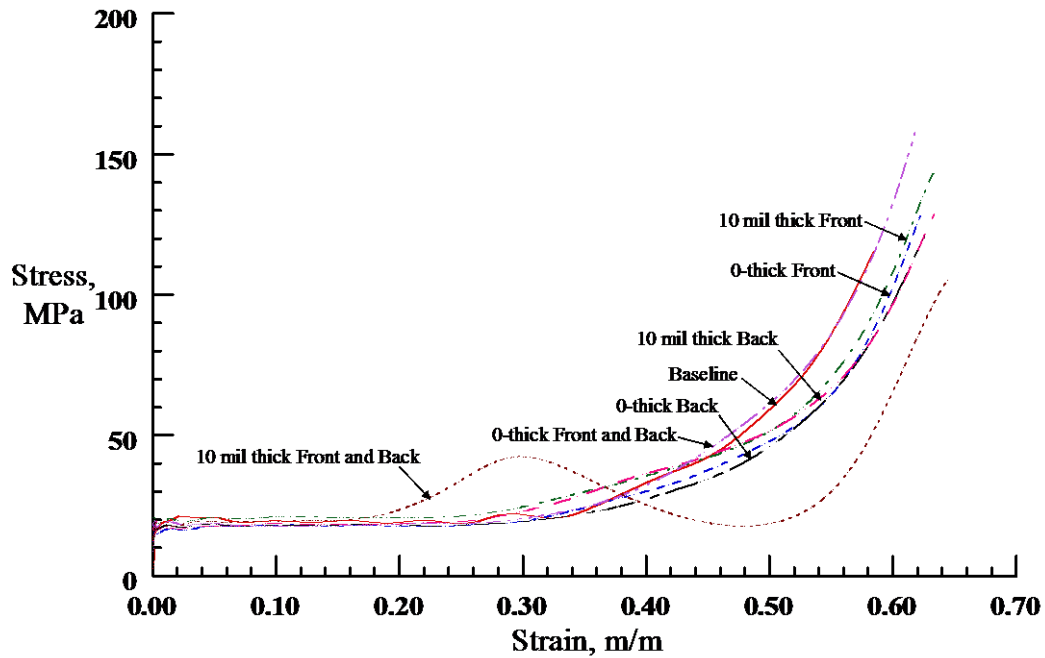


**Figure 5.55. Dynamic Compressive Stress-Strain Curves for PU Coated Eco-Core at a Strain Rate ~2,900/s**

Figure 5.56 summarizes the dynamic compressive stress-strain response of Eco-Core samples coated with polyurea in different arrangements at strain rates near 3,600/s. The plateau stress of all the coated Eco-Core samples was very close to that of the Eco-Core (20 MPa). It is clear from the Figure 5.56 that all the coated Eco-Core samples showed prolonged densification region when compared to that of Eco-Core except for the case of 0-PU front and 0-PU back coated specimens. It was also observed that for all coating arrangements, 0-PU coated specimens densified earlier than the 10-PU coated specimens. The 10-PU front-back coated specimen showed a prominent stress peak at strain level of 0.18 - 0.44.

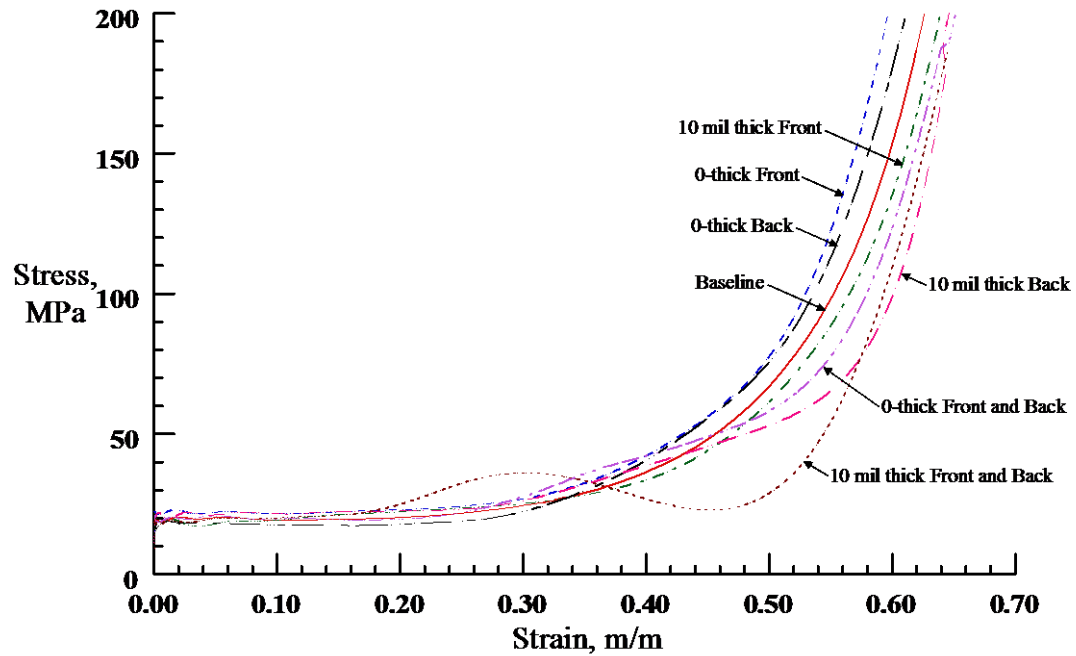


**Figure 5.56. Dynamic Compressive Stress-Strain Curves for PU Coated Eco-Core at a Strain Rate ~3,600/s**

#### 5.3.1.3.6 Energy Absorption

The energy absorption for the polyurea coated Eco-Core samples were calculated as per the methods explained in section 5.2.3.4. The calculated energy absorption density values were listed in Table 5.9 and 5.10 for 0-PU and 10-PU coated Eco-Core samples, respectively. For 10-PU front-back coated specimens, the energy absorption density was calculated by area method since these specimens showed a stress peak instead of plateau regime (refer Figures 5.48 and 5.49). From Tables 5.9 and 5.10 it is observed that the energy absorption values calculated from approximate method (Eq. 5.2) and area method were not in agreement. The difference between the two methods could be as high as 55% or more. This is due to the reason that the approximate method ignores the part of the area above the  $\sigma_c = \text{constant}$  line near the transition region between the plateau and the densification zone. Therefore, the approximate method was not used for comparing different materials performance.

**Table 5.9. Energy Absorption Density of 0-PU Coated Eco-Core at various Strain Rates**

Specimen#	Strain Rate, /s	Density, g/cc	Strength, $\sigma_c$ , MPa	Strain limit, $\epsilon_1$ , m/m	Energy Absorption Density, MPa	
					Approximate method	Area method
EPU0F-4	2,917	0.526	18.2	0.53	9.6	13.1
EPU0F-5	2,722	0.540	20.0	0.49	9.7	12.6
EPU0F-6	3,111	0.530	18.5	0.54	10.0	14.0
Average (%CV)		0.532 (1.4)	18.9 (5.1)	0.52 (5.7)	9.8 (2.1)	13.2 (5.5)
EPU0F-7	2,815	0.536	20.6	0.51	10.5	14.0
EPU0F-8	3,566	0.544	21.5	0.50	10.8	15.9
EPU0F-10	3,848	0.550	22.3	0.55	12.3	16.5
Average (%CV)		0.543 (1.3)	21.5 (4.0)	0.52 (4.7)	11.2 (8.4)	15.5 (8.4)
EPU0B-4	2,874	0.518	18.1	0.53	9.5	12.7
EPU0B-5	2,958	0.522	16.9	0.51	8.7	11.3
EPU0B-6	2,747	0.533	18.3	0.49	9.0	11.0
Average (%CV)		0.524 (1.5)	17.8 (4.2)	0.51 (3.1)	9.1 (4.7)	11.7 (8)
EPU0B-7	4,036	0.529	19.0	0.55	10.5	16.0
EPU0B-8	3,887	0.544	19.2	0.54	10.3	16.6
EPU0B-9	3,975	0.544	19.6	0.53	10.4	16.1
Average (%CV)		0.539 (1.6)	19.3 (1.7)	0.54 (2.3)	10.4 (0.9)	16.2 (1.8)
EPU0FB-4	3,247	0.557	18.4	0.54	10.0	14.0
EPU0FB-5	3,178	0.563	17.0	0.53	9.1	13.0
EPU0FB-6	3,040	0.558	17.7	0.53	9.3	14.6
Average (%CV)		0.56 (0.5)	17.7 (3.8)	0.54 (1.5)	9.5 (4.9)	13.8 (5.8)
EPU0FB-7	3,925	0.561	16.5	0.53	8.8	14.0
EPU0FB-8	3,844	0.583	17.7	0.50	8.9	14.1
EPU0FB-9	3,894	0.565	16.6	0.51	8.4	14.1
Average (%CV)		0.569 (2)	16.9 (3.8)	0.51 (2.7)	8.7 (2.5)	14.1 (0.6)

For 0-PU front coated samples, the energy absorption density at strain rates near 2,700/s was 31% higher than energy absorption density at strain rates near 3,900/s. Whereas, 0-PU back coated samples showed 46% higher energy absorption density at upper limit than at the lower limit. This indicated that the energy absorption density of both 0-PU front and back coated specimens were strain rate sensitive. From Figure 5.57 is evident that at a strain rate of 2,500/s, front-back coating showed 51% improvement in energy

**Table 5.10. Energy Absorption Density of 10-PU Coated Eco-Core at various Strain Rates**

Specimen#	Strain Rate, /s	Density, g/cc	Strength, $\sigma_c$ , MPa	Strain limit, $\epsilon_1$ , m/m	Energy Absorption Density, MPa	
					Approximate method	Area method
EPU10F-7	---	0.600	---	---	---	---
EPU10F-8	2,919	0.600	20.5	0.53	10.9	15.2
EPU10F-9	2,666	0.608	20.7	0.49	10.2	12.9
Average (%CV)		0.603 (0.8)	20.6 (0.8)	0.51 (5.2)	10.5 (4.5)	14 (11.7)
EPU10F-3	3,649	0.561	18.3	0.58	10.7	18.1
EPU10F-10	3,401	0.595	21.6	0.55	12.0	17.9
EPU10F-11	3,553	0.601	21.5	0.59	12.7	20.5
Average (%CV)		0.586 (3.6)	20.5 (9.1)	0.58 (3.3)	11.8 (8.5)	18.8 (7.6)
EPU10B-4	2,327	0.581	18.6	0.50	9.2	12.7
EPU10B-5	2,928	0.577	18.6	0.53	9.8	14.5
EPU10B-6	2,860	0.591	18.9	0.51	9.6	13.4
Average (%CV)		0.583 (1.2)	18.7 (1.0)	0.51 (3.0)	9.5 (3.1)	13.5 (6.6)
EPU10B-7	3,640	0.600	18.9	0.55	10.4	17.9
EPU10B-8	3,591	0.602	19.8	0.55	10.8	18.0
EPU10B-9	3,625	0.598	20.3	0.56	11.4	19.1
Average (%CV)		0.6 (0.3)	19.7 (3.4)	0.55 (1.6)	10.9 (4.7)	18.3 (3.7)
EPU10FB-4	2,761	0.667	---	---	---	13.6
EPU10FB-6	2,579	0.660	---	---	---	14.3
EPU10FB-14	2,429	0.661	---	---	---	13.8
Average (%CV)		0.663 (0.6)	---	---	---	13.9 (2.6)
EPU10FB-7	3,569	0.689	---	---	---	14.4
EPU10FB-8	3,572	0.685	---	---	---	15.0
EPU10FB-9	3,478	0.665	---	---	---	15.1
Average (%CV)		0.68 (1.9)	---	---	---	14.8 (2.6)

absorption density when compared base Eco-Core whereas front and back coatings showed an improvement of 33% and 12%, respectively. For 0-PU front coated samples, the energy absorption density at strain rates near 2,700/s was 31% higher than energy absorption density at strain rates near 3,900/s. Whereas, 0-PU back coated samples showed 46% higher energy absorption density at upper limit than at the lower limit. This indicated that the energy absorption density of both 0-PU front and back coated

specimens were strain rate sensitive. From Figure 5.57 is evident that at a strain rate of 2,500/s, front-back coating showed 51% improvement in energy absorption density when compared base Eco-Core whereas front and back coatings showed an improvement of 33% and 12%, respectively. At a strain rate near 3,100/s, the increase of energy absorption density was in the order of Front coating (23%) > Front-Back coating (21%) > Back coating (10%). Whereas at upper limit of strain rate (~3900/s), both front and back coated specimens showed 18% higher energy absorption density when compared to front-back coated specimens.

In order to check the effect of density on the energy absorption, the ratio of density of modified Eco-Core and Eco-Core ( $\rho_{\text{Modified}}/\rho_{\text{Eco-Core}}$ ) was used to normalize the energy absorption density data. The normalized energy absorption density for 0-PU specimens is illustrated in Figure 5.58. It is clear that all the 0-PU specimens showed the trend quite similar to that of Figure 5.57 except with a marginal reduction in the y-axis values. Results in Figure 5.58 show, for example, at a strain rate of 2,500/s, front-back coating showed 50% improvement in energy absorption density when compared base Eco-Core whereas front and back coatings showed an improvement of 39% and 19%, respectively. At a strain rate near 3,100/s, the increase of energy absorption density is in the order Front coating (26%) > Front-Back coating (19%) > Back coating (15%). Whereas at strain rate near 3,900/s, both front and back coated specimens showed 20% higher energy absorption density than front-back coated specimens.

Figure 5.59 summarizes the energy absorption density of 10-PU coated Eco-Core as function of strain rate. It was observed that the energy absorption density was found to be increasing linearly with an increase in the strain rate for all coating arrangements. The energy absorption density of 10-PU front coated samples at strain rates near 3,600/s was 59% higher than energy absorption density at strain rates near 2,600/s. Whereas, 10-PU back coated samples showed 50% higher energy absorption density at upper limit than at the lower limit. This indicated that the energy absorption density of both 10-PU front and back coated specimens were strain rate sensitive. Figure 5.59 it is clear that at a strain rate of 2,500/s, front-back coating showed 51% improvement in energy absorption density

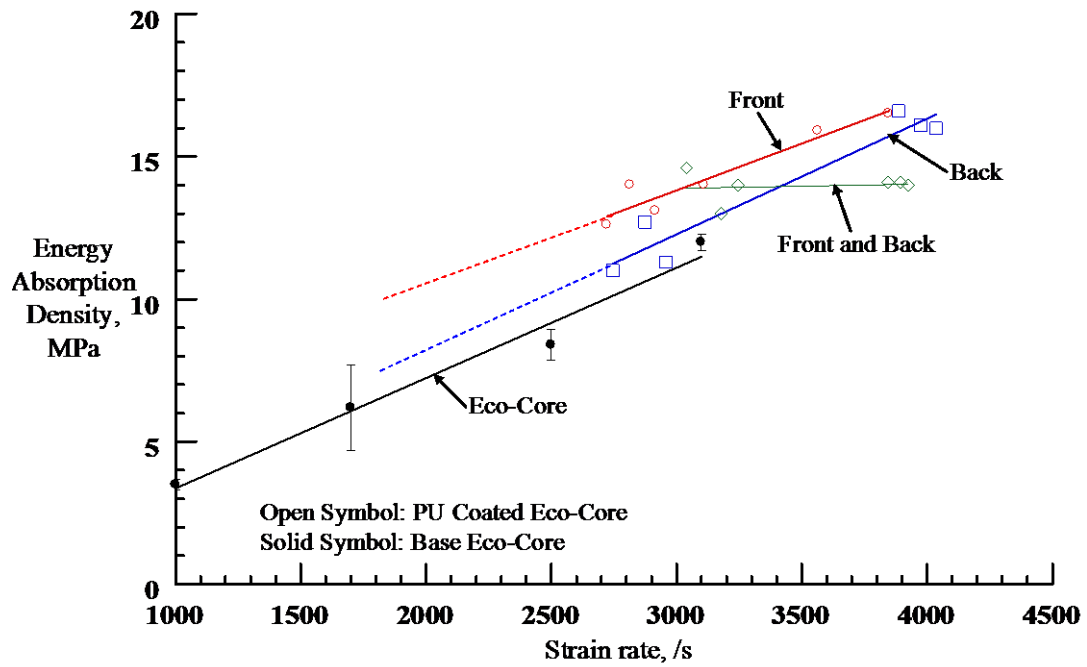


Figure 5.57. Energy Absorption Density vs. Strain Rate for 0-PU Coated Eco-Core

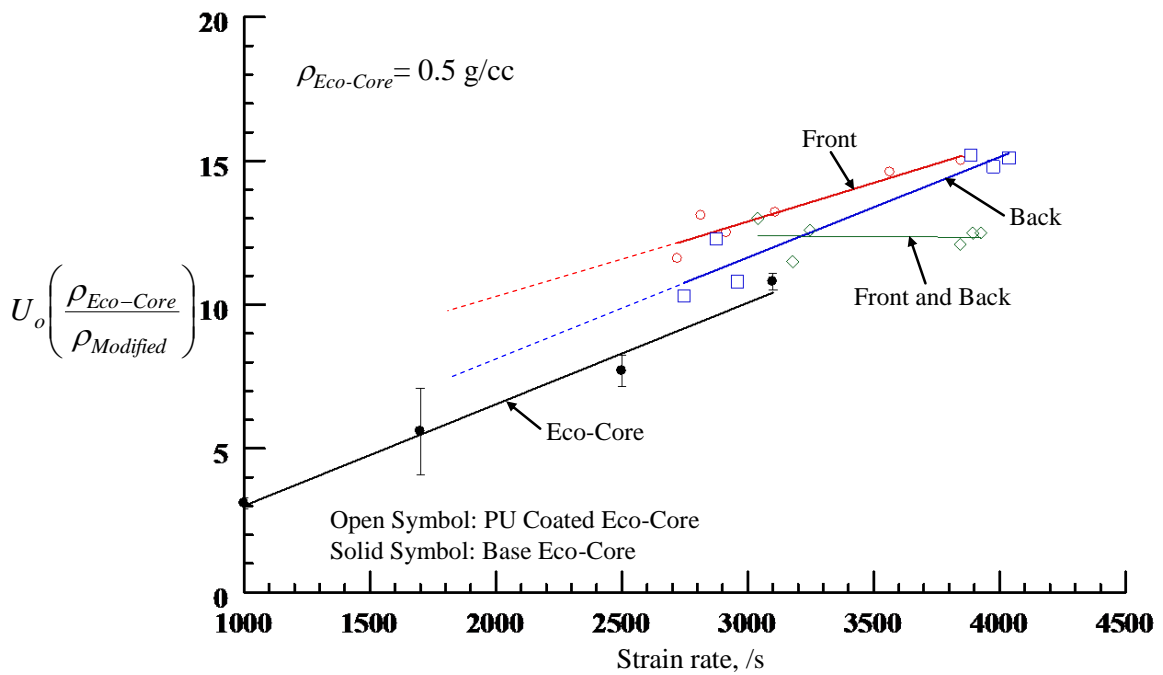


Figure 5.58. Normalized Energy Absorption Density vs. Strain Rate for 0-PU Coated Eco-Core

when compared base Eco-Core whereas front and back coatings showed an improvement of 33% and 39%, respectively. At a strain rate near 3,100/s, the increase of energy absorption density was in the order of Front coating (40%) > Back coating (36%) > Front-Back coating (25%). Whereas at strain rates near 3600/s, front and back coated specimens showed 37% and 27% higher energy absorption density than front-back coated specimens, respectively. The comparison of Figures 5.57 and 5.59 revealed that 10-PU coated Eco-Core showed higher energy absorption density than the 0-PU coated Eco-Core for all coating arrangements.

The normalized energy absorption density data for 10-PU specimens is illustrated in Figure 5.60. It is clear that all the 10-PU specimens showed the trend very similar to that of Figure 5.59 except with a marginal reduction in the y-axis values. Results in Figure 5.60 show, for example, at a strain rate of 2,500/s, front-back coating showed 26% improvement in energy absorption density when compared base Eco-Core whereas front and back coatings showed an improvement of 18% and 32%, respectively. At a strain rate near 3,100/s, the increase of energy absorption density was in the order of Front coating (29%) > Back coating (27%) > Front-Back coating (3%). Whereas at strain rate near 3,600/s, front and back coated specimens showed 56% and 47% higher energy absorption density than front-back coated samples, respectively.

### ***5.3.2 Polyurethane Impregnated Eco-Core***

#### ***5.3.2.1 Sample Preparation***

Details of preparation of polyurethane impregnated samples and the reason for this study is explained in section 3.3.2.2. The dynamic testing of polyurethane impregnated Eco-Core samples was performed. The additional details of specimen preparation for the dynamic test are explained in section 5.2.1. Table 5.11 lists the dimensions and density of the impregnated specimens. The density of the specimen lies in the range of 0.78 - 0.83 g/cc with an average value of 0.81 g/cc and coefficient of variation of 2%. The specimens length were quite uniform with variation from 3.12 to 3.20 mm. Figure 5.61 show photograph of specimens used in the current study.

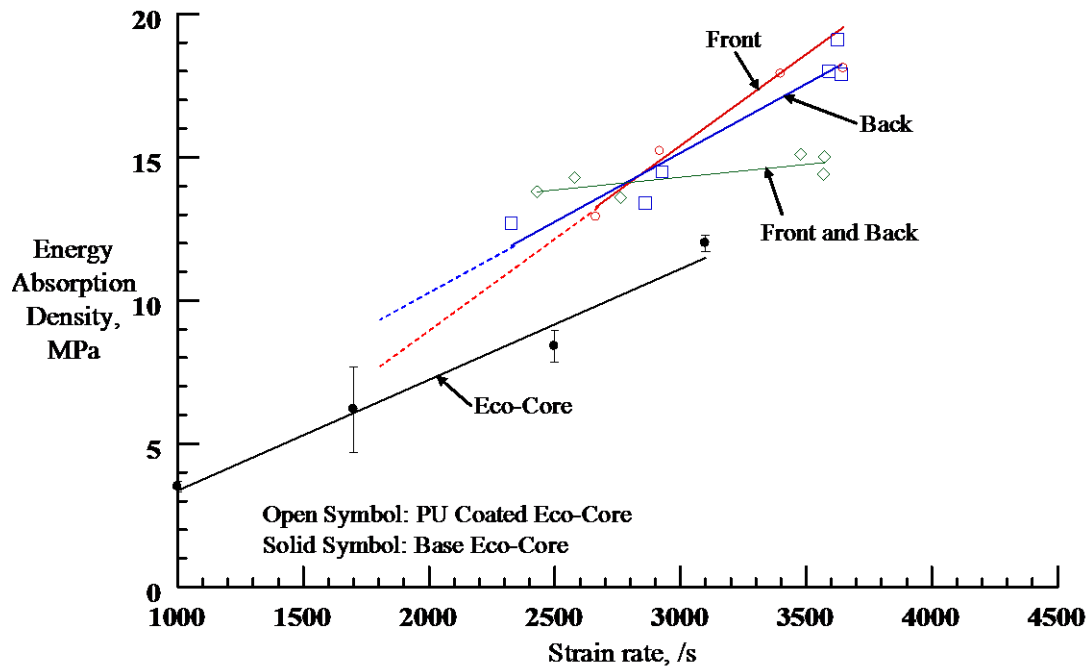


Figure 5.59. Energy Absorption Density vs. Strain Rate for 10-PU Coated Eco-Core

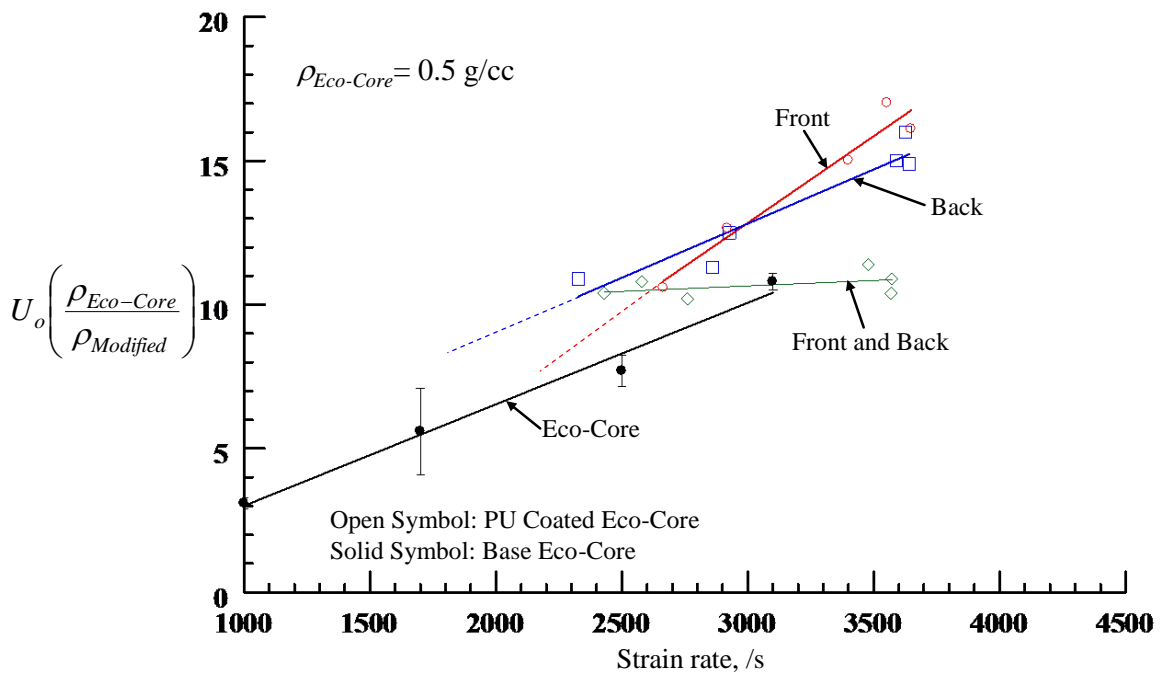


Figure 5.60. Normalized Energy Absorption Density vs. Strain Rate for 10-PU Coated Eco-Core

The dynamic characterization of polyurethane impregnated Eco-Core samples were carried out using Split Hopkinson Pressure Bar test by following the test procedure, data recording and analysis as outlined in section 4.7.

### **Figure 5.61. Polyurethane Impregnated Eco-Core Specimens**

#### *5.3.2.2 Test Matrix*

Dynamic characterization of impregnated Eco-Core samples was performed using Split Hopkinson Pressure Bar set up (SHPB). The effect of strain rate on the compressive stress-strain response of impregnated Eco-Core was studied. The strain rate was varied by changing the breech pressure which in turn changed the striker velocity. A range of strain rates from 1,000/s to 3,200/s were obtained by changing the breech pressure from 13 psi to 26 psi during SHPB tests. All tests were conducted in the ambient conditions. Three specimens were tested for each case.

#### *5.3.2.3 Results and Discussions – Impregnated Eco-Core*

##### (a) Dynamic stress-strain response

The high strain rate compressive behavior of the polyurethane (PUR) impregnated Eco-Core was measured using the SHPB apparatus at strain rates in the range 1,000/s to 3,200/s. Three experiments were conducted at each strain rate level to account for variations in specimen density and microstructure. Figure 5.62 illustrates the dynamic compressive

**Table 5.11. Density and Dimensions of Polyurethane Impregnated Eco-Core Specimens**

Specimen #	Diameter (D), mm				Length (L), mm				Weight, g	Density, g/cc
	1	2	3	Avg.	1	2	3	Avg.		
EPUR1	12.27	12.26	12.24	12.26	3.18	3.18	3.18	3.18	0.294	0.785
EPUR2	12.23	12.22	12.24	12.23	3.18	3.18	3.16	3.17	0.294	0.789
EPUR3	12.22	12.27	12.27	12.25	3.14	3.15	3.14	3.14	0.295	0.797
EPUR6	12.24	12.26	12.26	12.25	3.20	3.20	3.20	3.20	0.296	0.785
EPUR7	12.26	12.26	12.24	12.25	3.18	3.18	3.16	3.17	0.299	0.800
EPUR8	12.26	12.26	12.22	12.24	3.14	3.18	3.19	3.17	0.295	0.791
EPUR11	12.24	12.23	12.26	12.24	3.19	3.18	3.18	3.18	0.302	0.807
EPUR12	12.34	12.29	12.28	12.31	3.18	3.16	3.15	3.16	0.305	0.811
EPUR13	12.22	12.24	12.23	12.23	3.20	3.20	3.20	3.20	0.302	0.803
EPUR16	12.29	12.32	12.31	12.31	3.18	3.18	3.18	3.18	0.310	0.821
EPUR17	12.29	12.31	12.31	12.30	3.15	3.12	3.12	3.13	0.309	0.830
EPUR18	12.34	12.32	12.29	12.32	3.14	3.12	3.12	3.13	0.310	0.831
EPUR21	12.42	12.43	12.42	12.42	3.20	3.20	3.20	3.20	0.321	0.827
EPUR22	12.37	12.38	12.40	12.38	3.18	3.18	3.18	3.18	0.323	0.834
EPUR23	12.47	12.48	12.50	12.48	3.18	3.18	3.18	3.18	0.316	0.813

stress-strain response of PUR impregnated Eco-Core at strain rates near 1,000/s. The stress-strain curves are plotted in measures of engineering stress and engineering strain. All the dynamic compressive stress-strain curves showed very similar response, therefore the results were repeatable. There exists a nearly linear elastic region where the axial strain is less than 1%. Then the stress remained nearly constant with increasing strain until the strain reaches 13%. The peak dynamic compression strength was around 58 MPa and the dynamic plateau (cell collapse stress) stress was around 50 MPa which was 2.5 times higher than that of Eco-Core.

Figure 5.63 presents the dynamic compressive stress-strain response of polyurethane impregnated Eco-Core at strain rates near 1,700/s. The strain rate ranged from 1,636/s to 1,725/s. Dynamic compressive experiments on the impregnated Eco-Core showed constitutive behaviors very similar to the stress-strain curves shown in Figure 5.62, except for the strain levels. All the stress-strain curves were close to each other

regardless of strain rates. The peak dynamic compression strength was around 54 MPa and the plateau stress was around 48 MPa. Figure 5.63 revealed a linear elastic portion until approximately 0.5% strain and the flat region until the axial strain reached 30%.

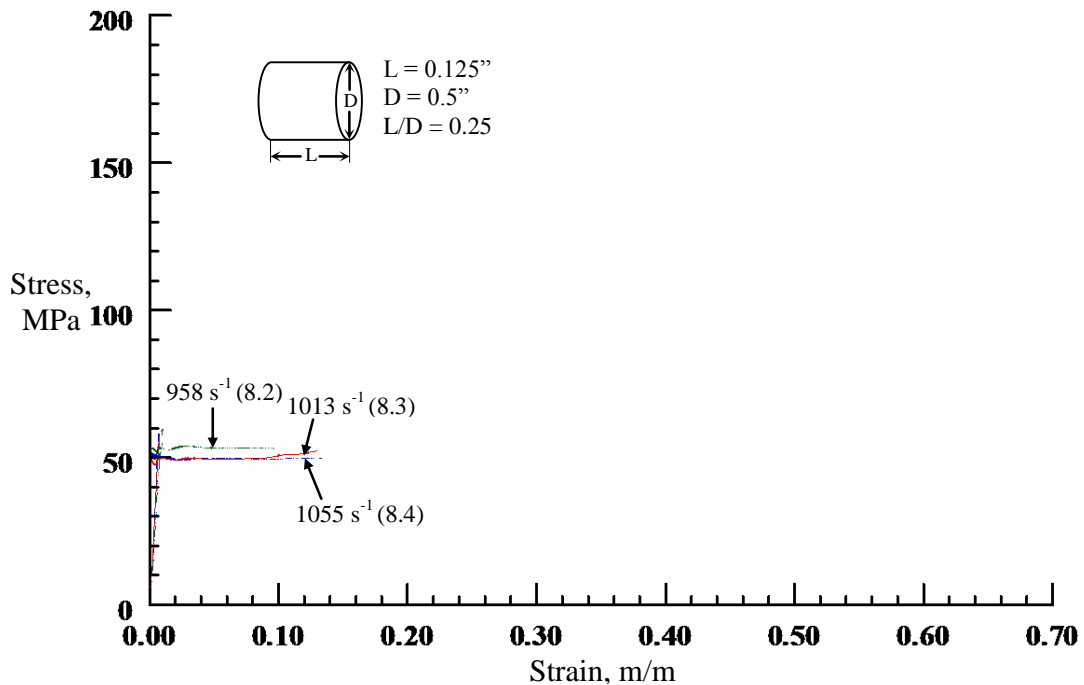
Figure 5.64 summarizes the dynamic compressive stress-strain curves for the PUR impregnated Eco-Core at strain rates near 2,300/s. The strain rate ranged from 2,246/s to 2,350/s. The peak dynamic compression strength was around 58 MPa and the plateau stress was around 54 MPa. There existed a nearly linear elastic region where the axial strain is less than 0.5%. After 0.5% axial strain, the curves showed little oscillations until about 4% strain. The stress-strain curves at strain level of 6 - 24% appeared puzzling because two of the specimens showed stress peaks while the other specimen showed stress softening effect. For all specimens, densification began at a strain of 24% where new and denser structures are being formed in the specimen. Furthermore, all the dynamic stress-strain curves overlapped each other at densification regime.

Figure 5.65 presents the dynamic compressive stress-strain response of the impregnated Eco-Core at strain rate near 2,800/s. The strain rate ranged from 2,795/s to 2,871/s. All the dynamic compressive stress-strain curves showed very similar characteristics. The peak dynamic compression strength was around 57 MPa and the plateau stress was around 52 MPa. Two of the specimens exhibited stress softening effect beyond 5% strain where the stress slowly decreases with increase in strain while the other specimen showed nearly flat stress zone until the strain reaches 17%. Beyond 17% strain, the stress-strain curve rose monotonically until unloading.

Figure 5.66 illustrates the dynamic compressive stress-strain curves for impregnated Eco-Core specimens at strain rates near 3,200/s. The strain rate ranged from 3,108/s to 3,206/s. Figure 5.66 again showed similar stress-strain curves as that of the impregnated specimens tested at strain rate near 2,800/s but with a prominent stress plateau and the densification stage. All the dynamic compressive stress-strain curves showed similar response. The peak dynamic compression strength was around 58 MPa and the plateau stress was around 56 MPa. There existed a nearly linear elastic region where the axial strain is less than 0.2%. After 0.2% axial strain, the curves showed little

oscillations till about 2% strain. Then the stress remained nearly constant with increasing strain until the strain reaches 21%, where the slope of the stress-strain curve becomes positive thereby indicating the onset of densification. The stress-strain curve then rose monotonically until unloading.

Figure 5.67 summarizes the dynamic compressive stress-strain curves at strain rates from 1,000 to 3,200/s for PUR impregnated Eco-Core. The stress-strain curves presented in Figure 5.67 were average curves of the repeatable data at each strain rate. At strain rates below 1,700/s, impregnated Eco-Core exhibited an initial elastic regime followed by a flat cell collapse phase whereas at strain rates above 1,700/s, the densification is observed as an addition mode of failure. Within strain rate of 1,700/s, all the dynamic stress-strain curves overlapped each other thereby indicating that the stress-strain response is insensitive to strain rate below 1,700/s. At strain rates above 2,300/s, the plateau stress was approximately 10% higher. This indicated that at strain rates beyond 2,300/s, the impregnated Eco-Core was mildly sensitive to strain rates.



**Figure 5.62. Dynamic Compressive Stress-Strain Curves for Polyurethane Impregnated Eco-Core at a Strain Rate ~1,000/s**

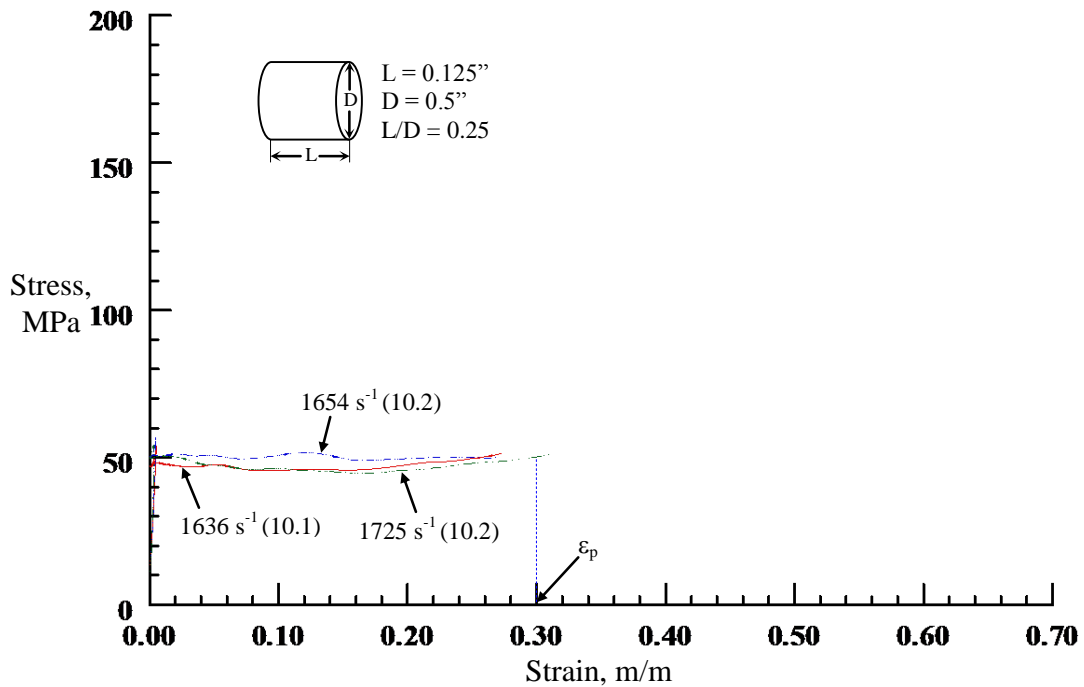


Figure 5.63. Dynamic Compressive Stress-Strain Curves for Polyurethane Impregnated Eco-Core at a Strain Rate  $\sim 1,700/s$

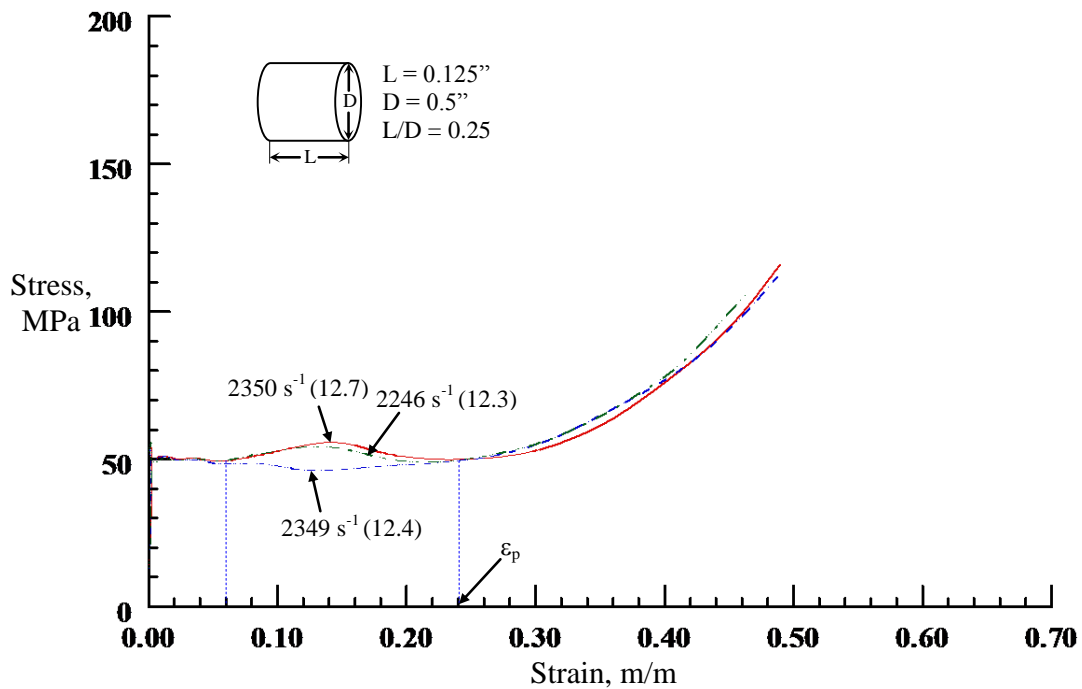


Figure 5.64. Dynamic Compressive Stress-Strain Curves for Polyurethane Impregnated Eco-Core at a Strain Rate  $\sim 2,300/s$

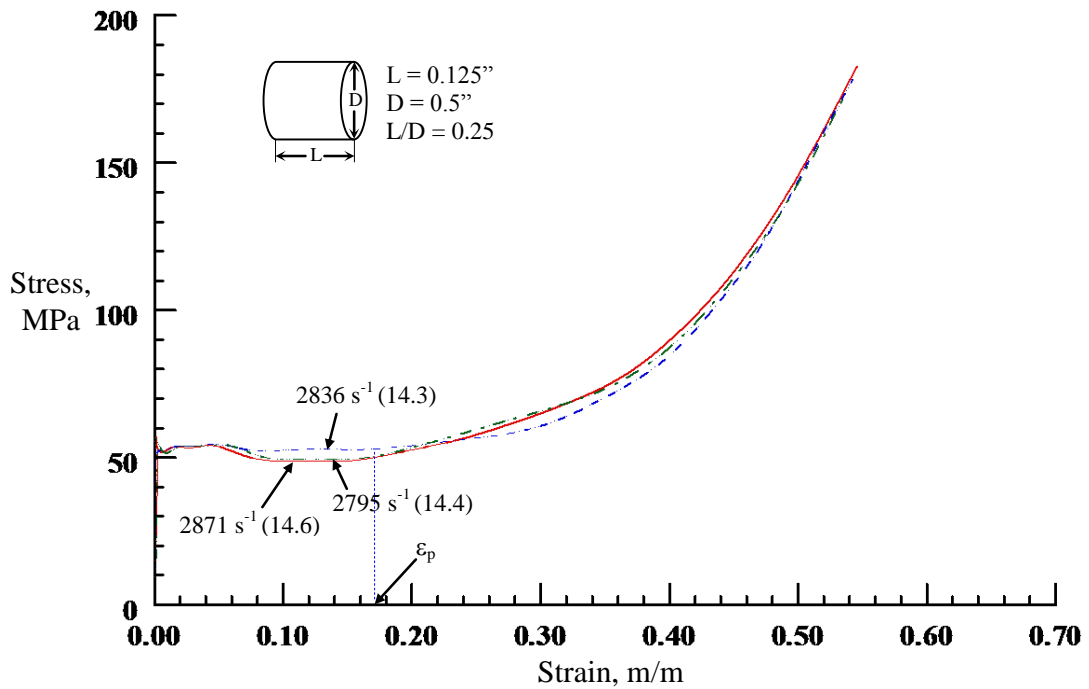


Figure 5.65. Dynamic Compressive Stress-Strain Curves for Polyurethane Impregnated Eco-Core at a Strain Rate ~2,800/s

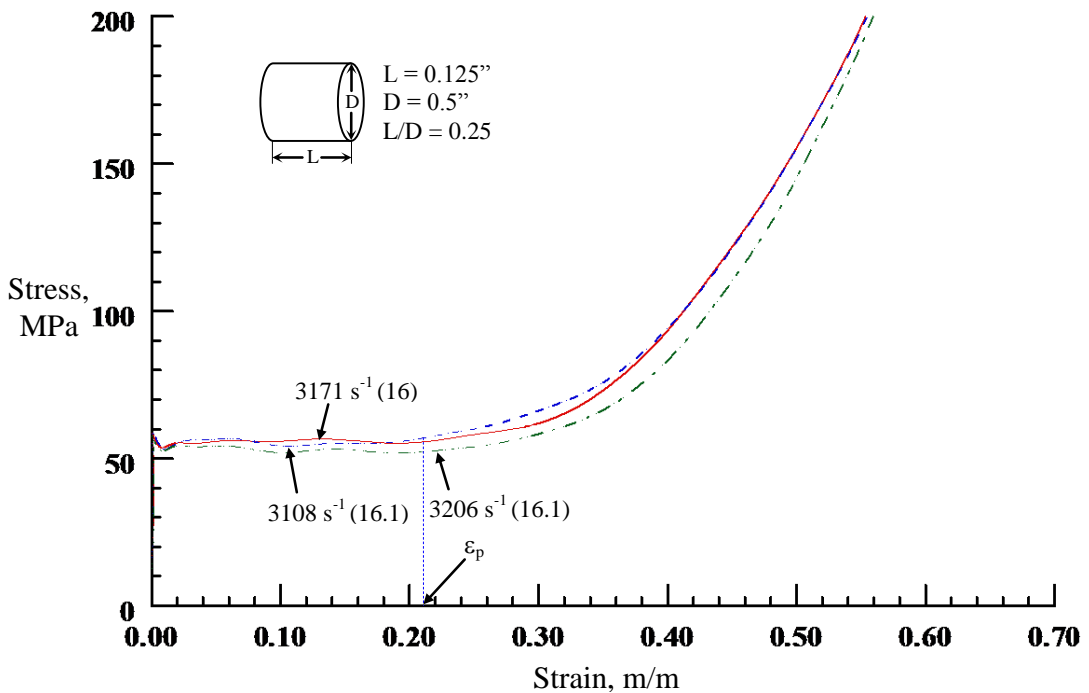
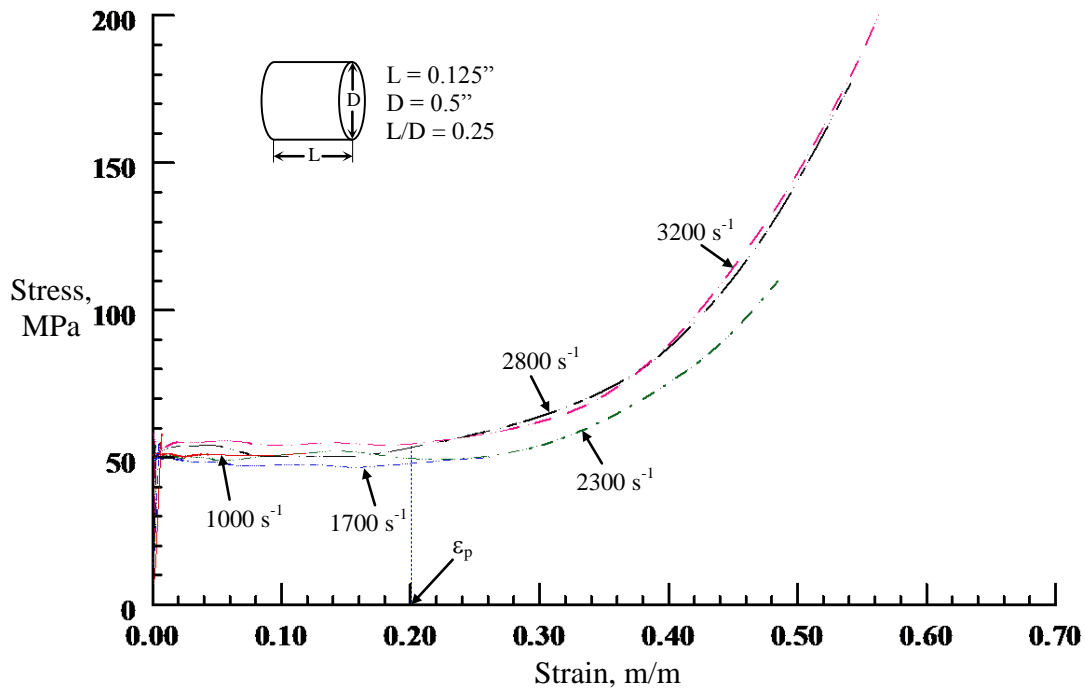


Figure 5.66. Dynamic Compressive Stress-Strain Curves for Polyurethane Impregnated Eco-Core at a Strain Rate ~3,200/s



**Figure 5.67. Average Stress-Strain Curves for Polyurethane Impregnated Eco-Core at Strain Rates from 1,000/s to 3,200/s**

(b) High Speed Image Analysis of the Dynamic Phenomenon

A Phantom 650 high-speed digital camera was employed to obtain high speed images of specimens during the dynamic deformation. Figure 5.68 shows a series of images at a time interval of 30.8  $\mu$ s during a SHPB test on impregnated Eco-Core sample at a strain rate of  $\sim 3000/s$ . Time  $t = 0$  occurred just before the loading pulse arrives at the incident bar/specimen interface. The sample deformed uniformly, obtaining nearly uniform homogeneous uniaxial compression deformation until approximately 154  $\mu$ s. Then the specimen crushed to multiple fragments. Unlike in the case of baseline Eco-Core and PU coated Eco-Core samples, no rapid lateral ejection of the crushed debris was observed. The photograph of the crushed specimen after dynamic testing is shown in Figure 5.69.

t = 0  $\mu$ s      t = 30.8 $\mu$ s      t = 61.6 $\mu$ s      t = 92.4 $\mu$ s      t = 123.2 $\mu$ s

t = 154.0 $\mu$ s      t = 184.8 $\mu$ s      t = 215.6 $\mu$ s      t = 246.4 $\mu$ s      t = 277.2 $\mu$ s

t = 308.0 $\mu$ s      t = 338.8 $\mu$ s      t = 369.6 $\mu$ s      t = 400.4 $\mu$ s      t = 431.2 $\mu$ s

**Figure 5.68. Photographs Recorded During a High Strain Rate Compression Test on PUR Impregnated Eco-Core at a Strain Rate  $\sim$  3,000/s (Time Interval: 30.8 $\mu$ s)**



**Figure 5.69. Impregnated Eco-Core Specimen after Dynamic Testing**

### 5.3.2.3.1 Energy Absorption

The energy absorption density for impregnated Eco-Core samples were calculated as per the methods explained in section 5.2.3.4. The calculated energy absorption density values were listed in Table 5.12 for polyurethane impregnated Eco-Core samples. From the Table 5.12 it is observed that the energy absorption density values calculated from approximate and area method were close to each other (with in 5%) at strain rates  $\leq 2,300/s$ . At strain rates above 2,300/s, the energy absorption density calculated from area method is 7% higher than energy absorption density calculated from approximate method. This is due to the reason that the approximate method ignores the part of the area under the curve.

**Table 5.12. Energy Absorption Density of Polyurethane Impregnated Eco-Core at Various Strain Rates**

Specimen#	Strain Rate, /s	Density, g/cc	Strength, $\sigma_c$ , MPa	Strain limit, $\epsilon_1$ , m/m	Energy Absorption Density, MPa	
					Approximate method	Area method
EPUR-1	1,013	0.785	49.6	0.13	6.4	6.3
EPUR-2	1,055	0.789	49.7	0.13	6.6	6.5
EPUR-3	958	0.797	53.3	0.10	5.2	4.9
Average (%CV)		0.79 (0.7)	50.9 (4.2)	0.12 (17.0)	6.1 (13.3)	5.9 (14.4)
EPUR-6	1,636	0.785	47.5	0.27	13.0	12.8
EPUR-7	1,654	0.800	50.5	0.27	13.6	13.4
EPUR-8	1,725	0.791	48.6	0.31	15.0	14.5
Average (%CV)		0.792 (1)	48.9 (3.1)	0.28 (7.7)	13.9 (7.6)	13.6 (6.4)
EPUR-11	2,350	0.807	50.1	0.39	19.6	20.9
EPUR-12	2,349	0.811	49.8	0.37	18.5	18.9
EPUR-13	2,246	0.803	50.3	0.36	18.2	18.9
Average (%CV)		0.807 (0.5)	50.1 (0.4)	0.37 (4.0)	18.8 (4.0)	19.6 (5.9)
EPUR-16	2,871	0.821	54.0	0.39	20.9	22.5
EPUR-17	2,836	0.830	53.8	0.39	21.2	22.5
EPUR-18	2,795	0.831	53.7	0.39	21.1	22.7
Average (%CV)		0.827 (0.7)	53.9 (0.3)	0.39 (1.1)	21.1 (0.8)	22.6 (0.5)
EPUR-21	3,171	0.827	55.7	0.39	21.6	23.5
EPUR-22	3,108	0.834	56.7	0.38	21.8	23.0
EPUR-23	3,206	0.813	54.0	0.40	21.8	22.8
Average (%CV)		0.825 (1.3)	55.5 (2.5)	0.39 (2.6)	21.7 (0.4)	23.1 (1.5)

Figure 5.70 shows the effect of strain rate on energy absorption density for polyurethane impregnated Eco-Core. The variation of energy absorption density with the strain rate was non-linear. The increase of energy absorption density with strain rate is due to the fact that crushing strain increased with an increase in strain rate, hence the energy absorption density. The energy absorption density of impregnated Eco-Core was higher than Eco-Core over the entire strain rate range studied. The improvement of energy absorption density was 19% at lower limit and as high as 125% at upper limit of strain rate. The energy absorption improved significantly but with a penalty of increased density (0.82 g/cc). Figure 5.71 illustrates the normalized energy absorption density data of impregnated Eco-Core. Even for the normalized data, the impregnated Eco-Core showed 53% improvement in energy absorption density when compared base Eco-Core. The enhancement in energy absorption density was due to the significant increase in compression strength of the material.

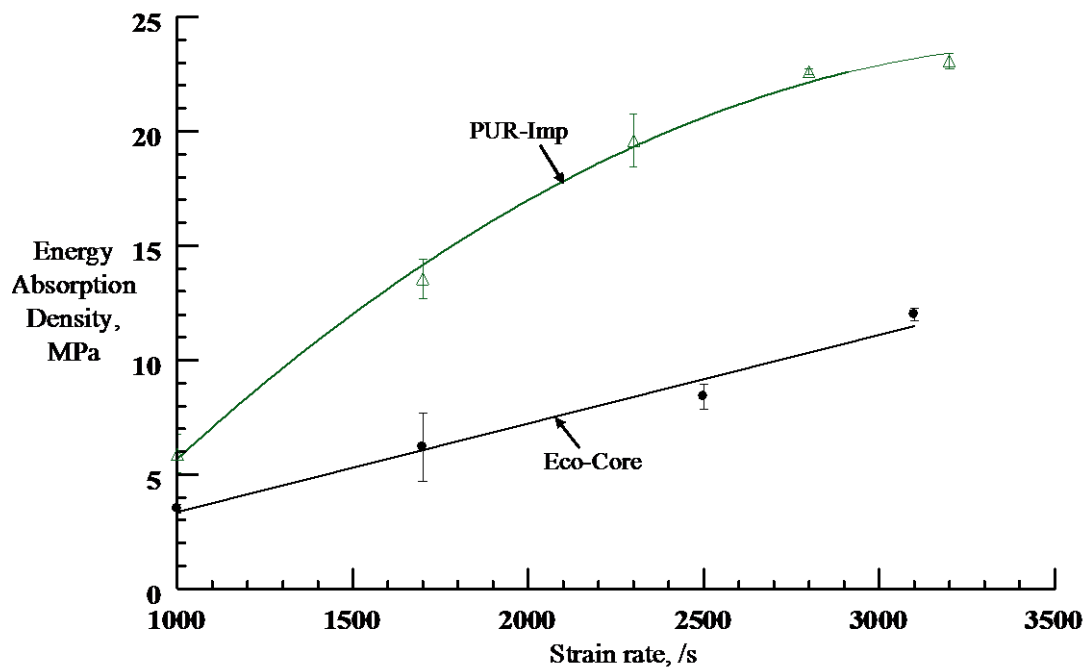


**Figure 5.70. Energy Absorption Density vs. Strain Rate for PUR Impregnated Eco-Core**

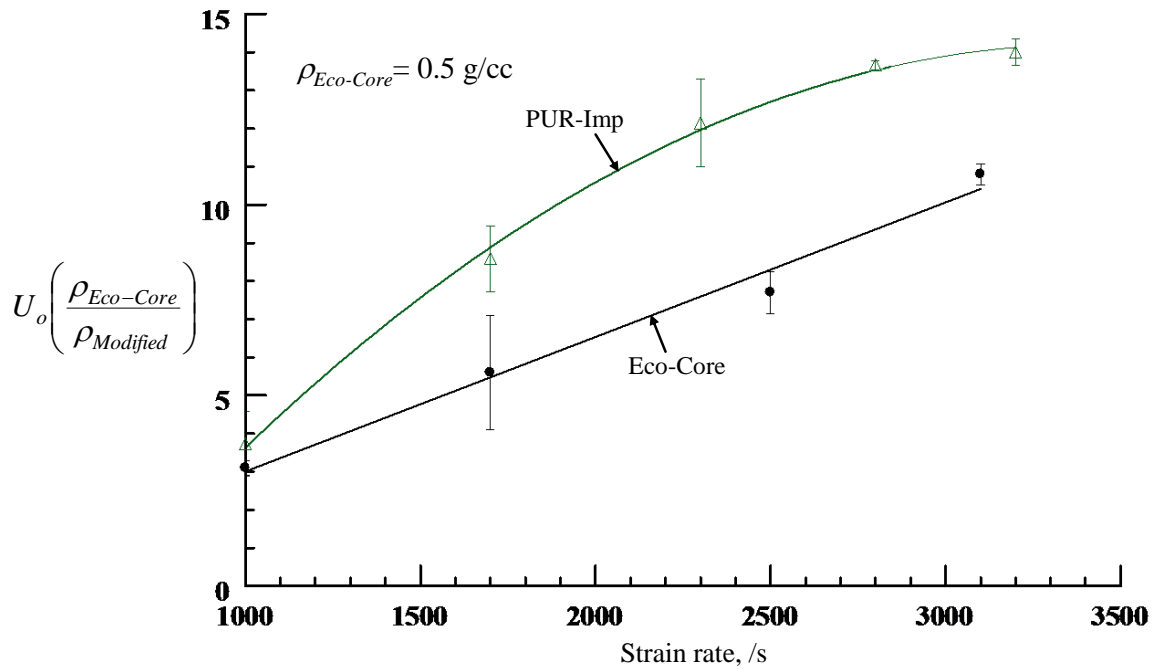
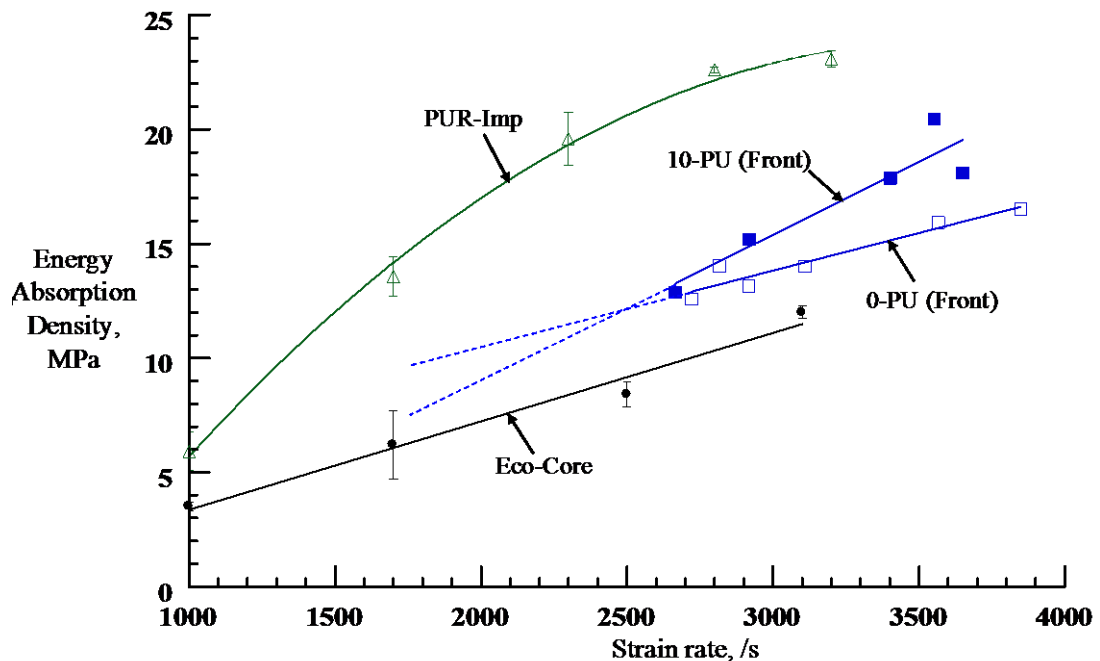


**Figure 5.71. Normalized Energy Absorption Density vs. Strain Rate for PUR Impregnated Eco-Core**

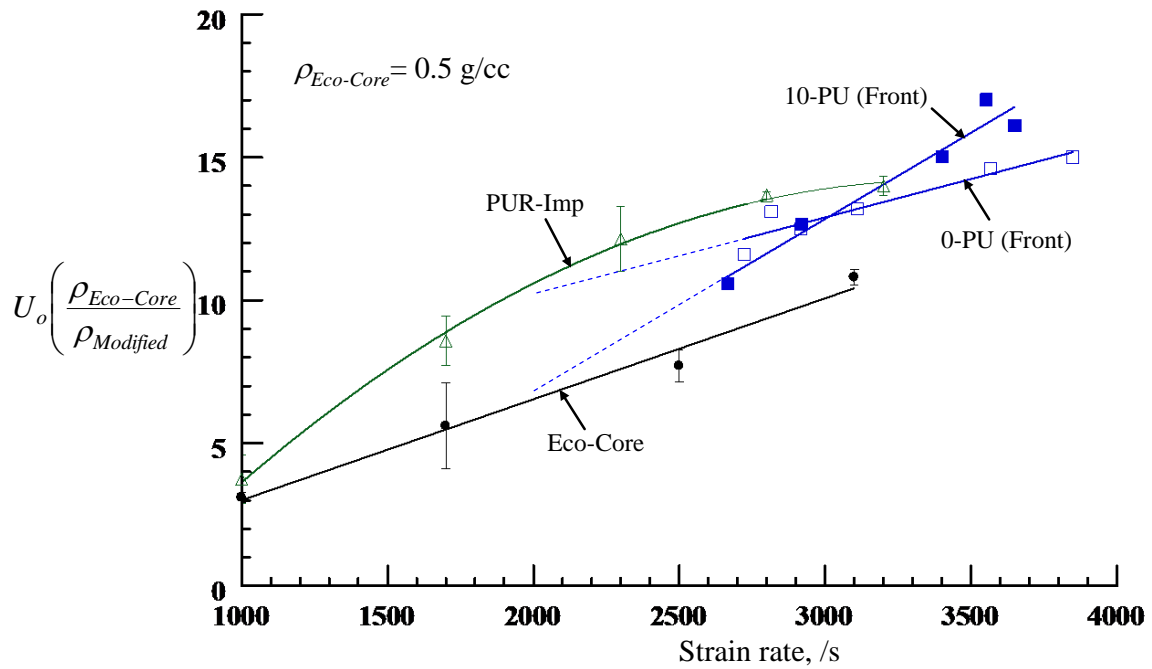
#### 5.4 Comparison of Energy Absorption Density of Eco-Core and Modified Eco-Core

Figure 5.72 shows comparison of energy absorption density for Eco-Core, polyurea coated Eco-Core, and polyurethane impregnated Eco-Core as a function of strain rate. For comparison purpose, the energy absorption density values calculated from area method was used. The energy absorption density of Eco-Core and polyurea coated Eco-Core varied linearly with strain rate whereas polyurethane impregnated Eco-Core showed non-linear trend. Both polyurea coated Eco-Core and polyurethane impregnated Eco-Core showed enhanced energy absorption density than the Eco-Core. From the Figure 5.72 is evident that at a strain rate of 2,500/s, impregnated Eco-Core showed very significant improvement of about 125% when compared base Eco-Core whereas both 0-PU front and 10-PU front coatings showed an improvement of 33%. At a strain rate near 3,100/s, the increase of energy absorption density was in the order of impregnated Eco-Core (102%) > 10-PU Front coating (39%) > 0-PU Front coating (23%).

In order to check the effect of density on the energy absorption, the ratio of density of modified Eco-Core and Eco-Core ( $\rho_{\text{Modified}}/\rho_{\text{Eco-Core}}$ ) was used to normalize the energy absorption density data. The normalized energy absorption density data for Eco-Core and modified Eco-Core specimens is illustrated in Figure 5.73. It is clear that all the specimens showed the trend very similar to that of Figure 5.72 except with a reduction in the y-axis values. Figure 5.73 showed, for example, at a strain rate of 2,500/s, polyurethane impregnated Eco-Core showed 53% improvement in energy absorption density when compared base Eco-Core whereas 0-PU and 10-PU front coatings showed an improvement of 39% and 18%, respectively. Where as at strain rates near 3,100/s, polyurethane impregnated Eco-Core showed 35% improvement in energy absorption density and 0-PU and 10-PU coated Eco-Core showed an improvement of about 26% and 29%, respectively.



**Figure 5.72. Comparison of Energy Absorption Density vs. Strain Rate for Eco-Core and Modified Eco-Core**



**Figure 5.73. Comparison of Normalized Energy Absorption Density vs. Strain Rate for Eco-Core and Modified Eco-Core**

### 5.5 Summary

The dynamic stress-strain response of base Eco-Core referred to as “Eco-Core” was measured over strain rates ranging from 1,000/s to 3,100/s with split Hopkinson pressure bar apparatus. Among various aspect ratio considered for Eco-Core specimens, specimen geometry of 3.2 mm length and 12.7 mm length with an aspect ratio  $L/D = 0.25$  were selected for the dynamic tests since it satisfied the dynamic stress equilibrium conditions. The SHPB experiments revealed that Eco-Core is independent of strain rate over the range of strain rates studied. Microbubble bond failure followed by crushing and solidification were the failure modes of Eco-Core under a dynamic loading. A phenomenological constitutive model was developed for Eco-Core and is given by

$$\frac{\sigma}{\sigma_c} = 1 + 90\varepsilon^{5.4} ; \text{ where } \sigma_c = \text{Static compression strength (20 MPa)}$$

The material model is valid for 16% and 28% strains for strain rates of 1,000 and 1,700/s respectively, and >50% strains for strain rates > 2,500/s. The SEM studies clearly showed that the amount of crushed microbubbles increases with increasing strain rate and proved that Eco-Core undergoes crushing mode of failure at high strain rates. The energy absorption density of Eco-Core linearly increases with increasing strain rate.

The dynamic compressive stress-strain responses of Eco-Core coated with polyurea in different configurations was measured at two strain rates near 3,000/s and 3,900/s. All the PU coated Eco-Core samples showed stress-strain response similar to that of Eco-Core but with a prolonged densification region. The plateau stress value of all the coated Eco-Core samples is close to that of the Eco-Core. The 10-PU front-back coated Eco-Core sample showed a prominent stress peak at strain level of 14 - 44%. Microbubble bond failure, crushing followed by formation of cleavage like straight cracks are the failure modes of polyurea coated Eco-Core under a dynamic loading. All the PU coated Eco-Core samples showed enhancement of energy absorption density. Among all the coating arrangements and thickness, 10-PU front-back Eco-Core samples showed about 51% increase of energy absorption density at a strain rate 2,500/s. Even a very thin coating (0-thickness) of polyurea on front side of Eco-Core has improved the energy absorption by 33%.

The high strain rate compressive behavior of the polyurethane impregnated Eco-Core was measured using the SHPB apparatus at strain rates 1,000/s to 3,200/s. The dynamic plateau stress is around 50 MPa which is 2.5 times higher than that of Eco-Core. The impregnated Eco-Core is not sensitive to strain rates and at strain rates below 1,700/s but at strain rates beyond 1,700/s, the impregnated Eco-Core is mildly sensitive to strain rates. Uniform crushing is the failure mode of polyurethane impregnated Eco-Core under a dynamic loading. Unlike the case of Eco-Core, no rapid lateral ejection of the crushed debris is observed for impregnated Eco-Core. The energy absorption density of Polyurethane impregnated Eco-Core varies non-linearly with strain rate. At strain rates near 3,100/s, polyurethane impregnated Eco-Core samples showed very significant improvement of about 125% increase of energy absorption density in comparison with Eco-Core but with a penalty of increased density.

## CHAPTER 6

### CONCLUDING REMARKS AND FUTURE WORK

#### 6.1 Concluding Remarks

Eco-Core was previously developed as a fire resistant core material for composite sandwich structures. It was made using a large volume of fly ash (Cenosphere) and a small volume of high char yield binder by a syntactic process. The cellular structure of the material offers a potential for shock and blast mitigation applications. The research first focused on reprocessing the Eco-Core material for its reproducibility and repeatability of static properties. Eco-Core was subsequently modified to enhance energy absorption capability. Modified Eco-Core was characterized by static confined compression tests. Because of unavailability of high strain rate test facility a compression split Hopkinson pressure bar test apparatus was designed, fabricated and validated. Both base Eco-Core and modified Eco-Core were tested at high strain rates to understand the dynamic properties of the materials.

Based on the present study, it was concluded that processing of Eco-Core is repeatable and static properties were reproducible. The confined compression testing of Eco-Core revealed different failure stages and their mechanisms such as an initial elastic regime, followed by a plateau phase and the densification. From this study a constitutive material model was developed and is given by

$$\frac{\sigma}{\sigma_c} = 1 + 45\varepsilon^{5.4}$$

where  $\sigma_c$  = compression strength (20 MPa) of the material. This equation is similar to Romberg-Osgood equation for metals. Based on the static tension, compression, flexure, shear and fracture test data, the following conclusions were made.

- The compression strength of Eco-Core was approximately 21 MPa which was nearly four times that of tensile strength and shear strength; and twice that of flexural strength
- The compression modulus of Eco-Core was approximately 1.2 GPa which is nearly one-half of the tensile modulus; 40% of the flexural modulus; and nearly same as that of shear modulus
- Fracture toughness is low and Eco-Core is brittle in nature.

The Eco-Core was modified by surface coating with polyurea and impregnation by polyurethane to improve compression strength and energy absorption density. Quasi-static confined compression tests were performed for modified Eco-Core. Surface coating with polyurea resulted in an improvement in compression strength by 12%; compression modulus by 64%; and energy absorption density by 14%. The impregnation of Eco-Core with polyurethane enhanced the compression strength by 138% with a penalty of increased density and decreased modulus.

A compression SHPB test apparatus with 7075 T6 aluminum pressure bars was successfully designed, fabricated, and developed for high strain rate testing of materials. The SHPB apparatus was verified for 6061-T651 aluminum and polycarbonate specimens and the results were in good agreement with the research literature.

The dynamic compressive stress-strain response of Eco-Core was measured over strain rates ranging from 1,000/s to 3,100/s with a split Hopkinson pressure bar apparatus. A pulse shaper was required to minimize the time required for the sample to reach force equilibrium during the high strain rate tests. Among various aspect ratio considered for Eco-Core specimens, specimen geometry of 3.2 mm length and 12.7 mm length with an aspect ratio  $L/D = 0.25$  were selected for the dynamic tests since it satisfied the dynamic stress equilibrium conditions. The SHPB experiments revealed that Eco-Core is independent of strain rate over the range of strain rates studied. Microbubble bond failure followed by crushing and solidification are the failure modes of Eco-Core under a dynamic loading. The SEM studies clearly showed that the amount of crushed microbubbles

increased with increasing strain rate and proved that Eco-Core undergoes crushing mode of failure at high strain rates. A phenomenological constitutive model was developed for Eco-Core and is given by

$$\frac{\sigma}{\sigma_c} = 1 + 90\varepsilon^{5.4}$$

where  $\sigma_c$  = Static compression strength (20 MPa) of the material. The material model is valid for 16% and 28% strains for strain rates of 1,000 and 1,700/s respectively, and >50% strains for strain rates > 2,500/s. The value of model parameter  $k$  for dynamic model is twice that of the  $k$  value of the quasi-static model ( $k = 45$ ). Therefore, one can easily obtain the dynamic characteristics of Eco-Core from the quasi static test results without having to conduct SHPB test for Eco-Core at high strain rate. The energy absorption density of Eco-Core linearly increases with increasing strain rate.

The dynamic compressive stress-strain responses of Eco-Core coated with polyurea in different configurations was measured at two strain rates near 3,000/s and 3,900/s. All the PU coated Eco-Core samples showed stress-strain response similar to that of Eco-Core but with a prolonged densification region. The plateau stress value of all the coated Eco-Core samples is close to that of the Eco-Core. The 10-PU front-back coated Eco-Core sample showed a prominent stress peak at strain level of 14 - 44%. Microbubble bond failure, crushing followed by formation of cleavage like straight cracks were the failure modes of polyurea coated Eco-Core under a dynamic loading. All the PU coated Eco-Core samples showed enhancement of energy absorption density. Among all the coating arrangements and thickness, 10-PU front-back Eco-Core samples showed approximately 51% increase of energy absorption density at a strain rate of 2,500/s. Even a very thin coating (0-thickness) of polyurea on front side of Eco-Core improved the energy absorption by 33%.

The high strain rate compressive behavior of the polyurethane impregnated Eco-Core was measured over strain rates 1,000/s - 3,200/s. The dynamic plateau stress is around 50 MPa which is 2.5 times higher than that of Eco-Core. The impregnated Eco-Core is not sensitive to strain rates below 1,700/s but at strain rates beyond 1,700/s, the impregnated

Eco-Core is mildly strain rate sensitive. Uniform crushing is the failure mode of polyurethane impregnated Eco-Core under a dynamic loading. The energy absorption density of Polyurethane impregnated Eco-Core varies non-linearly with strain rate. At strain rates near 3,100/s, polyurethane impregnated Eco-Core samples showed a very significant improvement of approximately 125% increase of energy absorption density in comparison with Eco-Core with a penalty of increased density.

## **6.2 Future Work**

The high strain rate characterization of base and modified Eco-Core introduced in this research establish a foundation for new areas of potential research for Eco-Core. Some of these areas are listed below.

- Incorporation of momentum trap for existing SHPB apparatus so that one can study the microstructural damage progression in the materials by applying a predetermined level of impact loading
- Modification of SHPB apparatus to simulate lower strain rates 100 – 1,000/s
- Characterization of Eco-Core at intermediate strain rates of 10 – 500/s to understand the response of Eco-Core at low velocity impacts
- The dynamic performance of Eco-Core under tensile, flexure, shear and fracture loading
- Blast characterization of Eco-Core. This study will be useful in exploring Eco-Core for blast mitigation applications
- High strain rate characterization of sandwich materials containing Eco-Core as a core material
- Incorporation of nanofillers/nanoreinforcements in the binder resin used for Eco-core in order to improve the strength and toughness
- FE simulation of the SHPB testing of Eco-Core using the developed constitutive model (Eq. 5.11)

## BIBLIOGRAPHY

- [1] R. A. Malloy and J. A. Hudson (1990): Foamed Composites, in S. M. Lee, ed., *International Encyclopedia of Composites*, VCH Publishers, New York, Vol. 2, pp. 257
- [2] Hiel, C., Dietman, D., and Ishai, O. (1993): Composite sandwich construction with syntactic foam core, *Composites Part A*, Vol. 24, pp. 447
- [3] Shutov, F. A. (1985): Syntactic polymer foams, *Advanced Polymer Science*, Vol. 73, pp. 63
- [4] Deanin, R. D. (1996): Polymeric Materials Encyclopedia, edited by J. C. Salamone, Vol. 4, CRC Press, New York, pp. 2554
- [5] Campbell, F.C. (2004): The Case Against Honeycomb Core, *SAMPE 2004*, May 16-20, Long Beach, CA
- [6] Sorathia, U. (2004): Improving the Fire Safety of Composite Materials for Naval Applications, *SAMPE 2004*, May 16-20, Long Beach, CA
- [7] Karthikeyan, C. S., Sankaran, S., Jagdish Kumar, M. N., and Kishore (2001): Processing and compressive strength of syntactic foams with and without fibrous reinforcements, *J. Appl. Polym. Sci.*, Vol.81, pp. 405-411
- [8] Rizzi, E., Papa, E., and Corigliano, A. (2000): Mechanical behavior of a syntactic foam: experiments and modeling, *Int. J. Solids. Struct.*, Vol. 37 (40), pp. 5773–5794
- [9] Bunn, P. and Mottram, J. T. (1993): Manufacture and compression properties of syntactic foams, *Composites*, Vol. 24(7), pp. 565–571
- [10] Gupta, N., Woldesenbet, E., and Mensah, P. (2004): Compression properties of syntactic foams: effect of cenosphere radius ratio and specimen aspect ratio, *Composites Part A*, Vol. 35, pp. 103 - 111
- [11] Kim, H. S. and Khamis, M. A. (2001): Fracture and impact behaviors of hollow micro-sphere/epoxy resin composites, *Composites Part A*, Vol. 32, pp. 1311-1317
- [12] Kim, H. S. and Oh, H. H. (2000): Manufacturing and impact behavior of syntactic foam, *J. Appl. Polym. Sci.*, Vol. 76, pp. 1324-1328

- [13] Olson, K. (2003): Keynote Lecture, *Proceedings of 6<sup>th</sup> International Conference on Sandwich Structures*, Fort Lauderdale, FL, March 31-April 2
- [14] Shivakumar, K., Argade, S. D., and Sadler, R. L. et al. (2006): Processing and properties of a lightweight fire resistant core material for sandwich structures, *J. Advanced Materials*, Vol. 38(1), pp. 32-38
- [15] Argade, S., Shivakumar K., and Sadler, R. L. et al. (2004) Mechanical fire resistance properties of a core material, *SAMPE 2004*, May 16-20, May 16-20, Long Beach, CA
- [16] Shivakumar, K., Sharpe, M., and Sorathia, U. (2005): Modification of Eco-Core to enhance toughness and fire resistance, *SAMPE 2005*, May 1-5, Long Beach, CA
- [17] Shivakumar, K., Sadler, R., Sharpe, M., and Argade, S. (2003), North Carolina A&T State University, Greensboro, NC, U. S. Patent Application for a “Fire Resistant Structural Member”, Docket No. 10/702,063, filed Nov. 2003
- [18] Sadler, R., Sharpe, M., and Shivakumar, K. (2007): A Comparison of Mechanical and Fire properties of Eco-Core with a Competitive Commercial Material, *SAMPE 2007*, June 4-7, Baltimore, MD
- [19] Panduranga, R., Shivakumar, K., and Russell, Jr. L. (2007): Energy Absorption Performance of an Eco-Core – A Syntactic Foam, *48<sup>th</sup> AIAA/ASME/ASCE/AHS/ASC Structures, Structural Dynamics, and Materials Conference*, April 23 – 26, Honolulu, HI
- [20] Sadler, R. L., Sharpe, M., Panduranga, R., and Shivakumar, K. (2009): Water immersion effect on swelling and compression properties of Eco-Core, PVC foam and balsa wood, *Composite Structures*, Vol. 90, pp. 330-336
- [21] Panduranga, R., Russell, Jr L., and Shivakumar, K. (2007), Fracture toughness enhancement of fly ash based Eco-Core by glass fiber reinforcement, *22<sup>nd</sup> Annual technical conference of the American Society for Composites*, September 17-19, Seattle, WA
- [22] Nemat-Nasser S. (2000): Introduction to high strain rate testing, *ASM Handbook* Vol. 8, Mechanical Testing and Evaluation, ASM Int, Materials Park OH, pp. 427
- [23] Meyers, Marc A.(1994): Dynamic behavior of materials, John Wiley & Sons, Inc., New York, NY, pp. 82-84

- [24] ASM Int (2000): *ASM Handbook*, Mechanical Testing and Evaluation, edited by Howard Kuhn and Dana Medlin, Vol 8, ASM Int, Materials Park OH, pp. 436, 462-476
- [25] Hopkinson, J. (1901): On the rupture of iron wire by a blow (1872), Article 38, *Original Papers-by the late John Hopkinson, Vol II, Scientific Papers*, B Hopkinson (ed.), Cambridge Univ Press, pp.316-320
- [26] Hopkinson, J. (1901): Further experiments on the rupture of iron wire (1872), Article 39, *Original Papers-by the late John Hopkinson, Vol II, Scientific Papers*, B Hopkinson (ed.), Cambridge Univ Press, pp. 316-320
- [27] Hopkinson, B. (1914): A method of measuring the pressure produced in the detonation of high explosives or by the impact of bullets, *Philos. Trans. R. Soc. London, Ser. A* 213, pp. 437-456
- [28] Davies, R. M. (1948), A critical study of the Hopkinson pressure bar, *Philos. Trans. R. Soc. London, Ser. A* 240 (821), pp. 375-457
- [29] Love, A. E. H. (1934): *Mathematical Theory of Elasticity, 2nd edition*, Cambridge Univ Press.
- [30] Pochhammer, L. (1876): Uber Fortplanzungsgeschwindigkeiten kleiner Schwingungen in einem unbergrenzten isotropen Kreiszyylinder, *J. Reine Angew. Math.*, Vol. 81, pp. 324 (German)
- [31] Chree, C. (1889): The equations of an isotropic elastic solid in polar and cylindrical coordinates, their solution and applications, *Trans. Cambridge Philos. Soc.*, Vol. 4, pp. 251-369
- [32] Bancroft, D. (1941): The velocity of longitudinal wave in cylindrical bars, *Physical Review*, Vol. 59, pp. 588-593.
- [33] Kolsky, H. (1949): An investigation of the mechanical properties of materials at very high rates of loading, *Proc. Phys. Soc. London, Sect. B* 62 (II-B), pp. 676-700
- [34] Boltzmann, L. (1876), *Pogg Ann Erg*, Vol. 7, pp. 624
- [35] Taylor, G. I. (1946), *J Instn Civ Engrs*, Vol. 8, pp. 486
- [36] Gray III, G. T. and Blumenthal, W. R. (2000): Split-Hopkinson pressure bar testing of soft materials, *ASM Handbook*, Vol. 8, Mechanical Testing and Evaluation, ASM Int, Materials Park OH, pp. 488-496

- [37] Subhash, G. and Ravichandran, G. (2000): Split-Hopkinson pressure bar testing of ceramics, *ASM Handbook*, Vol. 8, Mechanical Testing and Evaluation, ASM Int, Materials Park OH, 488-496
- [38] Gray III, G. T., Idar, D.J., Bluementhal, W.R., Cady, C. M., and Peterson, P.D. (2000): High- and low-strain rate compression properties of several energetic material composites as a function of strain rate and temperature, *11th Detonation Symposium*, Snow Mass CO, edited by J. Short, Amperstand Publication
- [39] Field, J. E., Walley, S.M., Bourne, N.K., and Huntley, J. M. (1998): Review of experimental techniques for high rate deformation studies, *Proc Acoustics and Vibration Asia '98*, Singapore, pp. 9-38
- [40] Gray III, G. T., Bluementhal, W.R., Trujillo, C. P., and Carpenter II, R. W. (1997): Influence of temperature and strain rate on the mechanical behavior of Adiprene L-100, *J Phys (France) IV Colloq, C3 (EURODYMAT 97)*, Vol. 7, pp. 523-528
- [41] Gary, G., Klepaczko, J. R., and Zhao, H. (1995): Generalization of split Hopkinson bar technique to use visco elastic materials, *Int. J. Impact Eng.* Vol. 16, pp. 529-530
- [42] Gary, G., Rota, L., and Zhao, H. (1996): Testing viscous soft materials at medium and high strain rates, *Constitutive Relation in High/Very High Strain Rates*, edited by K. Kawata and J. Shioiri, Springer-Verlag, Tokyo, pp. 25-32
- [43] Chen, W., Zhang, B., and Forrestal, M. J. (1999): A split Hopkinson bar technique for low impedance materials, *Exp. Mech.* Vol. 39, pp. 1-5
- [44] Rogers, W. P. and Nemat-Nasser, S. (1990): Transformation Plasticity at High Strain Rate in Magnesia-Partially-Stabilized Zirconia, *J. Am. Ceram. Soc.*, Vol. 73, pp. 136-139
- [45] Chen, W. and Ravichandran, G. (1997): Dynamic Compressive Failure of a Glass Ceramic Under Lateral Confinement, *J. Mech. Phys. Solids*, Vol. 45, pp. 1303-1328
- [46] Frew, D. J., Forrestal, M. J., and Chen, W. (2001): A Split Hopkinson Bar Technique to Determine Compressive Stress-strain Data for Rock Materials, *Experimental Mechanics*, Vol. 41, pp. 40-46
- [47] Franz, C. E., Follansbee, P. S., and Wright, W. J. (1984): New Experimental Techniques with the Split Hopkinson Pressure Bar, *8th International Conference on High Energy Rate Fabrication, Pressure Vessel and Piping Division. ASME*, edited by L. Berman and J. W. Schroeder, San Antonio, TX.

- [48] Follansbee, R S. (1985): “The Hopkinson Bar”, Mechanical Testing, *Metals Handbook*, 9th ed., Vol. 8, American Society for Metals, Metals Park, Ohio, pp.198-217
- [49] Follansbee, P. S., and Franz, C. E. (1983): Wave Propagation in the Split Hopkinson Pressure Bar, *Trans. ASME, J. Eng. Mat. Technol.*, Vol. 105, pp. 61-66
- [50] Ellwood, S., Griffiths, L. J., and Parry, D. J. (1982): Materials Testing at High Constant Strain Rates, *J. Phys. E: Sci. Instrum.*, Vol. 15, pp. 280-282
- [51] Duffy, J., Campbell, J. D., and Hawley, R. H. (1971): On the Use of a Torsional Split Hopkinson Bar to Study Rate Effects in 1100-0 Aluminum, *ASME J. Appl. Mech.*, Vol. 37, pp. 83-91
- [52] Wu, X. J. and Gorham, D. A. (1997), Stress Equilibrium in the Split Hopkinson Pressure Bar Test, *J. Phys. IV France*, Vol. 7, C3, pp. 91-96
- [53] Togami, T. C., Baker, W. E. and Forrestal, M. J. (1996): A Split Hopkinson Bar Technique to Evaluate the Performance of Accelerometers, *J. Appl. Mech*, Vol. 63, pp. 353-356.
- [54] Christensen, R. Z, Swanson, S. R, and Brown, W. S. (1972): Split-Hopkinson-Bar Tests on Rock Under Confining Pressure, *Experimental Mechanics*, Vol. 29, pp. 508-513
- [55] Nemat-Nasser, S., Issacs, J. B., and Starrett, J. E. (1991): Hopkinson techniques for dynamic recovery experiments, *Proc. R. Soc. London Ser. A*, Vol. 435, pp. 371–391.
- [56] Ravichandran, G. and Subhash, G. (1994): Critical Appraisal of Limiting Strain Rates for Compression Testing of Ceramics in a Split Hopkinson Pressure Bar, *J. Am. Ceram. Soc.*, Vol. 77, pp. 263-267
- [57] Chen, W., Song, B., Frew, D.J. and Forrestal, M.J. (2003): Dynamic Small Strain Measurements of a Metal Specimen with a Split Hopkinson Pressure Bar, *Experimental Mechanics*, Vol. 43, pp. 20-23
- [58] Chen, W., Wu, Q., Kang, J.H. and Winfree, N.A.(2001): Compressive Superelastic Behavior of a NiTi Shape Memory Alloy at Strain Rates of 0.001 to 750 s<sup>-1</sup>, *International Journal of Solids and Structures*, Vol. 38, pp. 8989-8998
- [59] Chen, W. and Ravichandran, G. (1996): Static and Dynamic Compressive Behavior of Aluminum Nitride under Moderate Confinement, *Journal of the American Ceramic Society*, Vol. 79, pp. 579-584

- [60] Song, B., Chen, W. and Weerasooriya, T. (2003): Quasi-Static and Dynamic Compressive Behaviors of a S-2 Glass/SC15 Composite, *Journal of Composite Materials*, Vol. 37, pp. 1723-1743
- [61] Song, B. and Chen, W. (2003): Dynamic Compressive Constitutive Behavior of EPDM Rubber, Transactions of the ASME, *Journal of Engineering Materials and Technology*, Vol. 125, pp. 294-301
- [62] Chen, W., Lu, F. and Winfree, N. (2002): High-Strain-Rate Compressive Behavior of a Rigid Polyurethane Foam with Various Densities, *Experimental Mechanics*, Vol. 42: pp. 65-73
- [63] Rizzi, E., Papa, E. and Corigliano, A. (2000): Mechanical Behavior of A Syntactic Foam: Experiments and Modeling, *International Journal of Solids and Structures*, Vol. 37, pp. 5773-5794
- [64] Corigliano, A., Rizzi, E. and Papa, E. (2000): Experimental Characterization and Numerical Simulations of a Syntactic-Foam/Glass-Fibre Composite Sandwich, *Composites Science and Technology*, Vol. 60, pp. 2169-2180
- [65] Palumbo, M. and Tempesti, E. (1998): On the Nodular Morphology and Mechanical Behavior of A Syntactic Foam Cured in Thermal and Microwave Fields, *Acta Polymer*, Vol. 49, pp. 482-486
- [66] Song, B., Chen, W., Dou, S., and Winfree, N. A. (2005): Strain-rate Effects on Elastic and Early Cell-collapse Responses of a Polystyrene Foam, *International Journal of Impact Engineering*, Vol. 31, pp. 509-521
- [67] Frew, D.J., Forrestal, M.J. and Chen, W. (2002): Pulse Shaping Techniques for Testing Brittle Materials with a Split Hopkinson Pressure Bar, *Experimental Mechanics*, Vol. 42, pp. 93-106
- [68] Song, B., Chen, W., and Frew, D.J. (2004): Dynamic Compressive Response and Failure Behavior of an Epoxy Syntactic Foam, *Journal of Composite Materials*, Vol. 38, pp. 915-934
- [69] Woldesenbet, E., Gupta, N., and Jadhav, A.(2005): Effects of Density and Strain Rate on Properties of Syntactic Foams, *Journal of Materials Science*, Vol. 40, pp. 4009-4017
- [70] Wehmer, P. (2008): High Strain Rate Characteristics of Rubber Modified Syntactic Foams, M. S. Dissertation, Mechanical Engineering Dept., Louisiana State Univ., Baton Rouge, LA

- [71] Peter, S. and Woldesenbet, E. (2008): Nanoclay syntactic foam composites-High strain rate properties, *Materials Science and Engineering A*, Vol. 494, pp. 179-187
- [72] Ashby, M. F. (1983): The Mechanical Properties of Cellular Solids, *Metallurgical Transactions A*, Vol. 14A, pp. 1755-1769
- [73] Broek, David (1987): Elementary Engineering Fracture Mechanics, Martinus Nijhoff Publishers, 3<sup>rd</sup> revised edition, pp. 181
- [74] Gupta, N., Karthikeyan, C. S., Sankaran, S., and Kishore (1999): Correlation of Processing Methodology to the Physical and Mechanical Properties of Syntactic Foams with and without Fibers, *Materials Characterization*, Vol. 43, pp. 271-277
- [75] Gupta, N. and Woldesenbet, E. (2005): Characterization of Flexural Properties of Syntactic Foam Core Sandwich Composites and Effect of Density Variation, *Journal of Composite Materials*, Vol. 39, No. 24, pp. 2197
- [76] Mock, W. W. and Balizer, E. (2005): Penetration protection of steel plates with a polyurea layer, presented at Polyurea Properties and Enhancement of Structures under Dynamic Loads, Airlie, VA
- [77] Roland, C.M., Twigg, J.N., Vu, Y., and Mott, P.H. (2007): High strain rate mechanical behavior of polyurea, *Polymer*, Vol. 48, pp. 574-578
- [78] <http://www.polyurethane-1.com/tensile-strength.htm>
- [79] Zukas, A. J., Nicholas, T., Swift, F. H., Greszczek, B. L., and Curan, R. D. (1982): Impact Dynamics, John Wiley & Sons, ISBN 0-471-28677-0, pp. 289
- [80] Hall, I. W. and Guden, M. (2003): Split Hopkinson Pressure Bar compression testing of an aluminum alloy: Effect of lubricant type, *Journal of Materials Science Letters*, Vol. 22, pp.1533-1535
- [81] Salisbury, C., (2001): Wave Propagation Through A Polymeric Hopkinson Bar, M. S. Dissertation, Mechanical Engineering Dept., Univ. of Waterloo, Waterloo, Ontario, Canada
- [82] Tagarielli, V. L., Deshpande, V. S., and Fleck, N. A. (2008): The high strain rate response of PVC foams and end-grain balsa wood, *Composites: Part B*, Vol. 39, pp. 83-91
- [83] Bonora, N. and Milella, P.P. (2001): Constitutive Modeling for Ductile Metals Behavior Incorporating Strain Rates, Temperature and Damage Mechanics, *International Journal of Impact Engineering*, Vol. 26, pp. 53-64

- [84] Dighe, M.D., Gokhale, A.M., Horstemeyer, M.F. and Mosher, D.A. (2000): Effect of Strain Rate on Damage Evolution in a Cast Al-Si-Mg Base Alloy, *Metallurgical and Materials Transactions A*, Vol. 31A, pp. 1725-1731
- [85] Song, B., Chen, W. and Weerasooriya, T. (2003): Quasi-Static and Dynamic Compressive Behaviors of a S-2 Glass/SC15 Composite, *Journal of Composite Materials*, Vol. 37, pp. 1723-1743
- [86] Randles, P.W. and Nemes, J.A. (1992): A Continuum Damage Model for Thick Composite Materials Subjected to High-Rate Dynamic Loading, *Mechanics of Materials*, Vol. 13, pp. 1-13
- [87] Park, S.W. and Schapery (1997): A Viscoelastic Constitutive Model for Particulate Composites with Growing Damage, *International Journal of Solids and Structures*, Vol. 34, pp. 931-947
- [88] Li, Y., Ramesh, K.T. and Chin, E.S.C. (2000): Viscoplastic Deformations and Compressive Damage in an A359/SiCp Metal-Matrix Composite, *Acta Materialia*, Vol. 48, pp. 1563-1573
- [89] Hilfi, H. and Brar, N.S. (1996): Johnson cook model Evaluation of Johnson-Cook Model Constants for Aluminum Based Particulate Metal Matrix Composites, *Proceedings of American Institute of Physics 96*, pp. 560
- [90] Gupta, N. and Maharsia, R. (2005): Enhancement of Energy Absorption in Syntactic Foams by Nanoclay Incorporation for Sandwich Core Applications, *Applied Composite Materials*, Vol. 12, pp. 247-261